



**University of
Nottingham**

UK | CHINA | MALAYSIA

*University of Nottingham
Faculty of Medicine and Health Sciences
School of Medicine
Division of Cancer and Stem Cells
Cancer Biology Unit Cancer
Genetics & Stem Cell Group*

**Genetic Screens in Intestinal Organoid (mini-gut)
Culture using CRISPR-Cas-9 System and Studying
the Role of FBXL5 in Colorectal Cancer Cells**

Nicholas George Jinks

MSc., BSc.

Thesis submitted to the University of Nottingham in
fulfilment for the degree of Doctor of Philosophy

November 2021

Declaration

Except where acknowledged in the text, I declare that this thesis is my own work and is based on research undertaken under the supervision of Dr Abdolrahman Shams-Nateri in the Cancer Genetics and Stem Cell Group, School of Medicine, University of Nottingham, United Kingdom.

Nicholas George Jinks

University of Nottingham Student ID: 4309885

Acknowledgements:

I would like to thank Dr Abdolrahman Shams-Nateri for his supervision of this project and Dr Hossein Kashfi for collaborating on the organoid experiments. I would like to thank the National Centre for the Replacement, Refinement and Reduction of Animals in Research (NC3Rs) for funding this research project.

I would also like to thank Dr David Onion of the University of Nottingham Flow Cytometry facility for his assistance with the Flow Cytometry experiments and Prof. Nigel Mongan for his assistance with the processing and initial analysis of the RNA-Seq data.

Finally, I would like to thank all members of Cancer Genetics and Stem Cells group and the Tumour and Vascular Biology division for their friendship and assistance during this project.

Abstract

Current *in vitro* research methods are often difficult to translate into successful gene(s) functional and clinical applications. Immortalised cell lines are monocellular, 2-dimensional and do not accurately encapsulate the *in vivo* microenvironment, while *in vivo* animal models are often impractical, prohibitively expensive and ethically contentious. As such, novel *in vitro* experimental models are required to facilitate research and improve translatability, particularly in colorectal cancer, which demonstrates great genetic and phenotypic heterogeneity. Recently, methods for the *in vitro* culture of three-dimensional (3D) derived “organoids” have been established, which faithfully reproduce the genetic, proteomic and pharmacological characteristics of their original tissue. Organoids present the opportunity to elucidate molecular mechanisms underlying functional genetic modelling, personalised medicine and drug discovery *in vitro*, thereby replacing and reducing the use of *in vivo* animal models.

In this study, we have initially combined the CRISPR/Cas-9 genome editing system and murine intestinal/colon epithelial organoid cultures to study the functional impact of genetic knockouts of the F-box family of E3 ligases, which are poorly understood in colorectal cancer development and progression. Among the 32 F-box genes we screened, five F-box knockout murine intestinal organoid lines demonstrated differential growth pattern and morphology characteristics from healthy/normal control organoids: the *fbxl5*, *fbxo31*, *fbxl18*, *fbxo17* and *fbxl17* genes.

Moreover, we selected FBXL5 (F-box/LRR-repeat protein 5) for additional functional analysis. Previous studies reported that FBXL5 plays a key role in iron homeostasis by promoting ubiquitination and degradation of the IRP2 protein and other molecules, maintaining of hematopoietic and neural stem/progenitor cell pool, hypoxia and drug

response and epithelial-to-mesenchymal transition (EMT). However, the role of FBXL5 in colorectal cancer cells is less characterised.

Furthermore, we generated CRISPR-Cas-9-mediated knockout DLD-1 and SW480 colorectal cancer cell lines to investigate the loss of FBXL5 in colorectal cancer function and activity.

We found that FBXL5 knockout significantly reduces wound healing and colony formation efficiency, and dysregulates cell morphology, epithelial-to-mesenchymal transition activity, iron homeostasis, autophagy, hypoxic cell activity and drug response in colorectal cancer cells.

In addition, toward a mechanistic approach for the characterisation of FBXL5 function and gene downstream analysis, differentially expressed genes (DEG) were identified using RNA-Seq analysis of *FBXL5*-knockout and parental DLD-1 colorectal cancer cells. Pathway mapping of the DEGs identified numerous novel FBXL5 roles, particularly under hypoxic conditions, including colorectal and pancreatic cancer, immune system function, spliceosome activity and carbon metabolism in cancer. However, further investigation is required to explore the significant loss of FBXL5 E3 ligase function and targeted proteins in patients with colorectal cancer.

In conclusion, we have demonstrated the value and practicality of organoids as a flexible *in vitro* model system for functional genetic studies, representing an important tool for improving research methodology and reducing and replacing the use of *in vivo* models in research. We also demonstrated that FBXL5 may be a key player in colorectal cancer progression, metastasis, and relapse via influences in iron homeostasis, autophagy, hypoxic cell activity and drug response.

List of publications from this study and in cooperation with other projects in the lab:

Kashfi H*, **Jinks N***, Nateri AS. Generating and Utilizing Murine Cas-9-Expressing Intestinal Organoids for Large-Scale Knockout Genetic Screening. *Methods in Molecular Biology* (Clifton, NJ). 2020; 2171:257-69. (* equal contribution)

Ahmed M, **Jinks N**, Babaei-Jadidi R, Kashfi H, Castellanos-Uribe M, May ST, et al. Repurposing Antibacterial AM404 as a Potential Anticancer Drug for Targeting Colorectal Cancer Stem-Like Cells. *Cancers*. 2019;12(1):106.

Kashfi SMH, Almozyan S, **Jinks N**, Koo B-K, Nateri AS. Morphological alterations of cultured human colorectal matched tumour and healthy/normal organoids. *Oncotarget*. 2018;9(12):10572-84.

List of Figures

Figure 1.1: Human primary tissues suitable for organoid isolation.....	34
Figure 1.2: The various application of organoids in biosciences.	35
Figure 1.3: Diagram of the Intestinal Crypt and role in epithelial homeostasis.	37
Figure 1.4: CRISPR/Cas-9 mediated immunity in prokaryotes.....	40
Figure 1.5: Diagram of the Ubiquitin-Proteasome System (UPS).....	43
Figure 1.6: Structure of the SCF E3 Ligase Complex	49
Figure 1.7: F-box interactions with the Hallmarks of Cancer	50
Figure 1.8: Interactions between FBXW7 and Hallmarks of Cancer	57
Figure 1.9: <i>FBXL5</i> expression is downregulated in colorectal adenocarcinoma.	60
Figure 1.10: Protein structure of FBXL5 showing hemerythrin-like domain....	63
Figure 1.11: Diagram of Epithelial-to-Mesenchymal Transition	65
Figure 1.12: The mTOR Pathway.....	69
Figure 2.1: Flow diagram for alkaline lysis (Mini-prep) isolation and purification of DNA plasmid from <i>e.coli</i>(Roche Scientific 03143414001).....	89
Figure 2.2: Example cytotoxicity plate diagram.	97
Figure 3.1: Diagram of method of generating CRISPR/Cas-9 expressing murine intestinal organoids via lentiviral transduction.....	107
Figure 3.2: Secretion of recombinant Noggin protein in cell culture media post- transfection confirmed by Western Blot.	109
Figure 3.3: Schematic presentation of pLv-U6g/PGK-Puro-2a-tBFP plasmid.	112

Figure 3.4: Restriction Enzyme Digestion analysis of plasmids constructed for <i>FBX03</i>-gRNAs (A1 & A2) and <i>FBXL15</i> (A3 & A4) using EcoRI and EcoRI/PvuII enzymes.	113
Figure 3.5: Transfection efficacy of lentiviral F-box gRNA plasmid expressing BFP (Figure 3.3) and a control lentiviral (PLV_x-eGFP) plasmid in transfection of HEK293-T cells by fluorescent microscopy.	115
Figure 3.6: Diagram of crypt, villus and lumen regions of murine intestinal organoids.	116
Figure 3.7: Murine intestinal organoid growth Day 1-6 post isolation demonstrate crypt and villus regions similar to <i>in vivo</i> structures.	118
Figure 3.8: Validation of Cas-9 protein expression in murine intestinal organoids using Western Blot Analysis.	120
Figure 3.9: Knockout of <i>fbxl5</i> in murine Cas-9 expressing organoids significantly affects growth pattern.	124
Figure 3.10: Surface Plots of control and <i>fbxl5</i> knockout organoids show incohesive vertical growth in knockout organoids.	125
Figure 3.11: <i>FBXL5</i> KO induced changes to murine intestinal organoid surface area and growth rate.	126
Figure 4.1: DLD-1 and SW480 cell lines expressing constitutively Cas-9 validated using Western Blot.	133
Figure 4.2: The depletion of <i>FBXL5</i> expression in <i>FBXL5</i> KO cell was evaluated by Western Blot (A) and RT-qPCR analysis (B).	135
Figure 4.3: Phenotypic analysis of DLD-1 and SW480 <i>FBXL5</i> KO cells shows significant morphology alterations.	139

Figure 4.4: FBXL5 knockout does not significantly affect cell proliferation/population increase in Growth Curve Assay.	142
Figure 4.5: (A) DLD <i>FBXL5</i> KO cells showed accumulation in G1 and SuperG2 phases. (B) No significant change was detected in SW480 cells	146
Figure 4.6: FBXL5 knockout significantly reduces wound healing rate in colorectal cancer cells.	149
Figure 4.7: DLD-1 and SW480 cells lines with FBXL5 knockout demonstrated altered protein expression related to EMT markers.	153
Figure 4.8: FBXL5 knockout significantly alters mRNA expression of core EMT markers.	154
Figure 5.1: Fluorescence of Calcein AM staining of DLD-1 and SW480 <i>FBXL5</i> KO after 90 minutes incubation shows increased labile iron levels in DLD-1 KO cells	167
Figure 5.2: FBXL5 knockout increased resistance of DLD-1 and SW480 cell lines to Salinomycin treatment.	171
Figure 5.3: FBXL5 knockout significant affects iron homeostasis marker protein expression in DLD1 and SW480 cells.	174
Figure 5.4: FBXL5 knockout significant affects iron homeostasis marker mRNA expression in DLD1 and SW480 cells.	177
Figure 5.5: FBXL5 knockout significant dysregulates downstream iron homeostasis marker protein expression.	180
Figure 5.6: FBXL5 knockout significant affects iron homeostasis downstream marker mRNA expression.	182

Figure 5.7: Western Blot and Densitometry of <i>ATG5</i>, <i>LC3B</i> and <i>Beclin1</i> expression in DLD-1 and SW480 cells.....	186
Figure 5.8: RT-qPCR analysis of <i>ATG5</i>, <i>LC3B</i> and <i>Beclin1</i> expression in DLD-1 and SW480 cells.....	187
Figure 5.9: Colony Formation Efficacy Assay of DLD-1 and SW480 <i>FBXL5</i> KO cells shows significantly reduced colony number in SW480 cells at normoxia but in both cell lines at hypoxia.	191
Figure 5.10: Colony size in Colony Formation Assay of DLD-1 and SW480 <i>FBXL5</i> KO cells shows significant changes to DLD-1 cell colonies.....	192
Figure 5.11: <i>FBXL5</i> KO significantly affects hypoxia marker RNA expression in colorectal cancer cells in both normoxia and hypoxia conditions.	197
Figure 5.12: Effect of Oxaliplatin, Cisplatin and 5-FU treatment on DLD-1 and SW480 <i>FBXL5</i> KO cells shows significant alterations in drug resistance.....	202
Figure 5.13: <i>FBXL5</i> KO significantly increases Etoposide resistance in both DLD-1 and SW480 cells after 48-hour treatment.	205
Figure 6.1: STRING analysis of <i>FBXL5</i> showing 20 nodes of highest confidence (average confidence: 0.971).	219
Figure 6.2: GEPIA and UALCAN analysis showing 25 genes with most significantly altered gene expression correlated with <i>FBXL5</i> in colorectal adenocarcinoma:	227
Figure 6.3: Chromosome mapping of GEPIA and UALCAN analysis of genes most significantly altered expression correlated with <i>FBXL5</i>.	228
Figure 6.4: RT-qPCR analysis of genes identified by GEPIA and UALCAN analysis shows significant alterations in <i>FBXL5</i> KO DLD-1 and SW480 cells.	229

Figure 6.5: Diagram of RNA-Seq analysis workflow from pre-read library preparation to final data analysis.	235
Figure 6.6: VENN diagram of RNA-Seq analysis results of DLD-1 <i>FBXL5</i> KO normoxia and hypoxia samples.	239
Figure 6.7: Volcano plots representing RNA-Seq results from DLD-1 <i>FBXL5</i> cells	241
Figure 6.8: Heat map representing RNA-Seq results from DLD-1 <i>FBXL5</i> cells	242
Figure 6.9: Validation of RNA-Seq data using RT-qPCR of most significantly differentiated genes.	243
Figure 6.10: WebGestalt pathway mapping analysis of RNA-Seq normoxia data of DLD-1 and DLD-1 <i>FBXL5</i> KO cells.	248
Figure 6.11: WebGestalt pathway mapping analysis of RNA-Seq normoxia data of DLD-1 and DLD-1 <i>FBXL5</i> KO cells.	250
Figure 6.12: WebGestalt pathway mapping analysis of RNA-Seq hypoxia data of DLD-1 and DLD-1 <i>FBXL5</i> KO cells.	251
Figure 6.13: WebGestalt pathway mapping analysis of RNA-Seq hypoxia data of DLD-1 and DLD-1 <i>FBXL5</i> KO cells.	253
Figure 8.1: Additional representative image of <i>FBXL5</i> KO murine intestinal organoids on Days 1, 3 and 7 of growth. Scale bar 75µm.	272
Figure 8.2: Additional representative DAPI/Phalloidin staining images of DLD-1 control and <i>FBXL5</i> KO cells	273

Figure 8.3: Additional representative DAPI/Phalloidin staining images of SW480 control and *FBXL5* KO cells 274

Figures 8.4: Original Western Blot Images 275

List of Tables

Table 1.1: Prevalence and Molecular Features of CMS in CRC.....	28
Table 1.2: F-box involved in cancer	54
Table 2.1: List of Human Cell Lines used in this project.....	74
Table 2.2: List of Antibodies used in this project.....	74
Table 2.3: List of Buffers used in this project	76
Table 2.4: List of Primers used in this project	77
Table 2.5: List of Plasmids used in this project.....	80
Table 3.1: F-box candidates for further functional analysis identified using Cas-9-expressing transgenic organoid screening through transduction of F-box gRNA lentiviruses.	121
Table 6.1: Potential FBXL5 associations identified using STRING Database. .	221
Table 6.2: Genes expression correlated with <i>FBXL5</i> with PCC ≥ 0.7 identified using GEPIA and UALCAN databases.....	226
Table 8.1: F-box gRNA data sheets	280
Table 8.2: Statistical analysis of organoid growth	288
Table 8.3: Significant Differentially expressed genes in DLD-1 <i>FBXL5</i> knockout cells vs controls under normoxia conditions as mapped to KEGG pathways..	289
Table 8.4: Significant Differentially expressed genes in DLD-1 <i>FBXL5</i> knockout cells vs controls under hypoxic conditions as mapped to KEGG pathways.....	295

Abbreviations

2D or 3D	2-dimensional or 3-dimensional
3R's	Replace, Reduce and Refine
5-FU	5-Fluorouracil
APC	Adenomatous Polyposis Coli
aSC	Adult stem cell
ATCC	American Type Culture Collection
BFP	Blue Fluorescent Protein
BMP	Bone Morphogenic Protein
BP	Base pair
BSA	Bovine Serum Albumin
Cas-9	CRISPR-Associated protein 9
CBCs	Crypt Base Columnar Cells
cDNA	Complementary DNA
CDK	Cyclin-dependent kinases
CMA	Chaperone-Mediated Autophagy
CMS	Consensus Molecular Subtype
CRC	Colorectal Cancer/Carcinoma
CRISPR	Clustered regularly interspaced short palindromic repeats
CSC	Cancer Stem-Like Cells
C-terminus	Carboxyl terminus
DAPI	4', 6-diamidino-2-phenylindole
dH ₂ O	Distilled water
DMEM, ADMEM	Dulbecco's Modified Eagle Media, Advanced DMEM
DMSO	Dimethyl sulfoxide
DNA	Deoxyribonucleic Acid
dNTPs	Deoxyribonucleotide triphosphates
dPBS/PBS	Dulbecco's Phosphate-Buffered Saline
ECM	Extra-cellular matrix
EDTA	Ethylenediaminetetraacetic acid
EGF/mEGF	Epidermal growth factor (murine)
eGFP	Enhanced Green Fluorescent Protein
EHS	Engelbreth-Holm-Swarm Cells
EMT	Epithelial-to-Mesenchymal Transition
FACS	Fluorescence-activated cell sorting
FAP	Familial Adenomatous Polyposis
-fc	Fusion protein
FBXO	F-box only
FBXW	F-box with WD40 domain
FBXL	F-box with Leu-rich repeat
FBS	Fetal Bovine Serum
FDA	United States Food and Drug Administration
GEPIA	Gene Expression Profiling Interactive Analysis
GFP	Green Fluorescent Protein
gRNA	Guide RNA
GSK-3 β	Glycogen Synthase Kinase-3 Beta
HECT	Homologous to E6-Ap carboxyl terminus
HPV	Human Papillomavirus

HIV	Human Immunodeficiency Virus 1 and 2
IF	Immunofluorescence
IHC	Immunohistochemistry
iPSCs	Induced pluripotent stem cells
IRE/IRP	Iron Regulatory Element, Iron Regulatory Pathway
ISCs	Intestinal Stem Cells
kDa	Kilo Dalton
KO	Knockout gene
LB Medium	Lysogeny Broth
Lg	L-Glutamine
Lgr5	Leucine-rich repeat-containing G-protein coupled Receptor 5
LRR	Leucine-rich repeat
LV	Lentivirus
mAB/pAB	Monoclonal/Polyclonal Antibody
ML	milliliter
mM	millimolar
mRNA	Messenger RNA
MSI	Microsatellite Instability
NC3R	National Centre for the Replacement, Reduction and Refinement of Animals in Research
NG	Nanogram
NGS	Next generation sequencing
NHEJ	Nonhomologous end joining
NSPC	Neural Stem Progenitor Cells
PAM	Protospacer Adjacent Motif
PDO	Patient derived organoid
PEI	Polyethylenimine
PFA	Paraformaldehyde
PI	Propidium Iodide
PVDF	Polyvinylidene Fluoride
RT-qPCR	Quantitative Real Time-PCR
RBR	RING-between-RING
RING	Really Interesting New Gene
RIPA	Radioimmunoprecipitation Assay Buffer
RNA	Ribonucleic Acid
RPMI	Roswell Park Memorial Institute Media 1640
ROS	Reactive Oxygen Species
SCF	Skp, Cullin, F-box containing complex
SDS-PAGE	Sodium Dodecyl Sulfate Polyacrylamide Gel Electrophoresis
sgRNA	Single gRNA
STRING	Search Tool for the Retrieval of Interacting Genes/Proteins
SRB	Sulforhodamine B
TCGA	The Cancer Genome Atlas
UBA1	Ubiquitin
UALCAN	University of Alabama at Birmingham Cancer Database
UPS	Ubiquitin-Proteasome System

WB
WT

Western blotting
Wild Type

Contents Page

Abstract	4
List of publications from this study and in cooperation with other projects in the lab:	6
List of Figures	7
Abbreviations	14
Chapter 1: General Introduction.....	24
1. General Introduction.....	25
1.1. Colorectal Cancer	25
1.2. Modelling Colorectal Cancer	28
1.2.1. Immortalised Cell Lines	28
1.2.2. Animal Models	31
1.3. Organoids	33
1.3.1. Intestinal Organoids	36
1.4. CRISPR/Cas-9 Genomic Editing.....	39
1.5. The Ubiquitin-Proteasome System.....	41
1.5.1. E1 Enzymes	43
1.5.2. E2 Enzymes	44
1.5.3. E3 Enzymes	44
1.5.4. UPS in Colorectal Cancer	46

1.5.5.	The SCF Complex (Skp1, Cul1 and F-box) E3 Ligases	48
1.5.6.	F-box in Cancer.....	53
1.5.7.	FBXL5.....	59
1.6.	Aims and Objectives	71
Chapter 2: Materials and Methods		73
2.	Materials and Methods.....	74
2.1.	Materials	74
2.1.1.	Cell Lines	74
2.1.2.	Antibodies.....	74
2.1.3.	Buffers.....	76
2.1.4.	Primers.....	77
2.1.5.	Plasmids and Lentiviral Vectors	80
2.1.6.	Animals	80
2.2.	Methods.....	81
2.2.1.	Culture, Freezing and Thawing of Epithelial Cells	81
2.2.2.	Colony Formation Efficiency Assay/ Clonogenic Assay.....	82
2.2.3.	Flow Cytometry and Propidium Iodide staining	82
2.2.4.	Growth Curve/Proliferation Assay	83
2.2.5.	Wound Healing Analysis	84
2.2.6.	Immunofluorescence (IF) and Phalloidin staining	85
2.2.7.	Transfection.....	86
2.2.8.	Transduction	87

2.2.9.	Plasmid Amplification	88
2.2.9.1.	Bacterial Transformation.....	88
2.2.9.2.	Alkaline Lysis Purification.....	88
2.2.10.	Restriction Enzyme Digest and Gel Electrophoresis	90
2.2.11.	Protein Extraction and Quantification using RIPA-mediated Cell Lysis and Bradford Assay	91
2.2.12.	SDS-PAGE and Western Blot.....	92
2.2.13.	RNA extraction, reverse transcription and RT-qPCR.....	93
2.2.14.	Cytotoxicity Assay/IC₅₀ Proliferation Determination Assay. .	96
2.2.15.	Murine Intestinal Organoid Methodology	97
2.2.15.1.	Preparation of Murine Intestinal Organoid Culture Media...	97
2.2.15.2.	Luciferase Reporter Assay	99
2.2.15.3.	Isolation of Murine Intestinal Crypts and Culture of Murine Intestinal Organoids	100
2.2.15.4.	Transduction of Intestinal Organoids with Lentiviral Particles. 101	
2.2.15.5.	Isolation of RNA from Organoid samples	102
2.2.15.6.	Isolation of Protein from Organoid samples	102
2.2.15.7.	Fixation and immune-histochemical staining of organoid samples	102
2.2.16.	Statistical analysis	103

Chapter 3: Utilising Murine Cas-9-Expressing Intestinal Organoids for screening of F-box Genes Function.....	104
3. Brief Introduction	105
3.1. Results	108
3.1.1. HEK293-T cells were transfected to express and secrete Noggin protein and validated by Western Blot.	108
3.1.2. R-Spondin 1 Conditional Media was produced using R-Spondin 1 expressing stable cells.	109
3.1.3. Amplification and Validation of F-box gRNA plasmid library	110
3.1.4. Generation of Cas-9 and F-box gRNA containing lentiviral particles	114
3.1.5. Culturing and expansion of wild type mouse intestinal organoid cultures by crypt isolation.	115
3.1.6. Generation of transgenic mouse intestinal organoids overexpressing Cas-9 using lentiviral transduction.....	119
3.1.7. Selected candidates of F-box from organoid screening.....	120
3.1.8. Loss of intestinal <i>fbxl5</i> in mouse organoids leads to significant morphological changes	121
3.2. Discussion	127
Chapter 4: Loss of Functional Analysis of FBXL5 cultured colorectal cancer cells	130
4. Brief Introduction	131

4.1.	Results	132
4.1.1.	Generation of DLD-1 and SW480 Cas-9 expressing cells and <i>FBXL5</i> KO cell lines using <i>FBXL5</i> - gRNA constructs.	132
4.1.2.	Studying the loss of <i>FBXL5</i> in growth, morphology, migration and EMT activities in DLD-1 and SW480 CRC cell lines	136
4.1.2.1.	Phalloidin staining shows that <i>FBXL5</i> knockout causes cellular elongation defects in DLD-1 and SW480 cells.	137
4.1.2.2.	Loss of <i>FBXL5</i> does not affect the cell population increase over time in DLD-1 and SW480 cells	140
4.1.2.3.	<i>FBXL5</i> KO of DLD-1 cell line showed a slight increase in G0 and SuperG2 cell population, while <i>FBXL5</i> KO SW480 cell line showed no differences in cell cycle.....	143
4.1.2.4.	Loss of <i>FBXL5</i> significantly reduced cell migration <i>in vitro</i> in both DLD-1 and SW480 cells	146
4.1.2.5.	Western Blot and RT-qPCR analysis of <i>FBXL5</i> KO DLD-1 and SW480 shows significant deregulation of EMT-related markers.....	150
4.2.	Discussion	156
Chapter 5: The role of <i>FBXL5</i> in the Iron Metabolism, Autophagy, Hypoxia and Drug Response in Colorectal Cancer		162
5.	Brief Introduction	163
5.1.	Results	163
5.1.1.	<i>FBXL5</i> -mediated cellular iron regulation in colorectal cancer cells	163

5.1.1.1.	Calcein AM staining shows significant variations in DLD-1 FBXL5 KO cytosolic labile iron levels compared to controls.	165
5.1.1.2.	<i>FBXL5</i> KO causes increased resistance to Salinomycin treatment in colorectal cancer cells	168
5.1.1.3.	<i>FBXL5</i> KO DLD-1 and SW480 cells shows altered expression of iron-homeostasis related markers.	172
5.1.1.4.	<i>FBXL5</i> KO has significant impact on IRP downstream gene expression	178
5.1.2.	The role of <i>FBXL5</i> in regulation of Autophagy	183
5.1.2.1.	Western Blot and RT-qPCR analysis of <i>FBXL5</i> KO DLD-1 and SW480 cells finds significant dysregulation of autophagy markers.....	185
5.1.3.	The role of <i>FBXL5</i> in Hypoxia	188
5.1.3.1.	Colony Formation Efficiency assay shows significant impact of <i>FBXL5</i> KO under normoxic and hypoxic conditions	189
5.1.3.2.	RT-qPCR analysis of <i>FBXL5</i> KO DLD-1 and SW480 Cas-9 expressing cells shows significant effects on hypoxia markers.	193
5.1.4.	The role of <i>FBXL5</i> in Drug Response.....	197
5.1.4.1.	<i>FBXL5</i> KO increases resistance to platinum-based chemotherapeutics in DLD-1 cells but reduced resistance in SW480 cells...	200
5.1.4.2.	<i>FBXL5</i> KO significantly alters Etoposide resistance in colorectal cancer cells	203
5.2.	Discussion	206

Chapter 6: Bioinformatics and RNA-Seq analysis of <i>FBXL5</i> KO cells identified novel substrates and pathways.....	214
6. Brief Introduction.....	215
6.1. Results.....	216
6.1.1. Analysis of public NGS databases to predict novel <i>FBXL5</i> associations. 	216
6.1.1.1. STRING analysis of predicted <i>FBXL5</i> protein associations identified potential novel protein interactors.	218
6.1.1.2. GEPIA and UALCAN analysis of RNA expression databases identifies several novel potential <i>FBXL5</i> associated genes.....	223
6.1.2. RNA-Seq analysis of DLD-1 <i>FBXL5</i> KO cells identifies novel, differentially expressed genes.....	230
6.1.2.1. RNA-Seq analysis of DLD-1 <i>FBXL5</i> KO cells and post validation analysis using RT-qPCR on selected targets.	232
6.1.2.2. Pathway mapping of RNA-Seq data from DLD-1 <i>FBXL5</i> KO cell lines identifies novel pathways affected by <i>FBXL5</i> knockout.....	245
6.2. Discussion	253
Chapter 7: General Discussion	257
7. Overview	258
7.1. Future Directions and Project Limitations	265
7.2. Conclusions.....	268
Chapter 8: Appendices	271
References	310

Chapter 1: General

Introduction

1. General Introduction

1.1. Colorectal Cancer

Colorectal Cancer (CRC) is the third most common cancer in both genders over 65 years old and the second leading cause of cancer mortality worldwide, with 1.8 million cases and over 880,000 deaths occurring in 2018 (Bray et al., 2018). CRC diagnoses vary primarily by socioeconomic status, with incidence and mortality correlating with periods of significant economic development, fluctuating as social development plateaus, and decreasing in the most developed regions (Siegel et al., 2020). 65% of CRC patients survive five years post-diagnosis, with early identification dramatically increasing survival rates. CRC typically occurs between ages of 50-79 (72%), with less than 11% of cases appearing before that age (Siegel et al., 2020). Early screening programs and awareness of lifestyle factors have contributed to dramatically reducing mortality rates since the 1970's (Siegel et al., 2020).

While CRC presentation and pathology can vary considerably, the TNM (Tumour, Node, Metastasis) classification of malignant tumours is used to define cancer pathology status and progression (Sobin, 2016). Tumour defines the growth status of colorectal cancer, ranging from no evidence to growing through the colorectal tissue into other organs, Node refers to the number of lymph nodes containing cancerous cells and Metastasis to the number of metastatic growths in organs or tissues other than the colon or rectum (Sobin, 2016), the combination of which determines cancer stage.

CRC initially manifests as abnormal growth of the intestinal mucous membrane ("adenomatous polyps") within the colon (41%) or rectum (28%) developing into adenocarcinomas (abnormal growths in colonic epithelial cells) mortality (Guinney et al., 2015). Polyps are typically benign, with approximately 1% of polyps smaller than

1cm being cancerous, but up to 40% of those greater than 2cm can develop into CRC (Ewing et al., 2014; Summers, 2010).

CRC is extremely heterogeneous, with a multitude of genetic and molecular mechanisms contributing to tumorigenesis, metastasis and mortality (Guinney et al., 2015). The most common genetic mutations in non-heritable (aka sporadic) CRC include chromosomal instability (CIN, 85% cases), wherein changes to chromosomal structure or number alter the expression of genes with oncogenic, tumour suppressive, cell cycle regulation and proliferation roles, leading to cancer development (Nguyen and Duong, 2018). The second most common mutation in non-heritable CRC is high-frequency microsatellite instability (MSI, 15% cases), wherein single-base/point mutations in hypermutable genomic regions are allowed to accumulate due to abnormal functioning of DNA mismatch repair pathways (Nguyen and Duong, 2018).

Heritable CRC has two primary types: Familial adenomatous polyposis (FAP, < 1% cases) is characterised by the inheritance of a non-functional *APC* (adenomatous polyposis) gene leading to dysfunction of the *APC/Wnt/β-catenin* pathway and *KRAS* (*KRAS* Proto-Oncogene, GTPase). The second type is hereditary non-polyposis colorectal cancer (HNPPC or Lynch syndrome, 1-3% cases) caused by microsatellite instability due to defective DNA mismatch repair (Lynch et al., 2015). Other heritable forms of CRC include hamartomatous polyposis syndrome (<1% cases) and those cases caused by other less penetrant inherited mutations (32% cases) (Nguyen and Duong, 2018).

In addition to chromosomal instability (CIN), microsatellite instability (MSI) and *APC/Wnt/β-catenin* and *KRAS* dysregulation, several other molecular pathways are commonly associated with CRC. Deletion of chromosome 18q tumour suppressor

genes such as *DCC* (DCC Netrin 1 Receptor), *SMAD2* and *SMAD4* (SMAD Family Members 2 and 4) is found in 70% of late stage CRC cases (Nguyen et al., 2020). Additionally, *TP53* is the most commonly mutated gene in human cancer (60% of chromosomal instability CRC tumours), with the P53 protein regulating DNA repair and cell response to oxidative stress (Yurgelun et al., 2015). CIMP-subtype CRC (CpG island methylator phenotype, approximately 20% cases) involves the inactivation of DNA expression due to hypermethylation of tumour suppressor genes including *CACNA1G* (Calcium Voltage-Gated Channel Subunit Alpha1 G), *IGF2* (Insulin-like Growth Factor 2) and *RUNX3* (RUNX Family Transcription Factor 3) (Nazemalhosseini Mojarad et al., 2013). Finally, mutations in *BRAF* can cause abnormal polyps called serrated polyps to develop, which may cause 15% of non-heritable CRC cases (Hazewinkel et al., 2014)

Recent research has identified four specific molecular subtypes of CRC divided by pathological presentation (such as lesion location and stage) and molecular background: Consensus molecular subgroups 1-4 (CMS), (Table 1.1) (Guinney et al., 2015). CMS1 (MSI Immune, 14% of cases) refers to high microsatellite instability, abnormal epigenetic instability via CpG island hypermethylation (CIMP), *BRAF* mutations and immune infiltration and activation within CRC tissues. CMS1 has worse survival rates after CRC recurrence. CMS2 (canonical, 37%) is characterised by high SCNA (somatic copy number alterations) affecting gene expression, and both *Wnt* and *MYC* activation. CMS3 (metabolic, 13%) shows mixed MSI status, low SCNA and CIMP profiles, *KRAS* mutations and metabolic dysregulation. Finally, CMS4 (mesenchymal, 23%) shows high SCNA like CMS2, but also TGF- β , stromal infiltration and angiogenesis. CMS4 also has poor relapse-free and overall survival (Guinney et al., 2015). *BRAF*, *KRAS* and CIMP abnormalities are associated with

serrated-polyp type CRC, making CMS1 and CMS3 more associated with this route (De Palma et al., 2019).

Table 1.1: Prevalence and Molecular Features of CMS in CRC		
CMS	Prevalence	Molecular Features
CMS1 (microsatellite instability immune)	14%	Hyper-mutated, microsatellite unstable, strong immune reaction
CMS2 (canonical)	37%	Epithelial, marked EMT & MYC oncogene signal activation, limited environmental-immune activation/low immunogenicity.
CMS3 (metabolic)	13%	Metabolic dysregulation, KRAS mutation, low immunogenicity
CMS4 (mesenchymal)	23%	Significant growth factor Beta activation, angiogenesis, high inflammatory reaction.
Mixed	13%	Displays mixed subtype characteristics

1.2. Modelling Colorectal Cancer

There are three broadly defined categories of biological model utilised for research into CRC, prior to patient studies: Immortalised cell lines, animal studies and organoids.

1.2.1. Immortalised Cell Lines

Immortalised cell lines are monocellular cell cultures generally isolated from a tumour sample or created artificially that are capable of almost unlimited proliferation. The first immortalised cell line “HeLa” was isolated in 1951 from cervical cancer cells and has contributed to medical advances including polio vaccine, cancer, AIDS and influenza (Lucey et al., 2009). Thousands of unique immortalised cell lines have since

been generated, including dozens of CRC lines, and are valued for laboratory research for ease-of-use, practicality and low financial and technical cost (Duval et al., 2017). This diversity of cell lines available, the relative abundance of cells available during experiments and ease of use also lends them to novel methodology, such as the formation of 3D (3-dimensional) spheroids (“colonoids” or “tumourspheres” in CRC) or use in bioreactors and microfluidics studies, although these methods are equally compatible with stem cells (Hirt et al., 2015; Shaheen et al., 2016).

However, despite these advantages, the simplicity, two dimensional and monocellular nature of immortalised cell lines limits their overall validity as experimental models (Duval et al., 2017). Additionally, immortalised cell lines are often subjected to decades of repeated use, leading to accumulation of mutations beyond their original profile (Hughes et al., 2007). This genetic drift can make replicating results difficult, as even allegedly identical cell lines may possess significant genetic diversity, or mislabelling may result in contamination, with some estimates suggesting between 6-18% of cell lines being misidentified or contaminated in this fashion (Hughes et al., 2007).

One of the primary limitations of immortalised cell lines is their 2D growth, as this does not adequately encapsulate the 3D tissue environment. The use of both immortalised cell lines and stem cells to generate three dimensional models the tumour microenvironment has gained significant research interest, with prominent methods of generating 3D culture models *in vitro* including spheroids, 3-dimensional scaffold-based models and microfluidics.

Spheroid culture can involve either immortalised or stem cells, wherein cell cultured in adhesion-free plastics will spontaneously form spherical shapes (Fennema et al.,

2013). Spheroid culture can increase cell viability, improve cell-specific function and cell-cell interaction and ultimately provide a 3D rather than 2D tissue architecture, which may be critical to the study in question (such as vascular tissue) (Fennema et al., 2013). Spheroids are especially valuable for exploring pharmacokinetic, fluidic, inflammatory and hypoxic factors, which are heavily influenced by physical tissue structure (Fennema et al., 2013). It has been determined that spheroids derived from colorectal cancer tissues will maintain molecular and histological characteristics of their origin tissue, making them valuable for personalised medicine, such as patient-drug response studies (Lee et al., 2015). Scaffold-based models for CRC involve the culture of *in vitro* cell models in an artificial 3D scaffold to create a 3D culture model. Microcapsule methods produce a group of spheroids initially grown in a matrix or gel support system, then encapsulated with an alginate (typically a calcium-based gel) in a liquid core to provide physical, encapsulating support to the spheroids without altering cell-cell interactions (although microcapsules can be engineered to interact with their content) (Agarwal et al., 2013).

Microfluidic technology is used to explore vascularisation, tumour microenvironment, perforation, toxicity and metabolism by growing cells in a micro-engineered plate that enables extremely precise fluid control across multiple chambers or compartments simultaneously, creating biomolecular gradients within the plate (Buchanan et al., 2014). Different chambers within the plate can support different functions or cell types, enabling exploration of sequential experimental changes or across multiple tissue types (Huh et al., 2011). Unfortunately, such micro-engineering is limited to specialist laboratories and staff, being both expensive and requiring significant technical expertise to employ (Huh et al., 2011).

These alternative methods demonstrate improved viability and translational validity over immortalised cell culture, each with specific advantages and disadvantages. Spheroids and scaffold technologies are comparatively easy to culture and produce 3D *in vitro* cultures, but are still primarily monocellular (Fennema et al., 2013). Microfluidics can utilise multiple cell and tissue types and produce highly accurate drug-response data, but require precision engineering and technical skills to utilise (Huh et al., 2011), limiting their widescale use.

1.2.2. Animal Models

In vivo animal modelling is another research method in biosciences, with *in vivo* results more translatable than those from *in vitro* models (Wendler and Wehling, 2010). However, animal models are also expensive to utilise and maintain, difficult to handle and prone to confounding/external experimental factors such as gender and environmental effects (Schellinck et al., 2010). There are also ethical issues, with animals exposed to harmful conditions to provoke an experimental response or discarded as surplus to requirements. House mice (*mus musculus*) are the most popular *in vivo* model for functional genetic and cancer studies due to their small size, quick lifecycle and large breeding cohorts (Frese and Tuveson, 2007). Transgenic *in vivo* models facilitate more comprehensive and coherent manner than immortalised *in vitro* assays (Frese and Tuveson, 2007). Existing transgenic *mus musculus* cancer models include prostate cancer (Ponthan et al., 2019), liver and colon (Oh et al., 2017), lung (DuPage et al., 2009; Jänne et al., 2013), hematopoietic leukaemia (Ablain and de The, 2014), ovarian (Szabova et al., 2014) and brain cancer (Huse and Holland, 2009), among numerous other models for specific diseases and individual genes.

Despite the ubiquity of animal modelling, less than 8% of animal studies are successfully translated to clinical trials (Mak et al., 2014). This low translatability means a loss of time, financial investment and animals without a corresponding significant scientific gain, and makes pharmaceutical development prohibitively expensive (Mak et al., 2014). Mouse models have been shown as a poor substitute for human patient responses, radically differing from both humans and other genetically diverse mouse strains (Schuh, 2004; Seok et al., 2013). In CRC, mouse models are only suitable for early stages of cancer development and have high metastasis variability compared to human patients, limiting their ability to accurately reflect the tumour microenvironment (Oliveira et al., 2020). Transgenic mouse models are typically generated for specific processes and pathways, lacking the broad physiological changes that occur in patient settings (Fingleton, 2007). Even in highly conserved breeding lines, genetic drift and spontaneous but impactful mutations occur, eroding the advantage of breed-standardisation (Shi et al., 2016). Confounding, extraneous and environmental factors including animal handling, animal stress and housing conditions are known to significantly affect experimental results (Kafkafi et al., 2018; Mogil, 2009). Replication of transgenic animal studies is also challenging, with estimated at between 25-60% of animal studies unable to be replicated with published methodology (Errington et al., 2014; Landis et al., 2012). The combination of poor translation and limited replicability has encouraged the development of both novel 3D modelling systems and the establishment of more comprehensive experimental methods to make *in vivo* studies more scientifically valuable.

While *in vivo* models are accepted as necessary despite the limitations, the ethical use and treatment of animals is an important consideration. In particular, the principle of “The three R’s” (3R’s) has been encouraged in animal research, funding guidelines,

laws and procedures since inception in 1959, with varying degrees of success (Burch, 1959). The 3R's represent the efforts to *Replace*, *Reduce* and *Refine* the use of animals in research. Therefore, 3R's encourage the development of novel *in vitro* methods for replacing and reducing animals in research (Taylor, 2019), refined experimental and bioinformatics techniques and other technologies for extracting and utilising data from existing experiments (Craig, 2018) and new animal handling techniques to reduce animal stress and provide more accurate data during experiments (non-aversive handling (Gouveia and Hurst, 2017)).

1.3.Organoids

Organoids are 3D *in vitro* cultures which possess multiple cells of the same type, generated from stem cells harvested from the tissue of interest. Organoids accurately encapsulate the molecular and genetic characteristics of their original cells in tissue (Boretto et al., 2019). Once isolated, organoids can be passaged and expanded almost indefinitely and are compatible with most standard laboratory methods (Sato et al., 2011). Organoid cellular composition and molecular biology re-encapsulates the original tissue; however, they do not accurately represent the tissues physical anatomy and other cells present in the tissue microenvironment. For example: Intestinal organoids will produce regions with both crypt and villus similarities but do not represent stromal fibroblasts and gut immune cells (Sato et al., 2011), and brain organoids do not produce anatomical features that can be associated with any specific lobe, nor grooves or fissures characteristic of the brain (Marx, 2020).

Organoids have been successfully cultured from several different tissues such as: brain (Mohamed et al., 2019; Oliveira et al., 2019; Quadrato et al., 2017), liver (Artegiani et al., 2019; Fiorotto et al., 2019), lung (Barkauskas et al., 2017), intestine and colon

(Date and Sato, 2015; Kashfi et al., 2018), kidney (Cruz and Freedman, 2019; Forbes et al., 2018), pancreas (Boj et al., 2016), prostate (Gleave et al., 2020; Karthaus et al., 2014), stomach (Bartfeld et al., 2015), fallopian tubes (Kessler et al., 2015), testicles (Sakib et al., 2019), endometrial tissue (Boretto et al., 2019), breast (Sachs et al., 2018), bladder (Banerjee and Southgate, 2019; Said, 2019), taste buds (Ren et al., 2014), salivary glands (Maimets et al., 2016), oesophagus (DeWard et al., 2014) and retinal (Zheng et al., 2020) stem cells (Figure 1.1).

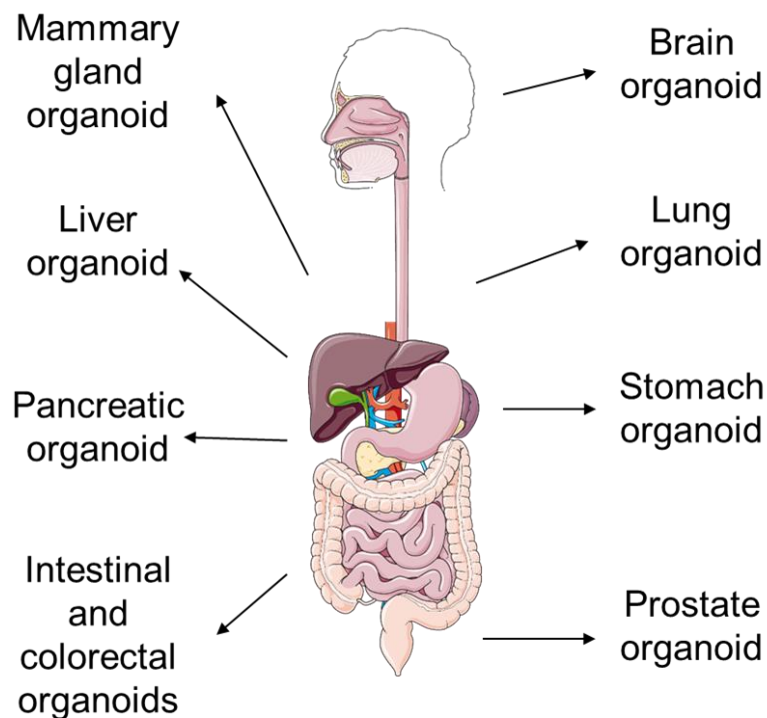


Figure 1.1: Human primary tissues suitable for organoid isolation

Since initially established from human intestinal stem cells (Sato et al., 2009b), organoids have been grown from a wide variety of human tissues (Huch and Koo, 2015).

Organoids have been rapidly adapted for various aspects of biomedical sciences research, including drug discovery and screening (Booij et al., 2019; Kondo and Inoue,

2019; Skardal et al., 2016), organoid patient biobanking (Kashfi et al., 2018), tumour immune microenvironment (Neal et al., 2018), proteomics (Lindoso et al., 2019), genetic-disease and cancer modelling (Di Donato et al., 2019; Geurts et al., 2020; Sun et al., 2019), parasite/immune infection reactivity (Heo et al., 2018) and targeted gene editing via CRISPR/Cas-9 (Kashfi et al., 2020; Schwank and Clevers, 2016) (Figure 1.2).

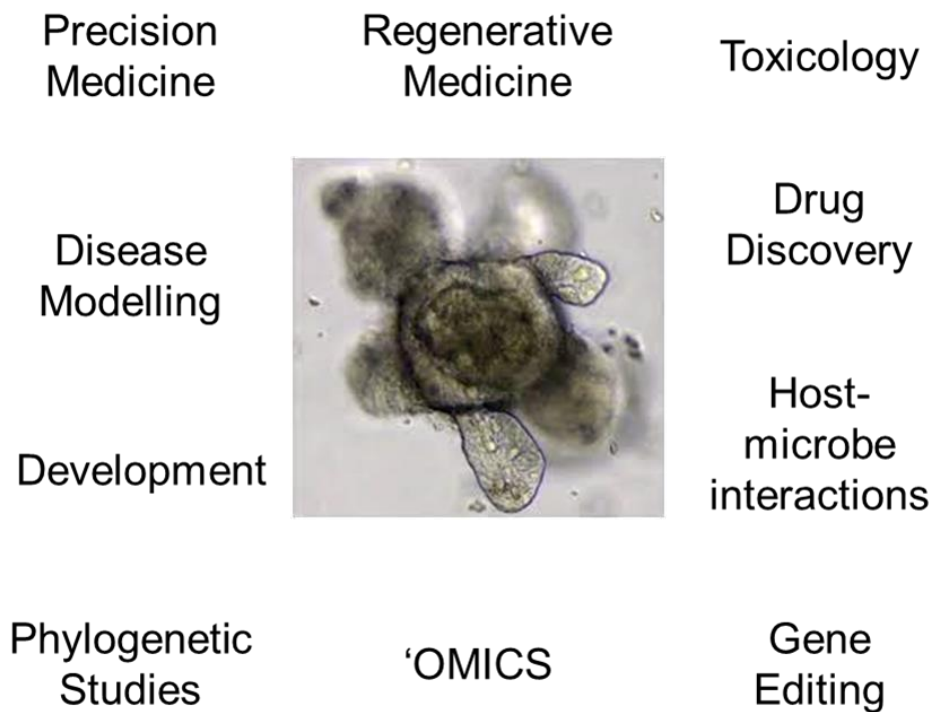


Figure 1.2: The various application of organoids in biosciences.

Organoids have many applications including drug screening and development, disease modelling, personalised and regenerative medicine, functional genomic studies and infectious disease modelling (Corrò et al., 2020) New methods and applications are being continually developed.

1.3.1. Intestinal Organoids

Intestinal organoids are cultured from *Lgr5*-positive multipotent intestinal stem cells (ISC) within the intestinal crypt (Sato et al., 2009b). Intestinal crypts are areas within the small intestine between villi that contain a number of cell types (Rao JN, 2010). Two conflicting theories suggest ISCs may either be located at the “+4 position” in the crypt, above Paneth cells, or be intermingled with Paneth cells (Figure 1.3) (Rao, 2010). Four to six actively proliferating intestinal stem cells (aISC’s) are located at the base of the crypt and differentiate into the Absorptive Progenitor (differentiating into enterocytes and M cell) and Secretory Progenitor (differentiating into Paneth, goblet, enteroendocrine and tuft cells) lineages (Bankaitis et al., 2018). Enterocytes are intestinal epithelial cells that absorb small molecules such as proteins, fats, sugars and vitamins from the intestine (Bankaitis et al., 2018). M cells act to monitor the intestinal immune environment and present antigens to trigger an immune response (Bankaitis et al., 2018). Paneth cells have antimicrobial and immunomodulating properties to regulate the intestinal environment (Bankaitis et al., 2018). Goblet cells both digest nutrients not absorbed by enterocytes, and secrete mucus into the intestine (Gehart and Clevers, 2019). Enteroendocrine cells are intestinal endocrine regulatory cells, secreting and regulating hormones in response to intestinal environmental changes. Finally, tuft cells facilitate immune response to parasites (Gehart and Clevers, 2019) (Figure 1.3).

As the intestinal epithelium is exposed to a highly corrosive environment, the cell turnover is high and requires intestinal stem cells to be exceptionally proliferative to maintain homeostasis (Barker et al., 2008). The anatomical location also makes intestinal stem cells access easier in both animal and human samples compared to other stem cell populations. For example, neural or bone marrow biopsies may be

significantly more invasive. These characteristics make intestinal organoids uniquely amenable to *in vitro* culture, and intestinal organoids have been more widely established and studied than any other type (Sato et al., 2009b). For a detailed method for isolating and culturing intestinal organoids, please see Materials and Methods section 2.2.15.

Image removed due to
3rd party copyright

Figure 1.3: Diagram of the Intestinal Crypt and role in epithelial homeostasis.

In both colon and small intestine, the intestinal crypt contains the intestinal stem cells that regenerate the intestinal epithelium in response to environmental damage. As stem cells migrate to the top of the crypt, they differentiate into the various cells required for intestinal function (Bankaitis et al., 2018).

Intestinal organoids have been instrumental in both refining organoid methodology and exploring possible applications. Among others, intestinal organoids have been used for studies in cancer (Drost et al., 2015; Vlachogiannis et al., 2018) high

throughput drug discovery (Bartfeld et al., 2015), personalised medicine and tissue synthesis (Todhunter et al., 2015), novel imaging methods (Bardenbacher et al., 2019), epigenetics and methylation (Kraiczy et al., 2019; Kraiczy and Zilbauer, 2019), molecular biology and genetic analysis (Fernandez-Barral et al., 2020) and model for infectious disease (Yin et al., 2015).

While *in vitro* and *in vivo* model systems have contributed incalculably to biosciences research, their limitations demand the development of novel methodologies that can more effectively translate *in vitro* results into clinical practice. Organoids represent an important step forward in both the methodology used in bioscience studies, and efforts to replace and reduce the use of animals in research. Future studies will continue to develop the organoid methodology, thereby improving overall accessibility and refining organoids into an effective tool for *in vitro* research into disease progression, tumorigenesis, drug screening, functional genomic studies, and personalised regenerative medicine.

1.4.CRISPR/Cas-9 Genomic Editing

The CRISPR/Cas9 system (Clustered Regularly Interspaced Short Palindromic Repeats) is natively found in prokaryotic bacteria and functions in a similar way to mammalian acquired immune systems (Deltcheva et al., 2011) (Figure 1.4). During initial viral infection, non-specific Cas enzyme (CRISPR-associated-enzyme) will cleave and render the virus inoperative (Mojica and Rodriguez-Valera, 2016). Subsequently, a small portion of the viral DNA or RNA (typically 20-40 base pairs) will be integrated into the CRISPR regions of the bacterial genome as a proto-spacer, downstream of a Protospacer Adjacent Motif (PAM) and bracketed by the dozens of AT repeats (Mojica and Rodriguez-Valera, 2016).

During subsequent viral infections and CRISPR activation, tracrRNA (trans-activating crRNA) simultaneously stimulates the expression of these proto-spacer regions into CRISPR RNA (crRNA), and subsequently binds to the newly expressed crRNA forming an RNA duplex (Mojica and Rodriguez-Valera, 2016). In turn, this duplex is cleaved by the RNase III ribonuclease to form a crRNA/tracrRNA hybrid guide for Cas9 (Mojica and Rodriguez-Valera, 2016). This complex binds to complementary regions on their respective virus, generating a double stranded region for Cas enzymes to cleave (Mojica and Rodriguez-Valera, 2016).

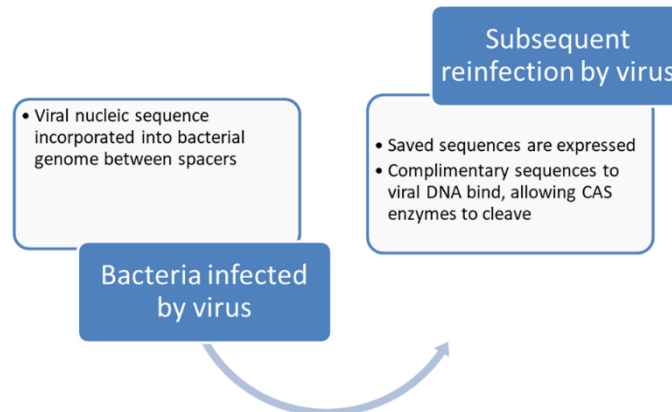


Figure 1.4: CRISPR/Cas-9 mediated immunity in prokaryotes

During bacterial infection by a virus, alien nucleic acid sequences are incorporated into the host bacterial genome between CRISPR spacers. During subsequent viral infection, these saved sequences are expressed and bind to complimentary alien sequences, facilitating their cleaving by Cas enzymes (Thurtle-Schmidt and Lo, 2018).

This method of generating targeted double-stranded breaks has been repurposed for laboratory use. Modern Cas-9 editing systems only require a single guide RNA (gRNA/sgRNA): a fusion of crRNA and tracrRNA to hybridise and generate a double-stranded cleave in a target region, streamlining and facilitating experimental use (Gasiunas et al., 2012). Research has identified Cas-9 as the sole Cas gene required for CRISPR-related immune activity, and that purified Cas-9 RNA can cleave targeted DNA *in vitro* (Jinek et al., 2012). This double stranded cleave is subsequently repaired by either non-homologous end joining (NHEJ) or homology-directed repair (HDR) (Jinek et al., 2014). However, NHEJ in particular frequently causes genetic errors at

the repair site, resulting in knockdown mutations in the cleaved gene, thereby facilitating the generation of transgenic knockout models (Jinek et al., 2014).

The advent of the CRISPR/Cas9 genomic editing system has enabled the rapid development and application of transgenic *in vitro* and *in vivo* strains for bioscientific research, enabling the more accurate and rapid study of individual genes and their role in molecular biology of both healthy and unhealthy tissues (Li et al., 2020). CRISPR/Cas9 editing also has potential in cancer immunotherapy treatment by editing patients own immune cells to target tumour antigens and treatment of disease caused by single-gene mutations (Li et al., 2020).

There are many genes and pathways that would benefit from further study by utilising CRISPR/Cas9 mediated transgenic models. Of these, the Ubiquitin-Proteasome System and F-box family of E3 ligases are some of the most promising.

1.5.The Ubiquitin-Proteasome System

The Ubiquitin-Proteasome System (UPS) is responsible for maintaining intracellular protein homeostasis by the degradation of proteins into either smaller polypeptides or amino acids in collaboration with proteasomes (Nandi et al., 2006). The UPS is a key aspect of post-transcriptional protein regulation; therefore, depending on other regulatory factors, proteolysis can occur both before and after the activity of a specific protein (Nandi et al., 2006). The UPS is also responsible for the targeting of damaged or dysfunctional proteins (Nandi et al., 2006; Wilkinson, 2005). The UPS targets approximately 90% of intracellular proteins, including many associated with cell cycle regulation, proliferation and apoptosis with the remaining 10% are generally degraded by autophagy and the lysosome proteolytic process (Hochstrasser, 2009).

The UPS functions by the addition of Ubiquitin (Ub, 8.6kDa) to a protein substrate. In addition to protein homeostasis, Ubiquitin also alters the cellular location of a protein (Glickman and Ciechanover, 2002; Schnell and Hicke, 2003) and protein-protein interactions (Mukhopadhyay and Riezman, 2007).

UPS activity and protein specificity is governed by the three ubiquitin enzyme families: ubiquitin-activating enzyme (E1), ubiquitin-conjugating enzyme (E2) and ubiquitin ligases (E3) (Nandi et al., 2006) (Figure 1.5). Ubiquitination follows three stages: Initially, the ubiquitin protein binds to an E1 via ATP, is subsequently passed to the E2 and together they form a protein complex with an E3 ligase (Nandi et al., 2006). The E3 ligase enables the binding and transport of ubiquitin from the E2 to the targeted protein as a signal for degradation by the proteasome (Nandi et al., 2006). Ubiquitin binding can be either mono or poly-ubiquitination, typically with larger proteins having greater ubiquitin binding (Kraft et al., 2010). Primarily, ubiquitin chains target proteins for degradation by the proteasome, although some chain configurations have roles in signalling, endocytosis, DNA repair, and macroautophagy (Kraft et al., 2010; Nathan et al., 2013). Once sufficient ubiquitin proteins are bound to the target protein, it is degraded by the proteasome into shorter polypeptides or amino acids and recycled (Reits et al., 2003). Currently; eight E1 enzymes, 60 E2 enzymes and between 600-900 E3 enzymes have been identified in humans (Wang et al., 2014c).

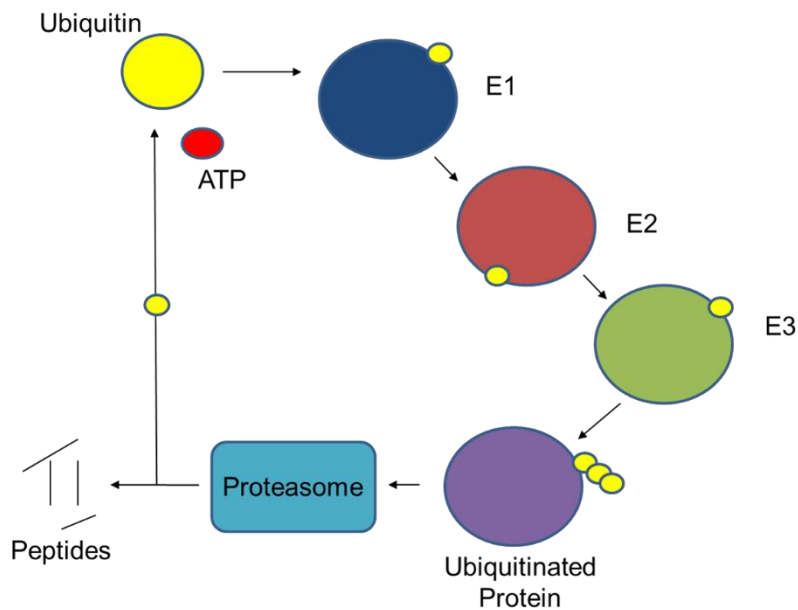


Figure 1.5: Diagram of the Ubiquitin-Proteasome System (UPS)

The UPS regulates protein homeostasis by the combination of E1, E2 and E3 ligases to facilitate ubiquitination of a target protein. This protein is subsequently recycled into peptides and amino acids for future use (Zerr, 2021). E3 ligases govern the majority of UPS specificity (Bedford et al., 2011).

1.5.1. E1 Enzymes

Unlike E2 and E3 enzymes, the eight human E1 enzymes require ATP, and have been noted as a possible therapeutic targets for ubiquitin-related diseases (Schulman and Wade Harper, 2009). Of the identified E1 enzymes, UBA1 is most well understood, with most studies focusing on E1 enzymes in general (Schulman and Wade Harper, 2009). The limited number of E1 enzymes compared to E2 and E3 may suggest that

E1 enzymes have broad rather than specialised roles in the UPS, with greater specificity determined by E2 and E3 enzymes.

1.5.2. E2 Enzymes

The primary role of E2 enzymes is mediation of the ubiquitin chain within the E3-ubiquitin ligase structure, with both length and structure of ubiquitin chains affecting subsequent protein activity prior to degradation (Ye and Rape, 2009). Some E2 enzymes are more involved in ubiquitin chain initiation than elongation, or *vice versa*, or even attach entire pre-made ubiquitin chains to substrates, and several E2 enzymes may work together to regulate ubiquitin binding on specific proteins (Rape et al., 2006). Alternatively, some E2 enzymes perform both roles, collaborate when environments are replete with misfolded or abnormal proteins or even directly interacting with proteins without the need for an E3 enzyme (Stewart et al., 2016). Evidence suggests that E2 enzymes have multiple E3 collaborators, or may only be active with a specific subgroup, with the E2 ligase UBE2L3 binding to many RING-type E3's, but only functional with HECT-type (Wenzel et al., 2011). As such, E2 enzymes may be possible therapeutic targets, with subgroups responsible for specific roles within the cell as well as within the UPS.

1.5.3. E3 Enzymes

E3 ligases can be divided into three structural categories: HECT (homologous to E6-Ap carboxyl terminus), RBR (RING-between-RING, (two RING fingers and a double RING finger linked)) and RING-finger (Really Interesting New Gene aka RING Finger/Motif/Domain) (Metzger et al., 2014).

HECT family E3 ligases have a HECT domain at the C-Terminus that binds ubiquitin, acting as intermediary between the E2 enzyme and protein substrate when transferring

ubiquitin (Metzger et al., 2014). The HECT family includes a further three subfamilies: NEDD4 (neural precursor cell expressed developmentally down regulated protein 4), HERC (Homologous to E6AP C-terminus) and the miscellaneous “other” family (Metzger et al., 2014). The 12 RBR ligases are the smallest family of HECT E3 ligases, but share features with both HECT and RING families, directly catalysing the ubiquitin transfer with the HECT C-terminal domain as well as utilising a RING domain to recruit E2 ligases (Spratt et al., 2014). The most well-known RBR enzyme is parkin, which has a prominent role in early-onset Parkinson’s Disease (Marin and Ferrus, 2002).

RING E3’s do not actively bind ubiquitin but activate the E2’s that transfer ubiquitin to the substrate directly (Metzger et al., 2014). This direct transfer of ubiquitin from the E2 makes RING E2-E3 bindings more specific, whereas HECT E3’s supersede E2 specificity (Kim and Huibregtse, 2009). The RING type E3 ligase family are the most numerous and has multiple subgroups: monomeric or homodimeric RING or U-BOX (Ubiquitin-box) (one RING zinc-finger binding domain or U-BOX non-zinc binding domain), homodimeric RING or U-BOX, heterodimeric RING (two or more different RING E3 required), Cullin-RING and “other.” RING E3 utilise zinc binding sites, while U-BOX utilise hydrogen bonds and salt conjugations to generate their protein structure (Nordquist et al., 2010).

The RING associated APC/C family (anaphase-promoting complex) of E3 ligases has 11-13 different subunits, making it the most complex E3 ligase rather than the most versatile (Schreiber et al., 2011). Alternatively, Cullin-RING E3 ligases (CLR’s) form an SCF complex of an adaptor protein (e.g. SKP1) and Cullin RING-box protein E2 ligase (RBX1 or 2), and an E3 ligase F-box protein (Fouad et al., 2019). Approximately

20% of all ubiquitin-mediated degradation is modulated by cullin-RING E3 ligases (Soucy et al., 2009). There are 69 F-box proteins in humans that may each act on multiple substrates, partially governing specificity within the UPS (Ho et al., 2008).

1.5.4. UPS in Colorectal Cancer

In addition to extensive roles in neurodevelopmental and degenerative diseases, the UPS is an important topic of cancer studies. Multiple SCF and APC/C subunits have been strongly linked to cell cycle control and cancer, and have been reviewed elsewhere (Bassermann et al., 2014; Borg and Dixit, 2017; Shi and Grossman, 2010; Young et al., 2019). Intracellular proteins are continuously degraded by the proteasome during infection or cancer, with those few surviving proteins presented on the cell surface for lymphocyte identification and subsequent T-cell destruction (Shin et al., 2006).

Both adult and paediatric brain cancer have recently been the target of comprehensive molecular analysis and characterisation, leading to the successful division into various molecular subtypes as well as identification of novel genes of interest (Guerreiro Stucklin et al., 2018; Orozco et al., 2018). Several dozen proteins have been correlated with paediatric brain cancer that are regulated by the UPS in a highly specific manner, suggesting that UPS activity may be a significant factor in brain cancer development and that modulation of proteasome or UPS activity may be a viable treatment strategy (Zaky et al., 2017).

In colorectal cancer, the oncogene FBXL20 is frequently overexpressed, and inhibition of FBXL20 suppresses cell proliferation and promotes apoptosis in CRC cell lines (Zhu et al., 2014a). UHRF2 (ubiquitin-like with PHD and ring finger domain 2) is upregulated in colorectal cancer tissues and is significantly associated with CRC

development clinical presentation (Lu et al., 2014) and overexpression with reduced survival rates. CHIP (C-terminal Hsp-interacting protein) is an E3 ligase with tumour suppressive properties, being downregulated in late-stage CRC and overexpression inhibiting tumour growth in mouse models (Wang et al., 2014b). NEDD4L (Neural precursor cell expressed, developmentally down-regulated 4-like) is similarly downregulated in CRC and inhibits the Wnt/ β -catenin pathway (Tanksley et al., 2013). FBXW7, as discussed in more depth below, is highly mutated in colorectal cancer and is associated with cell cycle regulation (Zheng et al., 2016a) and oncoprotein activity (Yeh et al., 2018).

The unique design of many E3 ligases makes them suitable for high throughput screening and targeted small molecule methods, either stabilising the interface between a mutated ligase and its substrate, or retargeting another ligase to replace a dysfunctional one (Skaar et al., 2013). Small molecule therapeutics directly targeting individual E2 and E3 ligases are currently in development such as MLN4924, which inhibits E3 ligase MDM2 activity in a highly specific manner (Zhou et al., 2018). Recently developed 2nd generation proteasome inhibitors attempt to ameliorate the short effect duration of 1st generation therapeutics by permanently binding to their substrate within the UPS, rather than reversibly binding (Manasanch and Orłowski, 2017). Carfilzomib has received much attention for low toxicity, extended treatment effect duration and strong efficacy on cancers already resistant to 1st generation inhibitors like Bortezomib and has demonstrated improvement to patient outcomes in Phase three trials. (Alsina et al., 2012; Stewart et al., 2015). The numerous roles of UPS in cell cycle regulation and association with various cancers has made the system a research topic of interest, and the SCF family of E3 ligases in particular has begun to attract greater attention for its high specificity.

1.5.5. The SCF Complex (Skp1, Cul1 and F-box) E3 Ligases

As previously outlined, the SCF (SKP1, Cul1 and F-box) complex is an important aspect of protein homeostasis and contributes to the degradation of proteins by the conjugation of ubiquitin to the targeted protein substrate. SCF complexes function by the combination of the Cul1 scaffold protein. The carboxyl terminus of CUL1 binds the FBX1 RING protein, which initially directs E2-E3 enzyme interaction, while the amino terminus the SKP1 and F-box binding which ultimately governs substrate specificity (Skaar et al., 2013). Alternative Cul proteins act as structural and scaffold proteins to other ubiquitin ligase complexes(Skaar et al., 2013).

There are currently 69 human F-box family E3 ligases (Marzio et al., 2019) (Figure 1.6). The F-box family can be divided into three subfamilies: The FBOW (F-box with WD40 domain), the FBXL (F-box with Leu-rich repeat) and FBXO (F-box only) groups. F-Box is named for Cyclin-F/FBXO1, a founding member of the FBXO subfamily (Augustine et al., 2017).

The WD40 repeat is a structural motif of approximately 40 amino acids of 4-16 repeating sequences. The 12 human F-box proteins in the WD40 subfamily have assorted roles including signal transduction, RNA synthesis, chromatin and cytoskeletal activity and cell-cycle regulation (Smith, 2008; Smith et al., 1999). LRR domains consist of 2-45 leucine-rich repeats which provide an extensive structural framework for protein interactions (Ng and Xavier, 2011). The most well-known human LRR protein is the ribonuclease inhibitor, but there are also approximately 21 human LRR F-box proteins, many of which have limited research. Finally, the 36 human ligases of the FBXO family have neither a WD40 motif nor LRR domain

associated with them, instead possessing conserved regions uncommon in other F-box proteins that have variable and unknown function (Augustine et al., 2017).

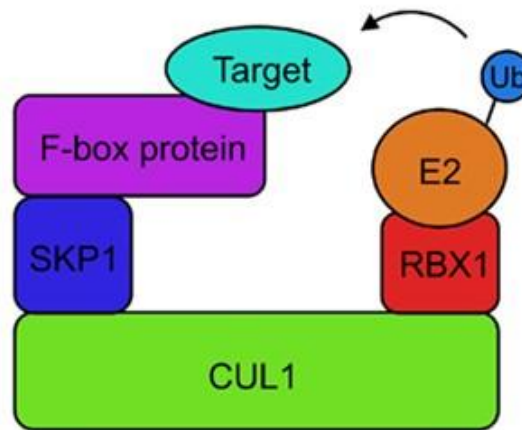


Figure 1.6: Structure of the SCF E3 Ligase Complex

The SCF E3 Ligase Complex is the combination of the Skp1, Cul1 and F-box E3 ligases and acts to ubiquitinate target proteins for degradation by proteasomes (Magori and Citovsky, 2011). 69 human F-box family E3 ligases with differing substrates, roles and pathway associations have been identified so far (Bassermann et al., 2014).

Recent interest in F-box has identified several alternative regulatory systems for F-box binding. F-box typically bind to their substrate without cofactor assistance, but several examples have demonstrated cofactor-dependent substrate recognition among F-box, implying a further regulatory mechanism in this system. p27 is a substrate for FBXL1 (aka SKP2), however mutual binding also requires assistances of CKS1 (CKD regulatory subunit 1), while FBXO4 requires $\alpha\beta$ -crystallin as a cofactor for substrate recognition (Ganoth et al., 2001; Lin et al., 2006). Methylation-dependent substrate recognition (Lee et al., 2012a), small molecule regulation, priming and inducible

degrons and alterations to the SCF structure have also been noted in F-box activity (Kaelin, 2005; Li and Hao, 2010; Skaar et al., 2013), further implying additional regulatory mechanisms in F-box protein activity.

F-box are known to have a variety of roles, including cell cycle regulation, developmental signalling pathways, circadian rhythm maintenance, cell survival and apoptosis among others (Zheng et al., 2016a). For example: numerous F-box proteins across all three subfamilies are associated with cell cycle regulation, notable examples in the FBXW family including FBXW1, FBXW5 and FBXW7, FBXL1 and FBXL2 of the FBXL family and FBX01, FBX07 and FBX011 of FBXO (Zheng et al., 2016a).

Image removed due to
3rd party copyright

Figure 1.7: F-box interactions with the Hallmarks of Cancer

Of the 69 human F-box E3 ligases identified, many have associations or interactions with cellular processes and pathways related to the Hallmarks of Cancer. Adapted from (Randle and Laman, 2016)

FBXW1 (aka β -TrCP1/2 (Beta-transducin repeats-containing proteins)) is a well characterised F-box which has numerous roles in cellular and physiological processes. Examples of processes and substrates of β -TrCP1/2 include cell cycle (BTG1, BORA, EMI1) and migration (cortactin, SNAIL), signal transduction (β -Catenin, FOBXP3), transcription (ATF1, FOBX03, p53, VEGFR2), immune regulation (PKD1, ACT1, CD4), apoptosis (BimEL, MAP3K5), DNA damage response (CLASPIN, ARID1A) and others. Additionally, β -TrCP has both tumour suppressor and oncoprotein substrates and is frequently mutated in cancers including CRC, despite it also being highly regulated {Bi, 2021 #1200}.

FBXW5 targets both Eps8 and DLC-1 (Deleted in liver 1) for ubiquitination and disruption of FBXW5 causes multipolar spindles and heavily disrupts chromosome migration, and is also associated with blood pressure regulation (Puklowski et al., 2011; Singh et al., 2019). Among the most well understood F-box proteins is FBXW7, regulating both Cyclin E and Aurora A and B, both having critical roles in cellular phase-phase transition as well as numerous oncoproteins including c-Myc, mTOR, Jun and Notch (Yeh et al., 2018). As a result, FBXW7 is strongly associated with several cancers (Babaei-Jadidi et al., 2011; Sailo et al., 2019), the epithelial-mesenchymal pathway and stem cell activity (Yang et al., 2015).

FBXL1 (aka SKP2) and FBXL2 are both noted for their regulatory role in cell-cycle and cyclin activity among two dozen other substrates related to gene transcription,

interferon signalling, transduction, apoptotic control and DNA repair (Frescas and Pagano, 2008; Zheng et al., 2016a). Depletion of FBXL1 decreases cell growth and increases apoptosis, as well as completely eliminating pituitary tumours in mice (Wang et al., 2009). Conversely, overexpression is found in lymphoma, prostate, pancreatic and breast cancer among others (Chan et al., 2010). FBXL1 regulates tumour suppressors p21, p57, RBL2, FOB01, and p27-KIP1, overexpression of which destabilises cyclin complexes and lead to uncontrolled proliferation (Bashir et al., 2004). FBXL1-p27 interactions may contribute to tumorigenesis, with reduced p27 and increased FBXL1 expression found in lymphomagenesis, prostate cell lines and breast cancer xenografts and other *in vitro* cancer cell lines (Frescas and Pagano, 2008). A mutant p27 knock-in mouse line demonstrated that FBXL1 dependent p27 degradation is crucial for progression of colon adenomas to carcinomas (Timmerbeul et al., 2006). FBXL2 is also associated with Cyclin activity and depletion of FBXL2 stabilises Cyclin D2 and D3 levels, which are required for leukemic, lymphoblastoid cell survival and lung cancer proliferation respectively, whereas overexpression arrests tumour development in mouse models (Chen et al., 2011, 2012).

FBX01 (aka Cyclin F), is both a Cyclin protein and an F-box substrate binding subunit of the SCF structure (Augustine et al., 2017). FBX01 has been associated with neurodevelopmental and degenerative diseases, with linkage analysis and *in-vitro* experiments suggesting that FBX01 mutations result in increased ubiquitination of the Cyclin F protein and possible damage to motor neurons (Hogan et al., 2017). FBX07 interacts with Parkin genes PARK2 and PARK6, cornerstones of Parkinson's Disease and autosomal recessive Juvenile Parkinson's Disease (AR-JP) (Zhou et al., 2016). AR-JP is an almost exclusively inherited form of Parkinson's Disease and mutations in FBX07 have been found in several families (Paisan-Ruiz et al., 2010). Cell models

deficient in FBX07 have similar loss of Parkin and resulting mitophagy characteristic of the disease. In a drosophila model of FBX07, disruption resulted in mitochondrial dysfunction, while overexpression of FBX07 repaired loss of Parkin (Burchell et al., 2013). Finally, FBX011 is an oncogene in several cancers including colorectal, lung, ovarian and nonspecific neck tumour growth (Schneider et al., 2016). It also degrades the BLMP-1 (B lymphocyte-induced maturation protein 1) protein in *C. elegans*, which regulates developmental timing and maturation (Horn et al., 2014). Additionally, a mouse model for Otitis Media, a form of hearing impairment in children, is FBX011 KO (Hardisty-Hughes et al., 2006). Postnatal mice heterozygotes express FBX011 in the middle ear at day 13, whereas homozygotes instead show severe facial clefting and perinatal lethality, implying a cross-species role in development (Hardisty-Hughes et al., 2006).

These specific examples of F-box roles and substrates demonstrate the singularly broad potential role in protein and cellular homeostasis. However, understanding of both individual F-box ligases and the family is lacking, especially given the little currently known about the family. Therefore, further research is required to explore the pathways, pathologies and regulatory mechanisms influenced by F-box activity.

1.5.6. F-box in Cancer

While the precise roles of F-box in cellular and protein homeostasis are still largely undetermined, F-Box association with both cancer and pathology is undeniable. This section attempts to briefly elaborate on current understanding of F-box in clinical diagnosis and treatment, justifying the need for further research. Table 1.2 and Figure 1.7 summarise the known F-box interactions with cancer.

Table 1.2: F-box involved in cancer	
F-box	Role in Cancer
FBXW1/β-TrCP	Colorectal (Ougolkov et al., 2004), Pancreatic, Prostate, Breast (Fuchs et al., 2004)
FBXW2	Lung (Xu et al., 2017)
FBXW5	Liver (Scholata. T, 2016)
FBXW7	Breast (Chen et al., 2018), Liver (Koch et al., 2005), Lung (Xiao et al., 2018), Oesophageal (Gong et al., 2016), Gastric/stomach (Uddin et al., 2016), Colorectal (Lorenzi et al., 2016b; Nateri et al., 2004)
FBXW11	Leukaemia (Wang et al., 2014a)
FBXL1 (aka SKP2)	Colorectal (Nakayama and Nakayama, 2006), Breast (Signoretti et al., 2002), Cervical (Narayan et al., 2007), Endometrial, Gastric, Glioma/Glioblastoma, Lung Lymphoma and Leukaemia, Myeloma, Melanoma, Ovarian (Frescas and Pagano, 2008; Xie et al., 2013),
FBXL3	Colorectal (Guo et al., 2017)
FBXL4	Prostate (Stankiewicz et al., 2017)
FBXL10 aka KDM2B	Pancreatic (Tzatsos et al., 2013) (Smits et al., 2012), Brain (Frescas et al., 2007), Breast (Kottakis et al., 2014)
FBXL14	Glioblastoma (Fang et al., 2017)
FBXL19	Colorectal (Shen et al., 2017)
FBXL20	Colorectal (Zhu et al., 2014b)
FBXO2	Gastric (Sun et al., 2018a)

FBXO3	Cancer (general) (Barbash et al., 2008; Kanie et al., 2012)
FBXO4	Breast (Liu et al., 2014), ovarian (Min et al., 2013)
FBXO5 aka EMI1	Ovarian, Breast, Lung (Wang et al., 2018b)
FBXO8	Gastric Cancer (Wu et al., 2015a)
FBX11	B-Cell Lymphoma (Duan et al., 2012)
FBXO22	Gastric (Donner et al., 2015)
FBXO25 aka NUDT16	Lymphoblastic Leukaemia (Anadón et al., 2017)
FBXO32	Breast Cancer (Zhou et al., 2017), Ovarian Cancer (Chou et al., 2010)
FBXO33	Breast Cancer (Hein et al., 2013)

Of those F-box with associations to tumour suppressive and oncogenic activity, FBXW7 is most well understood, acting as both an oncogene and tumour suppressive gene in multiple cancers (Yeh et al., 2018) (Figure 1.8). Interestingly, it is also the F-box gene with the highest mutational rate in human tumour samples at 2.54%, followed by *FBXW10* at 0.58% (Forbes et al., 2017). FBXW7 protein levels are found significantly depleted in liver, lung, melanoma, pancreatic, prostate, renal, skin, testis, thyroid and urothelial cancers, with differing oncogenic and tumour suppressive effects (Uhlen et al., 2015). FBXW7 targets the oncoproteins c-Myc, c-Jun, Cyclin E1 and Notch for ubiquitination, and has other roles in cell homeostasis, proliferation and genomic stability, making FBXW7 dysregulation a significant cancer risk marker (Tan et al., 2008). *FBXW7* is commonly mutated in colorectal cancer (7.5% Stage 1 & 2

CRC diagnoses), although *FBXW7* mutation has no significant impact on survival rates (Chang et al., 2015).

In breast cancer, *FBXW7* acts as a tumour suppressor by targeting the oncoprotein Metadherin for degradation. Metadherin expression increased substantially during *FBXW7* depletion, suggesting that abundant *FBXW7* expression could be a suitable therapeutic target for Metadherin-mediated breast tumour growth (Chen et al., 2018). *FBXW7* also acts as a tumour suppressor for lymphoblastic leukaemia by modulating Notch 1 and c-Myc expression, with combined loss of *FBXW7* and either PTEN or p53 causing enhanced tumorigenesis (Kumar et al., 2014). Low *FBXW7* protein expression is found in a significant proportion of early onset gastric cancers and is correlated with chemotherapy response (Calcagno et al., 2013; Milne et al., 2010). *FBXW7* expression is also down regulated in non-small cell lung cancer, with expression correlated with more aggressive cancer and greater mortality rates (Yokobori et al., 2014; Zhang et al., 2017). Recent evidence suggests that the miR-223/*FBXW7* axis is involved in drug resistance, with miR-223 expression correlating with Erlotinib resistance in lung carcinoma cells and subsequent downregulation of *FBXW7* (Zhang et al., 2017). Due to *FBXW7*'s multiple substrates and interactions, it has several potential roles drug resistance (Yan et al., 2020).

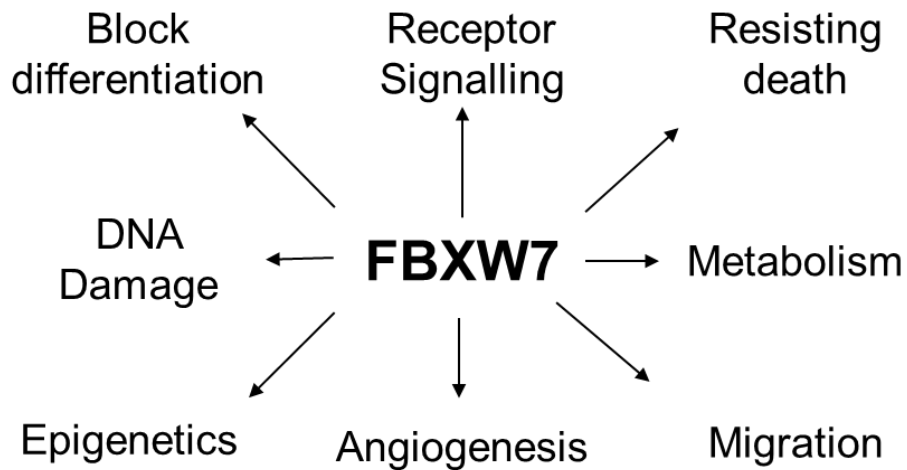


Figure 1.8: Interactions between FBXW7 and Hallmarks of Cancer

FBXW7 is the most well studied F-box E3 ligase, and is associated with receptor signalling, metabolism, resisting death, angiogenesis, DNA damage and cell proliferation (Babaei-Jadidi et al., 2011).

The published data on the wider role of F-box proteins in cancer drug resistance and cytotoxicity, and therefore on cancer treatment prognosis is inadequate. While FBXW7’s extensive substrate interactions propose multiple roles in cytotoxicity, information on other F-box proteins is currently limited.

Among the FBXO family: FBXO4 knockdown causes resistances to chemotherapeutic drugs in lung cancer (Feng et al., 2017). FBXO5 depletion causes chemosensitivity and radiosensitivity (Shimizu et al., 2013). FBXO6 enhances Cisplatin sensitivity by inhibition of checkpoint kinase1 (Cai et al., 2019). FBXO7 is inversely correlated with sensitivity to the immunomodulatory drugs lenalidomide and pomalidomide (Liu et al., 2019c). FBXO10 may affect resistance to ibrutinib in mantle cell lymphoma (Li et al., 2016). FBXO18 ’s regulation of homologous recombination via RAD51 may affect

resistance to DNA damaging agents camptothecin and hydroxyurea (Stanescu et al., 2014). FBXO21's impairment by the oncogene *CD44* leads to P-gp-overexpression mediated drug resistance (P-glycoprotein) (Ravindranath et al., 2015). FBXO22's ubiquitination of CD147 contributes to several types of chemoresistance (Wu et al., 2017), and FBXO31 and FBXO32 have roles in Cisplatin and 5-FU resistance respectively (Wang et al., 2018a), (Liu et al., 2018).

Among the FBXL and FBXW families: Abnormal FBXW1/ β -TrCP expression is associated with both various cancers and with drug reactivity, with β -TrCP suppression increasing Paclitaxel sensitivity in cancer cells both *in vivo* and *in vitro* and Berberine resistance in HepG2 hepatoma cells. (Su et al., 2011; Wang et al., 2016). FBXL1/Skp2 inhibition in lung cancer cells increases sensitivity to Paclitaxel, reduced Tamoxifen resistance in breast cancer, while upregulation causes Camptothecin and Cisplatin resistance in lung adenocarcinoma, Troglitazone in hepatocellular carcinoma, Actinomycin D resistance in gastric carcinoma, resistances to Cyclophosphamide, Adriamycin and 5-FU in breast cancer cells, sensitivity to Adriamycin, Daunorubicin and Arabinosylcytosine in leukaemia (Yan et al., 2020). FBXL7 expression is correlated with Paclitaxel resistance (Chiu et al., 2018) and FBXL10 overexpression is noted in aggressive brain and breast cancers (Frescas et al., 2007; Kottakis et al., 2014), and downregulation increases sensitivity to Cisplatin and Paclitaxel (Xiao et al., 2008).

F-box proteins are widely associated with drug resistance and cytotoxicity in cancer cells; however, this also demonstrates the incomplete and uncoordinated nature of available data, making prioritisation of F-box proteins as therapeutic or diagnostic targets difficult. Currently, there are no known drug or therapeutic agents or trials specifically targeting F-box for cancer therapy (Yan et al., 2020).

1.5.7. FBXL5

The human F-box and leucine-rich repeat protein 5 (*FBXL5*) gene encodes the FBXL5 protein of 78kDa (Benson et al., 2013) located on human chromosome 4 with 10 introns and 11 coding exons (2.1kb). Human and murine *FBXL5* both have nine predicted protein-encoding transcript variants (Howe et al., 2021). Mouse and human nucleotide *FBXL5* genome sequences are identical (Benson et al., 2013).

FBXL5 mRNA expression in colorectal adenocarcinoma mapped using the UALCAN cancer RNA-omics database (<http://ualcan.path.uab.edu/cgi-bin/TCGAExResultNew2.pl?genenam=FBXL5&ctype=COAD>) shows *FBXL5* expression is significantly lower in primary tumour samples compared to paired normal tissues (All comparisons $p \leq 0.001$), and this significance is consistent across all cancer stages (Chandrashekar et al., 2017; Yang et al., 2019) (Figure 1.9), although it is not specified which isoform was examined by this analysis. Similar results were found in analysis of colon adenocarcinoma lipid-metabolism-related genes, with *FBXL5* expression significantly reduced in colorectal adenocarcinoma tissues and potentially acting as a novel marker (Jiang et al., 2021). UALCAN data on *TP53* mutations also identified *FBXL5* expression as slightly higher in *TP53*-non-mutant samples compared to *TP53* mutant (Figure 1.9) (Chandrashekar et al., 2017).

This suggests that FBXL5 may act as a tumour suppressor in CRC, although this is in contrast to the limited published experimental data that shows FBXL5 protein expression is significantly upregulated in colorectal cancer, and that FBXL5 silencing inhibits cell proliferation in colorectal cancer cells (Yao et al., 2018). These differences will be discussed in more detail in Chapter 4.

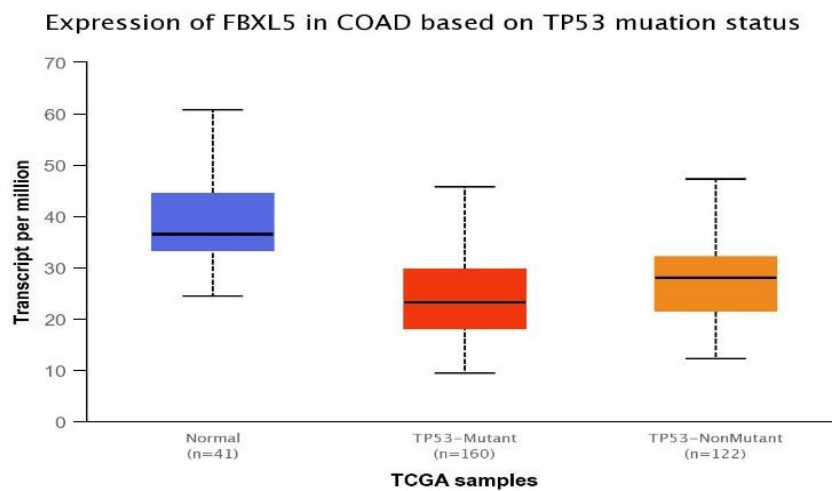
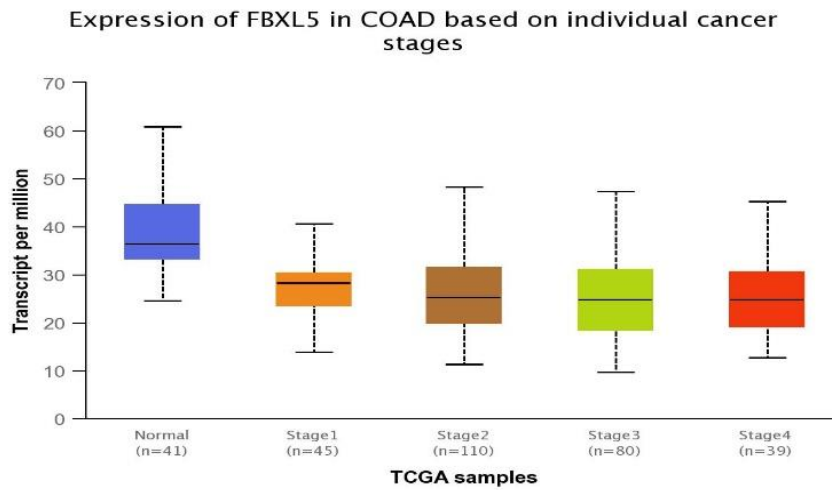
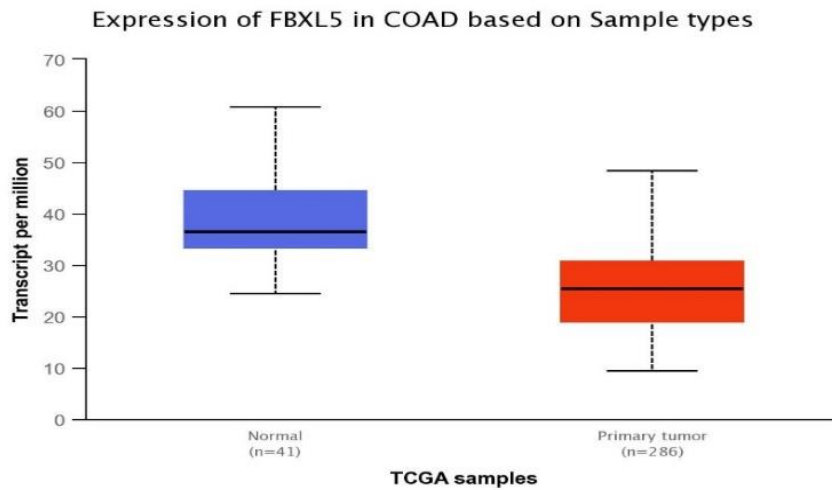


Figure 1.9: *FBXL5* expression is downregulated in colorectal adenocarcinoma.

FBXL5 expression is consistently downregulated across all four stages of CRC, and further downregulated in *TP53* mutant samples compared to non *TP53*-mutant samples in UALCAN cancer-omics data. All comparisons $p \leq 0.001$, total patient samples in analysis between 320-330. Data accessed Nov-Dec 2020 (<http://ualcan.path.uab.edu/cgi-bin/TCGAExResultNew2.pl?genenam=FBXL5&ctype=COAD>) (Chandrashekar et al., 2017).

FBXL5 was first identified in large scale sequencing and protein analysis studies (Cenciarelli et al., 1999), and since then several studies have been published linking *FBXL5* to a large variety of substrates and pathways including Dynactin in Motor Neuron Disease (Zhang et al., 2007), iron homeostasis (Moroishi et al., 2011), epithelial-to-mesenchymal transition (Findlay et al., 2014), *HIF-1a* in hypoxia (Machado-Oliveira et al., 2015a) and drug resistance (Ahmed et al., 2019; Wu et al., 2016). *FBXL5* itself may be targeted for silencing by MiR1306-3p (He et al., 2018), and depletion of the HECT-type ubiquitin ligase *HERC2* stabilises *FBXL5* activity (Moroishi et al., 2014), implying a role in upstream regulation of *FBXL5*.

One of the earliest studies of *FBXL5* identified it as the primary ubiquitinating substrate of *DCTN1* (Dynactin Subunit 1) (Zhang et al., 2007). Dynactin is a protein-binding complex component of the cytoskeletal microtubule motor Dynein-1, which moves membrane vesicles along microtubules *in vitro*. Dynactin dysfunction is linked to motor neuron disease (MND) (Lai et al., 2007). Homozygous knock-in *DCTN1* mice are embryonically lethal, while heterozygous mice develop a MND-like phenotype at 10 months old including loss of spinal motor neurons, reduced mobility and protein accumulation in neuromuscular junctions (Lai et al., 2007). The disease phenotype is

caused by abnormal vesicular movement in both mice and humans (Ferrara et al., 2018; Laird et al., 2008). It has previously been noted that DCTN1-associated cytotoxicity can be ameliorated by either the UPS or autophagy pathways, and overexpression of the *TFEB* (Transcription Factor EB) autophagy master transcription factor compensates for UPS inactivity (Wang et al., 2020b). One possible link between FBXL5 and MND may be the iron homeostasis pathway, as iron insufficiency has been shown to cause mitochondrial dysfunction within motor neurons (Jeong et al., 2011).

FBXL5 stabilises and accumulates in iron-replete and oxygen-replete conditions, while it is degraded by the proteasome when cellular iron is low (Chollangi et al., 2012). FBXL5's N-terminal folds into a hemerythrin-like domain that incorporates both iron during synthesis and interacts with oxygen in a real-time fashion (Chollangi et al., 2012) (Figure 1.10). Currently, FBXL5 is the only known mammalian protein with a hemerythrin-like domain for both iron and oxygen binding (Chollangi et al., 2012). Hemerythrin is a copper-based oxygen transport protein found in marine invertebrates, functionally similar to the iron-based haemoglobin in mammals (Shu et al., 2012). Deletion of this domain nullifies the iron-dependent regulation of FBXL5 (Chollangi et al., 2012). When oxidised, the C-terminal of FBXL5 contains a 2Fe2S cluster that binds and ubiquitinates IRP1 and IRP2 (iron regulatory protein 1 and 2) (Wang et al., 2020a) (Johnson et al., 2017), although IRP1 ubiquitination may only be active after impairment of CIA (Iron-sulphur cluster assembly) (Johnson et al., 2017). Interestingly, IRP2 is stabilised in hypoxia conditions while FBXL5 expression is reduced, implying that FBXL5 may be a dynamic oxygen sensor (Wang et al., 2020a). Mice lacking FBXL5 expression in neural stem progenitor cells (NSPC) have

increased concentration of NSPCs in the cortex and accumulation of ferric iron and reactive oxygen species (ROS) (Yamauchi et al., 2017).



Figure 1.10: Protein structure of FBXL5 showing hemerythrin-like domain.

FBXL5's hemerythrin-like domain is unique among mammalian proteins and may contribute to its interactions with both passive iron and active oxygen sensing.

Iron homeostasis and metabolism have a complex role in cancer, as while increased metabolism is emblematic of cancerous cell types, the corresponding increase in labile iron is cytotoxic. Both depletion of cellular iron and artificial iron overload are potential therapeutic targets, starving cells of iron required for proliferation or causing iron toxicity-induced apoptosis respectively (Brown et al., 2020). Regulation of iron metabolism also prevents free iron from forming free-radical ions that cause tissue, protein and DNA damage (Kakhlon and Cabantchik, 2002). Previous bioinformatic analysis and next generation sequencing across 31 different cancer types has identified 19 genes potentially related to iron homeostasis (Chen et al., 2019). Preoperative anaemia is common in CRC and treatment with iron supplementation has potentially detrimental effects (Wilson et al., 2018), while in liver and hepatocellular cancers, iron accumulation may cause hepatocellular injury and fibrosis of liver lobules (Baecker et al., 2018).

Iron accumulation and deficit also affects tumour metastasis and angiogenesis by deregulating epithelial-to-mesenchymal transition (EMT), promoting VEGF and altering Myc-relators (Jiang and Elliott, 2017). Ferritin, the primary storage media of intracellular iron, interacts strongly with tumour-associated macrophages (Costa da

Silva et al., 2017). Tumour-associated macrophages have roles in tumour progression, drug resistance and feedback effects between iron homeostasis and immune functions and have been successfully targeted to reinforce anti-tumour immune responses (Costa da Silva et al., 2017; Tang, 2013). By regulation of free radical formation, DNA and protein damage and tumour microenvironment and metastasis, iron metabolism has important roles in both cancer diagnosis, progression and treatment.

FBXL5-deficient mice are susceptible to liver carcinogenesis (Muto et al., 2019), while *FBXL5* double recessive mice are embryonically lethal (Moroishi et al., 2011). Current data suggests that *FBXL5* may be a cornerstone E3 ligase in the iron-homeostasis pathway, and further research may suggest possible diagnostic and therapeutic uses for *FBXL5*. Of note: hepatitis C (CHC) is a form of viral hepatitis that causes chronic liver disease and hepatic cancer (Nanba et al., 2016). *FBXL5* has been found significantly suppressed in CHC patients (Nanba et al., 2016). It is suggested that *FBXL5*'s role in the iron homeostasis pathway and oxidative stress may contribute to this relationship (Nanba et al., 2016). Recently, *FBXL5* has been found differently expressed in sepsis models, although the mechanisms involved are currently unknown (Zhao et al., 2020).

During Epithelial-to-Mesenchymal Transition (EMT), epithelial cells lose their cell-cell adhesion while gaining invasive and migratory properties to become mesenchymal cells, which is reversed during Mesenchymal-to-Epithelial Transition (MET) (Kalluri and Weinberg, 2009) (Figure 1.11). EMT/MET is critical for tissue development and healing, wherein multipotent cells will transition from epithelial to mesenchymal cells, migrate to a specific location, then transition back into epithelial cells and differentiate as required (Kalluri and Weinberg, 2009). Cancer metastasis is facilitated by EMT/MET, with cancerous cells developing migratory and invasive characteristics

and establishing secondary tumour metastases (Kalluri and Weinberg, 2009). EMT characteristics are a significant contributory factor in chemotherapy resistance (Qureshi et al., 2015).

Initial induction of EMT may be triggered by one of several oncogenic pathways, such as Wnt/ β -catenin, Notch and TGF β via PI3K/AKT, leading to downregulation of E-Cadherin (Larue and Bellacosa, 2005). Zinc Finger Protein SNAIL/SNAI1 downregulates E-Cadherin, thereby inducing EMT activity (Wu et al., 2015b). FBXL5 ubiquitinates SNAIL in the nucleus, inhibiting metastasis of cancerous cells, while loss of FBXL5 post-transcriptionally stabilises SNAIL and reduces E-Cadherin expression, promoting EMT activity (Wu et al., 2015b). Whether this loss of FBXL5 is sufficient to completely disable the EMT/MET pathway is not fully understood and varies between cell lines (Viñas-Castells et al., 2014; Wu et al., 2015b). Recently, it has been found that miR-1306-3p directly inhibits FBXL5 expression in HCCLM3 liver carcinoma cells leading to SNAIL accumulation, inducing EMT activity (He et al., 2018). Increased FBXL5 expression subsequently reduced miR-1306-3p expression and ameliorated the mesenchymal phenotype (He et al., 2018).

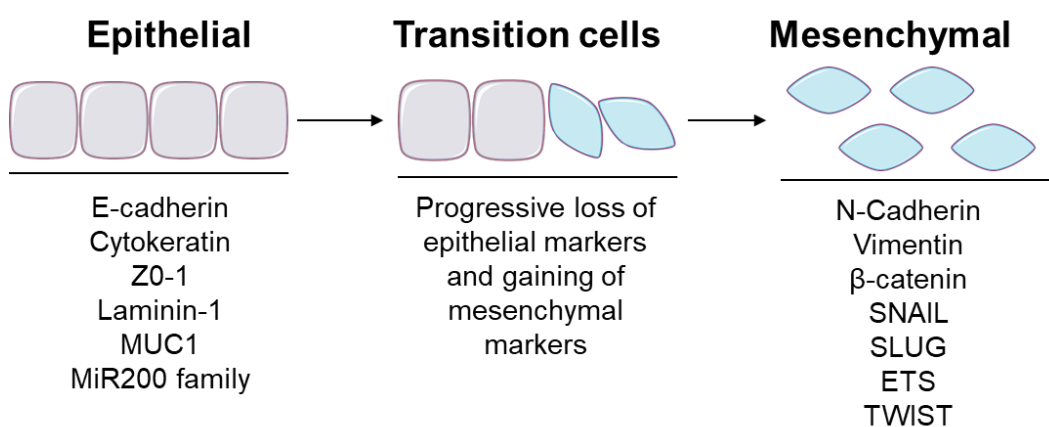


Figure 1.11: Diagram of Epithelial-to-Mesenchymal Transition

The Epithelial-to-Mesenchymal Transition involves epithelial cells losing cell cohesion, attachment and epithelial markers while gaining migratory and invasive characteristics and mesenchymal markers (Kalluri and Weinberg, 2009). This mechanism is frequently dysfunctional in cancer, and some tissues may display both epithelial and mesenchymal characteristics, presenting a “partial EMT” phenotype (Saitoh, 2018).

Another substrate of FBXL5 is CITED2 (Cbp/P300 Interacting Transactivator With Glu/Asp Rich Carboxy-Terminal Domain 2) protein, which negatively regulates the hypoxia master-regulator HIF-1 α (Machado-Oliveira et al., 2015a). Hypoxia is a common development in late stage tumour growth, wherein the capacity of tumour vascularisation to supply oxygen to the tumour mass is outstripped by the growth of the tumour itself (Muz et al., 2015). This causes alterations to cell metabolism and therapeutic resistance by reducing cell proliferation and inducing quiescence (Muz et al., 2015). CITED2 levels are inversely correlated to FBXL5, in turn dysregulating HIF-1 α expression. Given FBXL5’s oxygen-dependent stability, hypoxic conditions may lead to reduced FBXL5 expression, however compensating regulatory pathways ensure reduced CITED2 and upregulated HIF-1 α expression (Machado-Oliveira et al., 2015a).

In addition to its role in hypoxia regulation, CITED2 also has essential roles in tissue development, with *CITED2* KO mice being embryonically lethal with severe cardiovascular abnormalities including pulmonary valve stenosis and ventricular septal defects (Yin et al., 2002). Analysis of *CITED2* negative cardiac tissue shows reduced mRNA levels of several HIF-1 α target genes including vascular endothelial growth factor (VEGF), while Glut1 and phosphoglycerate kinase 1 (PGK1) were

increased (Yin et al., 2002). Of these, VEGF is most interesting, as VEGF overexpression embryos share similar debilitating cardiac phenotypes as CITED2 negative embryos, while overexpression of VEGF produces equally dramatic cardiac abnormalities (Yin et al., 2002). As such, FBXL5 via CITED2 may have a significant role in hypoxia response, VEGF regulation and cardiac development.

FBXL5 has been found to interact with Alpha-Synuclein (α Syn), the protein which gradually accumulates in neurons as Lewy Bodies, eventually propagating across neurons and leading to Parkinson's pathologies (Gerez et al., 2019). In mouse models, downregulation of FBXL5 expression induces α Syn accumulation and Parkinson's-like pathologies (Gerez et al., 2019). Remarkably, overexpression of FBXL5 via lentiviral transduction prevented α Syn accumulation and spread within the mouse neurons, suggesting that FBXL5 overexpression may be a therapeutic treatment for α Syn-pathologies (Gerez et al., 2019).

Some studies have presented evidence of FBXL5's role as an oncogene and tumour suppressor, including modulating the PI3K/AKT/mTOR pathway (Yao et al., 2018) and Cisplatin resistance in colorectal cancer (Wu et al., 2016), miR-20a regulation in cervical cancer (Xiong et al., 2017), hssB1-mediated DNA damage repair in lung cancer (Chen et al., 2014), as well as acting as a prognostic marker in renal cell carcinoma (Park et al., 2021). *FBXL5* was also found to be correlated significantly with immune cells CD8+T, CD4+T, macrophages and dendritic cells as well as Austocystin D and Bafilomycin, which act as tumour suppressors and immunotherapy modulators (Jiang et al., 2021).

The PI3K/AKT/mTOR pathway is associated with cell proliferation and cancer (Papadatos-Pastos et al., 2015) (Figure 1.12). In brief, a transmembrane receptor

triggers PI3K (phosphatidylinositol 3-kinase) which phosphorylates and activates AKT, in turn beginning a signalling cascade that activates the two mTOR complexes mTORC1 and mTORC2 (Mammalian target of rapamycin complex). mTOR downstream interactions include autophagy suppression, mitochondrial activity, cell survival, ion transport and epithelial growth factors (Zarogoulidis et al., 2014). PTEN (Phosphatase and Tensin homolog) negatively regulates AKT's activity by dephosphorylation, thereby reducing mTOR activation (Duronio, 2008). In colorectal cancer tissues and cell lines, FBXL5 has been shown to physically interact with PTEN and negatively regulate its expression, with corresponding increases in PI3K, AKT and mTOR expression (Yao et al., 2018). FBXL5 overexpression increased cell proliferation and tumour formation ability, with corresponding results for FBXL5 inhibition (Yao et al., 2018). PTEN also correlates with p53 protein expression (Freeman et al., 2003). FBXL5 protein expression is significantly upregulated in colorectal cancer compared to normal tissues, and greater FBXL5 protein expression was also found to correlate with lower 5-year post-surgical survival rates in colorectal cancer patients (Yao et al., 2018). This increased FBXL5 protein is in contrast to the UALCAL analysis, which shows consistently reduced *FBXL5* RNA expression across colorectal cancer patient samples (Chandrashekar et al., 2017)

In contrast to colorectal cancer, FBXL5 expression is associated with increased survival rates in cervical cancer (Xiong et al., 2017). As such, FBXL5 may be a new prognostic marker for colon cancer and novel therapeutic target.

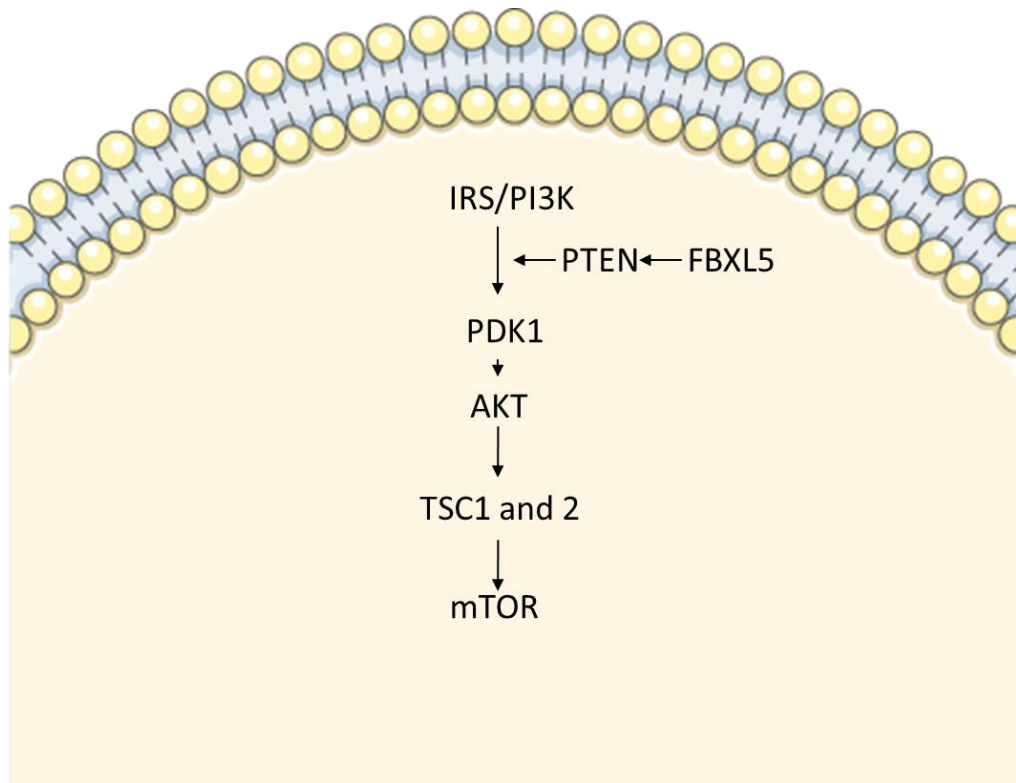


Figure 1.12: The simplified mTOR Pathway

The mTOR (Mammalian target of Rapamycin) pathway is a central regulator of cell metabolism and physiology. mTOR is frequently dysregulated in metabolic diseases and cancer (Zarogoulidis et al., 2014). Image adapted from (Wong M, 2012)

Another study found that FBXL5 increases Cisplatin resistance in gastric cancer cells by inducing phosphorylation of the ERK and p38 of the MAPK pathway (Wu et al., 2016). Interestingly, this study also determined that RhoGD12, a GTPase inhibitor which regulates actin cytoskeletal activity and is associated with acquired Cisplatin resistance and tumour metastasis, may promote the ubiquitination of FBXL5 itself in response to Cisplatin treatment (Wu et al., 2016). FBXL5 depletion increases Cisplatin

resistance by activation of MAPK pathway ERK and p38, while FBXL5 expression was depleted in RhoGDI2-overexpressing cells post-Cisplatin treatment (Wu et al., 2016). This implies a negative feedback loop between RhoGDI2 and FBXL5, with FBXL5 possibly binding RhoGDI2 and preventing its suppression of apoptosis (Wu et al., 2016). Silencing the p53 inhibitor iASPP reduces cervical cancer cell proliferation and sensitised the cells to Cisplatin treatment *in vivo*, while silencing FBXL5 and BTG3 expression reversed these changes (Xiong et al., 2017). This suggests that FBXL5 may be a therapeutic target in RhoGDI2-induced Cisplatin resistant cancers.

Human single-strand DNA binding protein 1 (hssB1) participates in the single-strand DNA damage response caused by environmental, carcinogenic and chemical exposure (Tang et al., 2014). Cells lacking hssB1 protein demonstrated increased genomic instability and radiation-induced DNA damage (Richard et al., 2008). FBXL5 has been shown to ubiquitinate non-phosphorylated hssB1. In lung cancer cell lines and clinical lung cancer samples, FBXL5 and hssB1 proteins show an inverse correlation, with FBXL5 overexpression causing sensitivity to DNA damage (Chen et al., 2014). Bioinformatic analysis has identified alternative splicing of FBXL5 as a prognostic biomarker for lung adenocarcinoma (Chang et al., 2020).

The evidence thus far shows that FBXL5 may have a substantial role in both cellular homeostasis and cancer response. Known interactions with iron homeostasis, hypoxia response, EMT/MET, PI3K/AKT/mTOR, drug resistance and several cancers strongly supports the study of FBXL5 and its association with colorectal cancer as an oncogene, tumour suppressor, prognostic marker and important therapeutic target.

1.6. Aims and Objectives

The UPS has been shown as an essential contributory factor in the development and progression of human cancers including colorectal cancer. However, current research fails to elaborate on a detailed understanding of the F-box gene associations, with only a few such as *FBXW7* studied in any depth. The remainder is limited to few studies focusing on single mechanisms or pathways rather than a comprehensive analysis of each F-box in a particular tissue. At the same time, the function of some F-box proteins is still unknown. Further research on F-box is a clear priority for a greater understanding of the role of F-box protein mediated ubiquitination in tissue homeostasis and cancer.

As outlined above, organoids are a novel, three-dimensional *in vitro* modelling system for functional genetics studies that demonstrate many advantages of *in vitro* immortalised cell lines and *in vivo* animal models. Combined with the CRISPR/Cas-9 editing system, organoids can largely overcome the limitations of current *in vitro* and *in vivo* methodology for functional gene analysis and other applications with an accessible, scientifically viable alternative.

Therefore, this project aimed to initially experimentally explore the role of F-box genes by utilising Cas-9 expressing murine intestinal organoids. After identifying the loss of F-box gene(s) that phenotypically or functionally impact intestinal organoids, this study aimed to investigate further the role of the candidate gene (i.e., *FBXL5*) in human colorectal cancer cells using cell and molecular techniques.

To achieve these:

- In Chapter 3, we generated Cas9 expressing transgenic murine intestinal organoids, then utilised an F-box gRNA library to generate F-box knockout

organoids. The growth and morphology of these organoids was analysed to investigate the possible impact of F-box knockout on murine intestinal organoid function. Once those F-box that caused significant organoid growth and morphology changes were identified, the selected loss-of candidate (i.e., FBXL5) was further examined in subsequent chapters using colorectal cancer cells.

- Chapter 4 investigated the functional role of F-box E3 ligase FBXL5 on growth and cell division in colorectal cancer by generating colorectal cancer cell lines (DLD-1 and SW480) knockout for FBXL5. This chapter further examined how FBXL5 knockout may affect cell morphology, cell proliferation, cell migration and epithelial-to-mesenchymal activity in these colorectal cancer cells.
- In Chapter 5, to further understand the role of FBXL5 in colorectal cancer, we studied FBXL5 and its possible association with Iron Metabolism, Autophagy, Hypoxia and Drug Response in colorectal cancer cells.
- Chapter 6 analysed publicly available transcriptomic and proteomic databases including STRING, GEPIA and UALCAN. Furthermore, differentially expressed genes (DEGs) were identified using RNA-Seq and analysed by Pathway Mapping Analysis to determine novel associations with FBXL5 in colorectal cancer.

Chapter 2: Materials and Methods

2. Materials and Methods

2.1. Materials

2.1.1. Cell Lines

Cell lines were purchased from ATCC between 2008-2010. Cells were regularly tested as mycoplasma free.

Table 2.1: List of Human Cell Lines used in this project		
Cell Line	Genetic Background	Media
DLD-1: DL Dexter Human Colorectal Cancer Cells (Epithelial)	DLD-1: <i>KRAS</i> G13B, <i>PI3K E545K</i> mutation, <i>D549N</i> mutation, <i>TP53</i> mutation (tumour suppressor) (Ahmed et al., 2013a)	RPMI, 10% FBS, 1% Lg, 1% P/S
SW480 Colorectal Cancer Cells (Epithelial)	Keratin, <i>p53</i> high expression, matrilysin not expressed (cell matrix/transformation), <i>GM-CSF</i> expressed (growth factor/migration factor) (Ahmed et al., 2013b)	RPMI, 10% FBS, 1% Lg, 1% P/S
HEK293: Human Embryonic Kidney Cells 293 (Contains SV40-T antigen, loss of function <i>p53</i> and pRb mutations (Lin et al., 2014).	RPMI, 10% FBS, 1% Lg, 1% P/S
R-Spondin 1 secreting HEK-293 T cells (HA-R-Spol-Fc cell line)	Zeocin resistance gene. Secrete R-Spondin 1 protein.	Culture: DMEM RPMI, 10% FBS, 1% Lg, 1% P/S R-Spondin 1 production: ADMEM 10% FBS, 1% Lg, 10% HEPES Buffer

2.1.2. Antibodies

Table 2.2: List of Antibodies used in this project		
Antibody	Source and Citation	Antibody concentration for Western lot

Anti-Mouse Cas-9	Cell Signalling 146975 (Müller et al., 2021)	1:1000
Anti-Noggin	BD Biosciences 560170 (Choi et al., 2007)	1:1000
Anti-FBXL5	Santa Cruz Biotechnology sc-376102 (no citations available)	1:100
Anti-β-Actin	Santa Cruz biotechnology sc-47778 (Lin et al., 2021)	1:5000-1:10000
Anti-β-Catenin	Cell Signalling 95615 (Wu et al., 2021)	1:1000
Anti-N-Cadherin	BD Biosciences 610920 (Bhowmick et al., 2001)	1:1000
Anti-E-Cadherin	BD Biosciences 610181 (Jaksits et al., 1999)	1:1000
Anti-Vimentin	Santa Cruz Biotechnology sc-32322 (Samson et al., 2021)	1:1000
Anti-SNAIL	Cell Signalling C15D3 (Barrallo-Gimeno and Nieto, 2005)	1:1000
Anti-IRP1 (Iron Regulatory Protein 1)	Santa Cruz Biotechnology sc-166022 (Miniaci et al., 2016)	1:1000
Anti-Ferritin	Santa Cruz Biotechnology sc-71102 (no citations available)	1:1000
Anti-Transferrin Receptor 1 (TfR aka CD71)	Santa Cruz Biotechnology sc-51829 (Rockfield et al., 2018)	1:250
Anti-RBCK1	Santa Cruz Biotechnology sc-365523 (Elliott et al., 2021)	1:1000
Anti-VHL	Santa Cruz Biotechnology sc-135657 (Liu et al., 2021)	1:1000
Autophagy Protein 5 (ATG5)	Cell Signalling 26305 (Zhu et al., 2021b)	1:500
Anti-Microtubule-associated proteins 1A/1B Lightchain 3B (LC3B)	Cell Signalling 27755 (Zhu et al., 2021a)	1:500

Anti-Beclin1	Cell Signalling D40C5 (Li et al., 2021)	1:500
Rabbit Anti-Mouse secondary HRP	Santa Cruz Biotechnology sc-2005	1:5000
Rabbit Anti-Mouse Fluorescent Secondary	Life Technologies A-21155	1:500-1:2000

2.1.3. Buffers

Protocol	Buffer	Ingredients
SDS-PAGE and Western Blot	Loading Buffer (5x)	250 mM Tris-HCL ph. 6.8, 10% SDS, 50% Glycerol, 5% β -Mercaptoethanol
	SDS-PAGE Running Buffer (10x)	10g SDS, 30g Trisma, 144g M Glycine 1ltr distilled water, 0.05% bromophenol blue
	Transfer Buffer (Semi Dry, 10x)	3g Tris HCL, 14.5g glycine, 200 ml methanol, 800 ml water
	Transfer Buffer (TURBO) 1x	600 ml double distilled water, 200 ml methanol, 200 ml x5 stock
	Tris Buffer Saline with Tween (TBS-T) 10x	24.23g Trizma, 88g NaCL, 800 ml distilled water, 20mM Tris 7.6pH, 130nM NaCL, 0.1% Tween 20, 3% BSA
<i>E.coli</i> Amplification	LB Bacterial Growth Media	20g LB powder (10g/l tryptone, 5g/l yeast extract, 5g/l NaCL) 1ltr distilled water
Alkaline Lysis	Suspension Buffer	50mM Tris-Cl pH 8.0, 10mM EDTA, 100 μ g/ ml RNase A
	Lysis Buffer	200mM NaOH, 1% SDS (w/v)
	Neutralisation Buffer	3.0M potassium acetate, pH 5.5

	Equilibration Buffer	750mM NaCL, 50mM MOPS pH 7.0, 15% isopropanol (V/V), 0.15% Triton X-100 (v/v)
	Wash Buffer	1.0 M NaCL, 50mM MOPS pH 7.0, 15% isopropanol
	Elution Buffer	1.25M NaCL, 50mM Tris-CL, pH 8.5, 15% isopropanol (V/V)
Agarose Gel Electrophoresis	TAE Buffer (50x)	242g Tris free base, Disodium EDTA 18.61g, Glacial Acetic Acid 57.1 ml. dH2O to 1l.
Cell Lysis	RIPA Buffer	10mM Tris-CL (pH 8.0), 1mM EDTA, 0.5mM EGTA, 1% Triton X-100, 0.1% Sodium Deoxycholate, 0.1% SDS, 140 mM NaCl, prior to use add 1 µl phosphatase inhibitor for every 1 ml RIPA)

2.1.4. Primers

Table 2.4: List of Primers used in this project	
Target	Sequence
<i>B-Actin</i> Human	F: GCGCGGCTACAGCTTCA R: CTTAATGTCCACGCACGATTTC
<i>FBXL5</i> Human	F: CTGCAGGGCTGTCTCATCTC R: TCTGAAGGATGGTCCTGGCT
<i>β-catenin</i> Human	F: GGAAGGTCTGAGGAGCAGC R: TCCAACCTCCATCAAATCAGCTTG
<i>N-Cadherin</i> Human	F: GACAATGCCCTCAAGTGTT R: CCATTAAGCCGAGTGATGGT
<i>E-Cadherin</i> Human	F: TGGAGGAATTCTTGCTTTGC R: CGTACATGTCAGCCAGCTTC
<i>Vimentin</i> Human	F: GAGAAGTTTGCCGTTGAAGC R: TCCAGCAGCTTCCTGTAGGT
<i>SNAI1</i> Human	F: AATCCAGAGTTTACCTTCCA R: AGAGTCCCAGATGAGCATTG

<i>IRP1</i> (Iron Regulatory Protein 1) Human	F: CTGGAGTGTGGTAGGAACACG R: TCCAATGGCTCAGCAAGGTG
<i>IRP2</i> (Iron Regulatory Protein 2) Human	F: TACCTGCCGAGGATCTTGHTG R: GAACTCCATCAGGCACTGGTT
<i>Ferritin Heavy</i> Human	F: CCAGAACTACCACCAGGACTC R: AAAGTAGTAAGACATGGACAG
<i>Ferritin Light</i> Human	F: CTTGCCAACCAACCATGAGC R: AGAAGCCCAGAGAGAGGTAGG
Transferrin Receptor 1 (<i>TfR</i> aka CD71) Human	F: GGACGCGCTAGTGTTCTTCT R: CATCTACTTGCCGAGCCAGG
<i>ALDH3B1</i> Human	F: CTTGGCAGAGCCTCAGGATG R: GTTTTCTTGCAGGAAGCGGC
<i>APP</i> Human	F: GCTGGAGGTACCCACTGATG R: TCTGCCACAGAACATGGCAA
<i>RBCK1</i> Human	F: AGACCAAGAAAGGCTGTGGG R: CAAGACTGGTGGGAAGCCAT
<i>VHL</i> Human	F: ATCCACAGCTACCGAGGTCA R: GGCAAAAATAGGCTGTCCGTC
<i>GLRX5</i> Human	F: GGAGCTCCGACAAGGCATTA R: CCCCCTACAAACTCGCCATT
<i>YBX-1</i> Human	F: AAGGAGAAAAGGGTGCGGAG R: CCTACGACGTGGATAGCGTC
<i>HOPX</i> Human	F: TCAACAAGGTCGACAAGCAC R: TCTGTGAGGATCTGCACTC
<i>LGR5</i> Human	F: GACAACAGCAGTATGGACG R: GCATTACAAGTAAGTGCCAG
<i>CD44</i> Human	F: ACTTTGCCTCTTGCAGTTGAG R: TTTCTCCACATGGAATACACCTG
<i>TERT</i> Human	F: GGCACGGCTTTTGTTCAGAT R: GGCATAGCTGGAGAGTCGCT
<i>HIF-1α</i> Human	F: GATAGCAAGACTTTCCTCAGTCG R: TGGCTCATATCCCATCAATTC

<i>CA9</i> Human	F: CTTGGAAGAAATCGCTGAGG R: TGGAAGTAGCGGCTGAAGTC
<i>VEGFR2</i> Human	F: GCAGCTTGAGTTAAACGAACG R: GGTTCCTCGAAACCCTGAG
<i>ANGPTL4</i> Human	F: GACAAGAAGTGCGCCAAGA R: GCCGTTGAGGTTGGAATG
<i>Cortactin</i> Human	F: CCGCAGGATCAGGAAACTCA R: AGTCCCGAGACATTTCCACG
<i>ATG5</i> Human	F: CAAGGTGGAGTTGGCGAGAC R: ACCAAAGCCAAACTTAGTAAGCA
<i>LC3B</i> Human	F: CCGCACCTTCGAACAAAGAG R: AAGCTGCTTCTCACCCCTTGT
<i>Beclin1</i> Human	F: GGGCTCCCGAGGGATGG R: CTCGTGTCCAGTTTCAGGGG

2.1.5. Plasmids and Lentiviral Vectors

Table 2.5: List of Plasmids used in this project	
Name	Source
PLVx-eGFP	Sigma Merck (no longer listed for purchase)
pCMVR8.74	Addgene #22036
pMD2.G	Addgene #12259
Noggin Plasmid	Generated by Wim de Lau and Hans Teunisse of Hubrect Institute, Netherlands
F-box CRISPR-gRNA Library	Kindly generated by Dr Emmanouli Metzakopian and colleagues of the Wellcome Trust Sanger Institute, Cambridge
pLv5-Cas-9-Neo Lentiviral vector	Sigma Merck Cas-9NEO-1EA

2.1.6. Animals

C57BL/6J mice of either gender at approximately 4-6 weeks old were used for organoid isolation experiments. Mice were housed and bred in the transgenic animal facility of the Biomedical Service Unit at the University of Nottingham. Animals sacrificed by cervical dislocation and confirmed by exsanguination.

2.2.Methods

2.2.1. Culture, Freezing and Thawing of Epithelial Cells

After seeding, immortalised cell lines were incubated at 37°C/5% CO₂ and sustained via cell growth media such as Roswell Park Memorial Institute Media 1640 (RPMI, Thermo Fisher Scientific, 25030-024) and Dulbecco's Modified Eagle's Media (DMEM, Sigma Aldrich, D5671), supplemented with L-Glutamine (Thermo Fisher Scientific, 25030-024), and Foetal Bovine Serum (Sigma; F7524). This media was replaced every 2-3 days as required. Once confluent, cells were subcultured/passaged: media was aspirated, the cells washed with PBS (Phosphate-Buffered Saline, Sigma; D8537) and cells detached from vessel using Trypsin (Sigma; T3924), a digestive protease. Once cells were completely detached and suspended, additional prewarmed growth media was added to dilute and inactivate the trypsin and the cell-containing media divided among required vessels as required.

Freezing media for cells used in this study was 90% FBS/10% DMSO (Dimethyl sulfoxide, Sigma; D4540). To freeze cells for storage: tryptonised cells were diluted with growth media and the entire solution centrifuged at 300xg for three minutes to form a pellet. Supernatant was removed and pellet resuspended in FBS supplemented with 10% DMSO and aliquoted to a freeze-safe storage vial and stored at -80 in a freezing container overnight. Vials were subsequently moved to longer term storage such as liquid nitrogen or -150 freezer facilities. To thaw cells: cell vials were completely thawed in a 37°C water bath. The content was aliquoted to a centrifuge-safe vessel, diluted with growth media and centrifuged at 300xg for three minutes to form a pellet. The supernatant was removed, the pellet resuspended in growth media and reseeded to suitable vessels. Cells were passaged at least once before experimental use.

2.2.2. Colony Formation Efficiency Assay/ Clonogenic Assay

The Colony Formation Efficiency/Clonogenic Assay determines the ability of individual cells to proliferate (Franken et al., 2006). Both colony quantity and size will differ between cell lines (Franken et al., 2006) (Rafehi et al., 2011) and according to experimental conditions.

To perform the colony formation efficiency assay: Cells were seeded in triplicate at 500 cells per 75cm² flask or 200 cells per 6-well plate, with either media changed every 3-4 days or no media change at all depending on cell requirements. 10-14 days post seeding, cell media was removed, and cells are washed with 6 ml PBS and fixed with 4% paraformaldehyde solution at room temperature (1 ml per well in 6-well plate or 6 ml per T75) for 20 minutes, washed with PBS and subsequently stained with 1 ml or 6 ml 0.01% crystal violet (Sigma Aldrich, 0775) in PBS for 20 minutes. Finally, the crystal violet dye was removed, and the flask washed again with PBS and air dried at room temperature overnight. The result should be numerous purple spots or dots of varying size across the growth surface of the flask that are visible without microscopy (Dong et al., 1984).

2.2.3. Flow Cytometry and Propidium Iodide staining

Flow Cytometry is a high throughput method of analysing the type and cell cycle status of single cells in suspension by their response to fluorescent light and light scatter. In this technology: single cells in solution are passed through a light beam one cell at a time, the beam scattering differently depending on cell morphology and fluorescent labelling, thereby allowing accurate cell counting and sorting of different cell types, as well as detection of chemical and clinical characteristics (Riccardi and Nicoletti, 2006). For this study, we utilised Propidium Iodide, a fluorescent molecule that binds

both DNA and RNA indiscriminately, therefore may be used in conjunction with flow cytometry to quantify DNA and RNA to determine cell cycle stage (Davies, 2021; Riccardi and Nicoletti, 2006).

Propidium Iodide staining was performed using manufacturer instructions (Propidium Iodide Flow Cytometry Kit ab139419 (Davies, 2021)): 10cm plates of 70% confluent cells were tryptonised and washed with PBS in triplicate. Cells were fixed with 1 ml ice cold 70% ethanol added dropwise while vortexing to reduce cell clumping. Cells were incubated at 4°C for 30 minutes and washed a further two times with PBS. To ensure only DNA is stained, cells were treated with 50 µl ribonuclease. Finally, 200 µl of propidium iodide solution was added (stock: 50 µg/ ml). Cells status was determined using Beckman Coulter FC500 Flow Cytometer by measurement of forward scatter/cell size (FS) vs side scatter/granularity of cells (SS) ratio and fluorescent expression. For this project, Flow Cytometry procedure was kindly performed by Dr David Onion of University of Nottingham Flow Cytometry Service. Data was analysed using WEASEL 3.7.1 and doublets removed from analysis.

2.2.4. Growth Curve/Proliferation Assay

The exponential proliferation of mutated cells and subsequent malignancy is a defining feature of cancer (Fouad and Aanei, 2017). The Growth Curve/Proliferation Assay measures the logarithmic proliferation rate of cells over time (Von Rosen, 1991). Precise cell seeding is important during the initial setup, which therefore requires repetition to ensure accuracy (Von Rosen, 1991).

Growth Curve Analysis was performed for a seven-to-eight-day period, with 3×10^4 cells/well seeded in triplicate using a 24 well plate. Each day, three wells from each condition were tryptonised with 100 µl 1x trypsin, centrifuged and counted manually

via haemocytometer or using an automated cell counter (Bio-Rad, Germany) (Von Rosen, 1991) for a total of 21-24 wells per condition over 7-8 days. Data was converted to logarithmic scale for analysis and compared against control growth to determine possible experimental effects.

2.2.5. Wound Healing Analysis

The Wound Healing Assay (aka Scratch Assay) is a simple and inexpensive method of investigating cell migration and attachment in a 2D environment without relying on more complex 3D assays or specialist equipment (Rodriguez et al., 2005). This assay mimics cell migration during wound healing by creating a “wound” in a cell monolayer and imaging this area at specific timepoints until the wound is closed (Rodriguez et al., 2005). To ensure experimental data is the result of cell migration rather than proliferation, cells are starved for 24 hours pre-assay using 1% FBS rather than 10% media, encouraging cells to synchronise at quiescent stage (Rodriguez et al., 2005).

For this assay; cells were seeded in triplicate in a 6-well plate to confluency. Cells were starved for 24 hours post-seeding using 1% FBS media, then the media was removed, cells washed with PBS, and a straight line scratched into the cellular monolayer by hand using a P20 pipette tip, held perpendicular to the adherent surface. A fresh P20 tip was used on each scratch for uniformity. Cells were washed twice more with PBS and complete 10% media added. The scratched area was immediately imaged in 3 places per well via microscopy, then imaged further at 24 and 48-hours post-scratch. The distance between two sides of the “wound” and the total area between each side was quantified using ImageJ software to determine possible experimental effects (ImageJ version 1.5A) (Abramoff et al., 2003).

2.2.6. Immunofluorescence (IF) and Phalloidin staining

To prepare cells for immunofluorescent staining (Donaldson, 2015): Standard cover slips were placed in each well of a 6-well plate, sterilised with 70% ethanol, washed twice with PBS and air-dried. Cells were then seeded at between $1-5 \times 10^5$ cells per well and incubated in growth media overnight. The following day, the growth media was removed, and cells washed with PBS twice before fixation in 1 ml of 4% paraformaldehyde (PFA, Sigma P6148) for 30 minutes at room temperature. After washing twice more, cells were permeabilised with 500 μ l 0.1% Triton (Sigma 9002-93-1) for 30 minutes and washed a further two times with PBS. At this point, protocols differ between Phalloidin staining (Sigma Aldrich, 1951) and probing with alternate primary antibodies:

For Phalloidin staining: Cells were then stained with 800 μ l 0.5% Phalloidin for 40 minutes in darkness. Slides were removed from the well and mounted to microscopy slides using Vectashield Mounting Media with DAPI (Abcam ab104139), incubated at room temperature for at least 20 minutes and fixed in place using nail polish. These slides were stored at 4°C and imaged using fluorescent microscopy the following day.

For alternative primary antibodies: cells were blocked with 3% BSA 500 μ l/well for one hour at room temperature, washed three times with 1 ml PBS for five minutes each, then probed with primary antibody in 2% BSA 400 μ l/well overnight at 4°C. The following day, cells were washed twice with PBS, and probed with secondary antibody at 1:500 for one hour at 4°C in the dark. Cells were washed twice more with PBS, then fixed using Vectashield Mounting Media with DAPI (Abcam ab104139), incubated at room temperature for at least 20 minutes and fixed in place using nail polish. These

slides were imaged using fluorescent microscopy the following day and stored at 4°C. Incubation time and antibody concentration was optimised for each assay.

Cells were imaged using Leica DMI3000 B fluorescence microscope (Leica Microsystems) and Leica Application Suite software (Version 2.5.0.6735). Samples were imaged using both brightfield and respective fluorescence setting. Fluorescence and image settings were adjusted uniformly across all images in each experiment.

To quantify changes to cellular morphology: The ImageJ software (ImageJ version 1.5A (Abramoff et al., 2003)) was used to measure total cell area, perimeter and both long and short cellular axes. As we could not locate a published method for quantifying cellular elongation from Phalloidin imaging: cell elongation was determined by the long/short cell axis ratio.

2.2.7. Transfection

Transfection is a method of introducing purified nucleic acids, such as plasmids, to cells without using viral vectors. In order to induce uptake in cells via endocytosis, DNA molecules are bound with polyethylenimine (PEI) (Polysciences; 23966-1). The positively charged PEI will bind and condense negatively charged DNA into positively charged bundles, which bind more effectively to the negatively charged cell membrane, facilitating endocytosis (Baker et al., 1997). In this state, plasmid sequences are expressed and act within that cell (Baker et al., 1997; Longo et al., 2013). As plasmid transfection is transient, plasmid expression will typically only last several days, with detectable expression gradually diminishing (Longo et al., 2013).

For polyethylenimine plasmid transfection: cells were grown to 70% confluency, the growth media removed and replaced with a solution of low-serum media (such as Opti-MEM, Thermo Fisher Scientific, 31985070) supplemented with PEI and the plasmid construct at a ratio of 4-15 μg PEI: 1 μg total DNA. The cells were incubated for 6-8 hours at 37°C, after which the Opti-MEM was replaced with appropriate complete growth media without antibiotics. If plasmids contain a fluorescent marker such as tBFP, this will typically be expressed 12-18 hours after initial transfection.

2.2.8. Transduction

This project utilised the pCMV R8.74 packaging plasmid (Addgene #22036) and pMD2.G (Addgene #12259) envelope plasmids to generate our lentiviral F-box gRNA-containing constructs. The plasmid backbone of our F-box gRNA library was the pLv-U6g/PGK-Puro-2a-tBFP transfer plasmid (Addgene, no longer available).

To generate gRNA-containing 3rd generation lentiviral particles: HEK293-T cells were grown to 70% confluency in T75 flasks using complete media at two flasks per construct. The following day, cells were transfected with the packaging, envelope and gRNA-containing transfer plasmids at the ratio of: 15 μg gRNA plasmid: 5 μg envelope plasmid: 10 μg packaging plasmid and between 4-15 μg PEI per 1 μg DNA in 1.5 ml Opti-MEM per T75 flask. After 6-8 hours, Opti-MEM was replaced with complete media and cells incubated overnight. The following day, flasks were checked for transfection efficiency via fluorescence.

For three days post transfection, the growth media was replaced, and old media filtered through 0.45 μm filter, aliquoted to 50 ml falcons and stored in suitable hazardous-sample containment. After three days of harvesting, the media was amalgamated into 50 ml falcon tubes with approx. 7-8 ml of virus sucrose solution and centrifuged at

25-27g for 4-4.5hours at 4°C. (Virus sucrose solution 50 ml in ultrapure water: 10% sucrose, 50 mM Tris HCL pH 7.4, 100 mM NaCL, 0.5 mM EDTA) (Jiang et al., 2015). After centrifugation, the supernatant was carefully discarded and either 500 µl organoid media or complete ADMEM was added to each tube at left overnight at 4°C. The following day, this concentrated virus-containing media was aliquoted in 50-100 µl volumes to 1.5 ml Eppendorf tubes and stored at -80°C (Kashfi et al., 2020).

2.2.9. Plasmid Amplification

Plasmid application consists of three stages: bacterial transformation with competent cells, bacterial amplification and plasmid purification via alkaline lysis.

2.2.9.1. Bacterial Transformation

The method for the heat-shock of bacterial transformation is as follows (Birnboim and Doly, 1979): 50 µl *Escherichia coli* (*E. coli*) chemically competent cells were combined with 1-5 µg of plasmid suspended in dH2O. This solution was incubated on ice for 10 minutes, then heated to 42°C for one minute and returned to ice for a further 10 minutes. This solution of transformed cells was initially amplified in 500 µl LB (Lysogeny Broth, Sigma Aldrich, L3022) for 90 minutes at 37°C while shaking. The transformed cells can be frozen in 50% glycerol at -80°C or amplified further in LB media for 12-18 hours at 37°C while shaking. Plasmids in this project used 1% ampicillin for antibiotic selection (Birnboim and Doly, 1979). An aliquot of bacterial solution was frozen at each stage of the amplification to ensure against accidental loss or for future use.

2.2.9.2. Alkaline Lysis Purification

Alkaline lysis is a method of isolating plasmid DNA or RNA from bacterial cells, relying on the size difference between bacterial and plasmid DNA, as the smaller

plasmid can easily re-nature after lysis and dissolve in solution, while larger bacterial chromosomal DNA will instead form white precipitate that can be purified from the solution. Alkaline Lysis method was adapted from manufacturer instructions (Genopure Plasmid Midi Kit, Roche Scientific 03143414001, 2020, Figure 2.1). All buffer preparations are found in Table 2.3.

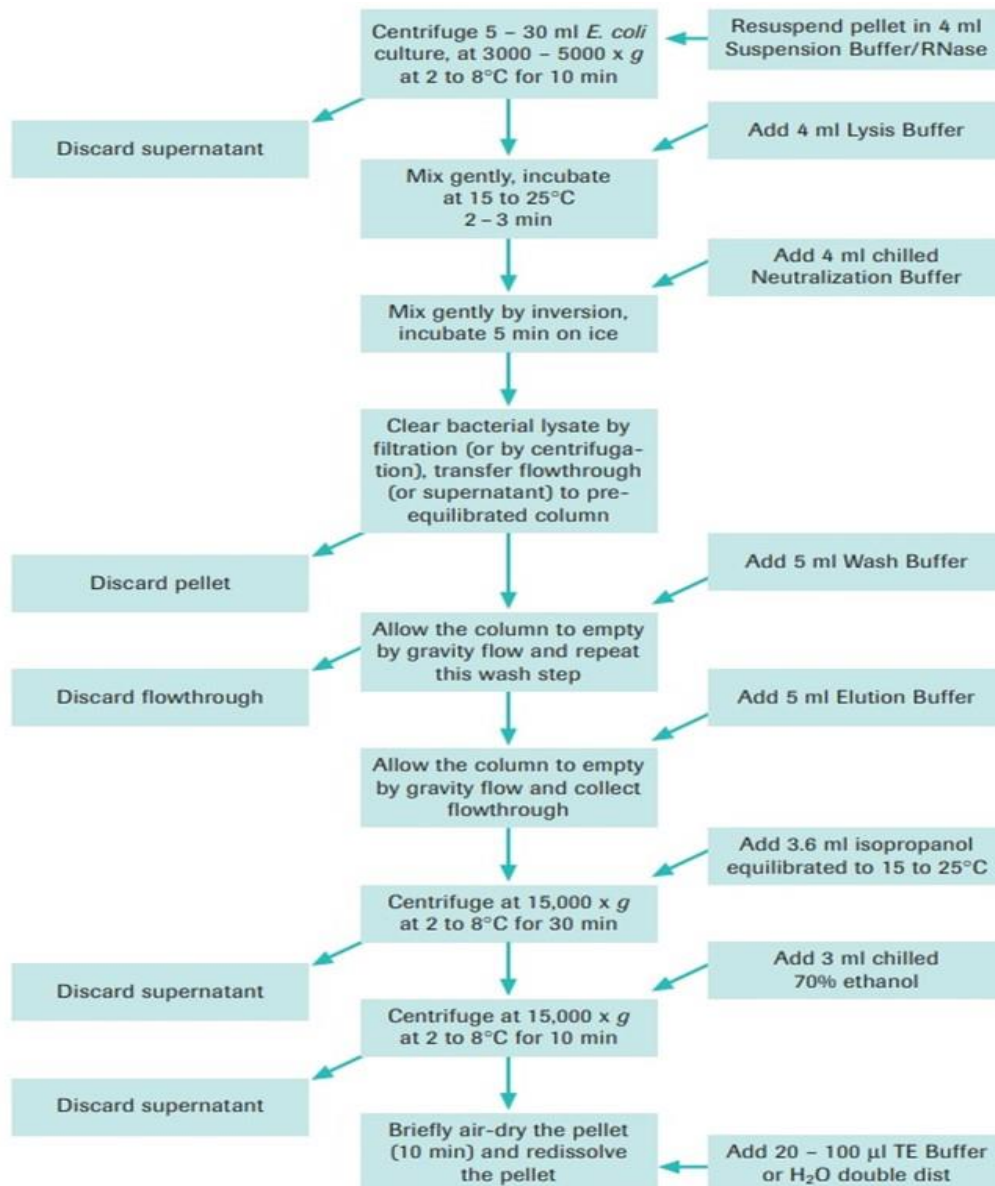


Figure 2.1: Flow diagram for alkaline lysis (Mini-prep) isolation and purification of DNA plasmid from *e.coli* (Roche Scientific 03143414001).

Post-amplification in LB, 50 ml of LB was pelleted by centrifugation at 3-5,000 x g at 4°C and the LB aspirated. The pellet was resuspended in 4 ml of Suspension Buffer. 4 ml lysis was added, and solution gently mixed by hand for 2-3 minutes. 4 ml neutralisation buffer was added to the solution and gently invert by hand until homogenous suspension is formed, then incubated on ice for five minutes. Lysate was cleared of debris by centrifugation for 30 minutes at 12,000 x g at 4°C, meanwhile elution buffer was prewarmed at 37-50°C and purification columns prepared by adding 2.5 ml equilibration buffer and allowing to clear by gravity. Once centrifuged, lysate was loaded into purification columns through filter paper. Lysate was allowed to clear column by gravity, flow through collected and reloaded into a column a second time. Flow through was subsequently discarded. Purification column was washed with 12 ml wash buffer and flow through discarded again. The column was finally inserted into a centrifugation tube and 5 ml prewarmed elution buffer was added and flow through collected. 3.6 ml room temperature isopropanol was added to precipitate plasmid DNA and solution centrifuged for 45-90 minutes at 15,000 x g at 2-8°C. This was repeated if a pellet did not form. The supernatant was removed, and plasmid DNA pellet washed with 3 ml chilled 70% ethanol (2-8°C) and centrifuged for a further 10 minutes at 15,000 x g at 2-8°C, after which ethanol was removed, and pellet air-dried for 10 minutes. The pellet was resuspended in 100-150 µl ddH₂O and DNA concentration measured by Nanodrop/spectrophotometer. Minimal DNA concentration should be >0.4 µg/ µl but can range as high as 3 µg/ µl. High concentration can be diluted and aliquoted to prevent repeat freeze-thaw cycles. Final product should be stored in -20°C.

2.2.10. Restriction Enzyme Digest and Gel Electrophoresis

The protocol for restriction enzyme digest is as follows (González-Ballester et al., 2005): on ice, 1 µg DNA sample, 2 µl 10x buffer and 1 µl of each chosen restriction

enzyme was mixed and volume made up to 20 µl with sterile water. The solution was incubated at digestion temperature (typically 37°C) for one hour and enzyme inactivated by incubating at 65°C for 15 minutes. The sample should be immediately visualised or store at -20°C. Agarose gel was prepared at 0.7%-2% using TAE-buffer, heated until agarose is completely dissolved, cooled at room temperature and supplemented with 0.15 µl/ ml ethidium bromide and poured into gel dock with suitable well combs inserted. Once set, the gel surface was covered with TAE buffer and combs carefully removed. Samples and ladder were mixed with 5x loading buffer. Gel should be run until loading buffer has reached the end of the gel. Gel should be visualised by UV light imaging, with DNA fragments appearing as orange bands on a black or purple background (Lee et al., 2012b).

2.2.11. Protein Extraction and Quantification using RIPA-mediated Cell Lysis and Bradford Assay

For this project, radioimmunoprecipitation assay buffer (RIPA, Sigma R0278) supplemented with 1x protease inhibitor cocktail (Sigma Aldrich, P8340) was utilised for cytoplasmic protein lysis.

To prepare cells for lysis using RIPA (method adapted from manufacturer's instructions): Cells were seeded to confluency in 10cm dishes and incubated overnight at 37°C in complete media. The following day, media was removed, and cells washed with PBS before 200-600 µl RIPA buffer was added on ice and incubated at 4°C for 20-25 minutes. Cell monolayer was transferred to eppendorf tubes and centrifuged at 12k RCF for 15 minutes. Supernatant was transferred to a fresh eppendorf and stored at -20°C until needed. Precipitated pellet is discarded.

Protein concentration in samples was quantified using the Bradford Assay. This assay utilises the Coomassie Brilliant Blue G-250 dye, which undergoes colorimetric change when bound to protein, changing from anionic (blue) to cationic (red) depending on protein concentration in a sample, which can be quantified via spectrophotometer and compared against known protein concentration standards (Bio-Rad Laboratories, 2000). Using this data, matched protein concentration can be used in comparative assays such as SDS-PAGE/Western Blot.

For the Bradford Assay: On ice, lysis samples were vortexed and 5 μ l of stock protein supernatant aliquoted to fresh tube and diluted 1:30 with dH₂O. Dilute 5x Coomassie Blue dye solution 1:5 with dH₂O and 200 μ l diluted dye solution was added to each required well in flat-bottomed 96 well plate. Next, 20 μ l of each stock standard and diluted sample was added in triplicate to the wells. Plate was incubated for 1-3 minutes at room temperature, shaken gently for 10 seconds and read at 620nm.

2.2.12. SDS-PAGE and Western Blot

SDS-PAGE (Sodium dodecyl sulphate-poly acrylamide gel electrophoresis) and Western Blot separate proteins according to their molecular weight. These proteins are subsequently transferred to a protein-binding membrane and probed with protein-sensitive antibodies to quantify the expression of proteins of interest.

SDS-PAGE and Western Blot protocol (Blancher and Jones, 2001): The SDS-PAGE gel was inserted into the electrophoresis apparatus and submerged in SDS-PAGE Running Buffer. A uniform concentration of sample proteins was mixed with loading buffer, denatured at 95°C for five minutes and loaded to individual wells within the gel. A protein ladder was loaded to an additional well. The gel was resolved until the

sample loading buffer was completely run through the gel and the ladder fully separated.

Transfer sponges were soaked in transfer buffer for several minutes and membrane activated before use. This project used PVDF membrane for western blot assays (polyvinylidene difluoride, GE Healthcare, RPN303F). After running, the gel was carefully extracted and placed within the transfer sandwich. Semi-Dry transfer systems were set at 15v for 40-50 minutes depending on protein size. Turbo Transfer systems were set according to manufacturer's instructions (Trans-Blot Turbo Transfer System, Bio Rad).

Once transferred, the membrane was blocked using 3% BSA (Bovine Serum Albumin, Sigma A3294) in PBS for at least one hour at 4°C, then the blocking buffer replaced with 2% BSA PBS supplemented with appropriate primary antibody and incubated according to manufacturer's instructions. Once incubation was complete, the membrane was washed twice with TBS for 10 minutes before probing with suitable secondary antibody in 2% BSA. Finally, the secondary antibody solution was removed, the membrane washed twice more and imaged using a fluorescent membrane reader (Licor Odyssey XF Imaging System).

Western Blot results were quantified by Densitometry analysis using Licor Image Studio Lite Version 5.2.5. Band intensity was quantified, and the result normalised for image background. β -Actin expression was subtracted from target band intensity and final result normalised against control sample.

2.2.13. RNA extraction, reverse transcription and RT-qPCR

RNA isolation protocol for this project was as follows (Rio et al., 2010): cells were seeded to confluency in 10cm dishes and incubated overnight. The following day 1

ml/10cm² TRIzol (acid guanidinium thiocyanate-phenol-chloroform, Invitrogen, 15596-018) reagent was added and dishes incubated for 3-5 minutes at room temperature. Lysate was homogenised and transferred to RNase free tube and 200 µl chloroform per ml lysate. The vial was shaken vigorously by hand for 30 seconds and incubated at 15-30°C for 2-3 minutes. Samples were centrifuged at 12,000g for 20 minutes at 4°C, causing phase separation of sample. Clear aqueous phase was removed from sample without disturbing interphase or organic supernatant and 0.5ul isopropanol alcohol for 1 ml sample was added. Sample was incubated at 15-30°C for a further 10 minutes and centrifuged at 12,000g for 10 minutes at 4°C. Supernatant was discarded and pellet washed by adding 1 ml absolute ethanol and sample homogenised with pipette. Finally, sample was centrifuged at 7,500 g for 20 minutes at 4°C. Supernatant was discarded and pellet air-dried for 5-10 minutes, then dissolved RNA in 20-25ul RNase free water.

Once isolated, RNA was used to generate complimentary DNA (cDNA) for the PCR reaction. Total RNA was reverse transcribed into cDNA using PrimeScript RT Reagent Kit following manufacturer instructions (Takara-Clontech Laboratories, RR037A). To generate cDNA, 1µg RNA sample was incubated with 0.5µl reverse transcriptase, 50pmol random six-mers primers and 1µl mRNA-binding Oligo dT primer for 30 minutes at 37°C, then at 85°C for five seconds to inactivate the enzyme activity. Result was stored in -20°C.

RT-qPCR is used to quantify cDNA amplification during the PCR amplification process. By utilising a non-specific fluorescent dye that binds to double stranded DNA, fluorescence is produced only when primers bind to cDNA fragments prior to polymerase activity. As amplification during PCR cycles is an exponential process, this fluorescence can be used to quantify initial concentration of targeted cDNA

sequence, either by absolute or relative to a standard curve or reporter such as β -Actin. This project utilised SYBR Green I (Roche, 04707516001), which absorbs 497nm light and emits 520nm light when bound to DNA, thereby enabling quantification of amplification between PCR cycles.

RT-qPCR protocol was as follows (Nolan et al., 2006): Each RT-qPCR reaction was prepared on ice: 1ul of each forward and reverse primers at 10mM concentration, 2ul cDNA solution diluted 1:10, 10ul SYBR Green 1 mix and 6ul purified water to a total of 20ul per sample/well. RT-qPCR was performed in triplicate to compensate for variability. This solution is pipetted to a 96 well plate and tested using a LightCycler 480 II (Roche) or similar instrument.

Relative fold change in RT-qPCR was calculated using the delta-delta CT method ($2^{-\Delta\Delta Ct}$ method), which determines the difference in CT values between experimental and control samples (Livak and Schmittgen, 2001). CT referring to cycle threshold (Ct), the point at which experimental sample fluorescence is detectable above background. Delta (Δ) referring to the difference between two numbers, in this case CT of each sample against the housekeeping gene (we utilised β -Actin as housekeeping gene in this project) (Livak and Schmittgen, 2001). Therefore the $2^{-\Delta\Delta Ct}$ method determines the Delta-CT values of control sample vs housekeeping sample, experimental sample vs housekeeping sample, then compares those resulting values against each other to determine significance (Livak and Schmittgen, 2001). Relative fold change is the ratio change between control (X) and experimental (Y) Delta-CT values as the formula $Y/X-1$.

2.2.14. Cytotoxicity Assay/IC₅₀ Proliferation Determination

Assay.

Protocol for this assay as follows (Ahmed et al., 2019): Cells were seeded at 3×10^3 cells/well in flat-bottom 96 well plate at 200 μ l total per well, Two experimental conditions in triplicate (3 columns each) with 10 different concentrations can be performed on a single plate using this approach (Figure 2.2). Cells were incubated at normal culture conditions for 24-48 hours to ensure resumption of cell function. Growth media was replaced with fresh media supplemented with drug of interest. Control wells should be supplemented solution used to initially dilute compound of interest (e.g., dH₂O, DMSO, methanol). Cells were cultured for the experimental time period, after which the media was removed and 200 μ l 15% trichloroacetic acid (TCA, Sigma Aldrich, T4885) added to each well and incubated for 60 minutes at 4°C for fixation. TCA was removed and wells washed with 200 μ l tap water. Water was removed and plate air dried for a further 1-2 hours. 0.4% Sulforhodamine B solution (SRB, Sigma Aldrich, 230162) in 1% acetic acid solution 50 μ l/well was added and plate incubated at room temperature for 20 minutes. The SRB solution was removed by washing each well 5x with 200 μ l 1% acetic acid until excess colour is removed. Plate was air-dried overnight at room temperature. The following day 200 μ l 10mM Tris (Sigma Aldrich, 93349) in dH₂O was added to each well and read using spectrophotometer at 492nm. The data was analysed using GraphPad Prism to generate IC₅₀ value at each experimental condition (Ahmed et al., 2019; Orellana and Kasinski, 2016).

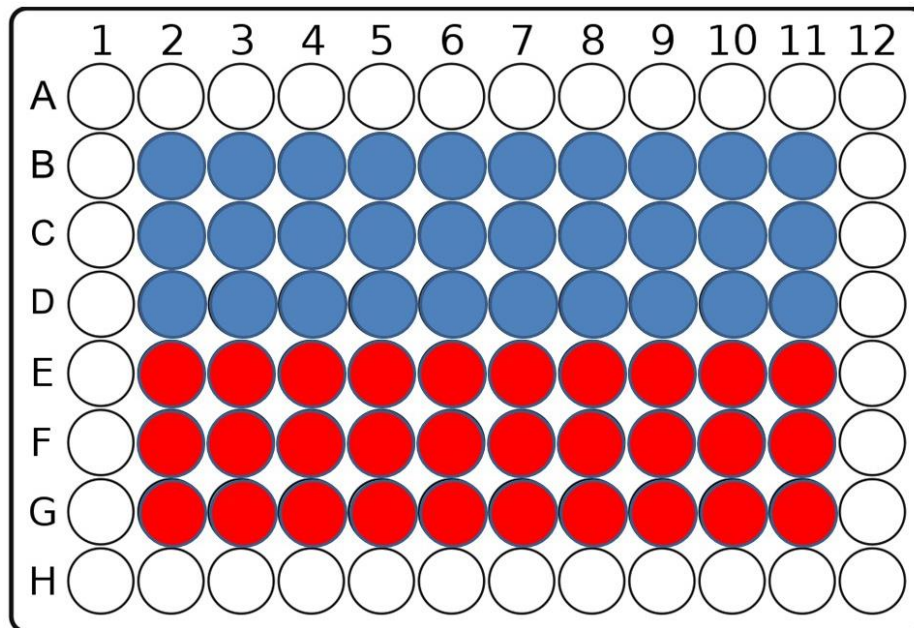


Figure 2.2: Example cytotoxicity plate diagram.

96 well plate was seeded with 3,000 cells per well in 200 μ l growth media, leaving outer edges blank, allowing for six rows of 10 wells each, suitable for two simultaneous experimental conditions (such as cell lines or drugs) shown here in blue and red.

2.2.15. Murine Intestinal Organoid Methodology

2.2.15.1. Preparation of Murine Intestinal Organoid Culture

Media

5 ml 2.5x intestinal organoid culture media was prepared as follows (Kashfi et al., 2020):

- 500 μ l B-27 50x supplement (Fisher Scientific, 12585-010)
- 1mM N-acetylcysteine

- 250ul 1x N2 supplement (Fisher Scientific, 17502048)
- Make up volume to 5 ml with Complete Advanced DMEM/F-12 media (1% L-Glutamine, 1% Penicillin/Streptomycin, 10% HEPES Buffer, Fisher Scientific, 17502048)

5 ml 1x intestinal organoid culture media was prepared as follows:

- 2 ml 2.5x intestinal organoid culture media as above
- 50ng/ ml murine recombinant epidermal growth factor (mEGF, Fisher Scientific, PMG8043)
- 100ng/ ml Noggin-containing media (Produced in-house)
- 1 µg/ ml R-Spondin 1-containing media (Produced in-house)
- Make up to 5 ml volume using Advanced DMEM as above

Noggin-rich media was produced inhouse by PEI-mediated-transfection of HEK293-T cells with the Noggin plasmid to cause Noggin secretion. HEK293-T cells were grown in complete RPMI and seeded to 10cm dishes at 70% confluency. The following day, the media was removed from each plate, cells washed with PBS and replaced with 1.8 ml Opti-MEM media containing 15 µg plasmid DNA with 45-60 µg PEI. Cells were incubated for 6-8 hours at cell culture conditions, then the Opti-MEM was removed, cells washed with PBS and replaced with complete ADMEM for seven days. After seven days, media was removed, centrifuged at 400g for three minutes, filtered through a 0.22 µl filter and stored at -80 until needed. Noggin expression was validated by western blot (see Results section 3.1.1).

R-Spondin 1 for this project was produced inhouse using R-Spondin 1-secreting HEK293-T cells (cells gratefully gifted by Prof. Hans Clevers). The cells were grown to 70% confluency in complete DMEM media, the media was then removed and

replaced with complete ADMEM (5% HEPES, 1% L-Glutamine, 1% Penicillin/Streptomycin) for one week, after which the media was harvested, centrifuged, filtered using a 0.22µm filter and stored at -80 °C. Concentration of R-Spondin 1 containing media was initially analysed in our research group by TOP Luciferase Assay and we determined experimentally that 500ul-750 µl infused media per 1x organoid media solution was sufficient for intestinal organoid culture (see Results section 3.1.2).

2.2.15.2. Luciferase Reporter Assay

To evaluate the activity of the R-Spondin 1 containing media, we used the TOP/FOP-flash dual-luciferase reporter assay (Promega E1910). This assay consists of two luciferase expressing plasmids transfected into HEK293-T cells, which are subsequently exposed to media containing R-Spondin 1. One plasmid contains two groups of three copies of the TCF/LEF bindings sites upstream of a *Firefly* luciferase reporter gene. TCF/LEF are Wnt-mediating transcription factors, as such will be more highly expressed in R-Spondin 1, therefore also expressing the *Firefly* luciferase. FOP-flash plasmid contained three non-functional copies of the TCF/LEF binding site as a negative control. The *Renilla* luciferase is used as a transfection control.

Assay was performed according to manufacturer's instructions (Promega E1910 (Lorenzi et al., 2016a)): HEK293 cells were seeded in triplicate in a six well plate to confluency and incubated overnight to 60-80% confluency, at which point they were transfected with both *Renilla* vector (0.05 µg DNA/well) and either TOP-flash/FOP-flash plasmids (0.2 µg DNA/well). After six hours, media was replaced with R-Spondin 1 containing media and incubated for a further 48 hours. After 48 hours, media was discarded, and cells lysed as previously outlined (Materials and Methods

section 2.2.11) Lysate was loaded in triplicate to flat bottomed 96 well plate and 50µl/well of Luciferase Assay Reagent II was added into the wells and the bioluminescence produced was detected by a Luminoskan Ascent Microplate Luminometer (Thermo Fisher Scientific, UK). In addition, the measurement of the *Renilla* luciferase activity was measured by adding 50µl/well of Stop & Glo® Reagent to the same wells. The *Firefly* luciferase readings were normalised to *Renilla* luciferase readings and then to the activity of the control samples.

2.2.15.3. Isolation of Murine Intestinal Crypts and Culture of Murine Intestinal Organoids

Method for isolating and culturing murine intestinal organoids was adapted from Sato et al 2009 (Sato et al., 2009b) and discussed in detail in (Kashfi et al., 2020).

Briefly, intestinal crypts were isolated from BL6J mice (approx. 4-6 weeks old). Mice were sacrificed by cervical dislocation and the whole intestine excised from the abdominal cavity. The sample was cleaned with ice-cold PBS, opened longitudinally, divided into 1mm sections and washed with cold PBS several times to remove intestinal contents until PBS became clear. The sample was incubated while rolling in 3mM EDTA for 45 minutes at 4°C to disassociate crypt regions from epithelial tissue. Afterwards, the sample was transferred to 10% FBS/PBS at room temperature, and repeatedly agitated and filtered through 70µm strainer 3-6 times to remove large solid debris. Subsequently, the sample was centrifuged at 300xg for five minutes to pellet crypts. Immediately after, the supernatant was removed, and crypts resuspended in ice-cold Matrigel (typically 200-300 µl Matrigel/8-12 wells per isolation), 25µL of which was seeded to the centre of a well in 96 well plates and incubated at 37°C for 5-10 minutes until Matrigel solidified. Finally, 300µL fresh mouse organoid media

prewarmed to 37°C was added to each well and the plate incubated at 37°C. Organoid growth was monitored by microscopy. Murine colorectal organoids take 6-9 days post isolation/passage to grow to maturity with multiple crypt/villus-like domains. Organoids can typically be kept in culture for a further 3-5 days, however organoid mortality will increase over time if not passaged.

2.2.15.4. Transduction of Intestinal Organoids with Lentiviral Particles.

Protocol as published (Kashfi et al., 2020). Protocol for generating lentiviral particles may be found in section 2.2.8.

Briefly: 40-80 mature murine intestinal organoids were removed from Matrigel, resuspended in 300µL 4°C PBS and disassociated by repeated pipetting as normal. These organoids were resuspended in 100µL high-titre virus containing media supplemented with 0.1% polybrene (8µg / ml concentration) and incubated at 37°C for four hours, agitating the mixture carefully using 200µL pipette every 30-45 minutes. Next, organoids were centrifuged for three minutes at 300xg, and virus-containing media carefully discarded. Organoids were resuspended in Matrigel and seeded to plates with organoid growth media as with normal organoid passaging. The following day, any fluorescent selection markers should be visible using fluorescent microscopy. At this point, organoid culture media can be supplemented with selection agent. Supplemented culture media should be replaced every 2 days until all control cells are dead. Continue selection process a further six days/3 media replacements, surviving organoids can then be cultured as normal for experimental purposes.

2.2.15.5. Isolation of RNA from Organoid samples

Organoids were incubated in Matrigel Cell Recovery Solution (Corning 354253) for three hours at 4 °C, subsequently washed with PBS 4°C and centrifuged at 300xg for three minutes in microcentrifuge tubes. The supernatant was removed, and organoid pellet homogenised with 500µL TRI reagent for five minutes at room temperature and agitated with 200µL pipette every minute. 100µL chloroform was added to samples and incubated for three minutes at room temperature. The sample was shaken vigorously by hand and centrifuged at 12,000xg at 4 °C for 15 min to separate RNA (aqueous phase). The pellet was washed twice with 4°C 75% ethanol by centrifugation at 7,400xg for eight minutes at 4°C, air-dried and re-suspend with 20 µl of DNase/RNase free water.

2.2.15.6. Isolation of Protein from Organoid samples

50-100 mature murine intestinal organoids were removed from Matrigel, resuspended in ice cold PBS and centrifuged as with normal passage. The supernatant was removed, and organoid pellet resuspended in 70-80 µl RIPA buffer for 20 minutes in 4°C, while rocking (20 oscillations/minute), occasionally agitating organoids using a 21-25-gauge syringe. The resulting protein lysate is suitable for use in Western Blot analysis.

2.2.15.7. Fixation and immune-histochemical staining of organoid samples

Organoids were removed from Matrigel as normal, resuspended in 500µL 4% PFA and incubated at 4°C for one hour. PFA was gently removed, organoids amalgamated to a single tube, washed with room temperature PBS and centrifuged for three minutes at 300xg. Washing and centrifugation was repeated three times in total. PBS was removed, and organoids permeabilised with 500µL 0.5% Triton X 100 for 30 minutes

at room temperature, then washed twice more with PBS for five minutes. For Phalloidin staining, 800 μ L 1:500 Phalloidin was added, and organoids incubated for 40 minutes at room temperature in darkness, washed twice in PBS and mounted to microscopy slides with DAPI mounting media.

2.2.16. Statistical analysis

All statistical analysis was performed using Microsoft Excel 2010 and GraphPad Prism 8 software. All experiments were independently performed 2-3 times or as noted in the text. Error bars represent standard deviation (STDEV). Significance was determined using Students t-test and P values = $P < 0.05$ (*), $P \leq 0.01$ (**), $P \leq 0.001$ (***), $P \leq 0.0001$ (****).

**Chapter 3: Utilising Murine
Cas-9-Expressing Intestinal
Organoids for screening of F-
box Genes Function**

3. Brief Introduction

Immortalised *in vitro* cell culture is an invaluable method in biomedical research, providing a cheap, easy-to-use and plentiful system for exploring experimental objectives ranging from drug discovery to functional genetics. However, *in vitro* cell cultures are mono-cellular and two-dimensional platforms, thereby failing to adequately encapsulate origin tissues, and genetic drift making results difficult to replicate. Studies using immortalised cell lines often cannot be replicated in *in vivo* animal models (Mak et al., 2014). Alternately, *in vivo* models more accurately predict patient/human responses to experimental conditions while also enabling more comprehensive analysis, but are also expensive, technically challenging and ethically contentious. This lack of translatability of cell lines and expense of animal models severely impacts biomedical research and therefore there is a need for novel, translatable, *in vitro* models

Recent advancements in stem cell methodology have introduced organoids as a novel *in vitro* culture system. Organoids are three-dimensional, multicellular *in vitro* cultures that accurately encapsulate the cells found within the original tissues (Boretto et al., 2019). Organoids have been generated from over a dozen tissue types including brain, intestine, breast, pancreas and lung, and employed in fields including drug discovery and screening, genetic modelling as well as disease and cancer modelling (Drost and Clevers, 2018; Holloway et al., 2019; Perkhofer et al., 2018; Takahashi, 2019). Intestinal organoids are initially isolated from *Lgr5*-positive multipotent stem cell within the intestinal crypt and were first established by Sato et al (Sato et al., 2009b). Owing to the highly corrosive environment of the intestine, intestinal stem cells are highly proliferative, making intestinal organoids one of the most popular types of organoids (Sato et al., 2009b). Recent data reports suggest that intestinal and colorectal

patient-derived organoids (CRC PDOs) may inherit genetic and pathological characteristics from the original tissue (Boretto et al., 2019; Kashfi et al., 2018). Therefore, organoids are emerging as a “middle ground” option between *in vitro* immortalised models and *in vivo* animal studies, and future organoid studies will continue to expand on the possible uses of this system.

The focus of this chapter is firstly to establish and optimise methodology for *in vitro* murine intestinal organoid functional screening by generating and validating the Cas-9-expressing organoids. Next, we utilised Cas-9 expressing organoid lines to generate F-box knockout organoids by transducing the F-box gRNA lentivirus library and exploring resulting effects on organoid growth and morphology (Figure 3.1). This chapter was accomplished in collaboration with Dr Hossein Kashfi in the Dr Nateri’s laboratory. The methodology section of this chapter has recently been published in *Methods in Molecular Biology* (Kashfi et al., 2020).

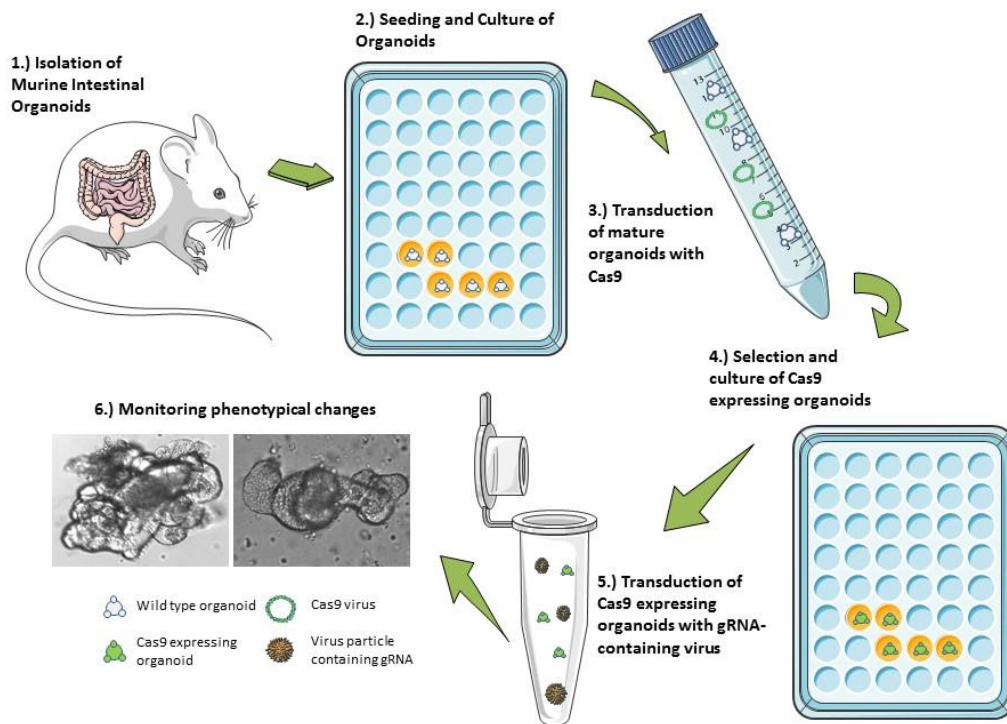


Figure 3.1: Diagram of method of generating CRISPR/Cas-9 expressing murine intestinal organoids via lentiviral transduction.

Intestinal crypts are isolated from the mouse small intestine and colon, seeded into Matrix and cultured. Once mature, these organoids are transduced with Cas-9 expressing vector, re-cultured and selected for expression. These transgenic organoids can be re-transduced with a Cas-9 gRNA plasmid to knockout expression of a target gene (Kashfi et al., 2020).

3.1.Results

3.1.1. HEK293-T cells were transfected to express and secrete Noggin protein and validated by Western Blot.

Healthy/normal murine intestinal organoids require highly specific culture media to maintain stemness and induce mitosis. One factor required in organoid culture media is Noggin, a 64kDa disulphide-bonded homodimer glycoprotein governing factor in Bone Morphogenic Protein activity (BMP). BMP affects intestinal stem cell self-renewal by suppressing Wnt- β -catenin signalling, and early studies demonstrated that Noggin supplementation is necessary for continued healthy/normal organoid viability *in vitro* (Sato et al., 2011; Sato et al., 2009b). To reduce the batch-to-batch variability of commercial Noggin, we determined to produce supplementary Noggin in-house by generating Noggin-secreting HEK-293-T cells.

HEK-293-T cells were cultured and seeded to 70% in T75 flasks. The following day, cells were transfected with 60 μ g:15 μ g PEI (Polyethylenimine): Noggin plasmid as outlined in Materials and Methods section 2.2.7. A separate flask was simultaneously transfected with GFP plasmid as a control for transfection efficiency. 24 hours-post transfection, fluorescence of the control was examined to determine transfection efficacy. Noggin-transfected cells were incubated in antibiotic-free media for seven days. Day seven post-transfection, Noggin-containing cell media was removed, centrifuged and subsequent filtered using a 0.22 μ m filter and aliquoted for freezing. Noggin expression of each batch was determined by Western Blot analysis using 10% SDS-PAGE gel and 1:1000 Noggin antibody concentration. Noggin recombinant produced in HEK-293-T cells is a disulphate-linked glycosylated homodimer with a

total molecular weight of 64-65 kDa (Figure 3.2). Therefore, conditional media was enriched with secreted Noggin suitable for organoid media supplementation.

We determined that 0.5-1 ml of Noggin-containing media per 5 ml 1x organoid culture media was most effective in stimulating organoid growth and maintaining stemness activity. Increasing Noggin concentration further had no noticeable impact on healthy/normal organoid growth. Removal of Noggin supplementation caused arrested growth and rapid organoid death as previously established (Kashfi et al., 2018).

Figure 3.2: Secretion of recombinant Noggin protein in cell culture media post-transfection confirmed by Western Blot.

Cell culture media was harvested and 20 µl filtered media was analysed via Western Blot using 10% SDS-PAGE gel and 1:1000 Noggin antibody concentration.

3.1.2. R-Spondin 1 Conditional Media was produced using R-Spondin 1 expressing stable cells.

Another factor required to maintain stemness activity for normal murine intestinal organoids *in vitro* is R-Spondin 1. R-Spondin proteins are Wnt/ β -catenin agonists and required for *LGR5* stem cell activity (Levin et al., 2020).. Like Noggin, R-Spondin 1 inclusion in intestinal organoid media is necessary for healthy/normal organoid growth and viability (Levin et al., 2020). We also determined to produce recombinant R-Spondin 1 in-house via HA-R-Spol-Fc cells (gratefully gifted by Prof. Hans Clevers).

HA-R-Spol-Fc cells were cultured to 70% confluency and incubated with antibiotic-free media for seven days. Media was then centrifuged, filtered using a 0.22µm filter and aliquoted for storage in a -80°C freezer. Due to lack of available R-Spondin 1

primary antibodies for western blot validation, suitable R-Spondin 1 media supplementation was determined experimentally, with 0.5-0.75 ml in 10 ml 1x organoid media deemed sufficient to sustain organoid cultures. R-Spondin 1 activity was also measured using TOP/FOP luciferase reporter assay (Materials and Methods Section 2.2.15.2, Data not shown) (Lorenzi et al., 2016a; Seyed Mohammad Hossein Kashfi, 2018).

3.1.3. Amplification and Validation of F-box gRNA plasmid library

Due to insufficient penetrative power, high toxicity and low transfection efficiency in organoids and complex tissues, Polyethylenimine-mediated transfection (PEI) as previously discussed (Materials and Methods section 2.2.7) was deemed unsuitable for 3D cultures. Methods such as electroporation also have low transfection efficiency in murine intestinal organoids (Fujii et al., 2015). To effectively utilise CRISPR-Cas-9-mediated gene editing in organoids we used a gRNA lentiviral library.

Prior to generation of lentiviral F-box gRNA-containing constructs (Figure 3.3), each plasmid was amplified using *E. coli* via plasmid transformation, amplification and alkaline lysis for DNA isolation. The initial F-box gRNA library was generated and validated by Dr Emmanouil Metzakopian at Sanger Institute (Cambridge, UK). This library contained 126 unique gRNA lentiviral vector DNAs (two copies of each known 63 murine F-box gene) and provided in competent *E. coli* bacteria. Each plasmid-containing bacterium was amplified to sufficient volume in LB media and their DNA's purified by alkaline lysis using the manufacturer's instructions. Post-purification DNA concentration was determined by Nanodrop/spectrophotometer analysis, which ranged between 0.1µg/µl to 3.0µg/µl. Following previous experience, DNA with

concentration $<0.4\mu\text{g}/\mu\text{l}$ could produce poor transfection efficiency in HEK293-T cells irrespective of final plasmid volume used in transfection protocol. Where necessary plasmids were repeatedly amplified and amalgamated to produce working concentration. A small number of plasmids repeatedly produced extremely poor plasmid DNA concentrations post-lysis and were removed from the project; however, we successfully amplified at least one plasmid for each F-box gRNA.

Validation of plasmids was performed using restriction enzymes digestion and gel electrophoresis. From plasmids which we successfully amplified and isolated suitable DNA concentrations, four were chosen at random for restriction enzyme digestion analysis (e.g., two copies of gRNA plasmids prepared for *FBXO3* (A1 & A2) and *FBXL15* (A3 & A4)). Validation utilised the *EcoRI* and *EcoRI/PvuII* enzymes (Figure 3.4). The *EcoRI* enzyme cut in a single site while the *PvuII* enzyme digest at multiple locations. It appears DNAs were partially cut by *EcoRI*. At the same time, *PvuII* resulted in completely digested gRNA plasmids with DNA bands on the gel corresponding to the size of DNA fragments calculated on the plasmids map and as expected following the manufacturer guideline (Sanger). Gel electrophoresis results indicate that plasmid library was uncontaminated and suitable for use. These plasmids were further sequenced, blasted and confirmed the insertion of their specified gRNA (data not shown (Kashfi, 2020)) Figure 3.3 shows the pLv-U6g/PGK-Puro-2a-tBFP plasmid schematic.

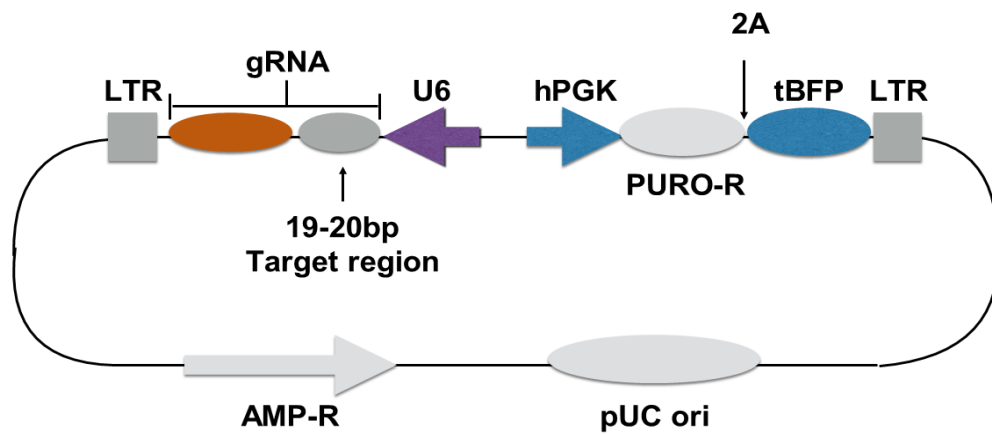


Figure 3.3: Schematic presentation of pLv-U6g/PGK-Puro-2a-tBFP plasmid.

Diagram showing structure of pLv-Ugg/PGK-Puro-2a-tBFP plasmid used in gRNA F-box library. The library utilised a backbone vector in constructing the F-box gRNA's library at the Sanger Institute.

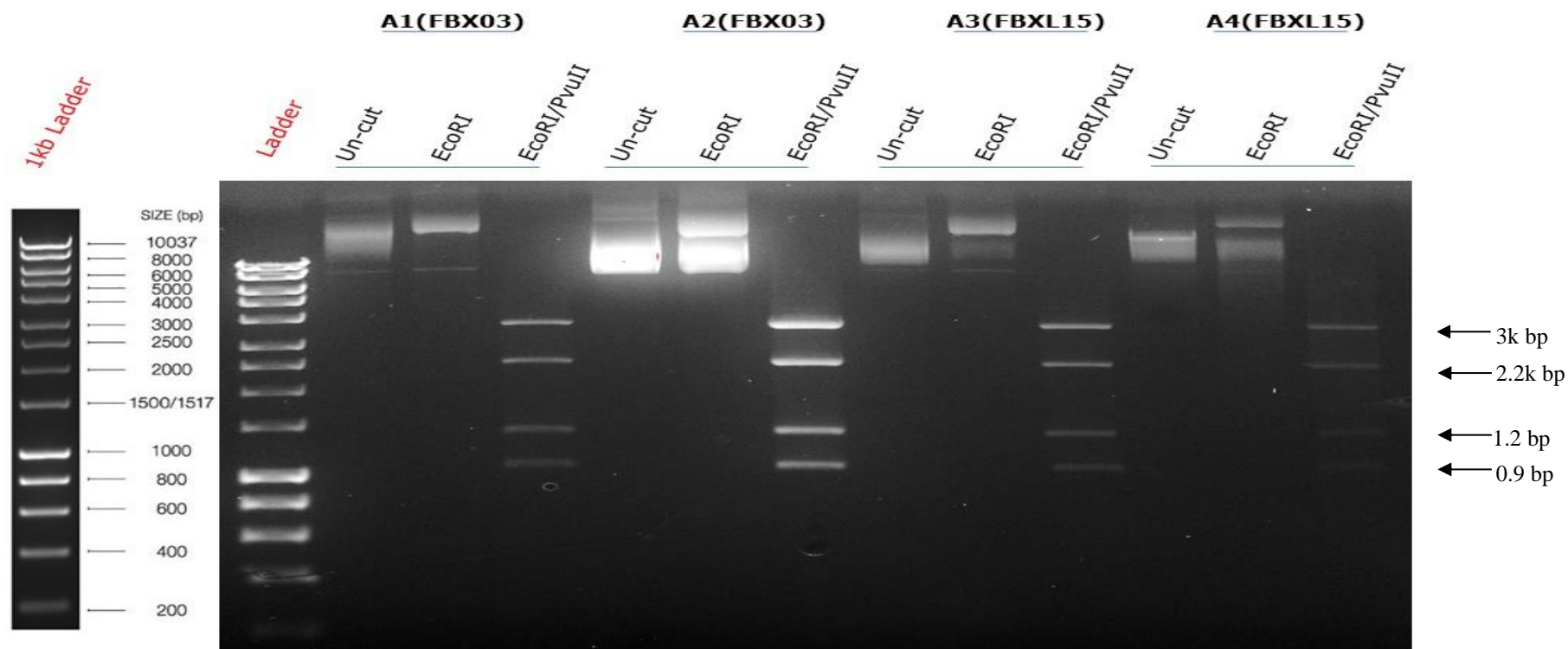


Figure 3.4: Restriction Enzyme Digestion analysis of plasmids constructed for *FBX03*-gRNAs (A1 & A2) and *FBXL15* (A3 & A4) using *EcoRI* and *EcoRI/PvuII* enzymes.

Plasmids were incubated with restriction enzymes and subjected to gel electrophoresis analysis. Results indicate that all four plasmid samples produced identical bands in both individual and mixed enzyme samples, therefore contain expected plasmid and no genetic contaminants. A1 and A2, and A3 and A4 representing the two copies of *FBX03*-gRNAs and *FBXL15*-gRNAs each plasmid within the F-box gRNA library.

3.1.4. Generation of Cas-9 and F-box gRNA containing lentiviral particles

Once plasmids were validated, the Cas-9 and F-box gRNAs expressing lentiviral particles were generated as previously outlined (Materials and Methods section 2.2.8). HEK293-T cells were grown to 70-80% confluency in T75 flasks. These cells were transfected using PEI and 3rd generation LV construct components (final concentrations per flask: 15µg LV construct, 5µg pMDG2 packaging, 10µg pCMV R8.74 packaging plasmid, 1.5 ml Opti-MEM) for 6-8 hours at 37°C. Following which, transfection media was replaced with antibiotic-free growth media and flasks incubated overnight. As all F-box gRNA lentiviral plasmids used in this project were engineered with blue fluorescent protein (BFP), transfection efficiency was determined by fluorescent microscopy 24 hours post transfection with green fluorescent protein efficiency (GFP) used as control (Figure 3.5). For three days post-transfection, the virus-containing media was harvested from flasks and replaced with fresh antibiotic-free growth media. The virus-containing media was filtered through 0.45µm filter unit and stored at 4°C in suitable hazardous-sample containment. After three days of harvesting, the cells were discarded, and virus-containing media was amalgamated to 50 ml falcon tubes with 7-8 ml of virus sucrose solution and centrifuged at 25-27g for 4-4.5 hours at 4°C. Subsequently the supernatant was carefully discarded, and either 500 µl 1x organoid media or complete ADMEM was added to each 50 ml falcon and left overnight at 4°C to resuspend virus particles. The following day, this media was aliquoted in 50-100 µl volumes to 1.5 ml Eppendorf tubes and stored at -80°C.

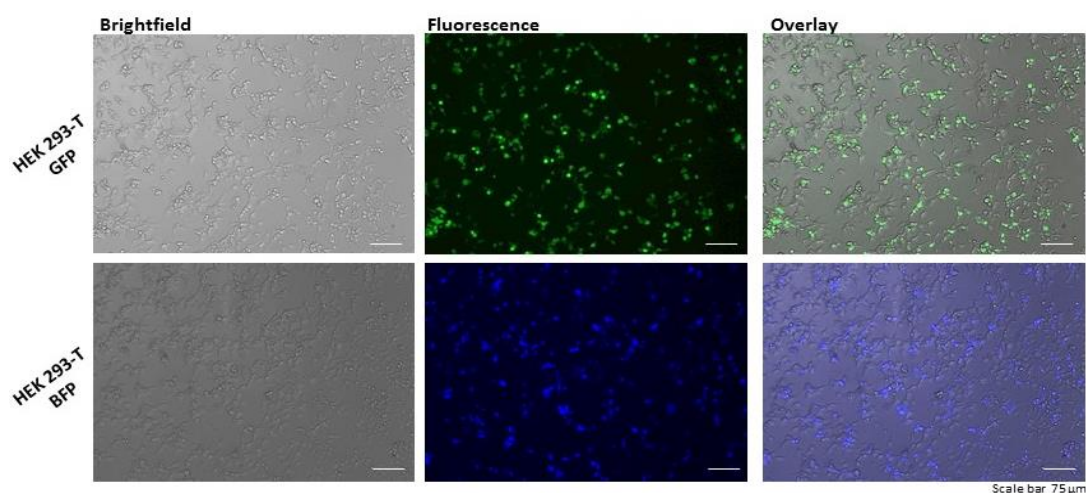


Figure 3.5: Transfection efficacy of lentiviral F-box gRNA plasmid expressing BFP (Figure 3.3) and a control lentiviral (PLVx-eGFP) plasmid in transfection of HEK293-T cells by fluorescent microscopy.

Lentiviral vectors were generated by co-transfection of 3rd generation lentiviral constructs with F-box plasmid into HEK-293-T cells. Transfection success was determined by fluorescence 24 hours post transfection, with $\geq 70\%$ fluorescence producing optimal results. Viral-rich media was harvested for three days post-transfection and titrated using sucrose solution. Scale bar 75 μm .

3.1.5. Culturing and expansion of wild type mouse intestinal organoid cultures by crypt isolation.

To generate Cas-9-expressing murine intestinal organoids, wild type murine intestinal crypts were first isolated from 4-6-week-old C57BL/6J mice and embedded in Matrigel and organoid culture media using the method previously described (Kashfi et al., 2020; Li et al., 2019b; Lorenzi et al., 2016a; Sato et al., 2009a) (Materials and Methods section 2.2.15). Organoid media was replaced every 2-3 days. Organoid

growth was monitored and imaged every 24-48 hours using brightfield microscopy. Fully matured organoids were passaged every 8-12 days as required.

Figure 3.7 shows representative images of murine intestinal organoid growth. Day 1 intestinal organoids displayed a spherical or “bubble” like appearance containing few cells (Figure 3.7, left first panels). Organoids began to develop initial stages of crypt and villus anatomical regions on day 2-3 post-isolation, with expansion accelerating from day 4 to produce mature organoid structures containing between 1-6 villus regions (bulging finger-like areas, Figure 3.6) linked by villus regions (indented or flattened areas closer to the organoid core) by day 7. After disassociation and passage, each developed villus region can establish a new organoid. Day 7 onwards the organoid continued to grow. After this point, the organoid central lumen began filling with necrotic cells and debris due to reduced nutrition supply to inner tissues, resulting in gradually increasing risk of organoid rupture and death. Organoids may survive up to 14 days or longer in culture before death, but typically required passage on day 7-10.

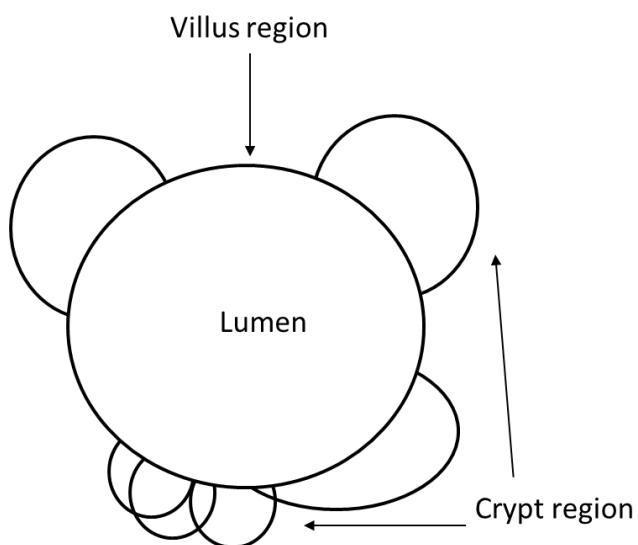


Figure 3.6: Diagram of crypt,

villus and lumen regions of murine intestinal organoids.

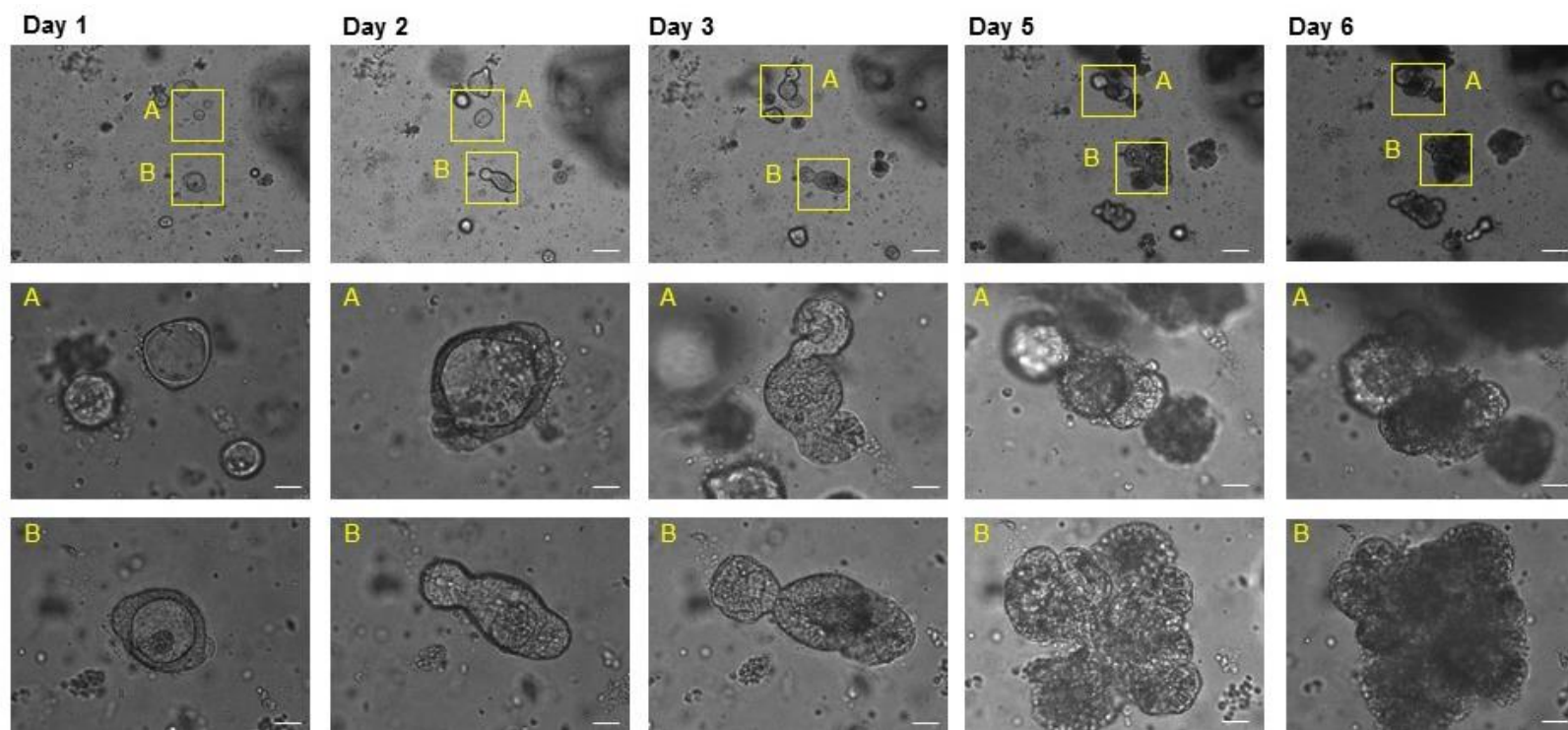


Figure 3.7: Murine intestinal organoid growth Day 1-6 post isolation demonstrate crypt and villus regions similar to *in vivo* structures.

Intestinal crypts were isolated, embedded in Matrigel and imaged each day to monitor growth and survival. Day 1-6 organoids gradually develop crypt and villus regions. Day 6 organoids are large enough to be passaged into further cultures. Organoid growth continued until day 8+, at which point increasing volume of debris in the lumen eventually causes organoid rupture and death. Scale bar: 25 μm top row & 75 μm middle and lower rows

3.1.6. Generation of transgenic mouse intestinal organoids overexpressing Cas-9 using lentiviral transduction.

In order to utilise the CRISPR F-box plasmid library with less variability among different and multiple organoid cultures, we were first required to generate Cas-9 expressing murine intestinal organoids. To generate Cas-9 expressing murine intestinal organoids, 30-40 mature organoids (Day 6+) were removed from Matrigel, resuspended in cold PBS and disassociated as previously described (Materials and Methods section 2.2.15.4). Following centrifugation, pelleted organoids were resuspended in 100 μ l concentrated viral media (based on transduction efficiency, Figure 3.5) with 0.1 μ l polybrene for four hours at 37°C and gently agitated every 30-45 minutes, after which the organoids were reseeded to Matrigel with 1x organoid growth media. The following day, growth media was replaced with fresh growth media supplemented by selection agent. Organoids were selected by 200 μ g/ μ l G418/Geneticin for two passages (approx. 14 days total) replacing media every 2-3 days. Following complete selection, organoids were expanded, and 80-100 organoids were lysed for protein using RIPA in the manner previously described (Materials and Methods section 2.2.15.6). Results indicate that organoids were successfully transduced to express Cas-9 enzyme. Cas-9 expression in intestinal organoids is comparable to DLD-1 Cas-9 expressing cells (Figure 3.8).

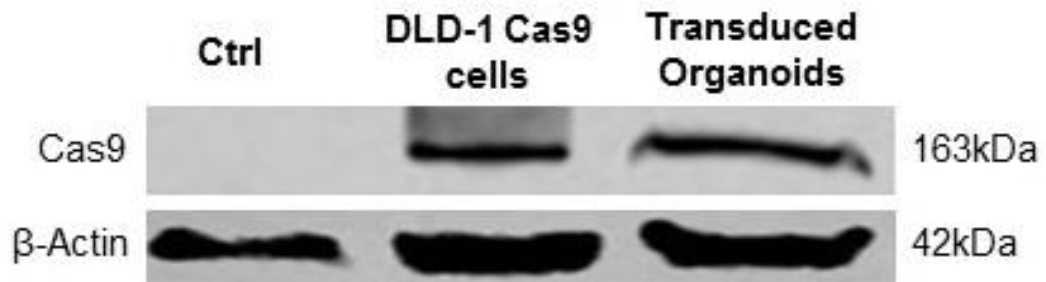


Figure 3.8: Validation of Cas-9 protein expression in murine intestinal organoids using Western Blot Analysis.

Results indicate the organoids were successfully transduced to express Cas-9 enzyme. Colorectal cancer DLD-1 cells expressing Cas-9 were used as a positive control. Western Blot was performed on 10% gel at 1:1000 antibody concentration with 24-hour incubation. Image taken in collaboration with Dr Kashfi, who produced the organoid protein and performed the western blot.

3.1.7. Selected candidates of F-box from organoid screening

Of the 63 murine F-box, we successfully screened 32 (51%) for significant morphological or growth abnormalities in murine intestinal organoids. We were unable to complete the remaining screen samples due to unknown contamination that repeatedly appeared in Cas-9 organoid lines. This contamination reduced organoid growth rate, presumably by consuming growth media and we were unable to completely eradicate it. As this contamination was combined with limited laboratory access during the COVID pandemic in the 3rd year of my PhD period, we determined to utilise other methods to analyse significant screening candidates further.

In the first stage of screening, we identified significant morphological or phenotypic differences in five F-box gRNA expressing (i.e., knockout (KO)) organoid lines: *fbxo17*, *fbxo31*, *fbxl17*, *fbxl18* and *fbxl5* (Table 3.1). Of these significant results, FBXL5 was chosen for further investigation due to the limited data published on FBXL5 in colorectal cancer (CRC).

Table 3.1: F-box candidates for further functional analysis identified using Cas-9-expressing transgenic organoid screening through transduction of F-box gRNA lentiviruses.		
F-box family	F-box gRNAs screened	F-Box with significant phenotypes
FBXL	FBXL2, FBXL4, FBXL5, FBXL7, FBXL8, FBXL13, FBXL14, FBXL17, FBXL18	FBXL5, FBXL17, FBXL18
FBXW	FBXW2, FBXW10	
FBXO	FBXO3, FBXO4, FBXO9, FBXO10, FBXO11, FBXO16, FBXO17, FBXO18, FBXO22, FBXO25, FBXO28, FBXO30, FBXO31, FBXO33, FBXO36, FBXO38, FBXO39, FBXO40, FBXO43, FBXO45, FBXO47	FBXO17, FBXO31

3.1.8. Loss of intestinal *fbxl5* in mouse organoids leads to significant morphological changes

As shown in Figures 3.8 and 3.9, by day 5-7 control GFP organoids grew in a tight, roughly spherical-like structure with cohesive, well-established crypt and villus regions surrounding the central lumen. However, organoids transduced with the FBXL5 gRNA grew in a less organised manner, displaying more lateral rather than roughly spheroid-like growth as well as less clearly defined crypt and villus regions that developed apparently at random rather than outwardly from the lumen (Figure

3.9). This suggests that FBXL5 may significantly affect stem cell and progenitor growth activities. We were unable to isolate sufficient protein to validate successful knockout of *fbxl5* in organoids, however the significant alterations in both cross-sectional area and growth rate suggest at least partial knockout of FBXL5.

Figure 3.10 shows surface plot graphs generated from representative GFP control and *fbxl5* transduced organoids, indicating that *fbxl5* organoids may have less cohesive growth both horizontally and vertically compared to controls. (Surface Plots generated using Interactive 3D Surface Plot 2.4 plugin for ImageJ. Grid Size 1024, Smoothing 20.0, Perspective 0, Lighting 0.21, Scale 1.4, z-Scale 0.58, Maximum 100%, Minimum 0% Inverted Enabled).

Organoid growth rate was measured by changes to perimeter, surface area and estimated 3D volume. Organoid volume was estimated by taking 3-4 measures of each organoid's diameter. Half the average of these measures was considered the organoid radius (r) and volume was estimated using the formula $V = 4/3\pi r^3$ (Cai et al., 2018; Nam et al., 2018; Pastuła et al., 2016). Quantification of crypt/lumen regions between organoid types was considered as an alternative method of comparative analysis, but difficulty in accurately identifying crypt/lumen regions in 2D brightfield images at different stages of growth made the method unsuitable. However, as shown in Figure 3.9 and Appendices Figure 8.1, *fbxl5* transduced organoids appeared to have fewer budding regions than Cas-9 murine intestinal organoids.

The full list of analysis measures and statistical significance used is shown in Table 8.2 in Appendices. The total WT organoid images $N = 140$ and total *FBXL5* KO images $N = 86$. Please see Appendices Figure 8.1 for additional representative images of FBXL5 transduced murine intestinal organoids.

Organoid growth rate and average surface area was analysed for both parental Cas-9 murine intestinal organoids and *FBXL5* KO organoids as outlined (Figure 3.11A and B). Results indicate that *FBXL5* KO organoids had significantly increased 2D surface area on days 1, 3 and 5, however despite their greater horizontal growth and morphological differences, this trend was reversed on day 7 (Figure 3.11A) (Day 1-Day 7 $p = < 0.001$). Organoid estimated growth rate by volume was not significantly different until day 7, at which point growth rate was reduced in *FBXL5* KO organoids (Figure 3.11B), which may account for the reduced overall surface area in *FBXL5* KO organoids on day 7.

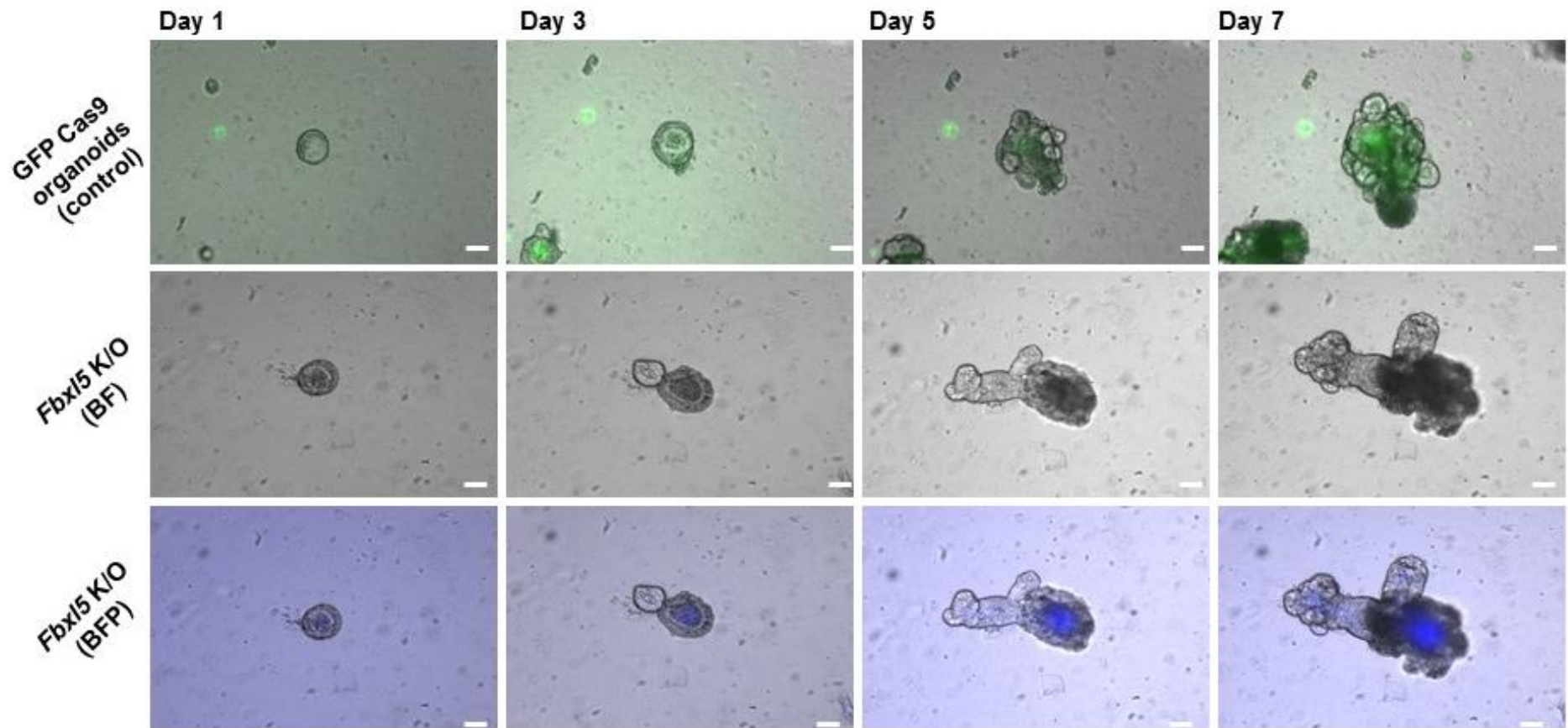


Figure 3.9: Knockout of *fbx/5* in murine Cas-9 expressing organoids significantly affects growth pattern Scale bar: 75µm.

Representative images of Cas-9 expressing murine intestinal organoids transduced with GFP-containing lentiviral construct or *fbx/5* CRISPR plasmid. As shown, control GFP organoids grow in a tight, 3-dimensional structure, whereas *FBXL5* KO organoids grow outwards laterally with less cell cohesion. This suggests that *fbx/5* may affect stem cell growth patterns. Scale bar: 75µm. *FBXL5* KO organoid images taken by Dr Kashfi. See Appendix Figure 8.1 for further representative images of *FBXL5* KO murine intestinal organoids.

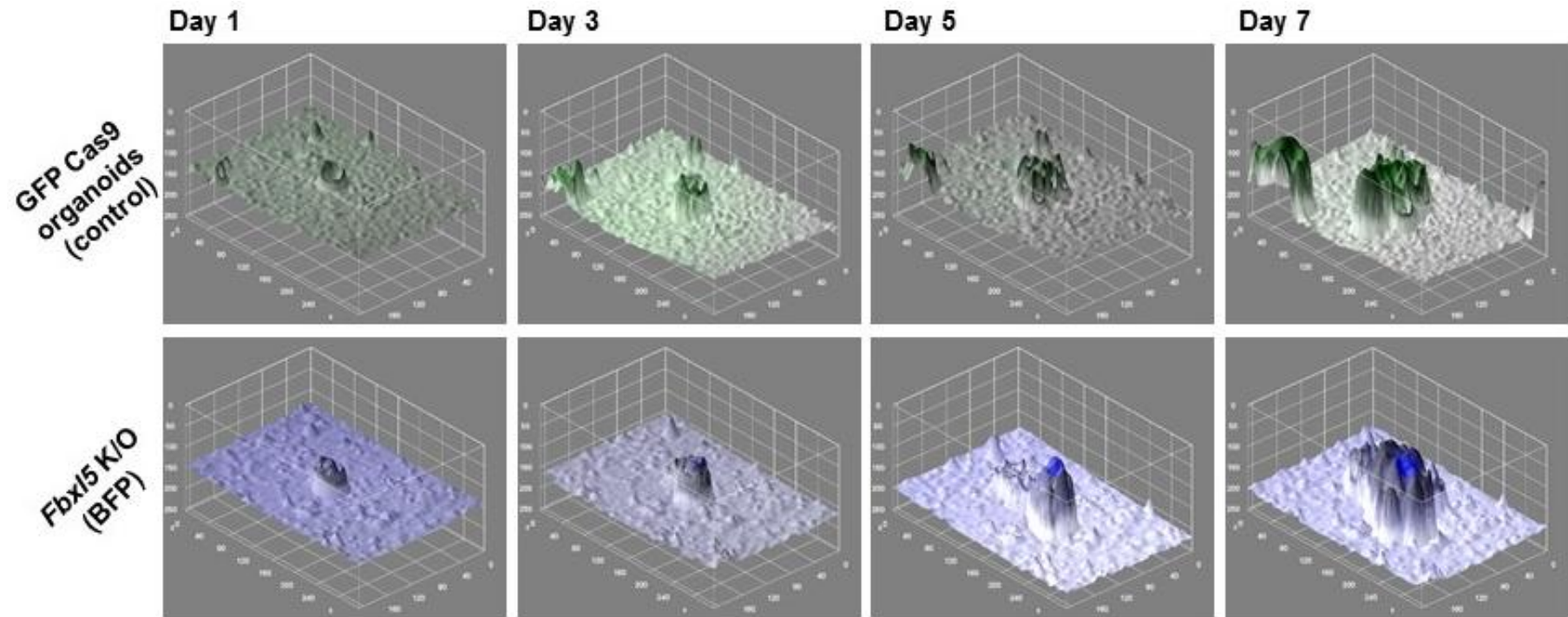
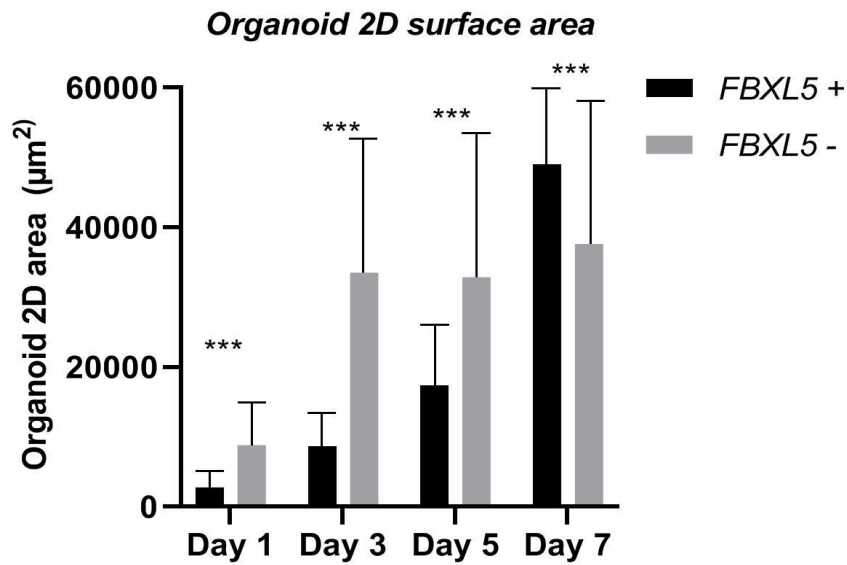


Figure 3.10: Surface Plots of control and *fbxl5* knockout organoids show incohesive vertical growth in knockout organoids

Surface Plots were generated from 2D fluorescent microscopy images of control and *fbxl5* knockout organoids, indicating that control organoids show broadly cohesive vertical growth, while *FBXL5* KO organoids grow in a less consistent manner. Surface plots generated from Figure 3.9 images via Interactive 3D Surface Plot 2.4 plugin for ImageJ.

(A)



(B)

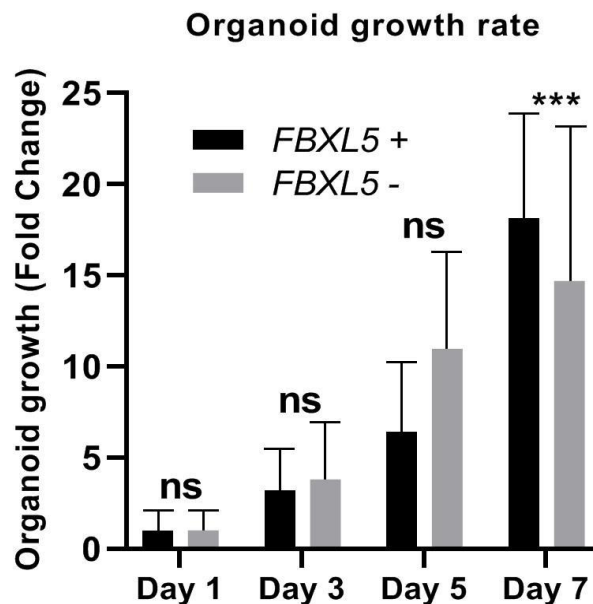


Figure 3.11: *FBXL5* KO induced changes to murine intestinal organoid surface area and growth rate.

(A) Results demonstrate that *FBXL5* KO organoid morphology differs substantially from wild type organoids by dramatically increased 2-dimensional surface area. (B) Analysis of estimated organoid growth rate by volume found that *FBXL5* KO significantly reduced growth rate between days 5-7 (Organoid volume was estimated by taking 3-4 measures of each organoid's diameter. Half the average of these measures was considered the organoid radius (r). Volume was estimated using the

formula $V = 4/3\pi r^3$). Student's T-Test was used to determine significance. Total WT images N = 140, total *FBXL5* KO images N = 86. Error bars represent standard deviation, $P < 0.05$ (*), $P \leq 0.01$ (**), $P \leq 0.001$ (***)

3.2. Discussion

In this chapter, we produced and validated the activity of Noggin-enriched cell media and R-Spondin 1-enriched cell media to supplement healthy/normal organoid growth media. We also showed the methods and materials used to generate Cas-9-expressing murine intestinal organoids, transduce knockout F-box gRNAs expression and subsequently determine significant effects on organoid growth and morphology by utilising brightfield microscopy.

As detailed in Introduction section 1.3, several previous studies have generated Cas-9-mediated genetic mutations in varying organoid types. Primarily, this has been achieved by simultaneous cellular introduction of both free-floating Cas-9 enzyme and plasmid, such as by electroporation or PEI-mediated transfection. <1% organoids used in these experiments survived and was successfully transduced, and therefore this method impractical for studies requiring large volumes of organoids (Drost et al., 2015; Fujii et al., 2015; Matano et al., 2015). As our method has both higher initial efficiency, potential for upscaling and requires no additional equipment beyond standard cell culture apparatus, we feel that a lentivirus-based approach is more suitable to wider adoption and screening development. To our knowledge, only one study has generated Cas-9 expressing murine intestinal organoids using polybrene-mediated transduction, which was published simultaneously with this project (Takeda et al., 2019) (Kashfi et al., 2020).

By generating a Cas-9-expressing murine intestinal organoid line, we have also reduced variability in organoids caused to repeated isolations and transductions. Control variability is vital in functional screening based on morphological examination among cultured organoids, and by generating our experimental organoids from a single line of Cas-9-expressing murine intestinal organoids, variability has been minimised.

We demonstrated a low cost and high efficiency method for generating Cas-9-expressing murine intestinal organoids and successfully screened 32 of the 63 possible murine F-box genes for effects on murine intestinal organoid growth or morphology and found significant effects in *fbx017*, *fbx031*, *fbxl17*, *fbxl18* and *fbxl5*.

FBXO17 is found overexpressed in certain lung adenocarcinoma cell lines and lung cancer samples (Suber et al., 2018), and overexpression may modulate both AKT and ERK kinase to increase cell proliferation and the Wnt/ β -catenin pathway in hepatocellular carcinoma (Liu et al., 2019b). Additionally, *FBXO17* may negatively regulate Type 1 interferon signalling in innate immunity (Peng et al., 2017a). *FBXO31* may target *MDM2* for degradation and facilitate *p53*-mediated cellular activity in response to cellular stressors (Malonia et al., 2015). *FBXL17* binds the oncogene UAP1 enzyme for ubiquitination, loss of *FBXL17* is noted in both breast and prostate cancer (Itkonen et al., 2015; Mason et al., 2020).

FBXL5 is poorly studied, and the mechanism by which *FBXL5* affects organoid morphology and growth rates is unclear. As elaborated in more detail in Introduction section 1.5.7: *fbxl5* knockout in mouse neural stem progenitor cells resulted in an increased number of neural stem progenitor cells (NSPCs) and accumulation of reactive oxygen species by activation of mTOR (Yamauchi et al., 2017). Human *FBXL5* also governs PTEN (Phosphatase and Tensin homolog, deleted on

chromosome 10) expression in the PTEN/PI3K/mTOR pathway by unknown means, which in addition to a central regulator for metabolism and physiology in cells, is frequently a vehicle for oncogenic and tumour suppressive signalling (Yao et al., 2018) and may therefore be responsible for the abnormal *FBXL5* KO organoid characteristics. *FBXL5* regulates EMT by ubiquitination of SNAIL (Wu et al., 2015b). Mesenchymal cells typically possess elongated morphology and increased migration and invasive properties, all of which may explain the novel *FBXL5* KO organoid phenotype. Organoids have been used as a model for EMT in several studies (Hahn et al., 2017; Zhao et al., 2021a). As *FBXL5* has limited available data, further downstream analysis of *FBXL5* may determine novel substrates and interactions that contribute to organoid morphology.

These results demonstrate both the validity and practicality of our method of utilising Cas-9 murine intestinal organoids as a method and tool for functional analysis of novel and unknown genes. However, further investigation of these significant F-box genes is necessary to determine how translatable these results are to human colorectal cancer. It must also be noted that murine intestinal stem cells and organoids may not actually express all F-box or have non-comparable functions or paralogs. Whether a gene of interest is expressed in murine intestinal organoids must be considered when evaluating the use of transgenic murine intestinal organoids as a model system.

**Chapter 4: Loss of Functional
Analysis of FBXL5 cultured
colorectal cancer cells**

4. Brief Introduction

The previous chapter described how the organoid screening project identified several functionally unknown F-box genes in the intestine, demonstrating potential impacts on intestinal organoid growth. Of these candidates, FBXL5 was chosen for further functional analysis in colorectal cancer (CRC) cells. In addition to the effect on intestinal organoid growth, FBXL5 was chosen due to the limited published data available on FBXL5 impact on colorectal cancer (Ruiz and Bruick, 2014), as outlined in chapter 3.

FBXL5 is a 78kDa F-box E3 ligase of the FBXL family that governs the specificity of protein substrates for degradation within the UPS. In colorectal cancer, *FBXL5* mRNA expression has been found significantly lower in primary tumour samples compared to paired tissues at all stages of cancer development (Figure 1.9) (Jiang et al., 2021), although other studies have shown that FBXL5 protein expression is upregulated in colorectal cancer (Yao et al., 2018).

Previous studies have demonstrated that FBXL5 impairs epithelial-to-mesenchymal transition (EMT) by targeting SNAIL protein for ubiquitination (Viñas-Castells et al., 2014). The PI3K/AKT/mTOR pathway is associated with cell proliferation and apoptosis and is a frequently dysfunctional pathway in colorectal cancer (Papadatos-Pastos et al., 2015). FBXL5 has been found to negatively regulate PTEN (Phosphatase and Tensin homolog, deleted on chromosome 10) expression in colorectal cancer tissues by negative regulation of PTEN protein (Yao et al., 2018). Results established that FBXL5 expression was also significantly increased in colorectal cancer tissues and greater FBXL5 expression correlated with lower post-surgical survival rates in colorectal cancer patients (Haifeng, 2017; Yao et al., 2018).

Additionally, loss of FBXL5 has tumour suppressive properties in cervical, lung and colorectal tissues by interfacing with PTEN signalling (Cen et al., 2014; Chang et al., 2020; Tang et al., 2014; Yao et al., 2018). However, there is still limited information on FBXL5 roles and mechanisms of action in colorectal cancer which might account for the morphological and growth alterations observed in the murine intestinal organoids.

Therefore, this chapter will initially characterise cell behaviour in cultured colorectal cancer cell lines DLD-1 and SW480 knocked out for FBXL5 gene (hereafter *FBXL5* KO), including morphology, growth patterns, cell migration/attachment, cell division and initial follow-up on potential epithelial-to-mesenchymal related mechanism mediated phenotypes.

4.1. Results

4.1.1. Generation of DLD-1 and SW480 Cas-9 expressing cells and *FBXL5* KO cell lines using *FBXL5*- gRNA constructs.

To further characterise FBXL5 function in CRC cell lines, we generated stability expressing Cas-9 DLD-1 and SW480 cells by transduction of 70% confluent cells with Cas-9 lentiviral vector as outlined in Materials and Methods section 2.2.7. Transduced cells with lentivirus expressing Cas-9, were selected using G418/Geneticin 200 µg/ µl for 2-3 weeks until all control cells were dead. Single cell derived colonies were carefully picked and amplified for further analysis. Subsequently, the Cas-9 protein expression was confirmed by western blot analysis (Figure 4.1). Confirmation blots were repeated twice.

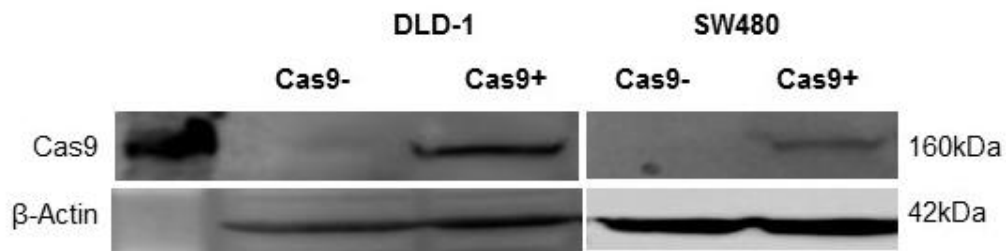


Figure 4.1: DLD-1 and SW480 cell lines expressing constitutively Cas-9 validated using Western Blot.

Expression of Cas-9 enzyme was validated post-transduction in DLD-1 and SW480 cells using Western Blot analysis (Cas-9 antibody 1:1000, in collaboration with Dr Kashfi who produced the DLD-1 image). 100µg protein lysate was loaded into each well of 10% SDS-PAGE gel.

The *FBXL5* plasmid gRNA sequence was conserved across all human and mouse genes and therefore should mutate both human and mouse *FBXL5* genes (AAATGGACAGCATTACCTCAGG, please see Appendices Table 8.1 for full list of F-box gRNA sequences) (Benson et al., 2013; Howe et al., 2021; NCBI, 2018). The Cas-9-expressing DLD-1 and SW480 cells were subsequently transfected with the 60 µg Polyethylenimine (PEI) and 15 µg *FBXL5*-gRNA plasmid to generate cell expressing stable *FBXL5* KO (as outlined in Materials and Methods section 2.2.7).

Fluorescent microscopy analysis showed approximately 15-20% transfection efficiency on both DLD-1 and SW480 cell lines (data not shown). Post-transfected DLD-1 cells were then selected by treating cell with Puromycin at 20µg/ ml and SW480 cells required 3µg/ ml Puromycin. Single cell derived/surviving colonies were isolated into separate wells and expanded for further analysis.

To validate successful *FBXL5* KO in DLD-1 and SW480 cells, cells were lysed using RIPA buffer and analysed using SDS-PAGE Western Blot assays. 100µg protein was loaded into 10% SDS-PAGE gels, transferred to PVDF membrane by semi-dry transfer, blocked with 3% BSA for one hour and probed with the anti-*FBXL5* antibody at 1:100 concentration for 48 hours at 4°C. Densitometry analysis of results was normalised to 1 against the control sample. Due to difficulty with the anti-*FBXL5* antibody, western blot was not repeated.

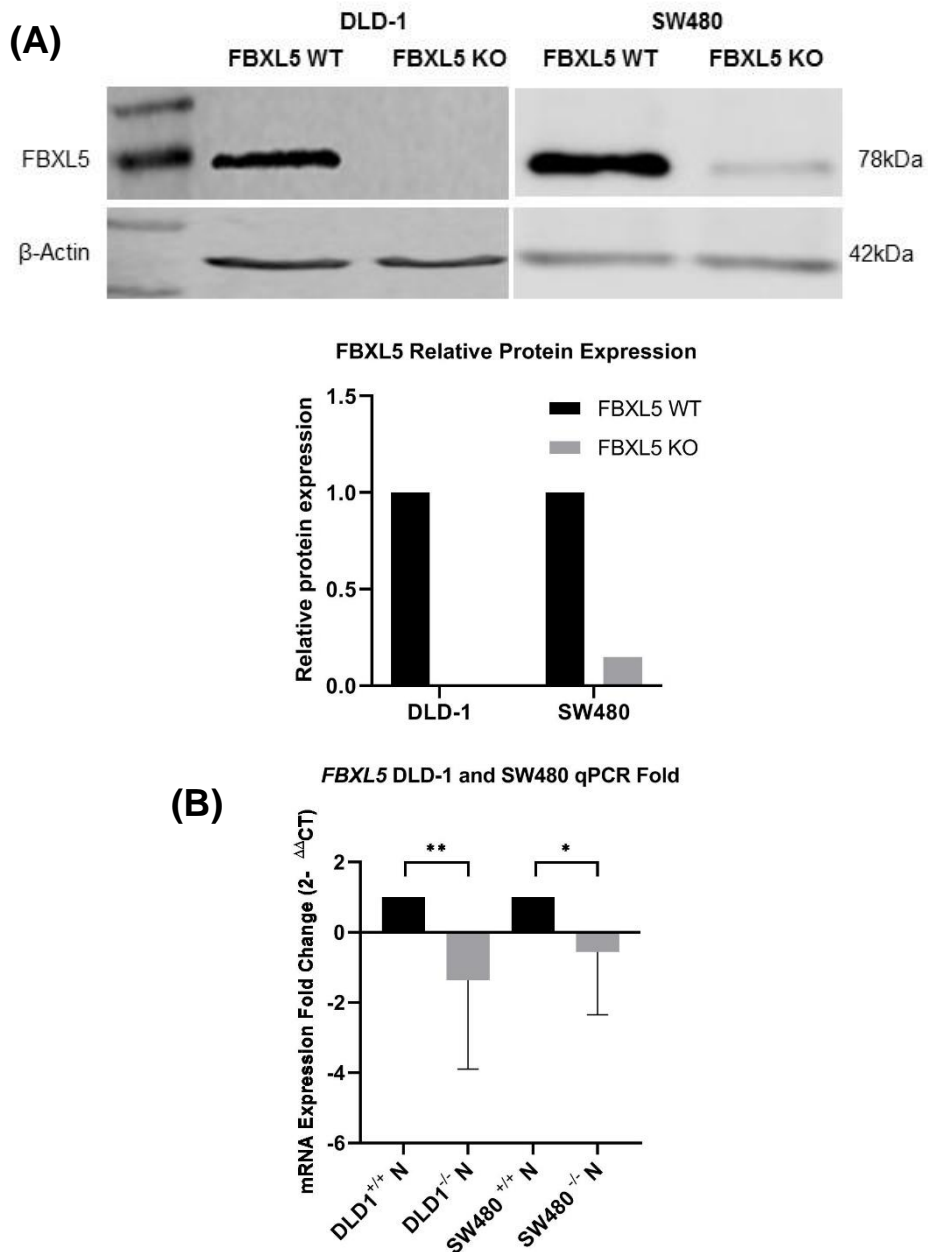
As shown in Figure 4.2A (left panel): DLD-1 *FBXL5* KO cell line demonstrated a complete knockout of *FBXL5* protein expression compared to the untransfected DLD-1 cells. However, SW480 Cas-9 expressing *FBXL5* KO cells showed an incomplete *FBXL5* protein knockout by 85.1% protein reduction at their first passage compared to control, possibly due to only a single allele deletion (Figure 4.2A right panel).

Further validation by RT-qPCR indicates effective knockout was achieved with both DLD-1 and SW480 Cas-9 expressing *FBXL5*-gRNA cells displaying significantly reduced *FBXL5* mRNA expression compared to control cells (DLD-1 $P = 0.0053$, SW480 $P = 0.038$, Figure 4.2B).

RT-qPCR oligos for human *FBXL5* was generated from the longest identified isoform (isoform 1, CCDS3415.1, exons 1 and 2) using the NCBI Blast tool and was specific to the largest possible number of isoforms. As outlined in Introduction section 1.5.7: the human *FBXL5* gene has nine predicted protein-encoding transcript variants (Howe et al., 2021). However, there is currently no experimental data available on differentially expressed or cellular differences among *FBXL5* isoforms and splicing variants, nor whether they are all protein-encoding. Our chosen antibody (Santa Cruz

sc-376102) could detect all known FBXL5 isoforms, with the epitope near the C-terminus and is preserved across isoforms.

Figure 4.2: The depletion of FBXL5 expression in *FBXL5* KO cell was evaluated



by Western Blot (A) and RT-qPCR analysis (B).

(A) Western blot analysis of FBXL5 protein expression in DLD-1 and SW480 cells showed a complete knockout of FBXL5 expression in DLD-1 KO cells and an 85.1% reduction in SW480 KO cells compared to control cells. 100µg protein lysate was loaded into each well of 10% SDS-PAGE gel. (B) mRNA *FBXL5* expression was also reduced in both DLD-1 and SW480 cells. RT-qPCR assay was performed in triplicate and repeated twice in total and result normalised to 1 for comparison. Error bars represent standard deviation. *P* values = $P < 0.05$ (*), $P \leq 0.01$ (**), $P \leq 0.001$ (***)

4.1.2. Studying the loss of *FBXL5* in growth, morphology, migration and EMT activities in DLD-1 and SW480 CRC cell lines

With the establishment and validation of stable *FBXL5* KO DLD-1 and SW480 cells, we conducted a series of experiments to evaluate the impact of *FBXL5* knockout on common cell behaviours, morphologies and cancerous characteristics: Phalloidin and DAPI staining determined phenotypical changes. Growth Curve Analysis and Propidium Iodine (PI) Flow Cytometry measured cell growth, cell cycle and division rate. The cell migration and attachment were examined by Wound Healing/Scratch Assay. In addition, we investigated the possible impact of *FBXL5* KO on epithelial-to-mesenchymal transition by examining expression of important EMT markers *Vimentin*, *β-Catenin*, *E-Cadherin* and *SNAIL* using western blot and RT-qPCR analysis.

4.1.2.1. Phalloidin staining shows that FBXL5 knockout causes cellular elongation defects in DLD-1 and SW480 cells.

Cell morphology is an important indicator of cell phenotype status and biological activities. For example, normal cells undergoing differential cell cycle phase retain variable phenotypic characteristics and shapes (Margineantu et al., 2002), and cancerous cells frequently display morphological changes, which denote potential oncogenic mutation and behaviours (Shia et al., 2017). Therefore, investigating phenotypic alterations in *FBXL5* KO cell lines is an appropriate initial step for characterising their biological activities.

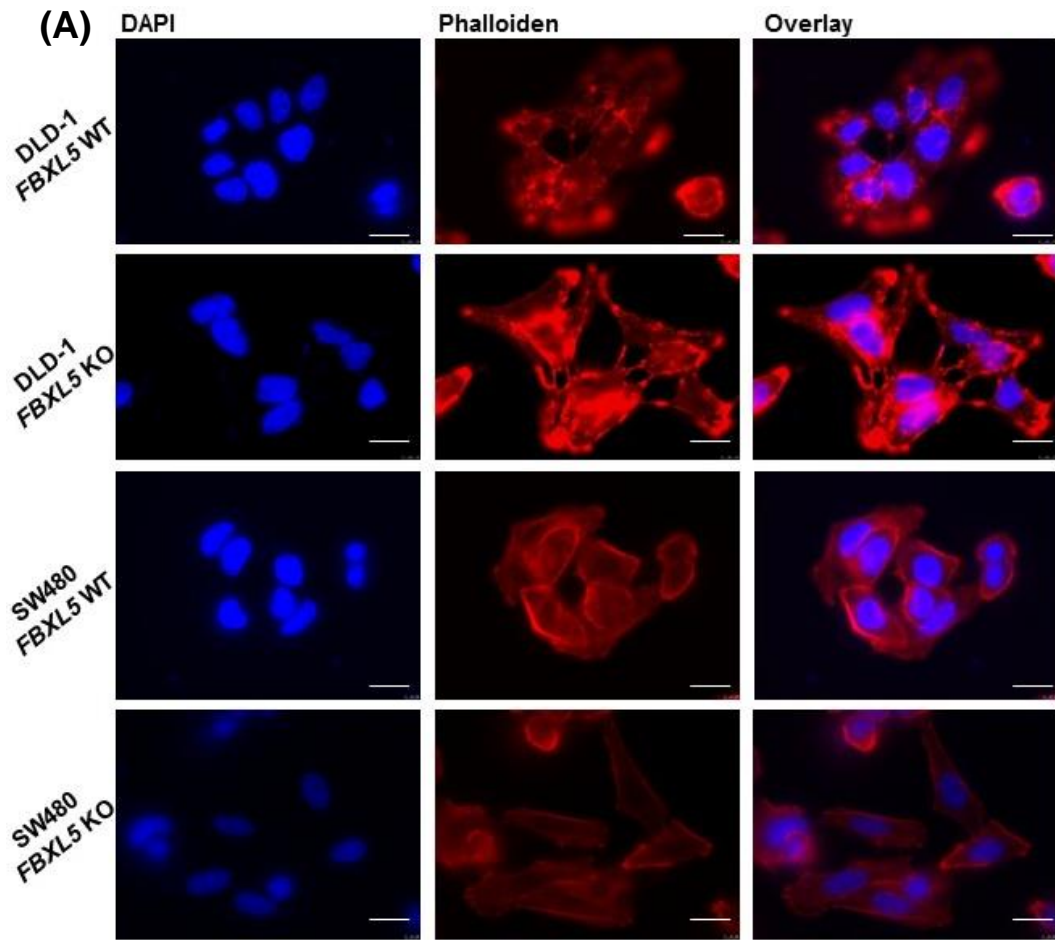
Cell lines DLD-1 *FBXL5* KO and SW480 *FBXL5* KO were seeded to cover slips within six well plates at 8.5×10^5 cells/well (Materials and Methods section 2.2.6). The following day, cells were fixed in 4% paraformaldehyde (PFA), slides extracted from plates and stained with 0.2% Phalloidin and DAPI and imaged with fluorescent microscopy. The ImageJ software (ImageJ version 1.5A (Abramoff et al., 2003)) was used to measure total cell area, perimeter and both long and short cellular axes. As we could not locate a published method for quantifying cellular elongation from Phalloidin imaging: cell elongation was determined by the long/short cell axis ratio. Additional representative DAPI/Phalloidin staining images of DLD-1 and SW480 *FBXL5* KO cells may be found in Appendices (Figure 8.2 and Figure 8.3). The total number of cell images for DLD-1 control was 36 and DLD-1 KO was 102, while SW480 control was 159 and SW480 KO was 129.

Results indicate that knockout of *FBXL5* in both DLD-1 and SW480 cells causes substantial increase in cellular elongation and demonstration of spindle-like morphology (Figure 4.3A). Comparison of ratio of long vs short cellular axis found

significant differences for both DLD-1 (Figure 4.3B, ratio of long/short axis = WT 1.63 vs KO 2.32, $P = 0.0026$) and SW480 (WT 2.15 vs KO 2.78, $P = 0.0003$) comparison (method adapted from (Cai et al., 2018)). Comparison of total cellular area between WT and KO cells of either cell line did not find significant differences (Figure 4.3C, Total Cell Area DLD-1 WT $50.47\mu\text{m}^2$ and KO $46.69\mu\text{m}^2$, SW480 WT $38.43\mu\text{m}^2$ and KO $39.14\mu\text{m}^2$). This assay demonstrates that *FBXL5* KO cell lines did not significantly change the total cellular area. In contrast, *FBXL5* KO cells shows altered phenotype, long/short cell axis ratio and elongation compared to parental DLD-1 and SW480 cells which possess circular cell morphology typical of *in vitro* epithelial cell lines (Figure 4.3A).

In addition, *FBXL5* DLD-1 and SW480 cells appeared to grow in a more spread-out, less cohesive manner with greater distance between the individual cells, although this was difficult to quantify. This reduced cohesion reflects the abnormal organoid phenotype found in *FBXL5* KO intestinal organoids, which also grew in a less cohesive manner and demonstrated altered 2D surface area and growth rate compared to controls (Figure 3.9 and 3.10).

These findings indicate that *FBXL5* knockout may alter colorectal cancer cell phenotype and may enhance cell elongation and attachments. This elongated phenotype is characteristic of mesenchymal rather than epithelial cells, which supports previously published data indicating that *FBXL5* ubiquitinates *SNAIL* for degradation in the SNU-5 stomach cancer cell line, AGS stomach adenocarcinoma cell lines and hepatocellular carcinoma (HCC) cell lines (He et al., 2018; Wu et al., 2015b). Interaction between *FBXL5* and *SNAIL* or EMT has not previously been demonstrated in CRC cell lines. Further analysis of EMT markers may clarify the role of *FBXL5* in EMT in CRC (Results section 4.1.2.5).



Scale bar 7.5 μ m.

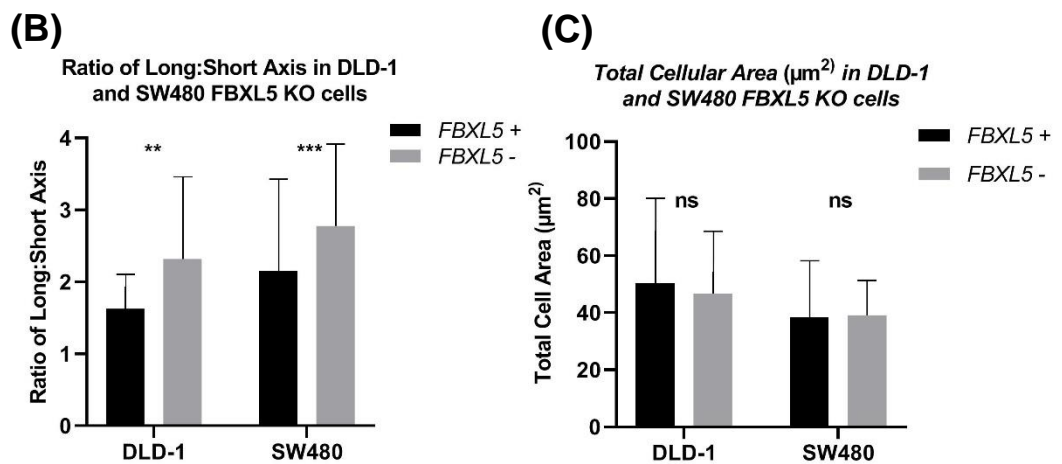


Figure 4.3: Phenotypic analysis of DLD-1 and SW480 *FBXL5* KO cells shows significant morphology alterations.

(A) DLD-1 and SW480 *FBXL5* KO cells were fixed and stained using Phalloidin. **(B)** The ratio of long vs short axis of stained cells was determined, and *FBXL5* KO cell

morphology was found elongated and had reduced cell-cell cohesion. Total cellular area was not significantly altered. Error bars represent standard deviation. (C) The total number of cell images for DLD-1 control was 36 DLD-1 KO was 102, while SW480 control was 159 and SW480 KO was 129. Scale bar 7.5 μ m. P values = $P < 0.05$ (*), $P \leq 0.01$ (**), $P \leq 0.001$ (***)).

4.1.2.2. Loss of FBXL5 does not affect the cell population increase over time in DLD-1 and SW480 cells

Mitotic cell division, migration and invasion are core behaviours of eukaryotic cells. Chronic cell proliferation/population increase is the quintessential defining characteristic of cancerous tissues and defining hallmark of cancer (Fouad and Aanei, 2017). Therefore, cell proliferation is an important experimental consideration in oncogenic studies. To further characterise FBXL5, we determined to investigate preliminary effects of FBXL5 knockout on cell proliferation/population increase by Growth Curve Analysis.

DLD-1 and SW480 *FBXL5* KO and parental control cell lines were seeded in triplicate to 24 well plates at 3×10^4 cells per well. Each day, three wells were washed, trypsinised and cells counted using the method previously outlined (Materials and Methods, section 2.2.4). The resulting cell count was analysed using Microsoft Excel and GraphPad Prism. This experiment was repeated on three occasions.

The growth curve analysis demonstrated that *FBXL5* KO growth rate was not significantly altered from parental cells. As such, FBXL5 does not significantly affect cell population increase rate in DLD-1 and SW480 CRC cell lines as shown in Figure 4.4 A and B. Only one study previously demonstrated that FBXL5 inhibition

significantly represses cell proliferation in SW480 cells, which is not in line with results found in this assay (Yao et al., 2018). It is currently unclear precisely why the results in these studies differ, however this may be caused by genetic drift between cell lines leading to differing results (Hughes et al., 2007) or use of differing methodology. This project utilising manual cell counting while the previously published study employed the CCK-8 chemiluminescence assay, which may produce different results to manual counting (Yao et al., 2018). Replication of this assay using both methods in a wider variety of colorectal cancer cell lines in the future may be beneficial. In addition, the residual FBXL5 protein expression in SW480 cells may also contribute to the differing results, as discussed further in section 4.2.

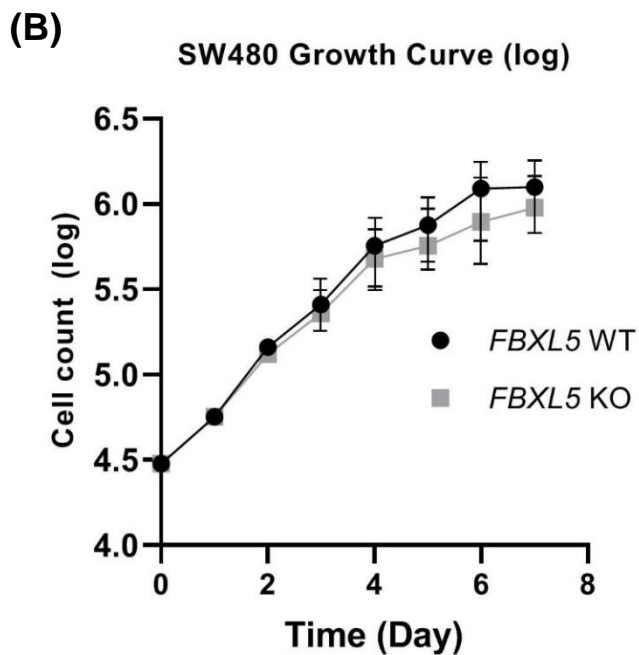
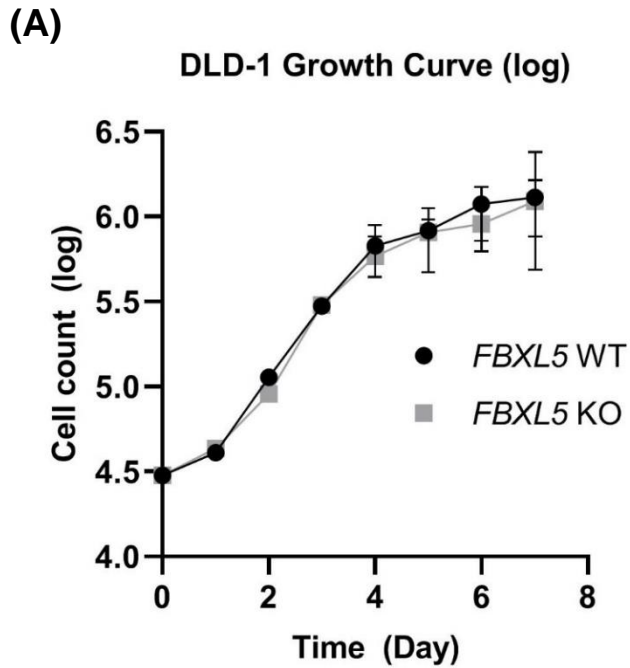


Figure 4.4: *FBXL5* knockout does not significantly affect cell proliferation/population increase in Growth Curve Assay.

Cells were seeded in triplicate at 3×10^4 cells/well and counted each day for 7-8 days. Cell counts between control and *FBXL5* KO cells do not significantly differ at any point in either DLD1 (A) or SW480 (B) cell lines, confirming *FBXL5*'s lack of interaction in

cell proliferation. Assay was repeated on three occasions. Error bars represent standard deviation. At no point were differences significant.

4.1.2.3. *FBXL5* KO of DLD-1 cell line showed a slight increase in G0 and SuperG2 cell population, while *FBXL5* KO SW480 cell line showed no differences in cell cycle

To further clarify the role of *FBXL5* in cell cycle and behaviour, one potential factor to consider is dysregulation of the cell cycle or the presence of quiescent cells. The cell cycle consists of four phases in addition to G0/Quiescence/resting phase. Interphase involves G1/Gap1 phase wherein cell size increases in preparation of DNA synthesis in S/Synthesis phase, after which the cell will enter G2/Gap2 phase in preparation for division of newly replicated chromosomal during mitosis and cell division proper during cytokinesis in M/Mitosis phase (Williams and Stoeber, 2012). SuperG2 indicates polyploidy (i.e., more than four complete sets of chromosomes), which may be caused by dysfunction in pathways associated with genomic stability that is common in cancer (Majuelos-Melguizo et al., 2015). After Mitosis phase, cells will return to G0/Quiescence.

Both cell behaviour within each stage and checkpoint, and progression to further stages of mitosis are heavily regulated, and dysfunction of cell cycle is a primary characteristic of many cancers (Otto and Sicinski, 2017). Cell cycle and checkpoint regulators are promising targets for novel cancer therapeutics (Otto and Sicinski, 2017). Additionally, numerous F-BOX proteins have been linked with timing regulation of the cell cycle and associated pathologies (Zheng et al., 2016a). Therefore, to explore how cell cycle may be altered in *FBXL5* KO cells, DLD-1 and SW480

FBXL5 KO cells were subjected to Propidium Iodide (PI) staining and Flow Cytometry analysis.

DLD-1 and SW480 control and *FBXL5* knockout cells were treated in triplicate with Propidium Iodide (PI) using manufacturer's instructions (Davies, 2021) as previously outlined (Materials and Methods, section 2.2.3), and fluorescence detected using Beckman Coulter FC500 Flow Cytometer (Abcam Propidium Iodide Flow Cytometry Kit ab139418). Flow Cytometry procedure was kindly performed by Dr David Onion of the University of Nottingham Flow Cytometry Service. The resulting data was analysed using WEASEL 3.7.1 and doublets removed from analysis. Assay was repeated once.

As shown in Figure 4.5A, DLD-1 *FBXL5* KO cells were more significantly concentrated in G1/growth phase and SuperG2/cell divisional cell cycle phases than controls. Figure 4.5B show that SW480 cells demonstrated no significant changes to cell cycle behaviour (DLD-1 $P = 0.036$, SW480 $P = 0.19$). Cell-specific differences in our results may possibly be explained by differing p53 expression between DLD-1 and SW480 cells, which is a master cell cycle regulator and tumour suppressor (Rochette et al., 2005) (Ahmed et al., 2013a).

As premature G0 progression/G1 phase accumulation may be triggered by environmental factors including oxidative stress and iron metabolism homeostasis, *FBXL5* may be affecting the cell cycle in this manner (Muto et al., 2017). *FBXL5* downregulation has previously been shown to promote cell cycle progression from G0 phase in hematopoietic stem cells, these cells may be prematurely progressing from G0 phase or accumulating in G1 phase (Muto et al., 2017). The mechanism by which

this occurs is currently unknown, however this may be related to FBXL5's interactions with PTEN and AKT/mTOR proliferation pathway (Yao et al., 2018).

SuperG2 refers to a cell population with higher DNA content than G2, such as polyploidy (more than four complete sets of chromosomes) (Majuelos-Melguizo et al., 2015). The G2/M checkpoint is highly regulated and F-BOX interactions with this pathway are poorly understood. FBXW8 down-regulation induced G2/M phase arrest in uterine cancer (Lin et al., 2011) and FBXW5 may partially regulated the G2/M transition (Di Fiore and Pines, 2007). Cycle arrest in colorectal cancer at G2/M phase transition may be caused by DNA damage checkpoint mechanism partially regulated by p53 and may also be impacted by *FBXL5* KO (Taylor and Stark, 2001).

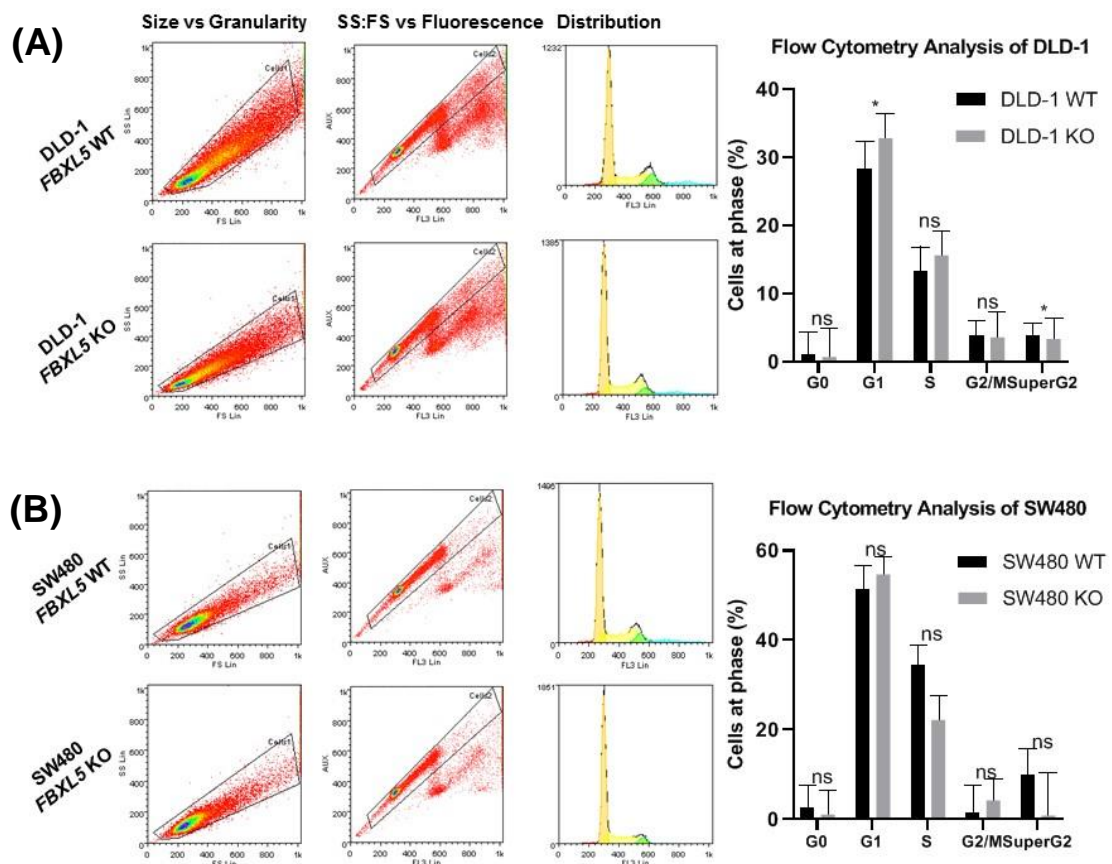


Figure 4.5: (A) DLD *FBXL5* KO cells showed accumulation in G1 and SuperG2 phases. (B) No significant change was detected in SW480 cells

DLD-1 and SW480 control and *FBXL5* cells were fixed in 70% ethanol, stained with propidium iodide and analysed using flow cytometry. Left column panels represent approximate cell populations divided by cell cycle status as determined by forward vs side scatter. Middle column panels represent cell cycle status as determined by side scatter: forward scatter vs PI fluorescence of cells (excluding side cell populations such as duplicated and other heterogenic cell populations). Right column panels show DNA content histogram of selected cells indicating PI stain in different cell cycles. Results determined that DLD-1 *FBXL5* cells accumulated in G0 and SuperG2 phases, whereas no significant change was found in SW480 cells (DLD-1 $P = 0.036$, SW480 $P = 0.19$). Error bars represent standard deviation, assay was repeated once.

4.1.2.4. Loss of *FBXL5* significantly reduced cell migration *in vitro* in both DLD-1 and SW480 cells

Controlled cell-cell attachment and migration are required for the correct development of organisms and tissues, the maintenance and repair of physical damage and cellular invasion of neighbouring tissues by cancerous cells. Dysfunction within cell-cell attachment, migration and invasion are important aspects of cell metastasis in cancer, causing cancerous cells to more readily transition to other tissues and establish malignancies (Fouad and Aanei, 2017). This attachment and migratory process is governed by the epithelial-to-mesenchymal/mesenchymal-to-epithelial (EMT/MET) pathway (Campbell and Casanova, 2016). As *FBXL5* has been shown in both published studies and data from this project to affect EMT (Wu et al., 2015b; Xiong et

al., 2017) (Figure 4.7A and B), we determined to investigate effects on cell migration within our DLD-1 and SW480 cell lines.

Cell lines DLD-1 and DLD-1 *FBXL5* KO, and SW480 and SW480 *FBXL5* KO were seeded in triplicate to six well plates for 100% confluency and incubated overnight (Materials and Methods section 2.2.5). The following day, to reduce proliferation effect, complete growth media (10% FBS) was replaced with low serum (1% FBS) alternative and incubated a further 24 hours to synchronise cells. Next, a scratch was made in each well with a P20 tip held perpendicular, wells gently washed with PBS twice and complete media added to wells. Each well was imaged in three different areas at 0, 24 and 48 hours post scratch to measure wound healing. The distance between cell boundaries and overall area were both measured and analysed for differences using ImageJ [(ImageJ version 1.5A (Abramoff et al., 2003), Materials and Methods, section 2.2.5)].

Results shown in Figure 4.6 indicate that by 24 hours post-scratch, DLD-1 KO cells had significantly reduced wound healing. 48 hours post-scratch, *FBXL5* KO significantly reduced wound healing rate in both DLD-1 and SW480 cells (wound closure 48h DLD WT: 59.5%, KO 39.9%, SW480 WT 17.74%, KO 9.57%) (DLD-1 24h $P = 0.0039$, 48h $P = 0.019$, SW480 24h $P = 0.94$, 48h $P = 0.0074$). These results suggest that *FBXL5* may have a role in modulating cell migration and attachment in colorectal cancer cells.

p53 has been linked to cell migration and invasion characteristics by modulation of RhoGTPases (He et al., 2019) loss may lead to an EMT-like phenotype (Muller et al., 2011). Physical interaction between *FBXL5* and PTEN reduces PTEN expression and leads to corresponding reduced p53 expression (Yao et al., 2018), and loss of function

p53 mutants may encourage cell migration in bladder and colorectal cancer cell lines (He et al., 2019). Whether p53 downregulation has similar impact to loss of function, and how PTEN overexpression may affect p53 expression under these circumstances is also unclear (He et al., 2019). However, *FBXL5* KO dysregulation of PTEN and p53 may partially explain these results.

Previous results from this study have suggested that colorectal cancer cell lines with *FBXL5* KO demonstrate a partial mesenchymal phenotype. As EMT is a fundamental process in cell migration and invasion, *FBXL5* interactions with EMT via SNAIL ubiquitination may account for differences in migratory properties in *FBXL5* KO cells, with SNAIL expression reducing E-Cadherin expression and promoting EMT (Viñas-Castells et al., 2014; Wu et al., 2015b). SNAIL itself impacts both EMT-related and EMT-independent cell adhesion and movement (Barrallo-Gimeno and Nieto, 2005), although the direct impact of SNAIL on cell migration is not clear. Therefore, overexpression of SNAIL due to *FBXL5* KO may contribute to the partial mesenchymal characteristics of these cells.

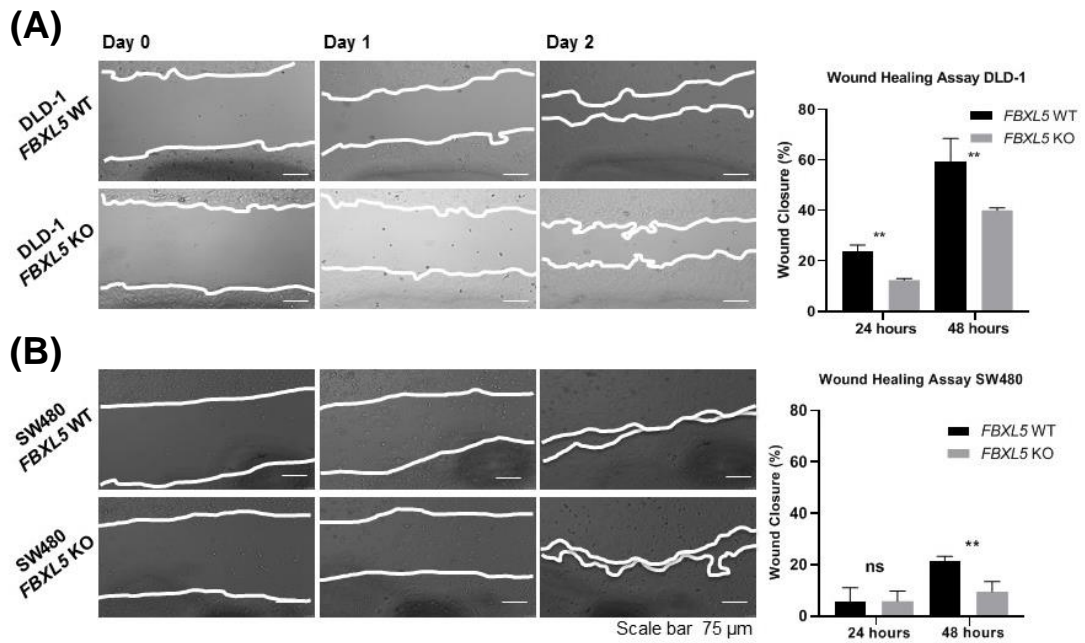


Figure 4.6: FBXL5 knockout significantly reduces wound healing rate in colorectal cancer cells.

DLD-1 (A) and SW480 (B) *FBXL5* KO cells demonstrated reduced cell migration in starvation state compared to control cells 48 hours post-scratch, suggesting that *FBXL5* KO modulates cell migration. 48h Wound Closure percentage DLD WT: 59.5%, KO 39.9%, SW480 WT 17.74%, KO 9.57%. Error bars represent standard deviation. *P* values = $P < 0.05$ (*), $P \leq 0.01$ (**), $P \leq 0.001$ (***), $P \leq 0.0001$ (****). Scale bar 75μm, assay was repeated once.

4.1.2.5. Western Blot and RT-qPCR analysis of FBXL5 KO DLD-1 and SW480 shows significant deregulation of EMT-related markers.

Results thus far associate FBXL5 with roles in CRC cell morphology and cell attachment/migration. Cancer cell morphological alternation may indicate a change in epithelial-to-mesenchymal activity, including epithelial-to-mesenchymal transition (EMT), which FBXL5 has previously been associated with via SNAIL ubiquitination in liver carcinoma cell lines (Wu et al., 2015b). EMT activation upregulates both EMT transcription factors (e.g. SNAIL) and other mediators (e.g. β -Catenin) and downregulates E-Cadherin expression (Kalluri and Weinberg, 2009). UPS-mediated ubiquitination and degradation of SNAIL protein promotes E-Cadherin expression, thereby inducing epithelial characteristics over mesenchymal (Tanaka et al., 2016). Activation of the Wnt pathway modular β -Catenin, loss of the epithelial adherent junction regulator E-Cadherin and acquisition of mesenchymal markers such as the intermediate filament protein Vimentin and adhesion protein N-Cadherin are the defining characteristic of EMT (Tanaka et al., 2016).

Thus, to further characterise the role of FBXL5 in colorectal cancer cells, we explored the mRNA and protein expression of primary EMT markers N-Cadherin, Vimentin, E-Cadherin, β -Catenin, and SNAIL in DLD-1 and SW480 FBXL5 knockout cells. (Figures 4.7 and 4.8)

DLD-1 and SW480 parental and *FBXL5* KO cells were lysed for cellular protein and probed using SDS-PAGE Western Blot analysis for expression of Vimentin (1:1000), β -catenin (1:1000), E-Cadherin (1:2500) and SNAIL (1:1000). 100 μ g protein lysate was loaded into each well of 10% SDS-PAGE gel (Materials and Methods, section

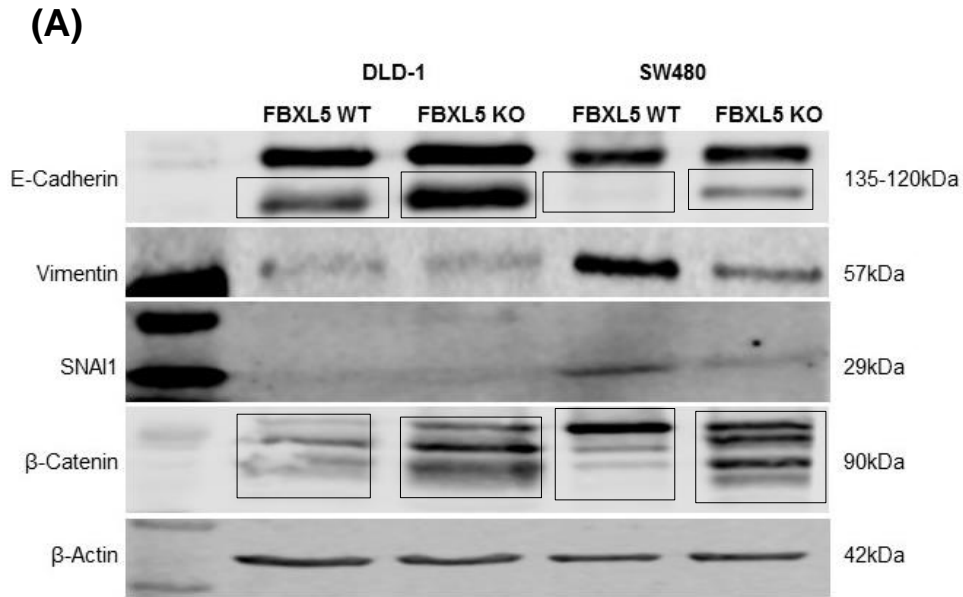
2.2.12). Densitometry analysis of results was normalised to 1 against the control sample and blots were repeated at least twice for validity where possible (Figure 4.7B). Western blot results indicate that both DLD-1 and SW480 KO cells have increased E-Cadherin precursor/premature transcript form and β -catenin general expression. DLD-1 cells show no change in Vimentin and may show very slight SNAIL protein expression increase while these are both decreased in SW480 cells, although these require further validation (Figure 4.7, DLD-1 KO expression change vs control: (B) E-Cadherin mature band expression was 1.1x control (no change to precursor protein band expression, E-Cadherin 80 kDa band was poorly detected with our antibody and excluded from analysis), (C) Vimentin protein expression was 1.0x control, (D) SNAIL protein expression was 2.13x control, (E) β -catenin protein expression was 2.61x control, SW480 KO expression change vs control: (B) E-Cadherin protein expression was 1.71x control, (C) Vimentin protein expression was 0.26x control, (D) SNAIL protein expression was 0.40x control, (E) β -catenin protein expression was 1.64x control).

Consistent with these results, it has been previously shown that DLD-1 cells express little to no Vimentin and SNAIL protein (Ahmed et al., 2013a; Tanaka et al., 2016). β -catenin has several possible bands representing multiple phosphorylated states (Gao et al., 2014). Only β -catenin band 1 (the longest) and band 3 (shortest) have been studied independently, finding roles in cell motility/mobility and immune function respectively (Land, 2018; Slorach et al., 2011). No information was available on the functionality of the different E-Cadherin fragments.

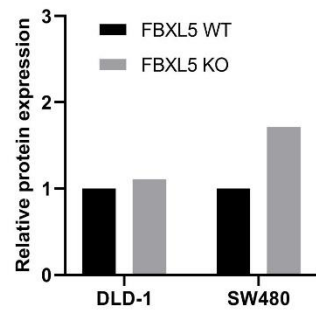
To further characterise the role of FBXL5 and compare previous protein expression analysis results, we determined to study the mRNA expression of the above genes. Previous studies have shown that mRNA expression is an unpredictable indicator of

protein expression (Gry et al., 2009) (Guo et al., 2008) (Edfors et al., 2016). Given experimental interference with the UPS via *FBXL5* KO, it is reasonable to presume this contributed to disjointed mRNA/protein expression results.

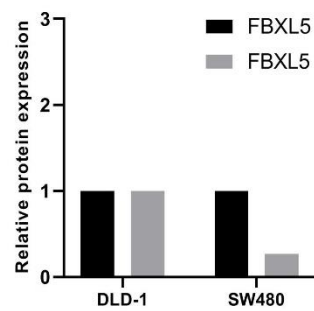
Results of RT-qPCR analysis indicate *E-cadherin* (*CDH1*) mRNA was downregulated in SW480 cells but not DLD-1 cells (Figure 4.8A), *Vimentin* (*VIM*) mRNA expression was downregulated in DLD-1 but not SW480 cells (Figure 4.8B) and *SNAIL* (*SNAI1*) mRNA was slightly downregulated in both DLD-1 and SW480 cells (Figure 4.8C). Significant *β-catenin* (*CTNNB1*) mRNA downregulation was found in both DLD-1 and SW480 cells constant with mesenchymal rather than epithelial cells (Figure 4.8: *E-Cadherin* (DLD-1 $P = 0.11$, SW480 $P = < 0.0001$), *Vimentin* (DLD-1 $P = < 0.0001$, SW480 $P = 0.97$), *SNAIL* (DLD-1 $P = 0.0099$, SW480 $P = 0.0001$), *β-catenin* (DLD-1 & SW480 $P = < 0.0001$)). Assay was repeated twice, and calculations performed by Delta-Delta CT method ($2^{-(\Delta\Delta Ct)}$ method) as outlined in Materials and Methods section 2.2.13.



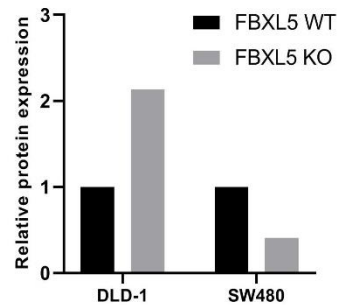
(B) E-Cadherin Relative Protein Expression



(C) Vimentin Relative Protein Expression



(D) SNAIL Relative Protein Expression



(E) β-Catenin Relative Protein Expression

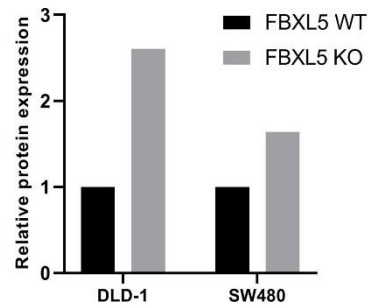


Figure 4.7: DLD-1 and SW480 cells lines with FBXL5 knockout demonstrated altered protein expression related to EMT markers.

(A) 100µg protein lysate was loaded into each well of 10% SDS-PAGE gel. DLD-1 KO cells had increased E-Cadherin short protein expression **(B)** and β-Catenin **(E)**,

while SW480 cells had reduced Vimentin (C) and may have reduced SNAIL (D) while increased β -catenin and E-Cadherin expression. Densitometry result was normalised to 1 against the control sample. DLD-1 KO expression change vs control: E-Cadherin mature band 1.1x, Vim 1.0x, SNAIL 2.13x β -catenin 2.61x, SW480 KO expression change vs control: E-Cadherin 1.712x, Vim 0.26x, SNAIL 0.40x, β -catenin 1.64x. Assay repeated twice where antibody was available.

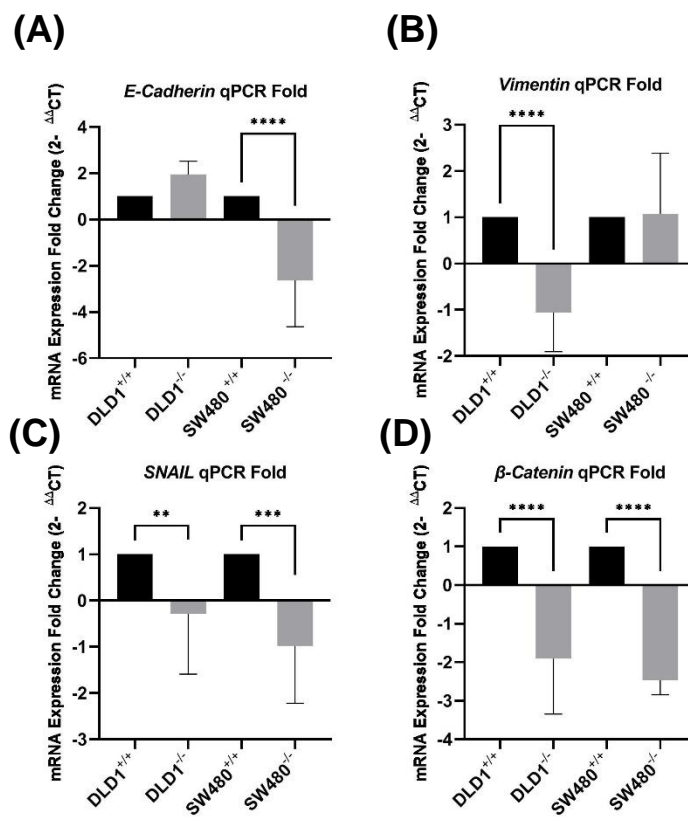


Figure 4.8: FBXL5 knockout significantly alters mRNA expression of core EMT markers.

Results of RT-qPCR analysis of EMT markers shows that *FBXL5* KO significantly alters *E-Cadherin* (A), *Vimentin* (B), *SNAIL* (C) and *β-Catenin* (D) mRNA expression to varying degrees in different cell lines (Figure 4.8). In contrast to Figure 4.7, RNA

expression of β -Catenin is constant with mesenchymal rather than epithelial cells, although *E-Cadherin* expression implies both, suggesting a partial EMT state caused by *FBXL5* KO. RT-qPCR assay was performed in triplicate and repeated twice in total and result normalised to 1 for comparison. Error bars represent standard deviation. *P* values = $P < 0.05$ (*), $P \leq 0.01$ (**), $P \leq 0.001$ (***), $P \leq 0.0001$ (****). Assay was repeated twice.

These results, while initially disparate, imply a partial mesenchymal state caused by *FBXL5* KO. In addition to “complete” EMT/MET, wherein cells completely transition between epithelial and mesenchymal states, epithelial cancer cells may simultaneously demonstrate both mesenchymal and epithelial characteristics, presenting enhanced invasive properties, resistance to related chemotherapeutics and an inability to either transition between or effectively regulate EMT/MET (Grigore et al., 2016). This hybrid epithelial/mesenchymal phenotype is known as “partial EMT” or “incomplete EMT” and may be caused by dysfunction of EMT transcription factors, wherein cells co-express epithelial and mesenchymal markers (Grigore et al., 2016; Saitoh, 2018; Yang et al., 2020). Partial EMT cells continue to express epithelial markers after migration while complete EMT cells normally lack both RNA and protein components (Aiello et al., 2018). The loss of epithelial state in tumour and cancerous cells is achieved post-transcriptionally, rather than transcriptional repression, through protein relocation and storage of E-Cadherin and other epithelial proteins in endocytic vesicles in mesenchymal partial EMT cells (Aiello et al., 2018). This leads to cell migration in clusters, in contrast to the single cell migration found in typical EMT/MET (Aiello et al., 2018). Dysregulation of Rab family of GTPases, which regulate vesicle and protein traffic and recycling, may be partially responsible for partial EMT by accumulation of

E-Cadherin (Aiello et al., 2018; Hutagalung and Novick, 2011). While FBXL5 and SNAIL protein expression has previously been reported as inversely correlated, with FBXL5 ubiquitinating SNAIL, this was not entirely supported by our data (Wu et al., 2015b). This result may be explained by the known lack of SNAIL protein expression in DLD-1 cells (Tanaka et al., 2016), but also the partial EMT phenotype displayed by both *FBXL5* KO cell lines, which may further dysregulate SNAIL expression and thus requires further validation.

Given experimental interference with the UPS via *FBXL5* KO shown by these results, it is reasonable to presume that a partial EMT phenotype contributed to disjointed mRNA/protein expression results. Furthermore, cells with a partial EMT phenotype show abnormal SNAIL2, ZEB1, E-Cadherin and Vimentin expression and only some demonstrated spindle-like mesenchymal morphology. (Basu et al., 2018; Harner-Foreman et al., 2017; Tanaka et al., 2016). Although further research is required to fully explore the mechanisms of action of FBXL5 in CRC cells, the above studies might suggest that the EMT/MET process as a gradual and multifaceted mechanism, of which FBXL5 may only be one regulatory factor.

4.2. Discussion

This chapter focused on the initial characterisation of *FBXL5* KO colorectal DLD-1 and SW480 cell lines including morphology, proliferation, cell attachment/migration and potential role in epithelial-to-mesenchymal activity. *FBXL5* KO was found to generate an elongated spindle-like phenotype within DLD-1 and SW480 cells. As shown previously, *FBXL5* KO organoids display an unusual incohesive phenotype differing from control organoids but no change to growth rate over seven days (Figure 3.9 and 3.10), while both DLD-1 and SW480 cells also displayed similar abnormal

morphology and properties without altered growth rates. Taken together, these results support our previous findings in murine intestinal organoids that FBXL5 modulates cell morphology. *FBXL5* KO also affected cell cycle activity and dysregulates primary EMT markers at both protein and mRNA level in colorectal cancer cells in a cell-specific manner. In combination, these factors indicate a partial EMT phenotype in colorectal cancer cells.

The data discussed in this chapter suggests that the impact of FBXL5 KO may be more pronounced when specific pathways are activated, particularly in cancer cells. We speculate that FBXL5 may require further cellular stimuli or environmental factors to demonstrate a significant effect, such as activation of EMT. This is explored further in Section 5.1.2 (Autophagy), 5.1.3 (Hypoxia Response), 5.1.4 (Drug Response) and Chapter 6 (Bioinformatics and RNA-Seq Analysis).

The cell proliferation/population increase data obtained during this project shows that *FBXL5* KO does not affect cell proliferation (Figure 4.4). However, Yao et al (Yao et al., 2018) found that FBXL5 silencing using *shRNA* (Short hairpin RNA) methodology inhibited cell proliferation and FBXL5 overexpression stimulated cell proliferation in SW480 and T84 colorectal cancer cells. Both these results may also conflict with the UALCAN analysis of FBXL5 expression in CRC (Figure 1.9), showing that FBXL5 protein expression is reduced in CRC, implying a potential tumour suppressor role.

It is currently unclear what technical factors may cause contrasting results between this project and the data published by Yao et al. Possible explanations may include a different cell culture environment, the methods utilised generating *FBXL5* KO cell lines, the different cell counting methods used and the genetic background of the

SW480 cell lines used in each set of experiments, some of which were outlined in the results section.

For example, Yao et al (Yao et al., 2018) utilised *ShRNA* (short hairpin RNA) knockdown vectors to repress the transcription and translation of *FBXL5*. However, it has previously been suggested *ShRNA* methodology may lack specificity and produce off-target effects (Jackson and Linsley, 2010), although Yao et al does not address this issue. Alternatively, the partial SW480 *FBXL5* knockout cell line (Figure 4.2) used in this project may account for the differences in cell proliferation, as Yao et al produced a complete SW480 knockout. Our project utilised manual cell counting to determine cell proliferation over 7-8 days period (Materials and Methods, section 2.2.4), whereas Yao et al used the CCD-8 chemiluminescence assay to determine cell proliferation at 0, 24, 48, 72 and 96 hours. Yao et al does not specify if this assay was repeated at any point. It would be beneficial in future studies to utilise both methods to produce more comprehensive results.

The discrepancy between DLD-1 and SW480 *FBXL5* protein and mRNA expression in early passage KO cells may indicate that complete *FBXL5* KO is lethal in SW480 cells, or that SW480 knockout caused a single allele deletion. This could be determined by genomic DNA sequencing of the *FBXL5* KO samples, which we intend to do in future continuations of this research project. SW480 has abnormal epigenetic activity in PI3K/AKT/mTOR related proteins leading to hyperactivity disruptions, which may indirectly affect *FBXL5* expression (Ahmed et al., 2013b), while DLD-1 does not natively express SNAIL protein, which is ubiquitinated by *FBXL5* (Tanaka et al., 2016). Additionally, recent identification of Consensus Molecular Subtypes in CRC may imply that DLD-1 and SW480 cells were derived from different subtypes, making comparison difficult (Guinney et al., 2015), however, this factor has not been

investigated. A detailed summary of the background of each cell line may be found in Materials and Methods Table 2.1.

Intriguingly, expression of the protein and mRNA EMT markers β -Catenin, N-Cadherin, Vimentin, E-Cadherin and SNAIL in *FBXL5* KO cells indicates a partial or incomplete epithelial/mesenchymal state. In wild type DLD-1 cells (which typically do not express SNAIL protein (Tanaka et al., 2016)), induction of SNAIL expression has previously been shown to reduce E-Cadherin expression, increase invasion, migration and trigger morphology changes associated with mesenchymal cells, demonstrating a partial EMT phenotype as described in above (Results section 4.1.2.5) (Tanaka et al., 2016).

Epithelial-to-Mesenchymal transition is highly regulated, with SNAIL acting as one of several factors. Other factors that govern EMT activation and the acquisition of epithelial and mesenchymal traits include TGF- β signalling such as ZEB1, Twist1 and SNAIL2/Slug, microRNA's miR-200 and miR-199 and Notch, and Wnt signalling (Drago-García et al., 2017) (Lin and Wu, 2020). As such, while *FBXL5* KO has significantly dysregulated SNAIL expression at both protein and mRNA level in colorectal cancer cells, this may only cause a partial mesenchymal phenotype. This is evidenced by decreased E-Cadherin protein and mRNA expression typical of mesenchymal cells, but also reduction of SNAIL and Vimentin protein expression typical of epithelial cells, while E-Cadherin, Vimentin and SNAIL mRNA expression were dysregulated. *FBXL5* KO may cause a partial EMT transition in colorectal cancer cells independent of normal EMT markers.

These results also support previous findings on the role of *FBXL5* in EMT, although unlike previously published results, *FBXL5* KO did not significantly increase SNAIL

expression in either DLD-1 or SW480 cells. In fact, mRNA expression decreased in both DLD-1 and SW480 cells, further supporting the supposition that alternative posttranscriptional regulatory mechanisms may modulate EMT in CRC. The differing levels of EMT marker expression at protein and mRNA level may be explained by feedback or regulatory mechanisms that rely on but do not strictly require FBXL5 to function adequately. Post-transcriptional regulatory mechanisms including methylation, ubiquitination, miRNA interference, disjointed half-life, alternative splicing variants and differences in transcription efficiency also may account for differing protein and mRNA expression. In particular, knock down of DNA methyltransferases radically dysregulated EMT and increased cell sensitivity to therapeutic agents (Galle et al., 2020).

Finally, genetic drift between apparently identical cell lines occurs due to the gradual accumulation of mutations during repeated cell passage (Hughes et al., 2007). As such, the SW480 cells used in this project may be genetically divergent compared to those used in Yao et al or vice versa. Alternatively, cell lines may be misidentified entirely. In future studies, a complete sequencing of the project cell genome may identify novel mutations compared to commercially available low-passage cells may be advantageous in identifying differences.

In this chapter, we examined the possible impact of FBXL5 KO on DLD-1 and SW480 CRC cell lines. From these results, we can conclude that FBXL5 knockout has a significant impact on cell morphology, colony formation efficiency and cell migration in colorectal DLD-1 and SW480 cells in a cell-specific manner. In addition, FBXL5 KO also affects EMT, generating a partial EMT phenotype in cells. This suggests that FBXL5 may have a greater role in CRC than previously known. Further exploration

of the impact of FBXL5 KO on CRC cell lines may identify and expand on novel associations, such as with iron homeostasis, autophagy, hypoxia and drug response.

**Chapter 5: The role of *FBXL5*
in the Iron Metabolism,
Autophagy, Hypoxia and Drug
Response in Colorectal Cancer**

5. Brief Introduction

The previous chapter established that FBXL5 partially regulates cell morphology and migration in CRC cells without affecting cell proliferation and partially modulates epithelial-to-mesenchymal transition activity, validating our results found in murine intestinal organoids and previously published data on FBXL5 function in colorectal cancer cell lines (Viñas-Castells et al., 2014; Wu et al., 2015b). Due to the limited published data on FBXL5 in CRC tumour microenvironments, in this chapter we determined to replicate previously published studies on FBXL5 roles and possible regulatory mechanisms from other cancerous cell lines on iron metabolism (Moroishi et al., 2011; Wang et al., 2020a) (Section 5.1.1), hypoxia (Machado-Oliveira et al., 2015a) (Section 5.1.3) and drug response (Wu et al., 2016) (Section 5.1.4). In addition, we intend to investigate the possible roles of FBXL5 in autophagy (Section 5.1.2), as it is an important consideration in oncogenic activity not previously explored in FBXL5 (Ji and Kwon, 2017).

5.1. Results

5.1.1. FBXL5-mediated cellular iron regulation in colorectal cancer cells

We have initially investigated the significance of FBXL5 in the iron homeostasis pathway in colorectal cancer by utilising iron measuring assays, examining the protein and mRNA expression of critical iron homeostasis markers, the effect of FBXL5 KO on iron-dependent chemotherapeutics and the potential implications of these results.

FBXL5 is unique among mammalian proteins for possessing a hemerythrin-like domain for both iron and oxygen binding, which is normally found in marine invertebrates (Wang et al., 2020a). FBXL5 also stabilises in iron-replete and oxygen-

replete conditions, being degraded when cellular iron is low (Chollangi et al., 2012). FBXL5 ubiquitinates IRP1 and IRP2 (iron regulatory protein 1 and 2) when oxidised, with IRP2 expression increasing in hypoxic conditions while FBXL5 is suppressed (Moroishi et al., 2011) (Johnson et al., 2017). The precise nature of FBXL5's role in iron homeostasis is uncertain and the majority of studies have been performed in haematopoietic cancer cells rather than CRC (Moroishi et al., 2014). As conventional *FBXL5* KO mice die *in-utero* due to iron excess which can be ameliorated by the addition of IRP2, it may be theorised that FBXL5 is necessary for IRP2 functioning (Jeong et al., 2011; Kuhn, 2009). Additionally, FBXL5 is associated with HERC2, which degrades FBXL5 and modulates its expression (Moroishi et al., 2014). HERC2 is also required for NCOA4-mediated ferritin regulation (Nuclear Receptor Coactivator 4), wherein NCOA4 expression is inversely correlated with ferritin accumulation (Moroishi et al., 2014).

Iron homeostasis dysregulation contributes to several cancers including colorectal and hepatic, and to tumour metastasis and angiogenesis (Chen et al., 2019), drug resistance (Brown et al., 2020) and immune dysregulation and tumour immune response (Costa da Silva et al., 2017). Dysregulation of iron homeostasis causes oxidative stress and altered cell cycle progression, with iron being required for G1 cycle progression via expression of cyclin D1, D2 and D3 in neuroepithelioma and breast cancer cells (Gao and Richardson, 2001).

Therefore, to analyse the role of FBXL5 in iron homeostasis in colorectal cancer cells, we examined the levels of protein and mRNA expression of key markers of iron homeostasis in FBXL5 KO vs parental control cells. These were iron regulatory protein 1 and 2 (IRP1 and 2) transferrin receptor (TfR) and Ferritin Light and Heavy chains (FTL1 and FTH1 respectively) and common downstream iron homeostasis

markers. Furthermore, we measured the labile iron levels by Calcein AM assay, and the effect of *FBXL5* KO on the iron homeostasis related chemotherapy agent Salinomycin.

5.1.1.1. Calcein AM staining shows significant variations in DLD-1 *FBXL5* KO cytosolic labile iron levels compared to controls.

Here, we utilised the Calcein AM (ThermoFisher C1430) method, a widely used assay to quantify the “labile iron pool” (LIP) (Tenopoulou et al., 2007) and variations caused by *FBXL5* KO and the dysregulation of iron regulatory pathways

Calcein AM is a transient transmembrane fluorescence dye (495-515nm) that reacts with cytosolic nonspecific esterases. Calcein AM is colourless and non-fluorescent until hydrolysed within the cell, wherein it is cleaved by nonspecific esterases, producing the fluorescent Calcein dye, which can remain in cells for many hours, and the AM ester, which is removed from cells within 15-60 minutes. Calcein fluorescence is quenched by chelation with redox-active iron (Fe^{2+}) in the labile iron. Therefore, greater fluorescence in sample may indicate lower labile iron concentration, thereby providing an estimate of labile iron within the cell cytosol. Calcein itself is membrane non-permeable and thus retained by the cytosol, but also unable to penetrate membrane-limited organelle-containing compartments within the cell, and lysosomes are noted as rich in cellular iron. Estimates suggest that cytosol labile iron represents <5% of total cellular iron (Kakhlon and Cabantchik, 2002). Therefore, Calcein AM will only measure cytosolic labile iron rather than total cellular iron.

We adapted the Calcein AM method from the manufacturer’s instructions and dosage concentrations recommended by the manufacturer: DLD-1 and SW480 parental and *FBXL5* KO cell lines were seeded to a 96 well plate in triplicate at 3×10^3 cells/well

and incubated for 24 hours in complete cell media. Solutions of 0 μ M, 2 μ M, 4 μ M, 6 μ M, 8 μ M and 10 μ M per well in 200ul were prepared in serum free media and cells incubated at 37°C for 90 minutes, after which media was replaced with complete media. Next, the plate was read using a spectrophotometer at 482nm every 15 minutes for 60 minutes total, while the plate was returned to the incubator between readings. Data were analysed in Microsoft Excel by conversion to Log10, normalised and plotted as standard for cytotoxicity dose-response curve experiments as previously outlined (Materials and Methods section 2.2.14).

As shown by Figure 5.1A, fluorescence was dramatically increased in DLD-1 *FBXL5* KO cells compared to DLD-1 control cells, suggesting a reduction in labile iron available to quench the fluorescence (DLD-1 WT IC₅₀: 2.235 μ m, KO 4.187 μ m). However, SW480 cells (Figure 5.1B) did not show a similar difference in fluorescence (SW480 WT IC₅₀: 4.291 μ m, KO 4.535 μ m), implying that *FBXL5* may not have the same role as in DLD-1 cells.

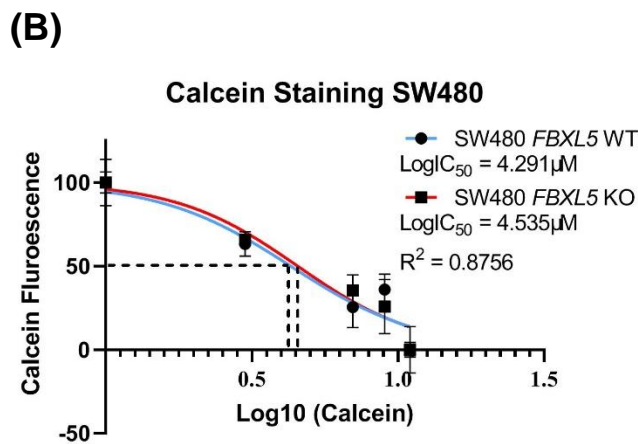
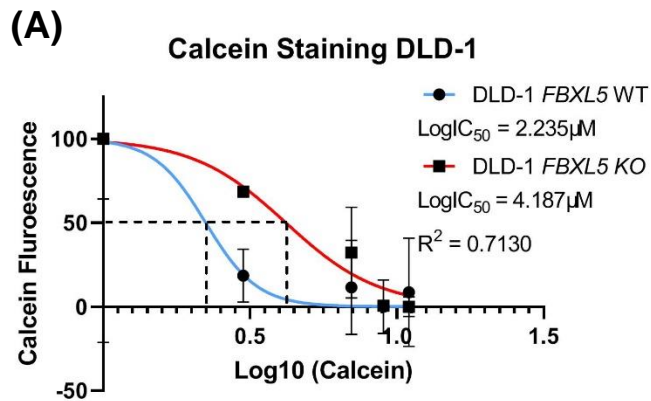


Figure 5.1: Fluorescence of Calcein AM staining of DLD-1 and SW480 *FBXL5* KO after 90 minutes incubation shows increased labile iron levels in DLD-1 KO cells

(A) Decreased fluorescence expression in DLD-1 *FBXL5* KO cells indicates increased labile iron compared to control cells, suggesting *FBXL5* has a significant influence on cytosolic labile iron levels in DLD-1 cells. (B) No significant change was found in SW480 cells. Dosages per well: 10 μM , 8 μM , 6 μM , 4 μM , 2 μM and 0 μM in 200ul serum free media. Final IC_{50} in μM : DLD-1 WT IC_{50} : 2.235 μM , KO 4.187 μM . SW480 WT IC_{50} : 4.291 μM , KO 4.535 μM . Error bars represent standard deviation. Assay was repeated once each condition.

5.1.1.2. *FBXL5* KO causes increased resistance to Salinomycin treatment in colorectal cancer cells

An alternative method for exploring the role of *FBXL5* in iron homeostasis is examining downstream markers and mechanisms. One such pathway is Reactive Oxygen Species (ROS) (Galaris et al., 2008), an essential cell-survival mechanism heavily related to iron homeostasis. Redox active iron (Fe^{2+}) in the labile iron pool can form reactive oxygen species (ROS) by direct interaction with hydrogen peroxide within cells and as by-products of mitochondrial function (Galaris et al., 2008). Antioxidant enzymes usually neutralise ROS. Excess ROS causes cellular oxidative stress, resulting in abnormal enzyme activity and cytotoxic release of labile iron, thereby interfering with DNA, protein, iron-related metabolic activity and leading to cell death (Galaris et al., 2008). A previous study found *FBXL5* knockout caused accumulation of ROS in mouse cerebral tissue, but the precise mechanism was not clear (Moroishi et al., 2014).

Salinomycin has traditionally been used as an anti-coccidial drug, has recently been shown to possess anti-cancer and anti-cancer stem cell (CSC) effects including colorectal, in addition to other antifungal, antiviral and anti-inflammatory properties (Verdoodt et al., 2012; Wang et al., 2019). Interestingly, Salinomycin may sensitise cancer cells to other agents including 5-FU and Oxaliplatin (Klose et al., 2019).

Salinomycin's primary mechanism is not fully known, and might act on cell proliferation via p38, AKT/mTOR and apoptosis via LRP6/Wnt, p53 and angiogenesis via VEGFR2a (Klose et al., 2019) (Dewangan et al., 2017), Salinomycin also inhibits mitochondrial respiratory chain complex 2, resulting in mitochondrial dysfunction and rapid accumulation of ROS leading to cell death and blocks β -catenin/TCF4E complex

formation in colorectal cancer cells (Wang et al., 2019). Salinomycin has also been reported to contribute to ROS formation as one possible mechanism of action (Verdoodt et al., 2012). Therefore, we aimed to examine the possible FBXL5 interaction with ROS to modulate colorectal cancer cell response to Salinomycin treatment.

DLD-1 and SW480 control and *FBXL5* KO cells were seeded to 96 well plates at 3×10^3 /well in 200 μ l complete growth media in triplicate and incubated for 48 hours at 37°C (Materials and Methods sections 2.2.14). Cell media was then replaced with complete media supplemented with 0, 0.5 μ M, 1 μ M, 1.5 μ M, 2 μ M, 3 μ M, 4 μ M, 5 μ M, 6 μ M or 10 μ M of Salinomycin (Wang et al., 2019). Salinomycin treatment and control cells were fixed, stained, and measured using the Sulforhodamine B (SRB) drug toxicity assay method outlined in Materials and Methods section 2.2.14.

Figure 5.2 shows that *FBXL5* knockout increased Salinomycin resistance in both DLD-1 (Figure 5.2A) at 48 hour and SW480 (Figure 5.2B) cells at 24-hour treatment. However, DLD-1 cells showed no significant results at 24-hour treatment duration, and 72-hour treatment caused complete cell death irrespective of treatment dosage. 48-hour treatment duration produced optimal results, with WT vs KO IC_{50} values of 1.691 μ M/Log10 0.2281 vs 1.924 μ M/Log10 0.2842 respectively.

In SW480 cells, treatment with Salinomycin caused complete cell death by 48-hours, therefore further optimisation of cell-specific treatment dosage may benefit future studies. 24-hour treatment results show WT vs KO IC_{50} values of 2.021 μ M/Log10 0.3055 and 2.373 μ M/Log10 0.3753 respectively.

From these results, we can conclude that FBXL5 may influence Salinomycin resistance, supporting prior research demonstrated Salinomycin antitumor properties in CRC and SW480 cells in particular (Klose et al., 2019).

The greater resistance of DLD-1 cells to Salinomycin implies that some aspect of DLD-1 or SW480 genome may affect response. As previously noted, Salinomycin has multiple possible interactions including p53, ROS and iron homeostasis (Verdoodt et al., 2012; Wang et al., 2019). Both DLD-1 and SW480 have different p53 mutations: DLD-1 at p.S241F and SW480 from R273H;P309S (Rochette et al., 2005). DLD-1 p53 functionality is unclear, and p53 functionality in SW480 is severely limited, and therefore R273H;P309S mutations may be more vulnerable to p53-mediating drug treatments (Rochette et al., 2005) such as Salinomycin. Alternatively, as our following experiments have demonstrated: DLD-1 and SW480 have differing protein and mRNA expression of iron homeostasis markers. These cell lines may also have an undocumented mutation in an iron homeostasis-related pathway that accounts for these results.

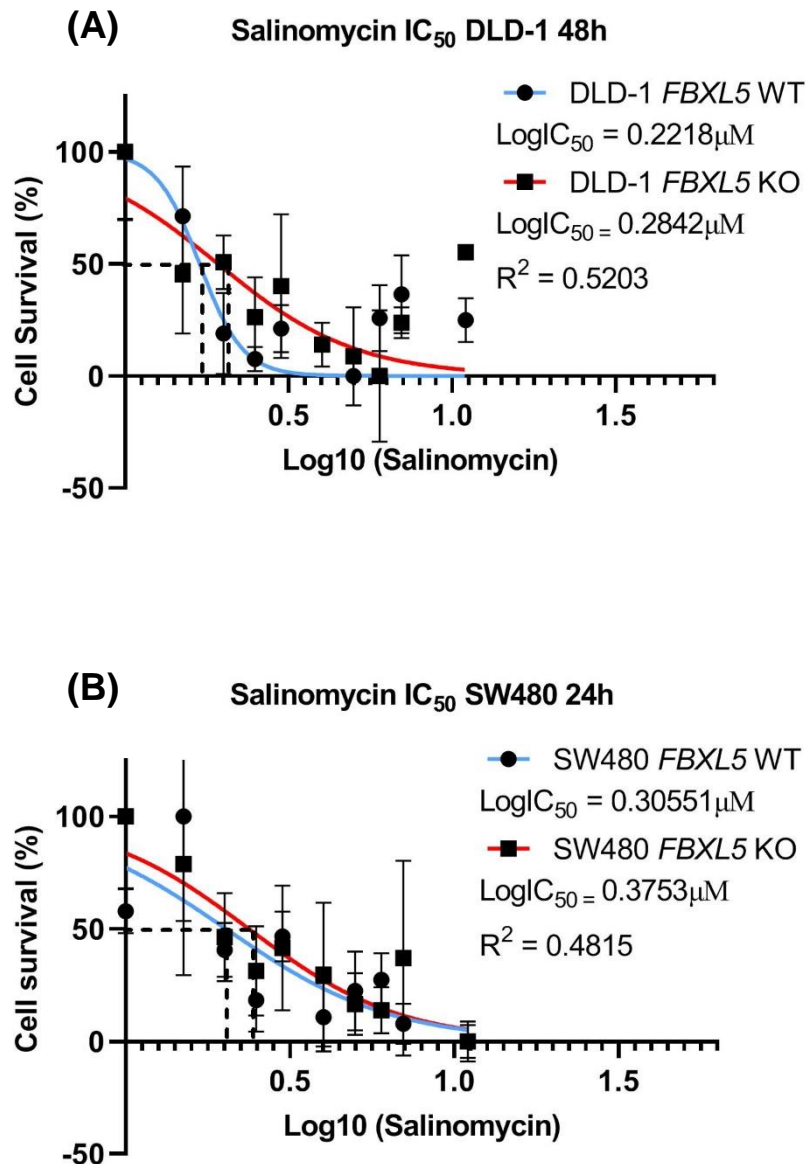


Figure 5.2: FBXL5 knockout increased resistance of DLD-1 and SW480 cell lines to Salinomycin treatment.

Cells were seeded at 3×10^3 /well in 96 well plates, incubated for 48 hours and treated for 24, 48 and 72 hours. Complete cell death occurred at 72 hours in DLD-1 and 48 hours in SW480 cells. (A) DLD-1 48-hour WT vs KO IC₅₀ in μM: 0.2281 μM vs 0.2842 μM (B) SW480 WT vs KO IC₅₀: 0.3055 μM and 0.3753 μM respectively at 0-

10µM Salinomycin per ml. Error bars represent standard deviation. Assay was repeated twice.

5.1.1.3. *FBXL5* KO DLD-1 and SW480 cells shows altered expression of iron-homeostasis related markers.

To further analyse the mechanism and role of *FBXL5* in CRC cells, we aimed to analyse the expression of primary iron homeostasis markers Iron Regulatory Proteins 1 and 2 (IRP1 and 2), Transferrin Receptor (TfR) and Ferritin Light and Heavy chain forms (FTL1 and FTH1 respectively) in both mRNA and protein expression. While *FBXL5* has been shown to ubiquitinate IRP1 and IRP2 (Moroishi et al., 2011) (Johnson et al., 2017), it is currently unclear precisely how *FBXL5* more broadly influences iron homeostasis in CRC, nor how IRP1 and IRP2 coregulate themselves and downstream targets. We can hypothesise that *FBXL5* KO will significantly affect either IRP1 and/or 2 protein expression, and also affect subsequent downstream iron homeostasis markers TfR and Ferritin.

DLD-1 and SW480 parental and *FBXL5* KO cells were lysed for cellular protein and probed using SDS-PAGE Western Blot analysis for expression of IRP1, TfR and Ferritin and incubated overnight (Materials and Methods sections 2.2.12 and 2.2.13). 100µg protein lysate was loaded into each well of a 10% SDS-PAGE gel. Figures 5.3 and 5.4 outline the results of protein and mRNA analysis of iron homeostasis markers. Densitometry analysis of results was normalised to 1 against the control sample and blots were repeated at twice where possible. Ferritin repeated once due to limited antibody supply. The IRP1 antibody produced a second non-specific band beneath the

expected IRP1 protein size in DLD-1 cells that may represent alternative isoforms and was excluded from densitometry analysis.

IRP1 protein expression was reduced in both DLD-1 and SW480 *FBXL5* KO (Figure 5.3 A and B). We were unable to probe IRP2 protein expression due to lack of antibody. TfR protein expression was slightly reduced in DLD-1 *FBXL5* KO cells while increased in SW480 *FBXL5* KO cells (Figure 5.3C). Ferritin protein expression was slightly reduced in both cell lines (Figure 5.3D) (DLD-1 KO expression change vs control: IRP1 0.54x, TfR 0.77x, Ferritin 0.68x. SW480 KO expression change vs control: IRP1 0.24x, TfR 1.53x, Ferritin 0.87x). As both TFR and Ferritin expression changes were so slight, they require further validation to account for experimental variance.

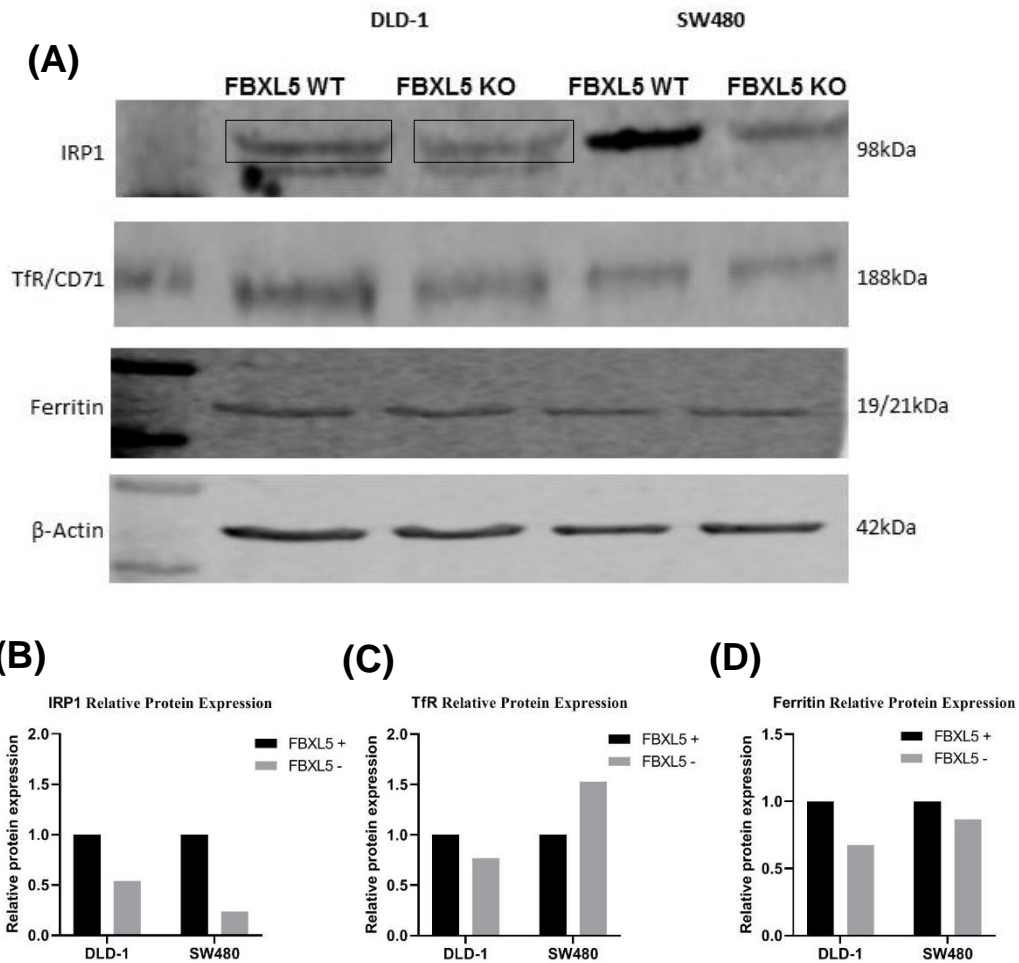


Figure 5.3: FBXL5 knockout significant affects iron homeostasis marker protein expression in DLD1 and SW480 cells.

IRP1 (B) and Ferritin (D) protein expression may be reduced in both cell lines, but TfR (C) may be reduced in DLD-1 cells and increased in SW480 cells, implying cell-specific FBXL5 activity. IRP1 (1:1000), TfR (1:250) and Ferritin (1:1000) with overnight incubation. 100 μ g protein lysate was loaded into each well of 10% SDS-PAGE gel and repeated. Densitometry analysis of results was normalised to 1 against the control sample from two repeated WB where antibody was available. Error bars represent standard deviation.

IRP1 mRNA expression was downregulated in SW480 (Figure 5.4A) but unaffected in DLD-1 cells (DLD-1 $P = 0.72$, SW480 $P = 0.0079$). *IRP2* mRNA was downregulated in DLD-1 *FBXL5* KO cells (Figure 5.4B) (DLD-1 $P = 0.012$, SW480 $P = 0.9$). *TfR* mRNA expression was significantly increased in SW480 *FBXL5* KO cells (Figure 5.4C, DLD-1 $P = >0.99$, SW480 $P = 0.0135$). *Ferritin Light* and *Heavy* chain mRNA expression were significantly downregulated and upregulated respectively in both cell lines (Figure 5.4D and E, *Ferritin L* (DLD-1 $P = <0.0001$, SW480 $P = <0.0001$) and *Ferritin H* (DLD-1 $P = <0.0001$, SW480 $P = <0.0001$)).

The reduction in overall Ferritin protein expression but alternate dysregulation of Light and Heavy chain mRNA expression in both cell lines also implies dysregulation of labile iron pool activity that may affect redox-active iron (Fe^{2+}) levels within *FBXL5* KO cells, as demonstrated by Calcein AM staining results (Figure 5.1) which indirectly measured dysregulation of cellular iron. This reduction of labile iron may have downstream effects on other pathways and processes affected by *FBXL5* KO. These results further imply that *FBXL5* has a regulatory role in *IRP1* and *IRP2* mRNA and protein expression, possibly in a cell-specific manner, thereby affecting immediate downstream targets *TfR* and *Ferritin* in a cell, however as the difference in protein expression was very small, it requires further validation.

Cell-specific differences in results may be explained by differing *p53* expression between DLD-1 and SW480 cells (Materials and Methods section 2.1.1). *p53* is associated with dysregulation of iron homeostasis by modulation of HAMP (Hepcidin Antimicrobial Peptide) (Weizer-Stern et al., 2007), ISCU (Iron Sulphur Cluster Assembly Enzyme) (Funauchi et al., 2015) and *Ferritin* and *TfR* expression in a cell-specific manner and may therefore be affected by *FBXL5* KO via *PTEN-p53* expression (Phosphatase and Tensin homolog, deleted on chromosome 10) (Zhang et

al., 2008) (Faniello et al., 2008) .

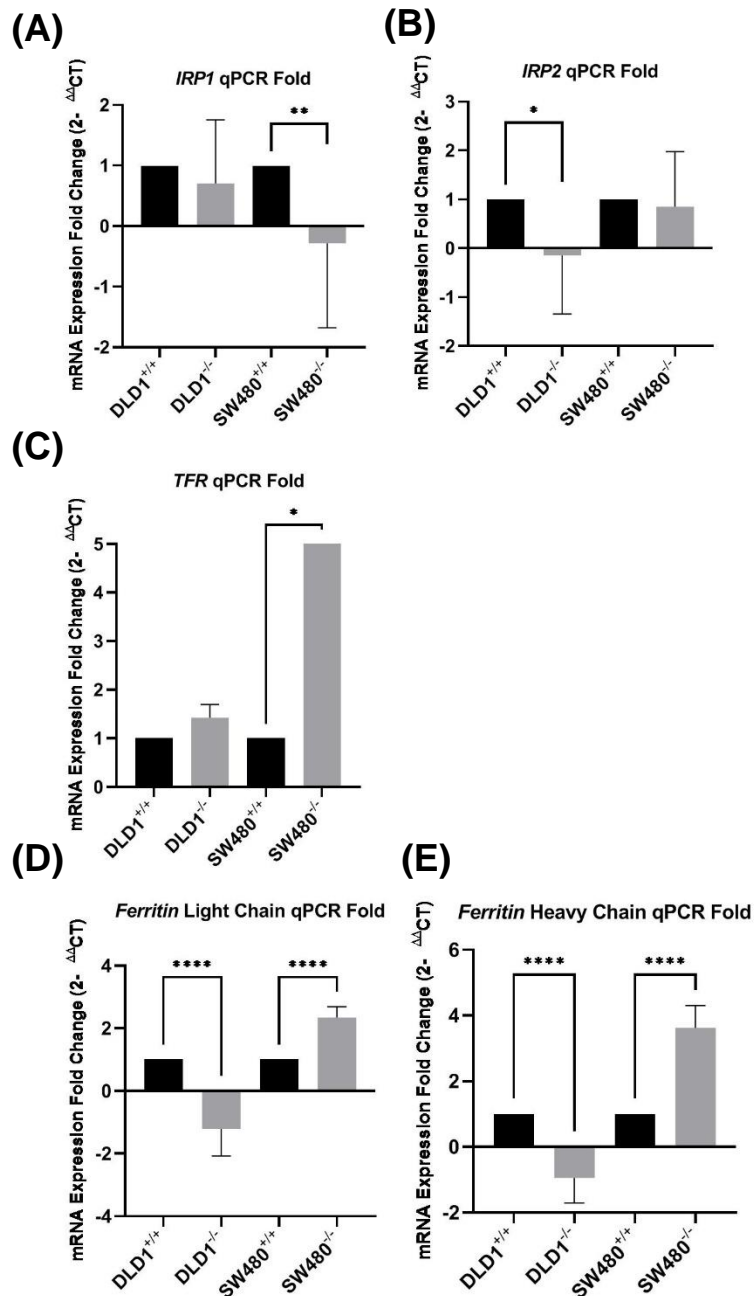


Figure 5.4: FBXL5 knockout significant affects iron homeostasis marker mRNA expression in DLD1 and SW480 cells.

IRP1 (A), *IRP2* (B), *TfR* (C) and *Ferritin Light & Heavy* (D and E) mRNA expression was significantly dysregulated in *FBXL5* KO cells in a cell-specific manner. This supports previous suggestions that *FBXL5* is required for *IRP2* functioning and an inverse correlation between *IRP1* and *IRP2* expression but does not support previous

data that FBXL5 ubiquitinates both IRP1 and IRP2. Assay was performed in triplicate and results normalised to 1 against the control sample. Error bars represent standard deviation P values = $P < 0.05$ (*), $P \leq 0.01$ (**), $P \leq 0.001$ (***), $P \leq 0.0001$ (****). *IRP1* (DLD-1 $P = 0.72$, SW480 $P = 0.0079$), *IRP2* (DLD-1 $P = 0.012$, SW480 $P = 0.9$), *TFR* (DLD-1 $P = >0.99$, SW480 $P = 0.0135$) *Ferritin L* (DLD-1 $P = <0.0001$, SW480 $P = <0.0001$) and *Ferritin H* (DLD-1 $P = <0.0001$, SW480 $P = <0.0001$).

5.1.1.4. *FBXL5* KO has significant impact on IRP downstream gene expression

As our previous results from this project demonstrated that *FBXL5* significantly affects primary iron homeostasis markers, we postulated that other downstream IRP1 or IRP2 targets might be similarly affected by *FBXL5* KO. As such, we selected six downstream genes, which were likely to have interactions with either iron homeostasis, IRP1, IRP2 or *FBXL5* regulators. Targets were chosen by a literature review of published research or predicted interactions using the STRING protein interaction database (Szklarczyk et al., 2019). STRING analysis was performed as described in Results section 6.1.1, with the highest confidence interaction (0.9) and including 10 closest direct or indirect interaction nodes. We used RT-qPCR and western blot analysis when possible, for downstream genes: *ALDH3B1*, *APP*, *RBCK1*, *VHL*, *GLRX5* and *YBX-1*.

ALDH3B1 (Aldehyde Dehydrogenase 3 member B1) is a detoxification isozyme that may assist with alcohol metabolism, is associated with schizophrenia (Marchitti et al., 2007) and may be a novel CRC biomarker (Matsumoto et al., 2017). *APP* (Amyloid precursor protein) is the pre-metabolised form β -amyloid peptide found in Alzheimer's Disease patients, stabilises the iron export protein ferroportin (FPN) and is regulated

by IRP1 and 2 (O'Brien and Wong, 2011). *RBCK1* (RanBP-type C3HC4-type zinc finger containing protein 1) is an E3 ligase that interacts with oxidised *IRP2* (Yamanaka et al., 2003) in addition to *TAB2/IRF3* (Toll-like receptor 3 and Interferon regulatory transcription factor 3), both important transcription regulators in innate immunity, and Wnt signalling via OTULIN complex (Yamanaka et al., 2003). *RBCK1* also contributes to chemoresistance and stemness in CRC (Liu et al., 2019d). *VHL* (Von Hippel-Lindau tumour suppressor) is a noted tumour suppressor and synonymous with the cancer Von Hippel-Lindau Syndrome, partially induces *HIF-1 α* expression, recruits E3 ligases to several HIF proteins and reduces labile iron concentration in renal cancer (Zhang et al., 2014) (Alberghini et al., 2005). *GLRX5* (Glutaredoxin 5) is related to the formation of iron sulphur clusters and some types of anaemia and encephalopathy (Baker et al., 2013). *YBX-1* (Y-Box binding protein 1) is an oncogene related to PI3K/AKT signalling but has no known interactions with *FBXL5* or iron homeostasis (Sinnberg et al., 2012).

100 μ g protein lysate was loaded into each well of 10% SDS-PAGE gel and densitometry analysis of results was normalised to 1 against the control sample (Materials and Methods sections 2.2.12 and 2.2.13) (*RBCK1* 1:1000, *VHL* 1:1000). Due to the limited quantity of antibody available in the lab, *RBCK1* and *VHL* blots were repeated once.

Figures 5.5 and 5.6 show that interestingly, *FBXL5* KO has a notable regulatory effect on all six chosen targets in one or both CRC cell lines analysed. *RBCK1* protein expression was slightly elevated in both cell lines (Figure 5.5A and B, DLD-1 KO expression change vs control: *RBCK1* 1.65x, *VHL* 0.83x, SW480 KO expression change vs control: *RBCK1* 1.24x, *VHL* 1.3x). *VHL* protein expression (Figure 5.5A

and C) may be slightly downregulated in both cell lines, however this difference was difficult to detect and requires further confirmation.

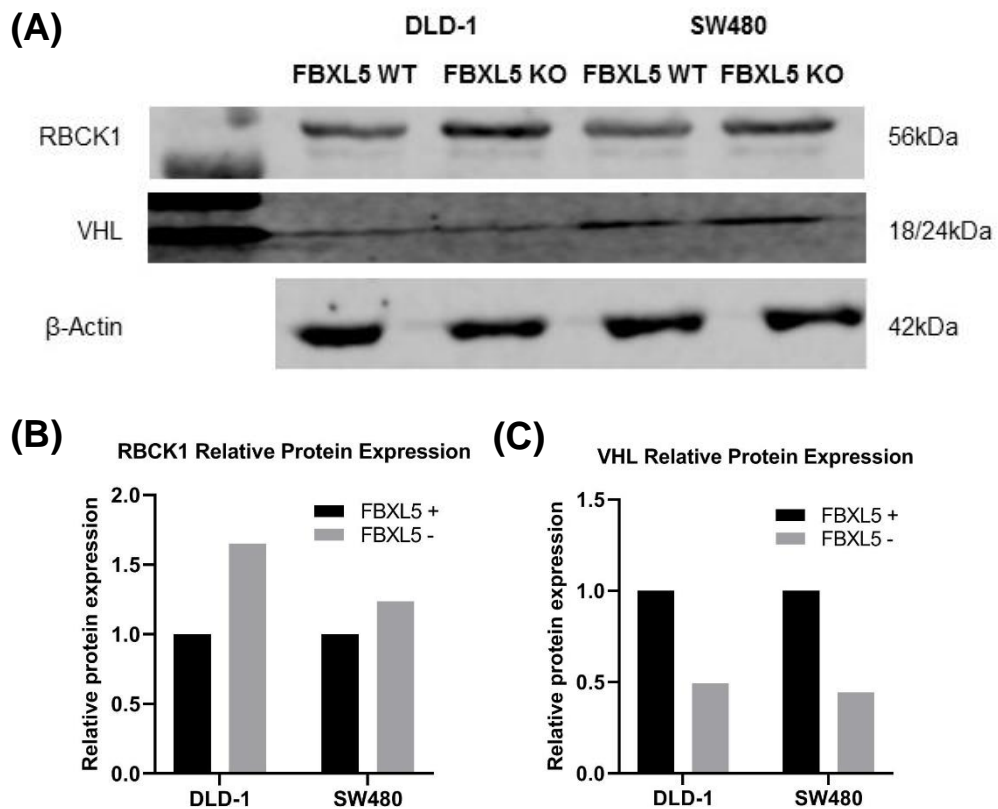


Figure 5.5: FBXL5 knockout significant dysregulates downstream iron homeostasis marker protein expression.

DLD-1 and SW480 cells were analysed for RBCK1 and VHL protein and RT-qPCR expression (A) RBCK1 protein expression (B) was upregulated and VHL protein (C) may be downregulated in both cell lines. 100 μ g protein lysate was loaded into each well of 10% SDS-PAGE gel and densitometry analysis of results was normalised to 1 against the control sample. Western blot was repeated once due to limited antibody.

Furthermore, *RBCK1* mRNA expression was significantly downregulated in DLD-1 FBXL5 KO cells (Figure 5.6A) (*RBCK1* mRNA expression DLD-1 $P = 0.0003$, SW480 $P = 0.9444$). The *VHL* gene expression was upregulated in DLD-1 KO cells but not in SW480 KO (Figure 5.6B, *VHL* mRNA expression DLD-1 $P = 0.0094$, SW480 $P = 0.9166$). The *ALDH3B1* mRNA was significantly reduced in SW480 KO cells (Figure 5.6C DLD-1 $P = 0.358$, SW480 $P = <0.0001$). The *APP* mRNA downregulated in DLD-1 but upregulated in SW480 cells (Figure 5.6D, DLD-1 $P = <0.0001$, SW480 $P = <0.0001$), *GLRX5* mRNA downregulated in DLD-1 (Figure 5.6E, DLD-1 $P = <0.0001$, SW480 $P = <0.974$), and *YBX-1* mRNA downregulated in both cell lines (Figure 5.6F, DLD-1 $P = 0.033$, SW480 $P = <0.0001$).

The precise mechanism by which FBXL5 regulates these downstream genes is unknown, although several have ties that suggest a role in iron homeostasis and signalling. For examples, RBCK1's role as E3 ligase interactor with IRP2 (Yamanaka et al., 2003), VHL's correlation with reduced labile iron pool in renal cancer cells (Alberghini et al., 2005), *GLRX5*'s potential role in iron sulphur cluster formation (Baker et al., 2013) and *YBX-1*'s interactions with PI3K/AKT signalling may all explain dysregulation due to *FBXL5* KO (Sinnberg et al., 2012). However, *ALDH3B1* interactions with either iron homeostasis or any FBXL5 substrate are unknown (Marchitti et al., 2007) and therefore alterations in mRNA expression due to *FBXL5* KO require further investigation.

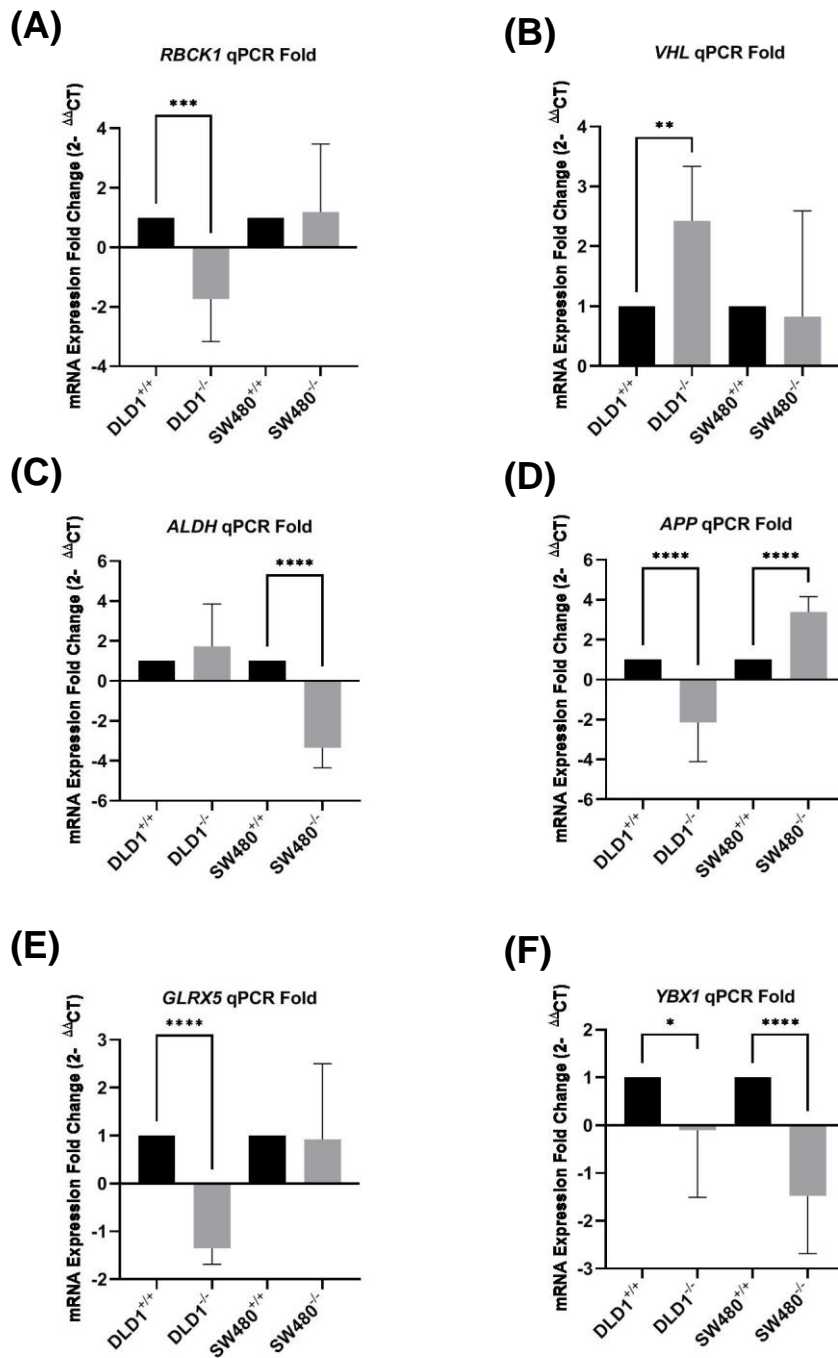


Figure 5.6: FBXL5 knockout significant affects iron homeostasis downstream marker mRNA expression.

DLD-1 and SW480 cells were analysed for mRNA expression of IRE downstream targets, finding that *RBCK1* (A), *VHL* (B) *ALDH* (C), *APP* (D), *GLRX5* (E) and *YBX1* (F) were significantly dysregulated in a cell-specific manner in response to *FBXL5*

KO. Error bars represent standard deviation. RT-qPCR assay was performed in triplicate and result normalised to control for comparison. Error bars represent standard deviation P values = $P < 0.05$ (*), $P \leq 0.01$ (**), $P \leq 0.001$ (***), RT-qPCR assay was repeated twice.

5.1.2. The role of FBXL5 in regulation of Autophagy

Autophagy regulates protein and cellular homeostasis by degradation of both long-lived and larger proteins in addition to dysfunctional, excess, or damaged cellular organelles (Galluzzi et al., 2015). Autophagy initially suppresses tumour growth by regulating cell homeostasis. However, autophagy also encourages cell survival under conditions typically found in tumours such as hypoxia, necrosis and nutrient deficiency, therefore acts simultaneously as a tumour suppressive and oncogenic process (Galluzzi et al., 2015). Autophagy functions by engulfing targeted debris in a phagosomal membrane and degrading the encapsulated detritus by the lysosome (Wirawan et al., 2012). The initiation, elongation and maturation of the phagosomal membrane is partially regulated by the *ATG5* (Autophagy Related Gene 5), *LC3B* (Microtubule-associated protein 1A/1B light chain 3B) and *Beclin1* genes (Nishida et al., 2009) (Ji and Kwon, 2017). These three markers were selected to evaluate the possible impact of FBXL5 on autophagy in colorectal cancer cells.

There are over 40 ATG genes, with ATG5 being critical to developing the phagophore membrane and LC3 pathway activation, although ATG5-independent autophagy has recently been demonstrated (Nishida et al., 2009). Depletion of ATG5 protein produces cancer-cell behaviour, with ATG5 negative mice developing benign tumours

and the suppression of autophagy, but overexpression of ATG5 increasing mouse lifespan (Nishida et al., 2009).

The precise role of LC3B is unclear in autophagy, with LC3B-negative mice developing normally (Bai et al., 2012). It is suggested that LC3B is the master regulator of the LC3 family in autophagy, having a role in post-transcriptional modification (Runwal et al., 2019). LC3B is required for ATG5/7 dependent autophagy (Runwal et al., 2019).

Beclin1 regulates and forms complexes with VPS-34 to induce autophagy and is required for both ATG5/7 dependent and independent autophagy (Galluzzi et al., 2015). Beclin1 dysregulation is found reduced in breast, prostate and ovarian cancer, as well as schizophrenia (Galluzzi et al., 2015), making Beclin1 a likely tumour suppressor (Galluzzi et al., 2015). Knockout of Beclin1 completely disables autophagy and is embryonically lethal to mice (Parzych and Klionsky, 2014). However, Beclin1 heterozygous mice develop lymphomas and liver and lung carcinoma (Galluzzi et al., 2015).

While FBXL5 currently has no published role in autophagy, autophagy and the UPS have multiple known interactions (Brown and Kaganovich, 2016). Autophagy is associated with several F-box proteins, for example including FBXW5 and UDR131C (Jeong et al., 2018; Shoket et al., 2020) and wider UPS interconnectivity (Ji and Kwon, 2017). Several FBXL5 substrates have indirect interactions with autophagy mechanisms, including Ferritin via NCO14 (nuclear receptor coactivator 4) and mTOR (Santana-Codina and Mancias, 2018; Yao et al., 2018). The UPS and autophagy have numerous interactions (Ji and Kwon, 2017), therefore FBXL5 as an E3 ligase may also have a role.

5.1.2.1. Western Blot and RT-qPCR analysis of FBXL5 KO DLD-1 and SW480 cells finds significant dysregulation of autophagy markers.

DLD-1 and SW480 cells were lysed for cellular protein and probed using SDS-PAGE Western Blot analysis for expression of ATG5 (1:500), LC3B (1:500) and Beclin1 (1:500) and incubated overnight. Western blots were repeated twice with 100 μ g protein lysate loaded into each well of 10% SDS-PAGE gel and densitometry analysis of results was normalised to 1 against the control sample (Materials and Methods sections 2.2.12 and 2.2.13). The ATG5 antibody identified both full-length and cleaved ATG5 forms and both were included in densitometry analysis (Besirli et al., 2011). The full-length ATG5 is critical for autophagosome formation (Besirli et al., 2011) and cleaved form may be associated with apoptosis (Yousefi et al., 2006).

Results shown in Figure 5.7 and Figure 5.8 indicate that loss of FBXL5 may have different impacts with ATG5, LC3B, and Beclin1 in both protein (Figure 5.7) and mRNA (Figure 5.8). Both full-length and cleaved ATG5 protein are upregulated in DLD-1 *FBXL5* KO but downregulated in SW480 (Figure 5.7A). LC3B protein is slightly upregulated in DLD-1 *FBXL5* KO and downregulated in SW480 KO, but this does not appear to be a substantial difference and requires further validation (Figure 5.7B). Finally, Beclin1 protein expression may be downregulated in both DLD-1 and SW480 *FBXL5* KO (Figure 5.7C). (Figure 5.7A-C, DLD-1 KO expression change vs control: ATG5 1.34x, LC3B 1.12x, Beclin1 0.95x, SW480 KO fold change from control ATG5 0.57x, LC3B 0.96x, Beclin1 0.74x)

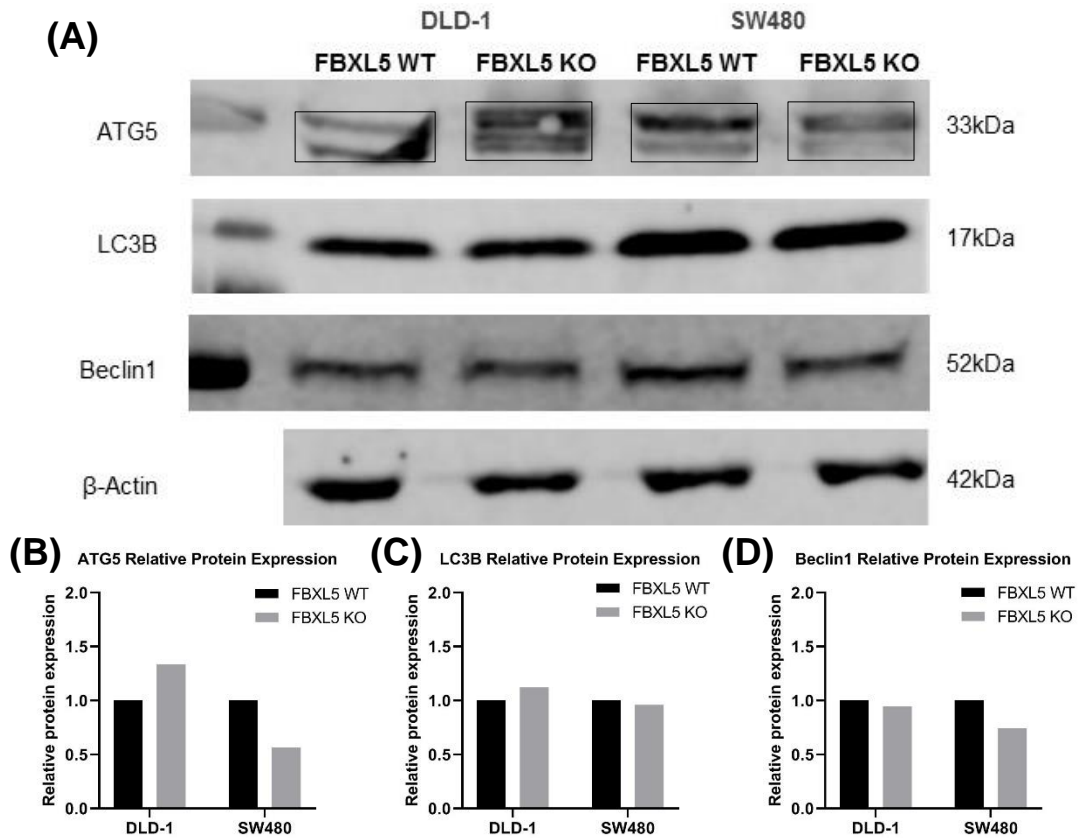


Figure 5.7: Western Blot and Densitometry of *ATG5*, *LC3B* and *Beclin1* expression in DLD-1 and SW480 cells.

(A) Western Blot and densitometry results of *ATG5* (B), *LC3B* (C) and *Beclin1* (D) probing. 100 μ g protein lysate was loaded into each well of 10% SDS-PAGE gel and densitometry analysis of results was normalised to 1 against the control sample. Blots were repeated twice.

ATG5 mRNA expression was downregulated in DLD-1 KO and SW480 KO cells (Figure 5.8A). However, *LC3B* mRNA expression is significantly downregulated in DLD-1 *FBXL5* KO cells and unaffected in SW480 KO (Figure 5.8B). Finally, *Beclin1* mRNA expression is downregulated in DLD-1 *FBXL5* KO but upregulated in SW480

(Figure 5.8C), (*ATG5* (DLD-1 $P = 0.002$, SW480 $P = 0.013$), *LC3B* (DLD-1 $P = < 0.0001$, SW480 $P = 0.510$), *Beclin1* (DLD-1 $P = 0.0007$, SW480 $P = 0.0036$))

These differences in expression suggest that FBXL5 has multiple regulatory roles in ATG5-dependent autophagy, although further studies are required to explore FBXL5 knockout significance in ATG5-mediated autophagy. As ATG5, LC3B and Beclin1 activate different pathways of phagophore development and form complexes in ATG5-dependent autophagy (Galluzzi et al., 2015; Nishida et al., 2009), FBXL5 may ubiquitinate these substrates at different rates or in tandem with other pathways or ligases, potentially regulating each substrate interdependently. Loss of FBXL5 expression therefore may dysregulate autophagy in a phase or pathway-specific manner.

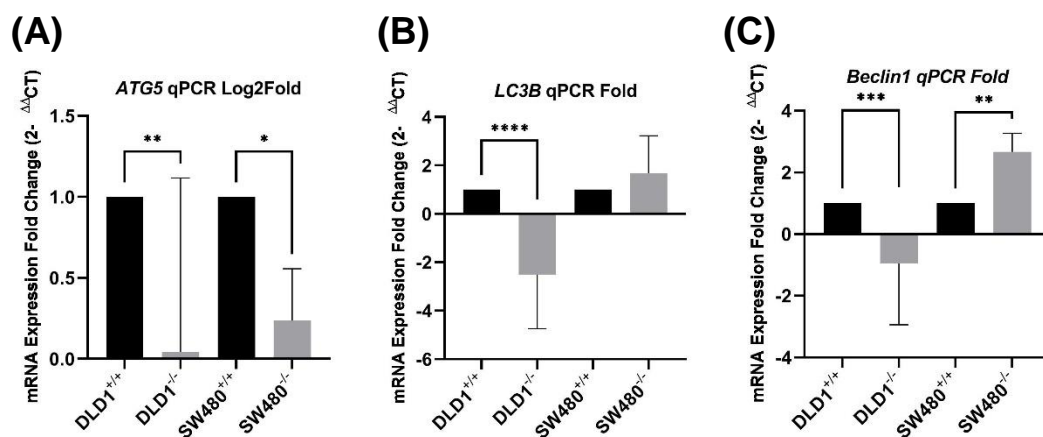


Figure 5.8: RT-qPCR analysis of *ATG5*, *LC3B* and *Beclin1* expression in DLD-1 and SW480 cells.

ATG5 (A) mRNA expression were significantly dysregulated in *FBXL5* KO, while LC3B (B) and Beclin1 (C) mRNA expression were dysregulated in a cell-specific manner, suggesting divergent roles for FBXL5 in different autophagy pathways. RT-qPCR assay was performed in triplicate and result normalised to 1 for comparison. P

values = $P < 0.05$ (*), $P \leq 0.01$ (**), $P \leq 0.001$ (***), $P \leq 0.0001$ (****). Assay was repeated once

5.1.3. The role of FBXL5 in Hypoxia

Hypoxia in late stage tumour growth is common, with tumour mass outgrowing vascularisation, thereby limiting blood flow and oxygen availability to cancerous tissues (Wouters and Koritzinsky, 2008). Hypoxic conditions alter cell metabolism and behaviour, typically reducing cell proliferation/population increase and inducing quiescence, limiting the effect of many chemotherapeutic methods reliant on cell cycle-mediated interaction (Muz et al., 2015).

FBXL5 expression is inversely correlated to CITED2, a HIF-1 α inhibitor (Machado-Oliveira et al., 2015a). Increased CITED2 levels cause decreased HIF-1 α expression, thereby reducing hypoxic response in cells (Yin et al., 2002). According to the only published study on this interaction: downregulation of FBXL5 expression may cause upregulation in CITED2, in turn downregulating HIF-1 α and suppressing hypoxic factors such as VEGF (vascular endothelial growth factor 1), GLUT1 and PGK1 (phosphoglycerate kinase 1) (Machado-Oliveira et al., 2015a).

Other F-box associated with hypoxia include FBXL14, which is potentially downregulated by hypoxia in mouse cell lines (Viñas-Castells et al., 2010) and both FBXW7 and FBX011 partially regulate HIF-1 α (Ju et al., 2015) (Cassavaugh et al., 2011). Despite FBXL5's real-time oxygen sensing hemerythrin-like domain and instability during low iron and low oxygen environments, FBXL5's precise role in hypoxia requires further investigation (Shu et al., 2012) (Wang et al., 2020a).

To determine whether *FBXL5* has any role in colorectal cancer cell growth under either normoxic or hypoxic conditions, we utilised the clonogenic assay. In addition, we intend to explore the role of *FBXL5* in hypoxia in colorectal cancer by quantifying RNA expression of hypoxia/vascularisation markers *HIF-1 α* , *VEGF*, *CA9* and *ANGPTL4* in both normoxic and hypoxic cells.

5.1.3.1. Colony Formation Efficiency assay shows significant impact of *FBXL5* KO under normoxic and hypoxic conditions

DLD-1 and SW480 WT and *FBXL5* KO cells were seeded to T75 flasks in triplicate at 500 cells/flask with 15 ml complete growth media and incubated at 37°C for 4 hours, after which hypoxia flasks were transferred to 1% oxygen conditions to trigger a hypoxic state (Materials and Methods sections 2.2.2). Normoxia flasks were incubated under standard culture conditions for 14 days. Hypoxia flasks remained at 1% oxygen conditions for 72 hours, after which they were returned to standard normoxia conditions for a further 11 days (14 days total incubation). After 14 days, media was carefully removed, and flasks washed with PBS. Flasks were subsequently fixed with 4% PFA and stained with Crystal Violet as outlined in Materials and Methods section 2.2.2. The colonies were counted and analysed using Microsoft Excel and Graphpad PRISM. The normoxia assay was repeated twice for accuracy, but due to COVID lockdown we were unable to repeat the hypoxia assay.

As shown in Figure 5.9, in DLD-1, there was no significant difference in number of colonies between control and *FBXL5* KO cells in normoxia, however there was a significant difference in control vs KO, normoxia control vs hypoxia control and hypoxia control vs hypoxia KO. In contrast, SW480 *FBXL5* cells showed a significant reduction in number of colonies in both normoxia and hypoxia, with similar significant

reductions to DLD-1 cells. (Figure 5.9, average number of colonies DLD-1 WT-Nor: 194, WT-Hyp: 74.3, KO-Nor 206.6, KO-Hyp 11.3, SW480 WT-Nor 53.6, WT-Hyp 6.3, KO-Nor 18.6, KO-Hyp 0.3). (DLD-1 (+/+ Nor vs -/- Nor $P = 0.49$, +/+ Nor vs -/- Hyp $P = 0.0008$, +/+ Nor vs +/+ Hyp $P = 0.0008$, -/- Nor vs -/- Hyp $P = <0.0001$) (SW480 (+/+ Nor vs -/- Nor $P = 0.0005$, +/+ Nor vs -/- Hyp $P = 0.0002$, +/+ Nor vs +/+ Hyp $P = <0.0001$, -/- Nor vs -/- Hyp $P = <0.0005$).

DLD-1 control and FBXL5 knockout colony size was significantly reduced in hypoxia (Figure 5.10A, average colony diameter DLD-1 WTN 1.18mm, WTH 0.7mm, KON 1.26mm, KOH 0.53mm) (DLD-1 (+/+ Nor vs +/+ Hyp $P = <0.0001$, -/- Nor vs -/- Hyp $P = <0.0001$). No significance difference in colony size was found in SW480 cells (Figure 5.10B, average colony diameter SW480 WTN 0.93mm, WTH 0.55mm, KON 0.9mm, KOH N/A). Due to the complete lack of visible colonies in SW480 *FBXL5* KO cells under hypoxic conditions, we can conclude that cell survival of seeded single cells are most significantly affected by hypoxic conditions.

This result supports previous findings that *FBXL5* expression may be destabilised in oxygen-depleted environments (Chollangi et al., 2012) and provides new evidence that *FBXL5* may affect colony formation efficiency at both normoxic and hypoxia conditions in a cell-specific manner. *FBXL5* interactions with EMT, mTOR and PI3K/AKT signalling may explain the reduction in colony number efficiency (Fokas et al., 2012; Kong et al., 2010). EMT, mTOR and PI3K/AKT are also affected by hypoxic conditions, with hypoxia-induced EMT and hypoxia-activated PI3K/AKT found in human cancer cells (Hapke and Haake, 2020) (Liu et al., 2019a). mTOR also has oxygen sensitive signalling pathways (Wouters and Koritzinsky, 2008). SNAIL dysregulation in DLD-1 cells may also cause cell-specific differences found in this assay (Wu et al., 2015b). *FBXL5* inverse correlation with *CITED2* which in turn

negatively regulates HIF-1 α may also contribute to hypoxia results (Machado-Oliveira et al., 2015a).

As shown in Figure 5.11, *FBXL5* KO reduced *HIF-1 α* expression in normoxia in both DLD-1 and SW480 cells, although this downregulation was reversed in DLD-1 *FBXL5* KO cells at hypoxic conditions. Additionally, multiple other hypoxia regulators and markers were dysregulated by *FBXL5* KO, likely contributing to these results.

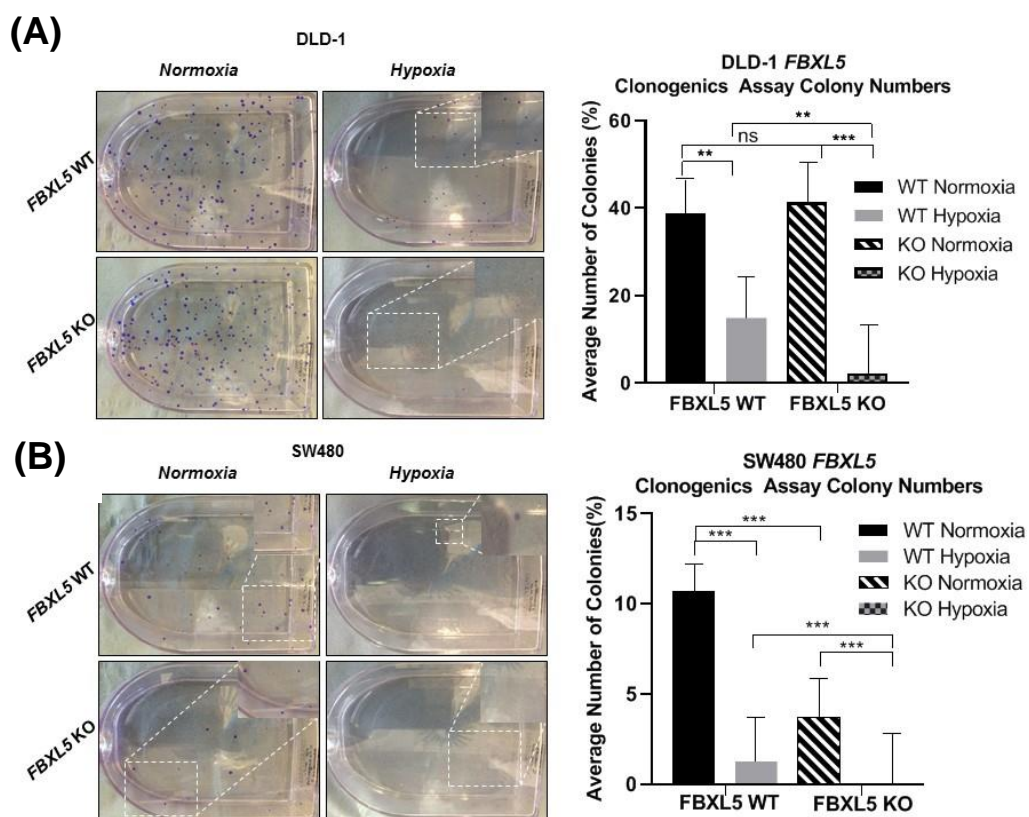


Figure 5.9: Colony Formation Efficacy Assay of DLD-1 and SW480 *FBXL5* KO cells shows significantly reduced colony number in SW480 cells at normoxia but in both cell lines at hypoxia.

Cells were seeded to T75 flasks in triplicate and incubated at 1% oxygen for 72 hours and standard cell culture conditions for a further 11 days (14 days total). Flasks were fixed with 4% PFA, stained with 0.4% crystal violet and colonies counted. (A) DLD-1 colony numbers were not significantly different between control and KO flasks at

normoxia, but both control and KO numbers were reduced in hypoxic conditions. (B) *FBXL5* KO affected SW480 colony numbers at both normoxia and hypoxic conditions. Average number of colonies DLD-1 WT-Nor: 194, WT-Hyp: 74.3, KO-Nor 206.6, KO-Hyp 11.3, SW480 WT-Nor 53.6, WT-Hyp 6.3, KO-Nor 18.6, KO-Hyp 0.3. Error bars represent standard deviation. *P* values = $P < 0.05$ (*), $P \leq 0.01$ (**), $P \leq 0.001$ (***). Normoxia flasks were repeated three times, hypoxia flasks were repeated once.

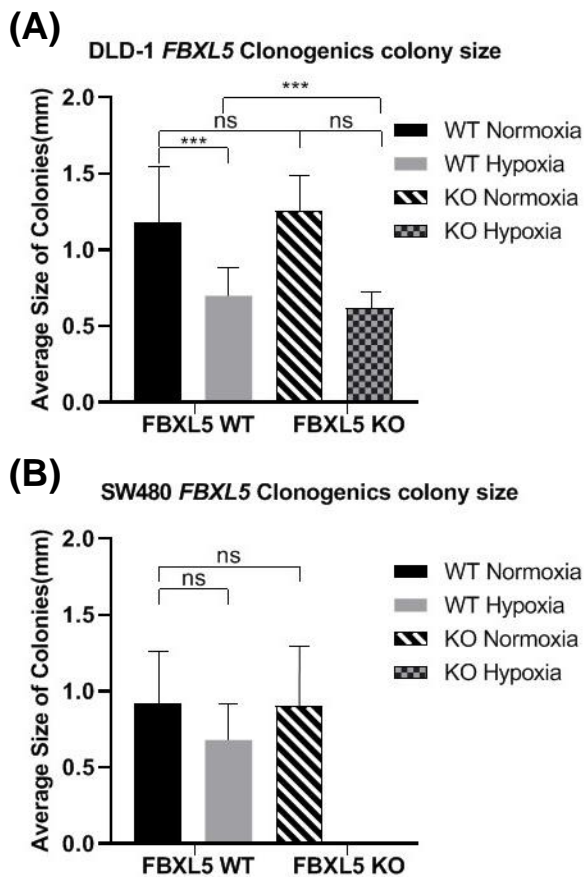


Figure 5.10: Colony size in Colony Formation Assay of DLD-1 and SW480 *FBXL5* KO cells shows significant changes to DLD-1 cell colonies.

Colony size analysis shows that DLD-1 control and *FBXL5* KO colony size was reduced by hypoxia, but more greatly reduced in *FBXL5* KO cells, whereas no effect was observed in SW480 cells. SW480 *FBXL5* KO sample had no colonies. Average colony diameter DLD-1 WTN 1.18mm, WTH 0.7mm, KON 1.26mm, KOH 0.53mm,

SW480 WTN 0.93mm, WTH 0.55mm, KON 0.9mm, KOH N/A. Error bars represent standard deviation (P values = $P < 0.05$ (*), $P \leq 0.01$ (**), $P \leq 0.001$ (***)). Average number of colonies DLD-1 WT-Nor: 194, WT-Hyp: 74.3, KO-Nor 206.6, KO-Hyp 11.3, SW480 WT-Nor 53.6, WT-Hyp 6.3, KO-Nor 18.6, KO-Hyp 0.3.

5.1.3.2. RT-qPCR analysis of *FBXL5* KO DLD-1 and SW480

Cas-9 expressing cells shows significant effects on hypoxia markers.

To further elaborate on hypoxia pathways in CRC impacted by *FBXL5* KO, expression of common hypoxia markers *HIF-1 α* , *HIF2 α* , *CA9*, *VEGFR2* and *ANGPTL4* in DLD-1 and SW480 *FBXL5* KO cells was examined using RT-qPCR analysis (Materials and Methods sections 2.2.13).

HIF-1 α and HIF2 α are master regulators of the hypoxia response in tissues and involved in numerous pathways in cancer, particularly tumorigenesis and angiogenesis under hypoxic conditions functions (Morris et al., 2009) (Kubaichuk and Kietzmann, 2019). Both bind to hypoxia responsive elements (HRE's). However, their effects on some genes is varied, with a highly complex inter-relationship between the two in hypoxia pathway response (Loboda et al., 2010). CA9 (Carbonic anhydrase 9) enzymes catalyse CO₂/H₂O reaction to CO₂ transport and is overexpressed in cancerous cells to compensate for abnormal vasculature and increased metabolic activity (Olive et al., 2001). CA9 expression is induced under hypoxic conditions and primarily regulated by HIF-1 α (Pastorekova and Gillies, 2019). VEGFR2 (Vascular Endothelial Growth Factor 2) is a primary angiogenesis regulator that is overexpressed in both hypoxic and tumour conditions and may competitively regulate HIF-1 α (Li et al., 2019a). ANGPTL4 (Angiopoietin-like 4) is induced at hypoxia and modulates

vascularisation among other processes and may be regulated by HIF-1 α in some cancer cell lines (Kubo et al., 2016) (Zhang et al., 2011).

To quantify changes to mRNA expression in *FBXL5* KO cells in normoxia and hypoxia, cells were seeded to 10cm dishes for mRNA extraction and lysed with TRIzol buffer while incubated at either normal cell culture conditions or at 1% oxygen to preserve the hypoxic condition of cells. Once lysed, RNA isolation and reverse transcription were continued at normoxic conditions as previously outlined (Materials and Methods section 2.2.13).

RT-qPCR analysis of hypoxia markers confirms the initial hypothesis that *FBXL5* KO dysregulates *HIF-1 α* expression in CRC in a cell-specific manner, with DLD-1 *HIF-1 α* and *HIF2 α* expression significantly upregulated in KO hypoxia more than either KO normoxic or WT hypoxic conditions (Figure 5.11 A and C). *HIF-1 α* and *HIF2 α* were both downregulated in SW480 KO cells at normoxia and hypoxia (Figure 5.11 B and D). *CA9* is normally upregulated in hypoxic conditions, however *CA9* mRNA expression was downregulated in DLD-1 and SW480 *FBXL5* KO normoxia and hypoxia cells (Figure 5.11 E and F). *VEGFR2* was also upregulated in DLD-1 and SW480 KO normoxic and hypoxic cells (Figure 5.11 G and H). *ANGPTL4* expression was significantly upregulated in both cell lines at normoxia and hypoxia (Figure 5.11 I and J). *HIF-1 α* : (DLD-1 $+/+$ Nor vs $-/-$ Nor $P = < 0.0001$, $-/-$ Nor vs $-/-$ Hyp $P = < 0.0001$), (SW480 $+/+$ Nor vs $-/-$ Nor $P = < 0.0001$, $+/+$ Hyp vs $-/-$ Hyp $P = < 0.0001$), *HIF2 α* : (DLD-1 $+/+$ Hyp vs $-/-$ Hyp $P = < 0.0001$, $-/-$ Nor vs $-/-$ Hyp $P = < 0.0001$), ($+/+$ Hyp vs $-/-$ Hyp $P = < 0.0055$, $-/-$ Nor vs $-/-$ Hyp $P = 0.041$), *CA9*: (DLD-1 $+/+$ Nor vs $-/-$ Nor $P = < 0.0001$, $+/+$ Hyp vs $-/-$ Hyp $P = < 0.0001$, $-/-$ Nor vs $-/-$ Hyp $P = < 0.0001$) (SW480 ($+/+$ Nor vs $-/-$ Nor $P = < 0.0001$, $+/+$ Hyp vs $-/-$ Hyp $P = < 0.0001$), $-/-$ Nor vs $-/-$ Hyp $P = < 0.0001$), *VEGFR2*: (DLD-1 $+/+$ Nor vs $-/-$ Nor $P = < 0.0001$,

+/+ Hyp vs -/- Hyp $P = <0.0001$, -/- Nor vs -/- Hyp $P = 0.0217$), (SW480 +/+ Nor vs -/- Nor $P = <0.0001$, +/+ Hyp vs -/- Hyp $P = <0.0001$), *ANGPTL4*: (DLD-1 +/+ Nor vs -/- Nor $P = <0.0001$, +/+ Hyp vs -/- Hyp $P = <0.0001$), (SW480 +/+ Nor vs -/- Nor $P = <0.0001$, +/+ Hyp vs -/- Hyp $P = <0.0001$, -/- Nor vs -/- Hyp $P = 0.0105$)

The inverse correlation between *FBXL5* and *CITED2* leading to *HIF-1 α* upregulation was evident in DLD-1 cells but not SW480 cell mRNA expression (5.11 A and B). Transcriptional activity of *CA9* is primarily induced by *HIF-1 α* and *HIF-1 β* and expression correlated with *HIF-1 α* in SW480 cells as expected (Figure 5.11 B and F), but only in DLD-1 normoxia cells rather than hypoxic (Figure 5.11 A and E). Therefore, disruption of *HIF-1 α* activity by *FBXL5* KO likely caused downstream disruption to *CA9* (Kaluz et al., 2009). *VEGFR2* expression was significantly upregulated in both normoxia and hypoxia KO DLD-1 and SW480 cells (Figure 5.11 G and H). *VEGFR2* and *ANGPTL4* are typically upregulated in hypoxia, but the corresponding increase at normoxia in *FBXL5* KO cells was unexpected and suggests that *FBXL5* may have an important regulatory role in *VEGFR2* and *ANGPTL4* mRNA expression, although *ANGPTL4* mRNA expression varies greatly between CRC cancer lines (Kubo et al., 2016). *ANGPTL4* expression is regulated by *HIF-1 α* , however expression is not found to correlate in either DLD-1 or SW480 cells (Figure 5.11 I and J).

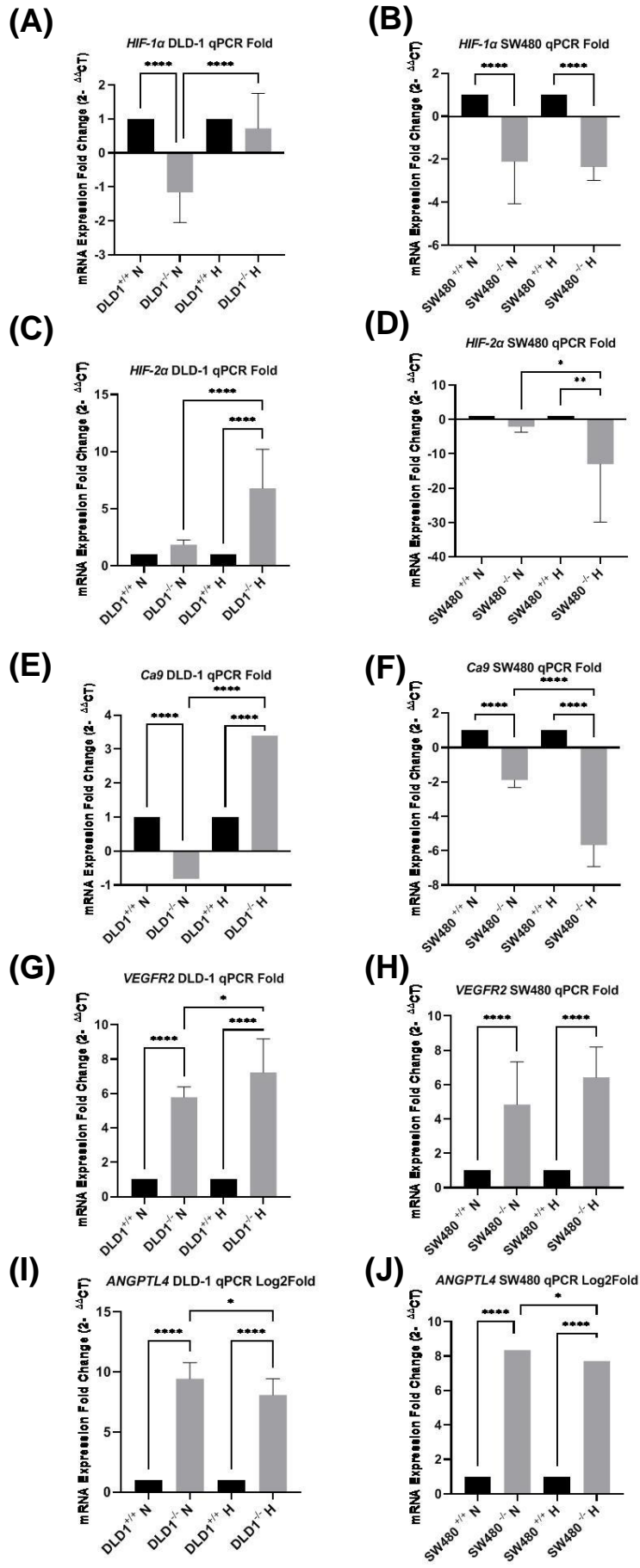


Figure 5.11: *FBXL5* KO significantly affects hypoxia marker RNA expression in colorectal cancer cells in both normoxia and hypoxia conditions.

RT-qPCR expression of common hypoxia markers is significantly affected by *FBXL5* KO across CRC cell lines. Significance was greater under hypoxic than normoxia conditions, further supporting previous evidence that *FBXL5* activity is affected by oxygen state. RT-qPCR analysis was performed in triplicate and result normalised to 1 for comparison. Error bars represent standard deviation P values = $P < 0.05$ (*), $P \leq 0.01$ (**), $P \leq 0.001$ (***), $P \leq 0.0001$ (****), assays were repeated twice.

5.1.4. The role of *FBXL5* in Drug Response

Drug resistance is a central characteristic of cancerous tissues (Fouad and Aanei, 2017). Chemotherapeutic compounds can interact with cells by varying mechanisms, suppressing proliferation, enzyme activity, genetic activity, or stimulating necrosis or apoptosis dependent on their function (Riddell, 2018). Abnormal cytotoxic response is typical in cancerous cells due to dysregulation of cell mechanisms, therefore investigation of cytotoxic response in potential oncogenic or tumour suppressive genes is important. In this study, we investigated the role of *FBXL5* in drug response to Oxaliplatin, Cisplatin, 5-FU, and Etoposide by cytotoxicity assay.

The UPS and other F-box ligases have previously been associated with drug resistance (Yan et al., 2020). Therefore, the potential impact of *FBXL5* on drug reactivity in cancer is an important consideration. Our group recently demonstrated that *FBXL5* KO stimulated sensitivity in CRC stem cells to AM404 (aka Acetaminophen), an anandamide uptake inhibitor and common antipyretic and antibacterial drug (Ctrl IC_{50} : 15.3 μ M vs *FBXL5* KO IC_{50} : 11.5 μ M) (Ahmed et al., 2019). AM404 was additionally

found to significantly reduce cell migration of DLD-1 cells, while *FBXL5* mRNA expression was significantly increased in AM404-treated colorectal cancer cells. *FBXL5* expression was also lower in normal/healthy tissues adjacent to CRC tumours than in the tumour itself (Ahmed et al., 2019).

To further examine the role of *FBXL5* colorectal cancer cell drug resistance, DLD-1 and SW480 *FBXL5* KO cells were treated separately with Oxaliplatin, Cisplatin, 5-FU and Etoposide. Oxaliplatin and Cisplatin are platinum-based chemotherapeutics that cause DNA crosslinking between non-adjacent nucleotides, inhibiting DNA repair and synthesis resulting in cell death (Riddell, 2018). Several mechanisms of action have been proposed for platinum-based chemotherapeutics (“platins”), including inhibition of DNA synthesis by interfering with translesion-synthesis polymerases, and transcription inhibition by arresting the cell cycle at G2/M, preventing continuation to mitosis (Riddell, 2018). Cisplatin-induced cell death is linked to *p53* activity via *PTEN* overexpression (Wu et al., 2016; Xiong et al., 2017).

FBXL5 depletion has previously been linked to RhoGDI2 (Rho GDP dissociation inhibitor 2)-induced Cisplatin resistance in gastric cancer cells but does not target RhoGDI2 for ubiquitination (Wu et al., 2016). RhoGDI2 is associated with colorectal tumour progresses and metastasis (Moon et al., 2010) and overexpression may cause depletion of *FBXL5* and increased Cisplatin (Wu et al., 2016) and 5-FU (Zheng et al., 2013) resistance in stomach cancer cells. *RhoGDI2* expression resulted in reduced *FBXL5* expression during Cisplatin treatment, but absence of *RhoGDI2* expression did not cause similar upregulation of *FBXL5* in Cisplatin treatment, therefore *RhoGDI2* may directly downregulate *FBXL5* expression (Wu et al., 2016; Xiong et al., 2017). As Cisplatin and Oxaliplatin share some mechanical interactions and pathways, *FBXL5* may have similar effects on both.

Fluoropyridines such as 5-Fluorouracil (5-FU) are anti-metabolite drugs that both inhibit DNA and RNA synthesis while also binding to DNA and RNA to impede their function (Longley et al., 2003). 5-FU is eventually metabolised to either fluorouridine triphosphate, which is incorporated into RNA and disrupts normal functioning, or into fluorodeoxyuridine diphosphate, which acts in the same manner on DNA (Longley et al., 2003). As with Oxaliplatin and Cisplatin: 5-FU sensitivity is highly dependent on *p53* activity, with *p53* downregulation causing 5-FU resistance, as the *p53*-mediated apoptosis caused by accumulated 5-FU DNA damage is prevented (Liang et al., 2002). Interestingly, several clinical studies have found *p53* overexpression caused similar resistance to 5-FU, although these finding may be explained by how *p53* overexpression not necessarily correlating with *TP53* mutation (Liang et al., 2002). *p38 MAPK* inhibition increases resistance to carboplatin in the same manner as Oxaliplatin and Cisplatin (Han et al., 2018).

Etoposide is a topoisomerase inhibitor chemotherapy agent, binding with topoisomerase II enzyme and preventing action to regulate DNA coiling, thereby inhibiting DNA synthesis and RNA transcription, leading to strand breaks and apoptosis (Montecucco et al., 2015). At high concentrations of Etoposide, cells are lysed upon entering mitoses, while at low concentrations cells are inhibited from entering prophase (Azarova et al., 2007; Zhou et al., 2001). Etoposide has noted interactions with both *p53*-mediated apoptosis and autophagy-mediated ATP production, with the nemo-like serine/threonine kinase (NLK) being required for *p53* activation only after Etoposide treatment (Fan et al., 2008). Suppression of NLK may increase sensitivity to Etoposide, although it is unclear whether this process modulates cell death or cell survival, or how FBXL5 may contribute (Dey et al., 2010; Fan et al., 2008).

5.1.4.1. *FBXL5* KO increases resistance to platinum-based chemotherapeutics in DLD-1 cells but reduced resistance in SW480 cells.

All IC₅₀ assays were performed as outlined in Materials and Methods section 2.2.14. In brief: 3,000 cells per well were seeded in triplicate on a 96 well plate in 200ul complete growth media. Plates were incubated under normal culture conditions for two days for attachment and resumption of proliferation. Complete growth media was replaced with media supplemented with drug dosage and incubated for a further 24-72 hours depending on experimental requirements. Media was then removed, wells washed and fixed with 15% trichloroacetic acid (TCA) for 60 minutes at 4°C. Wells were then washed with 200ul tap water, air dried for 1-2 hours at room temperature and cells stained with 0.4% Sulforhodamine B solution in 1% acetic acid for 20 minutes. Excess staining was removed by washing repeatedly with 1% acetic acid and the plate was air dried overnight at room temperature. The following day 200 µl 10mM Tris in dH₂O was added to each well and plate read at 492nm using a spectrophotometer.

Oxaliplatin treatment dosages: 0, 2, 4, 6, 8, 10, 12, 15, 20, 30µM/ ml, 72-hour treatment (Yang et al., 2016), Cisplatin treatment dosages: 0, 0.1, 1, 5, 10, 15, 20, 25, 30, 100µM/ ml, 72-hour treatment (Sun et al., 2018b), 5-FU treatment dosages: 0, 0.001, 0.1, 1, 2, 4, 5, 6, 10, 100µM/ ml, 72-hour treatment. (Choi et al., 2012).

As shown in Figure 5.12, results indicate that DLD-1 *FBXL5* KO cells were significantly more resistant to Oxaliplatin (A) treatment compared to controls (WT IC₅₀: 0.5183µM, KO 0.7135µM), while SW480 were less resistant (WT IC₅₀: 0.5068µM, KO: 0.4113µM). Interestingly, similar results were found for Cisplatin (B),

(DLD-1 WT IC₅₀: 0.2276μM, KO 0.3104μM, SW480 WT IC₅₀: 0.1556μM, KO 0.04076μM), and 5-FU (C) (DLD-1 WT IC₅₀: 0.4764μM, KO 1.073μM, SW480 WT IC₅₀: 0.6766μM, KO 0.6399μM). The consistent and cell-specific response of DLD-1 and SW480 *FBXL5* KO cells to Platin treatment suggests that the Platin mechanisms of action are significantly affected by both the genetic background of the cells and subsequent interaction with *FBXL5*.

Two possible factors that may account for these cell-specific responses are differing p53, or ROS and p38 expression within the two cell lines. *FBXL5* may downregulate p53 expression by negatively regulating PTEN (Yao et al., 2018). As p53 expression is increased in SW480 cells, platin suppression of p53 may not be fully active in SW480 cells or *FBXL5* KO may affect each cell line differently as a result (Ahmed et al., 2013a). Alternatively, platin interactions with reactive oxygen species (ROS) and p38-mediated SNAIL activation may be reduced in DLD-1 cells due to lack of SNAIL protein expression, leading to these cell-specific results (Cao et al., 2019; Jiao et al., 2016). However, there is currently no direct evidence available of this interaction. These results expand on previously limited understanding of *FBXL5*'s relationship with drug response and suggest that *FBXL5* has a significant effect on platin resistance in colorectal cancer cells by one of several possible mechanisms. Further mechanism-of-action studies are required to explore the mechanisms mediated by platinum-based chemotherapeutics and differential drug responses

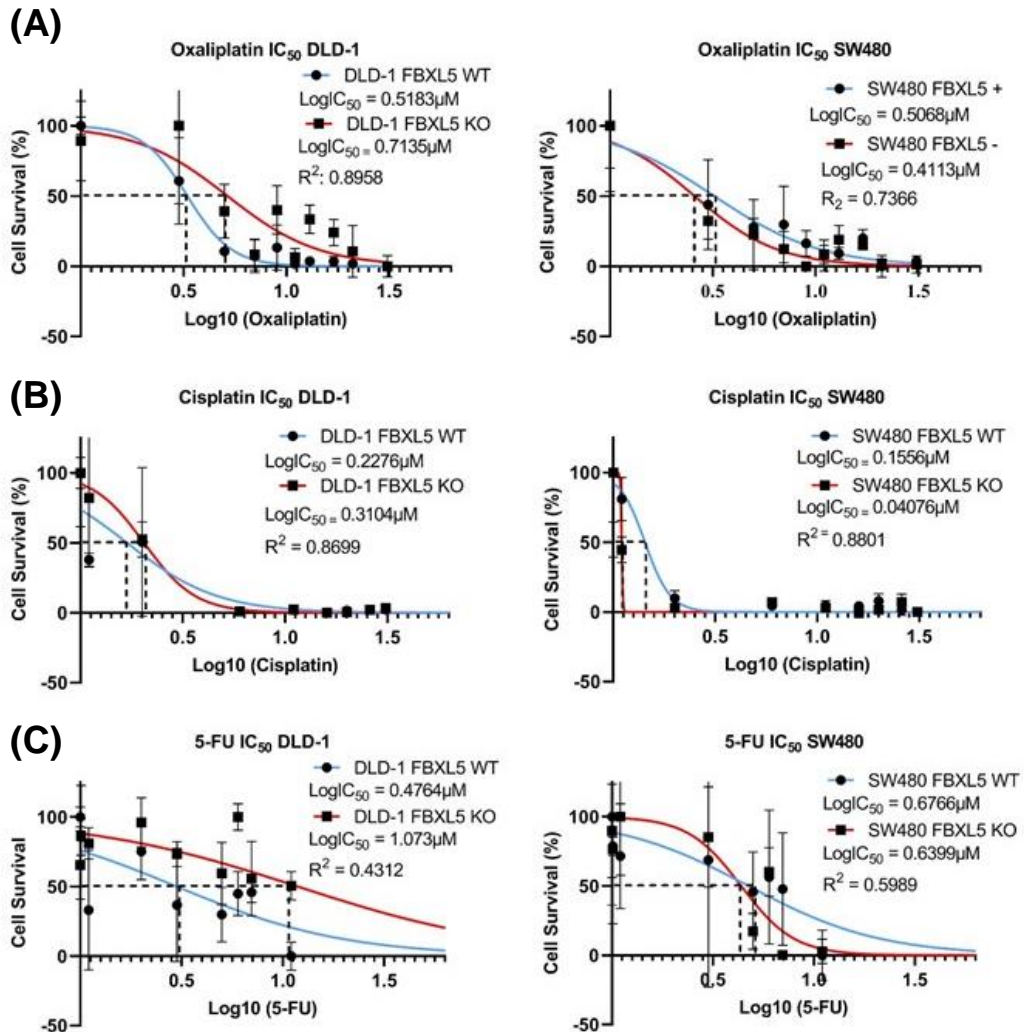


Figure 5.12: Effect of Oxaliplatin, Cisplatin and 5-FU treatment on DLD-1 and SW480 *FBXL5* KO cells shows significant alterations in drug resistance.

3,000 cells per well were seeded to 96 well plate, incubated for 48 hours and treated for 72 hours before being fixed with 15% TCA and analysed. DLD-1 *FBXL5* KO cells showed greater resistance to all three Platins while SW480 *FBXL5* KO resistance was decreased. This may be accounted for by differing p53, p38 or SNAIL expression between cell lines. **(A)** IC₅₀ in μM: DLD WT IC₅₀: 0.5183 μM, KO 0.7135 μM, SW480 WT IC₅₀: 0.5068 μM, KO: 0.4113 μM. **(B)** IC₅₀ in μM: DLD-1 IC₅₀: 0.2276 μM, KO 0.3104 μM, SW480 WT IC₅₀: 0.1556 μM, KO 0.04076 μM. **(C)** IC₅₀ in μM: DLD-1 WT

IC₅₀: 0.4764μM, KO 1.073μM, SW480 WT IC₅₀: 0.6766μM, KO 0.6399μM. Error bars represent standard deviation. Assays were repeated once.

5.1.4.2. *FBXL5* KO significantly alters Etoposide resistance in colorectal cancer cells

The IC₅₀ assay was prepared as previously outlined (Materials and Methods section 2.2.14). In brief: Cells were seeded at 3,000 cells/well in 96 well plates, incubated for 48 hours and treated with Etoposide for 24, 48 and 72 hours (Etoposide treatment dosages as recommended by manufacturer: 0, 0.5, 1, 5, 10, 20, 50, 100, 200, 500μM/ml), after which the plates were washed, fixed with 15% TCA, excess staining removed using 1% acetic acid and plates dried overnight. The following day 200 μl 10mM Tris in dH₂O was added to each well and plate read at 492nm using a spectrophotometer.

The Etoposide cytotoxicity assay results (Figure 5.13) demonstrate that at 24 hours, *FBXL5* KO reduces resistance to Etoposide in DLD-1 and SW480 cells. However, at both 48h and 72h *FBXL5* KO increases resistance to Etoposide treatment. As Etoposide primarily triggers apoptosis by interference with DNA synthesis and RNA transcription, full drug activity may take more than 24 hours. As with other chemotherapeutics investigated in this project: differing response between DLD-1 and SW480 cells may potentially be explained by the divergent genome, particularly in p53 pathways. However, further investigation of Etoposide mechanism of action may more accurately identify important molecular factors (Final IC₅₀: 24h: DLD-1 WT IC₅₀: 2.085μM, KO 1.847μM, SW480 WT IC₅₀: 23.31μM, KO 2.241μM. IC₅₀: 48h: DLD-1 WT IC₅₀: 2.949μM, KO 6.989μM, SW480 WT IC₅₀: 4.326μM, KO 11.82μM. IC₅₀:

72h: DLD-1 WT IC₅₀: 0.1533μM, KO 0.1934μM, SW480 WT IC₅₀: 0.1632μM, KO 0.5592μM).

These results suggest that FBXL5 not only affects DLD-1 and SW480 cells in a cell-specific manner but may also independently affect several etoposide-affected pathways, such as topoisomerase activity, p53-mediated apoptosis and autophagy-mediated ATP production. There is currently no evidence linking FBXL5 with topoisomerase activity, although p53 be downregulated by topoisomerase II inhibitors. This interaction is poorly understood and the potential involvement of FBXL5 requires further investigation (Valkov and Sullivan, 2003).

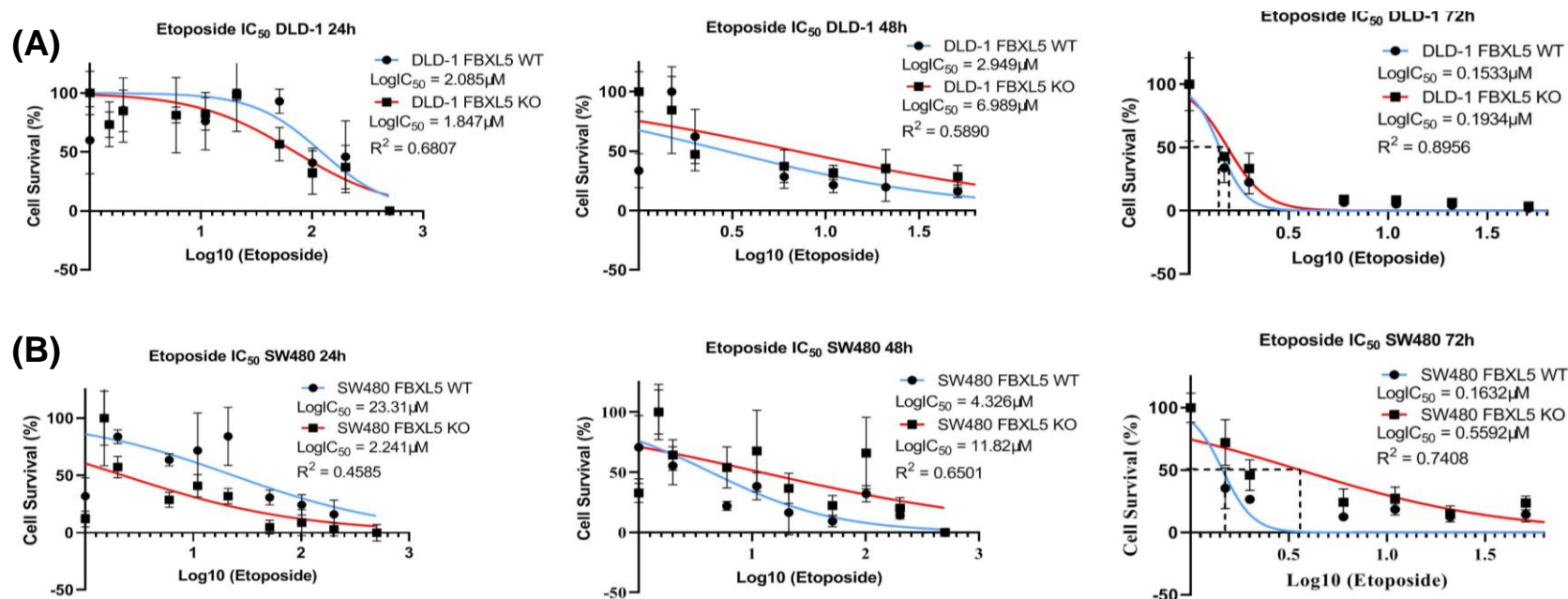


Figure 5.13: *FBXL5* KO significantly increases Etoposide resistance in both DLD-1 and SW480 cells after 48-hour treatment.

3,000 cells per well were seeded to 96 well plates, incubated for 48 hours and treated for 24, 48 and 72 hours before being fixed with 15% TCA and analysed. By the 24-hour mark both *FBXL5* KO cell lines showed reduced resistance to Etoposide, however by 48 and 72-hour timepoints *FBXL5* KO caused increased resistance in both DLD-1 (A) and SW480 (B) cells. 72 hours. Final IC₅₀: 24h: DLD-1 WT IC₅₀: 2.085 μM, KO 1.847 μM, SW480 WT IC₅₀: 23.31 μM, KO 2.241 μM. IC₅₀: 48h: DLD-1 WT IC₅₀: 2.949 μM, KO 6.989 μM, SW480 WT IC₅₀: 4.326 μM, KO 11.82 μM. IC₅₀: 72h: DLD-1 WT IC₅₀: 0.1533 μM, KO 0.1934 μM, SW480 WT IC₅₀: 0.1632 μM, KO 0.5592 μM. Error bars represent standard deviation, assay was repeated twice.

5.2. Discussion

The initial focus of this chapter was characterising the role of FBXL5 in iron homeostasis in DLD-1 and SW480 Cas-9 expressing cells, including effects on Iron Regulatory Proteins and both their immediate and tangential downstream targets, the possible effects of FBXL5 on labile iron pool regulation by Calcein AM staining and reactive-oxygen species activity by treatment with Salinomycin. The growing role of iron homeostasis in cancer biology and metastasis makes modulation of iron an attractive therapeutic target, either by depleting intracellular iron to prevent cellular metabolism, or causing excessive iron accumulation leading to cell death (Brown et al., 2020; Costa da Silva et al., 2017). Further understanding of the role of FBXL5 in iron homeostasis may present a suitable target for future clinical investigation, either in colorectal or another metastasis. In particular: a future examination of *FBXL5* KO role in iron homeostasis in patient derived organoids or tissue samples may more clearly define precisely how it affects IRP and whether this interaction may be utilised in the future.

Results demonstrated that FBXL5 has significant, wide-reaching effects on iron homeostasis in colorectal cancer cells by regulation of iron regulatory proteins at both protein and mRNA stage, confirming and expanding on existing understanding (Jeong et al., 2011). That *FBXL5* KO in colorectal cancer cell lines also has significant effects on several downstream targets with limited direct association to either iron homeostasis or the UPS implies that FBXL5 has broader regulatory roles than previously believed, either by direct ubiquitination of protein substrates, or by indirect regulation. Downregulation of *IRP2* mRNA in our *FBXL5* KO cells and dysregulation of other primary and downstream iron regulatory markers undeniably expands the potential role of FBXL5 in both molecular biology and as a possible therapeutic target,

although any direct interactions between FBXL5 and other downstream IRP1 and IRP2 substrates such as RBCCK1 and VHL is currently unknown. The cell-specific response to *FBXL5* KO in both Calcein AM staining and Salinomycin is also evident, even if the mechanisms and interactions with iron homeostasis require elaboration. Further investigation using patient-derived organoids or alternative models may uncover on how FBXL5 interacts with iron homeostasis and the possible influence on labile iron and Salinomycin response in patient care.

While the results of the Calcein AM staining assay demonstrated a significant dysregulation in labile iron concentration in DLD-1, Calcein is membrane non-permeable and may not accurately measure complete cellular iron levels (Tenopoulou et al., 2007). As such, future studies may benefit from more comprehensive and powerful methods of quantifying total cellular and labile iron. Several studies have quantified cellular iron using Mass Spectrometry (Amor et al., 2020; Ren and Walczyk, 2014; Tchaikovsky et al., 2020). Alternatively, the novel *u*-ferene colorimetric may be valuable for quantifying cellular and labile iron without the use of mass spectrometry (Abbasi et al., 2021).

From the results in this chapter, it can also be concluded that *FBXL5* KO significantly dysregulates ATG5-mediated autophagy markers in colorectal cancer cell lines in a cell-specific manner. The disparate changes in ATG5, LC3B and Beclin1 expression further imply that FBXL5 regulates these substrates and their associated aspects of autophagosome development independently. The connection between ATG5-independent autophagy and ATG5, LC3B, Beclin1 and FBXL5 also requires investigation, as it is currently unclear precisely how these factors may interact and how FBXL5 may modulate this process in colorectal cancer.

The source of cell-specific alterations to autophagy marker expression also requires further examination. ATG5 is strongly regulated by p53 transcription factors which are abnormally expressed in SW480 and may be affected by FBXL5 via PTEN (Yao et al., 2018). LC3B has a highly complex regulatory network that may be dysregulated in either cell line (Jia and Bonifacino, 2020). Beclin1 is ubiquitinated by FBXL1/SKP2, which stimulates EMT activity in breast cancer, and FBXL5 has existing interactions with EMT in CRC cell lines and SNAIL/EMT abnormalities in DLD-1 (Gassen et al., 2019; Wu et al., 2015b). These factors make cell-specific differences in autophagy markers expression difficult to identify. FBXL5 also interacts with the mTOR pathway, which has a regulatory role in autophagy (Yamauchi et al., 2017; Yao et al., 2018). Ferritin is associated with autophagy via NCOA4 (nuclear receptor coactivator 4) and data from this project found Ferritin dysregulated by *FBXL5* KO in colorectal cancer cells (Results section 5.1.1.3) (Santana-Codina and Mancias, 2018) (Yao et al., 2018).

Therefore, while these results support the hypothesis that FBXL5 may partially influence both ATG5-dependent and independent autophagy, the precise mechanism of action is currently uncertain. Further studies on direct protein-protein and substrate interactions or a broader study of ubiquitin associations with autophagy markers in patient derived organoids or tissue samples may provide further evidence of these connections. Additionally, assays that more directly quantify the autophagy process itself may be effective for future work. Such methods include quantification of LC3 activity in a cell sample via immunofluorescent microscopy, quantification and staining of autophagosomal membrane activity or the use of autophagy or lysosomal inhibitors (Orhon and Reggiori, 2017). This result also further supports our previous

supposition that FBXL5 KO may be most significant after the activation of specific cellular or environmental pathways.

To determine the role of FBXL5 in colorectal cancer cell response to hypoxia, we utilised the colony formation efficiency assay, and assessed mRNA expression of several important hypoxia regulators using RT-qPCR. The results indicate that FBXL5 may have a role in hypoxia response in colorectal cancer cells, more significantly affecting colony formation efficiency in hypoxic than normoxic conditions, and dysregulating mRNA expression of *HIF-1 α* , *HIF2 α* , *CA9*, *VEGFR2* and *ANGPTL4* in a cell-specific manner.

Surprisingly, SW480 *FBXL5* KO cells consistently demonstrated downregulation of hypoxia markers *HIF-1 α* and *HIF2 α* which should be induced by hypoxic conditions. However, DLD-1 mutations in PI3K may affect Reactive Oxygen Species (ROS) regulation, which has been linked to oxidative stress response, in addition to potentially regulating *HIF-1 α* expression, possibly accounting for the cell-specific results (Liu et al., 2019a) (Zhang et al., 2018).

FBXL5 is degraded at oxygen-depleted conditions, and via CITED2-mediated protein degradation (Cbp/P300 Interacting Transactivator with Glu/Asp Rich Carboxy-Terminal Domain 2) is one tangential aspect of the HIF-1 α regulatory network (Machado-Oliveira et al., 2015a). While HIF-1 α is typically induced under hypoxic conditions: downregulation or knockout of FBXL5 may cause overexpression of CITED2, in turn downregulating HIF-1 α under hypoxic conditions (Machado-Oliveira et al., 2015b). RT-qPCR results from this project largely support conclusion: with DLD-1 and SW480 *FBXL5* KO cells displaying atypical downregulated *HIF-1 α* in normoxia and SW480 KO cells in both normoxia and hypoxia. *HIF-2 α* has a diverse

regulatory network of transcription factors that only partially overlaps with *HIF-1 α* , therefore the precise interaction with *FBXL5* is difficult to ascertain (Loboda et al., 2010).

As *CA9* expression is primarily induced by *HIF-1 α* , it is reasonable to presume that dysregulation and cell-specific differences in *CA9* expression may be caused by upstream *HIF-1 α* dysregulation (Kaluz et al., 2009; Kubo et al., 2016). *VEGFR2* is also expressed in a tissue and cell-specific manner and has a highly complex regulatory network (Simons et al., 2016) (Barratt et al., 2018). *VEGFR2* is upregulated in some colorectal cancer cell lines under hypoxic conditions (Liu et al., 2017), and both DLD-1 and SW480 results from this project reflected this, although the corresponding upregulation in *VEGFR2* and *ANGPTL4* expression at normoxia in *FBXL5* KO cells suggests that *FBXL5* may also modulate their expression in normoxia, whereas that modulation by *FBXL5* is prevented in hypoxia where *FBXL5* is normally unstable and degraded.

Few studies have explored the role or changes to UPS activity in hypoxia, however one mouse study identified 198 peptides with significantly altered ubiquitination profiles under hypoxic conditions (Wade et al., 2017). Multiple E3 ligases are involved in hypoxic cell reactions, of which *FBXL5*'s precise role is yet to be determined (Kubaichuk and Kietzmann, 2019; Wade et al., 2017). Further studies using multiple cancer cell types and assessment of hypoxia markers using both RT-qPCR and western blotting would greatly expand current understanding of *FBXL5*'s role in hypoxia.

Finally, results in this chapter also demonstrate that *FBXL5* has a significant effect on drug resistance in human colorectal cancer cell lines in a cell-specific manner. The platinum-based therapeutics (Oxaliplatin, Cisplatin and 5-FU) all produced similar

results, with DLD-1 *FBXL5* KO cells having increased resistance while SW480 *FBXL5* KO cells having reduced resistance.

As all three platinum-based agents share mechanisms related to inhibition of DNA synthesis, transcription inhibition and cell cycle modulation via p53 suppression and immune modulation, (Focaccetti et al., 2015; Longley et al., 2003; Riddell, 2018) *FBXL5* likely has a role in one or several of these pathways. One possible clue is the differing reactions between DLD-1 and SW480 cells. SW480 cells have high p53 expression, therefore the p53-suppression action of platinum-based agents may not be fully active in SW480 cells, nor may *FBXL5*'s tangential interactions with p53 via the oncogenic gene *iASPP* (Yao et al., 2018) (Xiong et al., 2017). Alternatively: Oxaliplatin, Cisplatin and 5-FU also interact with reactive oxygen species (ROS) and p38 MAPK signalling pathways, which lead to EMT activation via *SNAIL* (Cao et al., 2019; Focaccetti et al., 2015; Jiao et al., 2016). Downregulation of *SNAIL* mRNA expression in turn reverses ROS-mediated EMT activity, suggesting another possible interaction with *FBXL5* (Jiao et al., 2016). The mechanisms of platinum-based chemotherapy agents are still being investigated; however, these results indicate at least one interaction pathway that may provide a valuable target for future studies into colorectal cancers with abnormal *FBXL5* expression. This also reinforces our previous hypothesis that *FBXL5* KO is most keenly demonstrated when specific situational cellular and environmental pathways are activated, rather than more directly affecting normal cell homeostasis.

FBXL5 depletion has previously been shown to increase Cisplatin resistance via depletion of *RhoGDI2* by activation of MAPK pathway ERK and p38, with *FBXL5* downregulated in *RhoGDI2*-overexpressing cells post-Cisplatin treatment (Wu et al., 2016). This implies a negative feedback loop between *RhoGDI2* and *FBXL5*, and

FBXL5 KO potentially causing RhoGDI2 upregulation. RhoGDI2 also positively correlates with 5-FU resistance in several human gastric cancer lines, although the exact mechanism is unclear. (Zheng et al., 2013). As such, RhoGDI2 may be a master regulator of platinum-based chemotherapeutic resistance, with *FBXL5* potentially acting as RhoGDI2 post-transcriptional regulator. Intriguingly, *FBXL5* does not directly target RhoGDI2 for ubiquitination (Wu et al., 2016), therefore *FBXL5* may have an indirect effect on RhoGDI2 and presents a novel therapeutic target for RhoGDI2-mediated drug resistance. RhoGDI2 itself has been tentatively identified as a metastasis suppressor in bladder cancer but oncogene in breast cancer (Moon et al., 2010) (Zhang and Zhang, 2006). Examination of RhoGDI2 and other MARPK pathway markers may further elaborate on the role of *FBXL5* in RhoGDI2-mediated drug resistance. These results also expand on previously limited understanding of *FBXL5*'s role in drug resistance and chemotherapeutic response in colorectal cancer, particularly expanding the interaction between *FBXL5*, RhoGDI2 and platinum-based therapeutics.

Etoposide triggers both p53-mediated apoptosis, with which *FBXL5* has previously been associated (Xiong et al., 2017), and autophagy, which as shown in Results section 5.1.2 *FBXL5* may interact with. Therefore, these different cellular pathways may act independently during etoposide treatment: *FBXL5* interactions with earlier activated pathways may reduce resistance, but interactions with later activated pathways increasing resistance. However, the limited understanding of *FBXL5* prevents more detailed characterisation of these interactions. *FBXL5* also ubiquitinates non-phosphorylated hssB1 (human single-strand DNA binding protein), which participates in DNA damage response (Chen et al., 2014). Further investigation may identify other *FBXL5* substrates within similar roles.

These findings also raise considerations on the future role of FBXL5 in clinical practice and patient care. There is currently no data on the impact of FBXL5 mutations on chemotherapeutic response, although FBXL5 is implicated in patient post-surgical survival rate (Haifeng, 2017), with increased FBXL5 expression correlating with increased patient mortality, therefore FBXL5 may present a novel therapeutic target for RhoGDI2 resistance in cancer (Yao et al., 2018). The effect of FBXL5 on Etoposide may also present similar clinical opportunities, however further studies on Etoposide mechanics of action are required to more accurately characterise interactions with FBXL5.

Taken together, these results further characterise the role of FBXL5 in drug resistance and drug response in colorectal cancer cells. Future studies using model systems such as primary tissue samples, patient-derived organoids or alternative cell lines may further develop current understanding and translate to patient care. Alternatively, due to the limited information available on FBXL5, bioinformatic and proteomic and transcriptomic sequencing of FBXL5 KO samples may identify novel associations with FBXL5 that may be more difficult to identify with *in vitro* methodology, which will be the focus of the following chapter.

**Chapter 6: Bioinformatics and
RNA-Seq analysis of *FBXL5*
KO cells identified novel
substrates and pathways**

6. Brief Introduction

This project has thus far attempted to validate and expand previous understanding of the impact of *FBXL5* in colorectal cancer using *in vitro* colorectal cancer cell models and assays that identify specific pathways and downstream target genes and proteins. However, the methods used such as western blotting and RT-qPCR are limited when attempting to categorise completely novel pathways and interactions that have not been previously considered. For example: our Results in section 5.1.2 demonstrated the role of *FBXL5* KO in autophagy regulation in colorectal cancer cells despite the lack of or limited previous experimental evidence.

Next Generation Sequencing (NGS) refers to high-throughput quantification analysis of genomic and transcriptomic data, thereby potentially identifying novel interactions and pathways (Stark et al., 2019). The Cancer Genome Atlas (TCGA, (Weinstein et al., 2013)) for example, has profiled and sequenced thousands of human tumours for DNA, RNA, protein and epigenetic abnormalities, which provide a comprehensive molecular background on human tumour types. Therefore, in this chapter, we analyse publicly available cancer tissue NGS sequencing databases to potentially identify *FBXL5* protein and genetic correlations and associations in cancer. We also investigate and discuss the results obtained from NGS RNA-Seq analysis of DLD-1 *FBXL5* KO cell lines generated during this project and how these results impact on current understanding of *FBXL5*.

6.1.Results

6.1.1. Analysis of public NGS databases to predict novel FBXL5 associations.

Next generation sequencing (NGS) has recently developed to enable large scale, quantitative analysis of biological samples, and the public sharing of that data in a manner that is amenable to further analysis by researchers with limited bioinformatics background. There are several publicly accessible collaborative datasets available that can predict genetic and proteomic associations by drawing information from sources including published experimental data, NGS datasets and predictive algorithms (Chandrashekar et al., 2017; Szklarczyk et al., 2019; Tang et al., 2017). Interrogation of these combined databases can provide scientists with an alternative approach that can advance their research, particularly in less well understood genetic or proteomic topics. However, any novel associations predicted by these methods must be validated *in vitro*. To attempt to predict novel FBXL5 associations and substrates, three publicly available bioinformatics databases: STRING, GEPIA and UALCAN were selected and interrogated. All these databases were accessed during Nov-Dec 2020.

Firstly; STRING (Search Tool for the Retrieval of Interacting Genes/Proteins, String-DB.org) (Szklarczyk et al., 2019) is a database of known and predicted proteomic interactions determined by physical and functional associations. Each potential association is scored between 0-1 on the strength of available evidence including published experimental data and research articles, co-expression and homology of proteins, text mining and proteomic association datasets made available for analysis. Proteomic associations which are well understood will score more highly in STRING

than novel associations only identified as correlations in high-throughput proteomics analysis.

Secondly, GEPIA (Gene Expression Profiling Interactive Analysis, gepia.cancer-pku.cn) (Tang et al., 2017) interrogates mRNA sequencing data from paired tumour and healthy tissue samples from the TCGA (The Cancer Genome Atlas Program, (Weinstein et al., 2013)) and GTEx (Genotype-Tissue Expression project, (Consortium, 2013)) databases, determining linear mRNA expression correlation between genes of interest. The TCGA database contains genomic, epigenomic, transcriptomic and proteomic data from 20,000 primary tissue samples across 33 different cancers, while GTEx is a collaborative database containing similar data from individual researchers and projects (Consortium, 2013; Weinstein et al., 2013).

Finally UALCAN (University of Alabama at Birmingham Cancer Database, ualcan.path.uab.edu) (Chandrashekar et al., 2017) also provides cancer genomic, transcriptomic and proteomic data analysis from TCGA, MET500 (Metastatic 500 (Robinson et al., 2017)) and CPTAC (Clinical Proteomic Tumour Analysis Consortium, (Whiteaker et al., 2014)) databases comparing tumour and healthy tissues with data categorised by cancer type, stage and *TP53* mutation status. Unlike TCGA, MET500 data is primarily generated from metastatic cancer samples, providing more focused data on advanced stages of cancers, while CPTAC specialises in colorectal, breast and ovarian cancer proteasome-genomic data associated with toxicity and resistance in clinical trials.

6.1.1.1. STRING analysis of predicted FBXL5 protein associations identified potential novel protein interactors.

STRING (Search Tool for the Retrieval of Interacting Genes/Proteins) (Szklarczyk et al., 2019) analysis of potential FBXL5 associations was performed using the online STRING interface (STRING-DB.org, (Szklarczyk et al., 2019)) at the highest confidence interaction (0.9) and expanded to 20 closest direct or indirect interaction nodes. Confidence interaction lower than 0.9 produced an exponential number of potential associations that was impractical to investigate thoroughly. Data was subsequently exported and examined in Microsoft Excel and the STRING-db online node visualiser. Co-occurrence, gene fusion and predictive neighbourhood options produced no data and were disabled to facilitate analysis. Permanent link (<https://version-11-0b.string-db.org/cgi/network?networkId=bFXGaA52lfnr>)

Examination of closest 20 nodes identified nine high probability associations with FBXL5 (average confidence scores 0.945) including components of the ubiquitin-proteasome regulation, SCF binding and other F-box E3 ligases (Figure 6.1). Of these nodes, only IREB/IRP2 was identified as a potential FBXL5 association not directly related to the ubiquitin-proteasome system. *FBXL5* KO impact on IRP2 has been discussed in detail in Chapter 1 and 5 (Terzi et al., 2021). Therefore, analysis tolerances were expanded from closest 20 to closest 100 direct and indirect associations. Other search parameters were unchanged. This search identified 44 total potential associations with FBXL5 with ≥ 0.9 confidence score (see Table 6.1). Of these potential associations; 16 were other F-box E3 ligases, 23 were ubiquitin modifying enzymes, SCF structural proteins or UPS regulating proteins. In addition to IREB/IRP2, this analysis identified VHL as a potential novel FBXL5 interactor outside UPS. As established in Results Section 5.1.1.4: VHL is a HIF-1 α regulator and

downstream target of iron homeostasis (Foxler et al., 2012) and *VHL* mRNA is shown to be significantly upregulated in *FBXL5* KO DLD-1 colorectal cancer cells in this project (Figure 5.6). STRING associations and confidence scores are determined by published experimental data, publicly available proteomic databases, co-expression and homology. Despite the limited available information on *FBXL5*, this was still sufficient for STRING to identify other potential novel associations. Further development of both the STRING system and access to additional proteomic databases may identify other associations in the future.

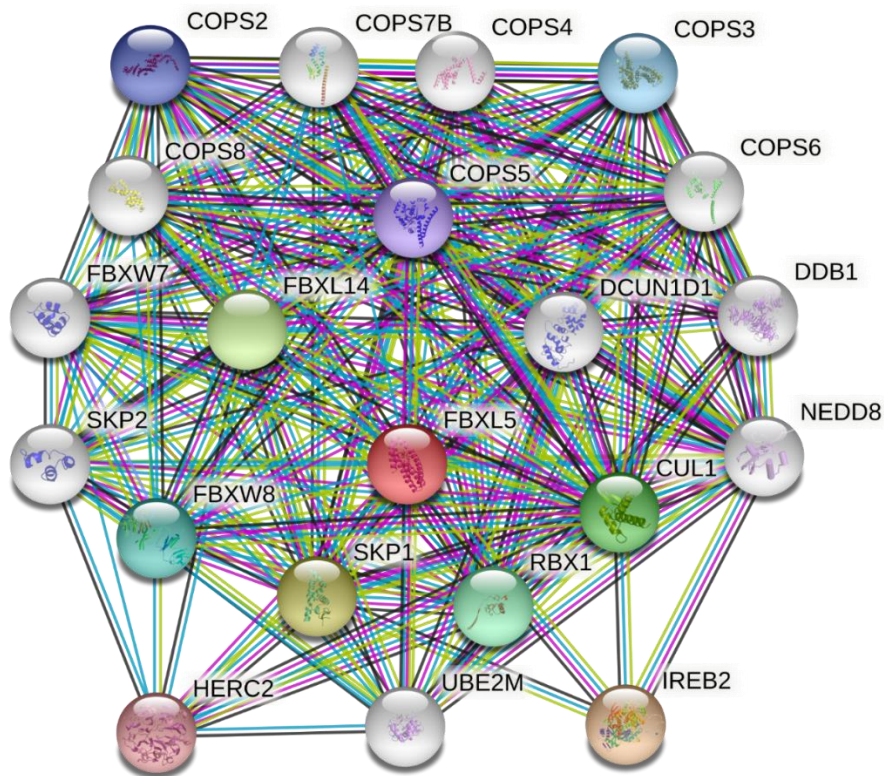


Figure 6.1: STRING analysis of *FBXL5* showing 20 nodes of highest confidence (average confidence: 0.971).

Results identified varying E3 ligases, SCF components and UPS regulators, only IREB2 (aka IRP2) was identified as an *FBXL5* association outside UPS. Coloured

lines represent evidence type including text mining, experimental evidence, database analysis and co-expression. Co-occurrence, gene fusion and neighbourhood options produced no data points and were disabled (Permanent link: <https://version-11-0b.string-db.org/cgi/network?networkId=bFXGaA52lfnr>).

Table 6.1: Potential FBXL5 associations identified using STRING Database

Node/interactor	Known roles	Experimental	Coexpression	Homology	Textmining	Database	Combined Score	
FBXL7	F-box E3 Ligase	0	0	0.555	0.166	0.9	0.905	
<i>FBXO11</i>		0	0.064	0	0.475	0.9	0.946	
FBXO17		0	0	0	0.155	0.9	0.911	
<i>FBXO18</i>		0	0	0	0.17	0.9	0.913	
FBXO2		0	0	0	0.288	0.9	0.925	
FBXO27		0	0	0	0.428	0.9	0.94	
<i>FBXO4</i>		0	0	0	0.367	0.9	0.934	
<i>FBXO44</i>		0	0	0	0.277	0.9	0.924	
FBXO6		0	0	0	0.275	0.9	0.924	
FBXO7		0	0	0	0.177	0.9	0.914	
FBXO9		0	0	0	0.169	0.9	0.913	
<i>FBXW11</i>		0	0.052	0	0.427	0.9	0.94	
<i>FBXW2</i>		0	0.058	0	0.103	0.9	0.908	
<i>FBXW7</i>		0	0.055	0	0.292	0.9	0.927	
FBXW8		0	0	0	0.575	0.9	0.955	
FBXW9		0	0	0	0.43	0.9	0.94	
FZR1		APC/C E3 ligase adapter	0	0	0	0	0.9	0.9
GLMN		SKP-Cullin-F-box-like complex	0	0.062	0	0	0.9	0.902
GPS1	<i>COP9</i> UPS regulating complex	0	0	0	0	0.9	0.9	
HERC2	E3 ligase	0.305	0	0	0.348	0.9	0.95	
IREB2	Iron Regulatory Protein 2	0.305	0.062	0	0.897	0.9	0.992	
KEAP1	Component of RBX1/CUL E3 ligase.	0	0	0	0.089	0.9	0.905	
LRR1	Leucine-rich-repeat protein 1.	0	0	0	0	0.9	0.9	
NAE1	NEDD8 activating E1 subunit	0	0	0	0	0.9	0.9	
NEDD8	NEDD E3 ligase activator	0	0	0	0.116	0.9	0.907	

RBX1	E3 ligase	0.313	0	0	0.501	0.9	0.962	
RNF7	RING-box protein 2	0	0	0	0.106	0.9	0.906	
SKP1	SKP protein of SCF complex	0.379	0.077	0	0.604	0.9	0.974	
SKP2	SKP protein of SCF complex	0	0	0	0.401	0.9	0.937	
TCEB1	Elongin C. RNA Polymerase II	0	0	0	0.065	0.9	0.902	
TCEB2	Elongin B. RNA Polymerase II	0	0	0	0.071	0.9	0.903	
UBA1	Ubiquitin-like modifier-activating enzyme	0	0.055	0	0	0.9	0.901	
UBA3		0	0.095	0	0	0.9	0.905	
UBE2B		0	0	0	0	0.9	0.9	
UBE2D1		0	0.064	0	0	0.9	0.902	
UBE2D2		0	0.061	0	0	0.9	0.902	
UBE2D3		0	0.108	0	0.122	0.9	0.914	
UBE2F		0	0	0	0.047	0.9	0.9	
UBE2G1		0	0.064	0	0	0.9	0.902	
UBE2K		0	0	0	0.138	0.9	0.91	
UBE2M		0	0	0	0.08	0.9	0.904	
UBE2R2		0	0.061	0	0	0.9	0.902	
UBE2S		0	0	0	0.384	0.9	0.935	
VHL		HIF-1 α regulator and IRP substrate	0	0	0	0.137	0.9	0.91

6.1.1.2. GEPIA and UALCAN analysis of RNA expression databases identifies several novel potential FBXL5 associated genes.

To identify additional novel *FBXL5* gene correlations and potential associations, the GEPIA and UALCAN RNA-omics databases were interrogated. GEPIA (Gene Expression Profiling Interactive Analysis, gepia.cancer-pku.cn) (Tang et al., 2017) analyses RNA transcriptomic data extracted from cancerous and healthy tissues in the TCGA (The Cancer Genome Atlas Program) and GTEx (Genome-Tissue Expression project (Consortium, 2013)) databases for possible genetic correlations with a gene of interest. The UALCAN system (University of Alabama at Birmingham Cancer Database, ualcan.path.uab.edu) (Chandrashekar et al., 2017) analyses cancer RNA-omics data obtained from the TCGA, MET500 and CPTAC databases (Robinson et al., 2017), with the MET500 database categorising RNA transcriptomic samples by cancer stage and *TP53* mutation status in addition to cancer type, allowing categorisation of gene expression and correlations during cancer progression, and CPTAC focusing on associations with clinical drug resistance and toxicity.

Analysis of RNA-omics data for gene expression correlation with *FBXL5* was conducted using the GEPIA and UALCAN online interfaces using COAD (Colon adenocarcinoma) Tumour and COAD Normal tissue datasets and significance detected by Pearson's Correlation Coefficient (PCC) of ≥ 0.7 , logfold change cut off: 1.0. Both GEPIA and UALCAN systems were examined with the same parameters. (GEPIA analysis link: <http://gepia.cancer-pku.cn/detail.php?gene=FBXL5>, UALCAN analysis link: <http://ualcan.path.uab.edu/cgi-bin/TCGAExCorrel.pl?genenam=FBXL5&cancer=COAD>)

Expression correlation analysis identified four genes within COAD datasets with PCC score of ≥ 0.7 . Expanding PCC score tolerances identified a further 93 genes with PCC between 0.6-0.5 and a further 637 with PCC between 0.59-0.5. Table 6.2 lists genes with PCC of 0.65 or greater when compared with *FBXL5* expression in colorectal adenocarcinoma. Figure 6.2 A and B and Figure 6.3 show heatmap and chromosomal distribution of the same data (Figure 6.2 A shows genes positively correlated; Figure 6.2 B are genes negatively correlated). Importantly; simultaneous analysis across all available cancer datasets rather than COAD alone did not identify any genes of PCC ≥ 0.7 , implying *FBXL5* oncogenic or tumour suppressive activity may be tissue and cancer specific. Highest PCC score across all cancer datasets was WDFY3 at 0.58, an autophagy regulator that may be linked to neurological disability and an autism risk gene (Napoli et al., 2018).

Other novel *FBXL5* correlations identified by significant PCC score include several RAS oncogenes, two Herpes Simplex viral interactors and other immune response regulators, and several genes associated with membrane integrity and ion channel activity (Table 6.2). *FBXL5* has not previously been associated with ion exchange or ion channel activity, and although engineered E3 ligases have been used to selectively manipulate ion channels, there is limited information available on F-box protein associations with ion channels (Kanner et al., 2017). Nor does *FBXL5* have published associations with *RAP1* signalling, *HCF2* or Herpes Simplex viral interactions. However, as RNF11 is part of the UPS, encoding RNG-H2 finger motif, association or interaction between itself and *FBXL5* are reasonable to presume (Mattioni et al., 2020). EID1 is implicated in transcription, differentiation, DNA repair and chromosomal maintenance and is targeted by FBXO21 for ubiquitination (Zhang et al., 2015), but currently no direct associations with *FBXL5* are known.

While GEPIA and UALCAN only performs expression correlation analysis and cannot experimentally validate results, this analysis was able to identify several novel genes with potential *FBXL5* associations. *In vitro* testing is required to validate these findings. Therefore, we quantified expression of those top associated genes with $PCC \geq 0.7$ (*RAP1A*, *HCFC2*, *RNF11* and *EIDI1*) in DLD-1 and SW480 *FBXL5* KO cells using RT-qPCR in triplicate as previously outlined (Materials and Methods section 2.2.13).

As shown in Figure 6.4: DLD-1 KO cells showed significant downregulation of all four target genes, while SW480 showed downregulation *RAP1A* (Figure 6.4 A), *EIDI1* (Figure 6.4 C), and *RNF11* (Figure 6.4 D), but not *HCFC2* (Figure 6.4 B), confirming the results obtained from GEPIA and UALCAN analysis *RAP1A* (DLD-1 $P = < 0.0001$, SW480 $P = < 0.0001$) *HCFC2* (DLD-1 $P = < 0.0009$, SW480 $P = 0.466$) *EIDI1* (DLD-1 $P = < 0.0001$, SW480 $P = < 0.0001$) *RNF11* (DLD-1 $P = < 0.0001$, SW480 $P = < 0.0001$). Differences in *RAP1A* expression may be attributed to DLD-1 *KRAS* *G13B* mutation or SW480 *K*, *H* or *N Ras* mutations (Ahmed et al., 2013a). Although, the precise mechanism is difficult to determine. *RAP1* may act as a Ras suppressor, although this is currently unclear (Nussinov et al., 2020).

Table 6.2: Genes expression correlated with *FBXL5* with PCC ≥ 0.7 identified using GEPIA and UALCAN databases

Gene	PCC CRC	PCC General	Known Roles
RAP1A	0.72	<0.45	RAS suppressor, EKR signalling, GTP binding
HCFC2	0.71	<0.45	Host Cell Factor C2, Herpes Simplex viral interaction
RNF11	0.7	<0.45	Ring Finger Protein 11 in UPS complex
EID1	0.7	<0.45	Transcription corepressor, cell differentiation
CGRRF1	0.69	<0.45	Cell growth regulator, cell differentiation
SNX6	0.68	<0.45	Sorting Nexin 6,
RAP1B	0.68	<0.45	RAS oncogene family, GTP binding
NR3C1	0.67	0.48	Glucocorticoid receptor, inflammation, cell proliferation and differentiation
PJA2	0.66	0.50	Ubiquitin ligase, inflammation, ubiquitinates cAMP dependent protein kinases I, II α/β
GLIPR2	0.66	<0.45	Protein homodimerization
MBNL1	0.66	<0.45	Muscle-blind Like Splicing Regulator 1, modulates alternative splicing of pre-mRNA's, muscle tissue development
IL6ST	0.66	<0.45	Interleukin 6 Signal Transducer, cytokine signal transducer.
SLC9A9	0.65	<0.45	Ion homeostasis and exchange
ZNF25	0.65	<0.45	Zinc Finger Protein 25, Herpes Simplex Viral Infection
TCEAL7	0.65	<0.45	Regulates NF-Kappa- β signalling in innate immunity, telomerase reverse transcription expression
STOM	0.65	<0.45	Integral membrane protein, ion channels, anaemia
CNRIP1	0.65	<0.45	Cannabinoid receptor 1 in neurotransmitter release and activity, deafness,
RAB18	0.65	<0.45	RAS oncogene family, eye and brain development
TNFSF12	0.65	<0.45	Tumour necrosis factor, apoptosis regulation along multiple pathways, angiogenesis
GIMAP6	0.65	0.53	GTPase immunity-associated proteins family, cell survival, lymphoma and lung cancer.
HACD4	0.65	<0.45	Fatty acid metabolism, Spinocerebellar Ataxia 34,

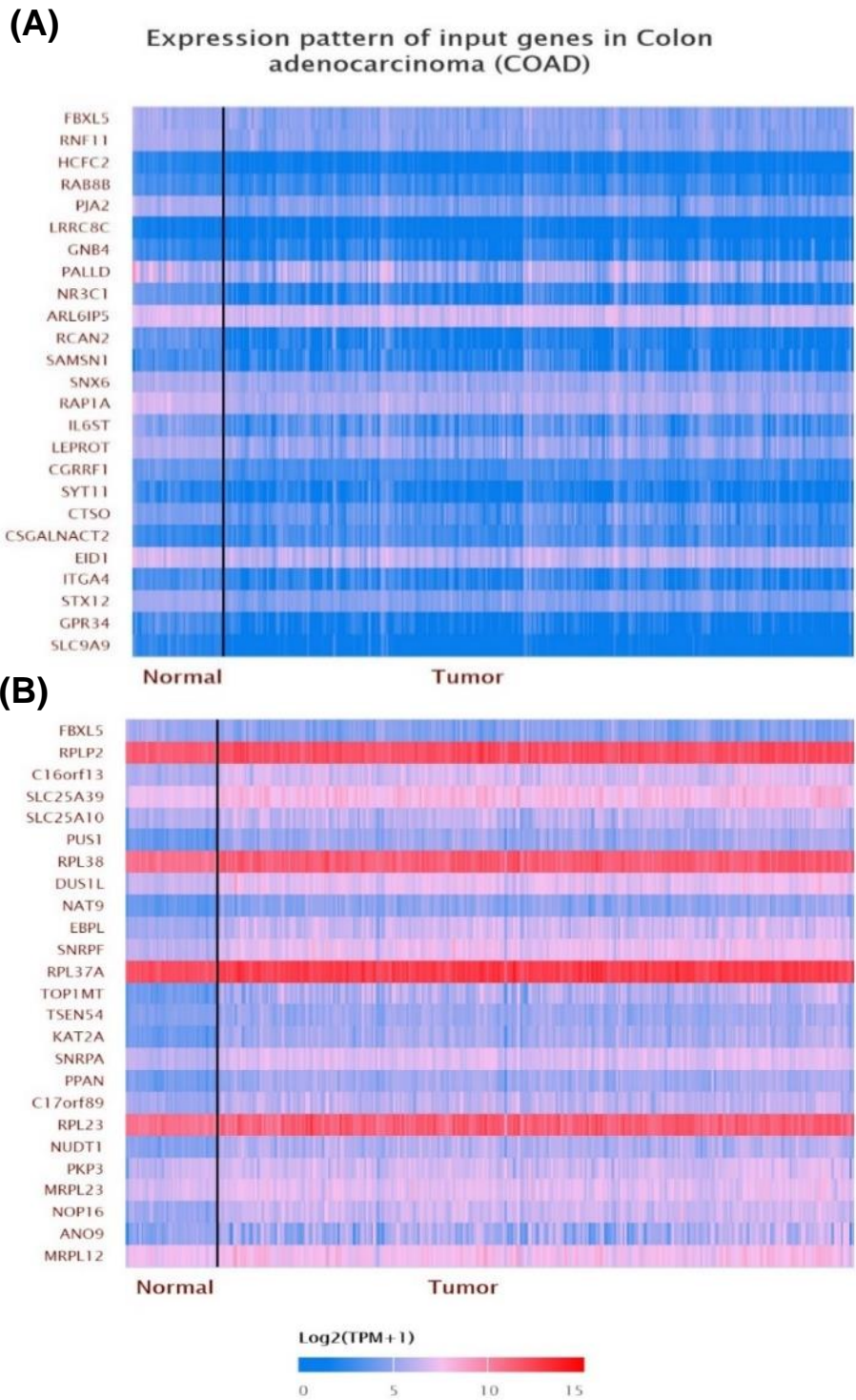


Figure 6.2: GEPIA and UALCAN analysis showing 25 genes with most significantly altered gene expression correlated with FBXL5 in colorectal adenocarcinoma:

Correlational analysis of RNA-Seq data identified numerous genes differentially expressed compared with FBXL5 in TCGA, GTEX, MET500 and CPTAC genomic

and proteogenomic databases. The most significant genes from this analysis were selected for *in vitro* validation. (A) 25 most significantly positively correlated genes with FBXL5 expression. (B) 25 most significantly negatively correlated genes with FBXL5 expression. Permanent link: (<http://ualcan.path.uab.edu/cgi-bin/TCGAExCorrel.pl?cancer=COAD&genenam=FBXL5>)

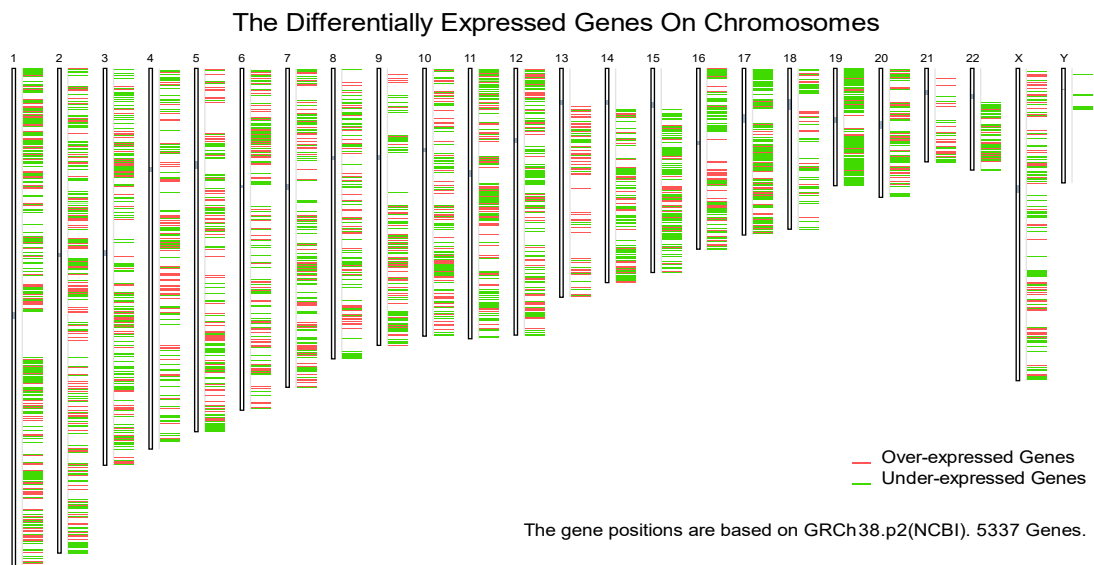


Figure 6.3: Chromosome mapping of GEPIA and UALCAN analysis of genes most significantly altered expression correlated with *FBXL5*.

Chromosomal mapping of differentially expressed genes correlated with *FBXL5* in colorectal cancer using TCGA, GTEX, MET500 and CPTAC genomic and proteogenomic databases. 5,337 genes total were identified as differentially expressed in this analysis (GEPIA analysis link: <http://gepia.cancer-pku.cn/detail.php?gene=FBXL5>).

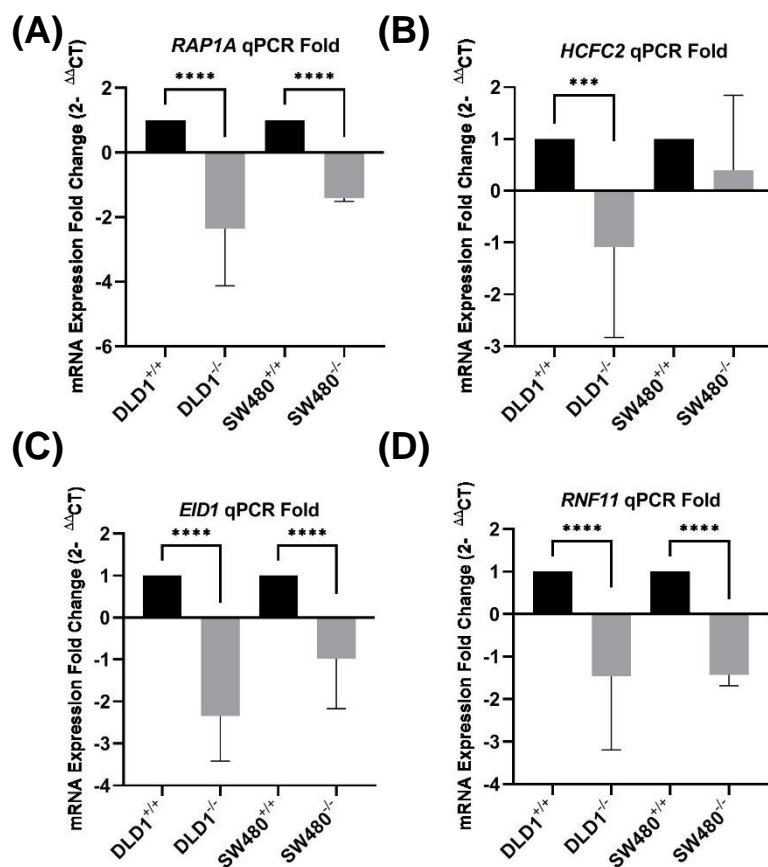


Figure 6.4: RT-qPCR analysis of genes identified by GEPIA and UALCAN analysis shows significant alterations in *FBXL5* KO DLD-1 and SW480 cells.

Analysis of GEPIA and UALCAN colon adenocarcinoma databases identified *RAP1A* (A), *HCFC2* (B), *RNF11* (C) and *EID1* (D) as potential *FBXL5* interactors. RT-qPCR analysis found significantly downregulation in *FBXL5* KO DLD-1 and SW480 cells for the majority of these targets as predicted. RT-qPCR assay was performed in triplicate and result normalised to 1 for comparison. Error bars represent standard deviation. $P < 0.05$ (*), $P \leq 0.01$ (**), $P \leq 0.001$ (***), $P \leq 0.0001$ (****).

This RT-qPCR data validates the analysis of GEPIA and UALCAN databases as a possible method of identifying novel gene associations and suggests several novel FBXL5 associated genes. Further examination of the novel associations identified by interrogation of the GEPIA and UALCAN databases would greatly expand current understanding of FBXL5 and suggest research goals for future projects. Additionally, corroboration of GEPIA and UALCAN database predicted gene associations using *in vitro* assays also validates their use as a preliminary step when investigating poorly understood genes such as FBXL5 and other F-box E3 ligases. A comprehensive analysis of these databases for other novel F-box associations may be beneficial for future studies.

6.1.2. RNA-Seq analysis of DLD-1 *FBXL5* KO cells identifies novel, differentially expressed genes.

RNA-Sequencing is a form of high-throughput RNA analysis that simultaneously quantifies the expression of different RNA sequences within a sample, including alternative splicing variants, SNP strand mutations and post-transcriptional modifications (Stark et al., 2019). As such, it is more efficient than the RT-qPCR array and similar methods when conducting exploratory research into novel aspects of functional genetics.

RNA Sequencing utilises either cDNA or fragmented RNA as a sample library for interrogation (Kukurba and Montgomery, 2015). Artificial fluorescent sequence adaptors unique to each nucleic sequence are ligated to both ends of the fragment or cDNA, which can be read and quantified by their unique fluorescent signature (Wolf, 2013). These sequences or “short sequence reads” are identified by high throughput

reading of the attached adapters, and subsequently quantified and mapped to the reference genome, also identifying isoforms and mutations within a transcriptome (Wolf, 2013). RNA-Seq experiments are dependent on “coverage” and “depth”, coverage referring to the total area of the reference genome read using fluorescent adapters, and depth being the number of reads of each area of the reference genome across all adapters to ensure accuracy (Wolf, 2013). Typical RNA-Seq projects have >90% coverage of a reference genome depending on experimental requirements, and between 1-500 million reads across the entire transcriptome (Kukurba and Montgomery, 2015).

RNA-Seq is superior to RT-qPCR arrays for high throughput RNA expression analysis due to its high coverage and number of reads. RNA-Seq may be unable to identify isoforms with high similarity (Stark et al., 2019). In addition, the sequencing depth of individual RNA-Seq experiments, possible transcript loss depending on library preparation and confounding technical noise caused by different technologies may make comparisons between RNA-Seq methodologies difficult {Chen, 2018 #1201}. Novel statistical methodologies such as normalisation via Fragments Per Kilobase Million (FPKM, discussed below) address these biases by giving greater statistical weight to areas of higher read depth and additional quality control to minimise variance caused by different methods (Zhao et al., 2021b).

Finally, as NGS sequencing is a continually evolving field with both new technologies, analysis methods and algorithms constantly developed, the appropriate methods must be selected, and their individual biases be considered. Any significant results obtained by these methods must be validated by RT-qPCR to ensure accuracy on targets of particular interest (Ozsolak and Milos, 2011; Stark et al., 2019). RNA-Seq is therefore

most suited for initially identifying novel biomarkers and functional genomic associations and pathways where comprehensive adaptor libraries exist.

6.1.2.1. RNA-Seq analysis of DLD-1 *FBXL5* KO cells and post validation analysis using RT-qPCR on selected targets.

Due to the limited information available on *FBXL5* associations, we elected to submit samples of DLD-1 parental and *FBXL5* knockout cells for RNA-Seq analysis. As *FBXL5* is unstable at low oxygen environments and has shown evidence of hypoxia associations (Machado-Oliveira et al., 2015a) (Results section 5.1.3), we submitted samples extracted under both normoxia and hypoxic culture conditions to determine how associations and correlations may change. SW480 cells were not submitted at this time due to cost constraints. mRNA was isolated as previously discussed (Materials and Methods section 2.2.13) and concentration measured by Nanodrop. Duplicate samples of total RNA (2 µg per sample tube) were submitted to Novogene (Cambridge, UK) for RNA sequencing. RNA was quality tested by Novogene using RNA integrity number (RIN) and samples processed for library preparation and RNA sequencing. Library preparation was performed by Novogene using either NEBNext® Multiplex Small RNA Library Prep Set for Illumina for sRNA-Seq or Illumina TruSeq RNA Library Prep kit for RNA-Seq. A minimum of 35 million paired end reads (fragments read from both ends) were generated for each sample from each library.

Processing of raw sequencing data obtained from Novogene and generation of LogFold data up to pathway mapping analysis as outlined below was kindly performed by Prof. Nigel Mongan (School of Veterinary Medicine and Sciences, University of Nottingham). The detailed pathway for the processing and analysis of RNA-Seq data is as follows:

As summarised in Figure 6.5: Raw sequencing data from Novogene was stored as FASTQ format files. This file format contains nucleotide sequences combined with a PHRED quality control score for each sequence, quantifying probability that the base was incorrectly identified (Cock et al., 2010). To more accurately align sequencing data to the reference genome, fluorescent/luminescent adapter sequences are removed (“trimmed”) using Trimgalore (Martin, 2011). This process is combined with quality control on the data contained in the original FASTQ file, with PHRED reads of >30 (i.e., 1:1000 chance of incorrect base read, 99.9% accuracy) being retained and others excluded from further analysis.

Once adaptors were trimmed, the resulting reads were aligned to a human reference genome to match the raw nucleotide information to known genetic sequences. Quality processing FASTQ reads were aligned to the Ensembl annotated reference genome (GRCh 38.83 human) using the STAR aligner (Spliced transcripts alignment to a reference) alignment tool 2.7.8a (Dobin et al., 2013). The resulting mapped data was stored as a .BAM file and gene expression was quantified using FeatureCounts (Liao et al., 2014). Once quantified, the differential expression of the RNA-Seq data was analysed using DESeq2 version 3.12 (Anders and Huber, 2010), determining differential significance with q value <0.05 and ± 1 log₂ fold change considered significant. Q value referring to the statistical significance of differential expression adjusted for False Discovery Rate (FDR), which is necessary when analysing multiple variables from the same dataset in sequence to prevent accumulation of false positive results. Transcriptome analysis of RNA-Seq data was quantified using Kallisto (version 0.46.1) (Bray et al., 2016). Alternative splicing variants were identified and quantified using rMATS tool version 4.1.1 and expressed as percent slice in (PSI) values (Shen et al., 2014). Comparison between two PSI values is a deltaPSI value

(Shen et al., 2014), with transcripts possessing FDR significant differential splicing with $\leq 5\%$ dPSI selected for further analysis. Finally, the identified genes were mapped to associated overrepresented pathways using the WebGestalt online tool and the KEGG pathway database (Liao et al., 2019). Final data was converted to log₂ foldchange and significance determined by adjusted *P* value to compensate for multiple comparisons.

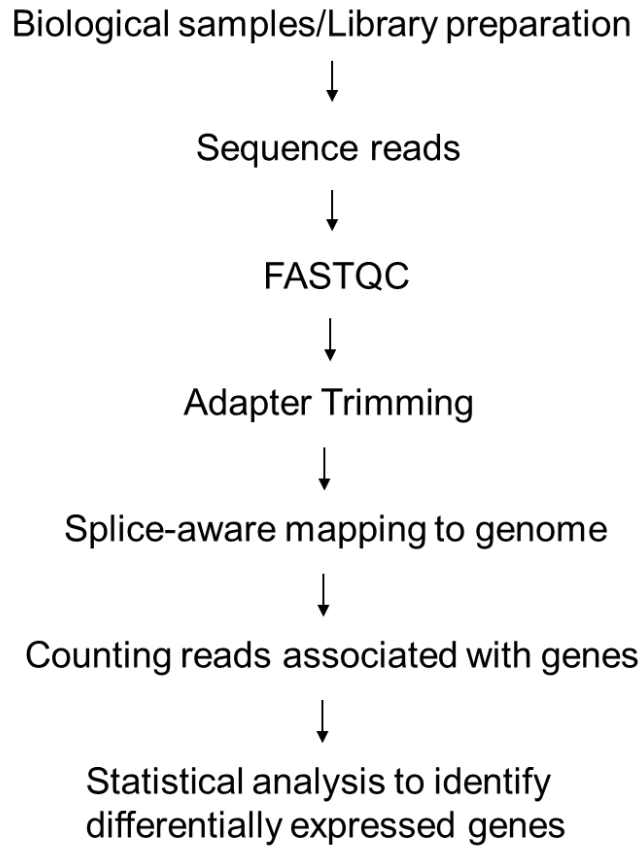


Figure 6.5: Diagram of RNA-Seq analysis workflow from pre-read library preparation to final data analysis.

FASTQC was performed using TrimGalore, mapping by STAR Aligner, FeatureCounts using Ensemble GRCh 38.83 and quantification and statistical analysis performed using DESeq2 and rMAT. Diagram adapted from ((HBC), 2021) (https://hbctraining.github.io/Intro-to-rnaseq-hpc-orchestra/lessons/07_rnaseq_workflow.html)

RNA-Seq analysis of DLD-1 parental and *FBXL5* KO cells at normoxic and hypoxic conditions identified several thousand differentially expressed genes in either normoxia, hypoxia or both (Figure 6.6-6.8). The greatest overlap (1,213 genes) was between WT Normoxia vs WT Hypoxia, and KO Hypoxia and KO Normoxia, showing genes unaffected by both *FBXL5* KO and hypoxic conditions. As outlined in Figure 6.6-6.8, the majority of significantly differentially expressed genes were only significant under hypoxic conditions. *FBXL5*'s hemerythrin-like domain, unique among mammalian proteins for both oxygen and iron binding, and reduced expression at hypoxic conditions offer further evidence that *FBXL5* may have a greater role in colorectal cancer hypoxia response than previously expected (Chollangi et al., 2012; Wang et al., 2020a).

Several genes previously investigated in this project were identified as significant in the RNA-Seq library results, including *Ferritin Light* and *Heavy* (Figure 5.3 and 5.4), *APP*, *RBCK1* and *VHL* (Figure 5.6), *ATG5* (Figure 5.7 and 5.8), *EID1* (Figure 6.4), and *HIF-1 α* and *VEGF2a* (Figure 5.11). The results were broadly similar between RT-qPCR and RNA-Seq, with variability in significance explained by the differing methodology of each technique, such different reference/housekeeping genes and methods used to normalise data. Both qPCR and RNA-Seq utilise different methods for scaling data. RT-qPCR is expressed as either relative fold change or Log₂/Log₁₀ scaling of relative fold change, while RNA-Seq analysis in this project exclusively utilised Log₂ fold change.

For normalisation, RT-qPCR assays in this project utilised β -Actin as reference/housekeeping gene, however the RNA-Seq analysis utilised Fragments Per Kilobase Million (FPKM) (Zhao et al., 2021b). The sequenced transcripts were quantified, divided by 1,000,000 and normalised against read depth to produce Reads

Per Million (RPM). As larger genes will have more cDNA fragments and therefore will have more reads during sequencing, RPM is divided by the size of the gene in kilobases to normalise and produce Reads Per Kilobase Million (RPKM). RPKM was established for single-end RNA-Seq methodology, whereas some RNA-Seq techniques utilise paired-end techniques wherein a fragment may be read from either end. Fragment Per Kilobase Million (FPKM) accounts for this by quantifying fragments rather than pure reads (Zhao et al., 2021b). As these methods of normalisation radically differ between RT-qPCR and RNA-Seq, they may produce disparate results.

RNA-Seq and RT-qPCR results may differ on between 15-20% of genes, particularly on short sequence or low expression genes (Coenye, 2021). To validate RNA-Seq findings, nine genes with the most significant expression difference for RT-qPCR validation in triplicate (see Figure 6.9 A-I): *RhoGDI2*, *FBX045*, *TPI*, *DDIT3*, *IER3*, *SCL2A*, *PER1*, *FOSL2* and *LDLR*.

RhoGDI2 is associated with acquired Cisplatin (Wu et al., 2016) and 5-FU resistance (Zheng et al., 2013) in gastric cancer cells, and may downregulate *FBXL5* (Moon et al., 2010), although absence of *FBXL5* does not cause a corresponding upregulation of *RhoGDI2* (Wu et al., 2016). Upregulation of *RhoGDI2* in response of *FBXL5* KO in hypoxia further supports previous suggestions of a feedback loop between these two genes, although this effect was not evident at normoxia, with *RhoGDI2* downregulated in *FBXL5* KO cells (Wu et al., 2016; Xiong et al., 2017). The two studies on this interaction between *RHOVDI2* and *FBXL5* focused on the protein-protein interactions, while our results were on mRNA expression, possibly explaining the discrepancy.

Additionally: FBXO45 binds FBXW7 for ubiquitination (Richter et al., 2020) and may be an important therapeutic target for chemotherapy (Lin et al., 2020a). TPI (triosephosphate isomerase 1) deficiency causes anaemia, reduces immune response and pulmonary and cardiac deterioration (Rodríguez-Almazán et al., 2008). DDIT3 (DNA damage-inducible transcript 3) is an apoptosis regulator (Rozpedek et al., 2016). IER3 (Immediate Early Response 3) is associated with cellular stress response, inflammation and tumorigenesis (Arlt and Schäfer, 2011). SCL2A (Solute Carrier Family 2, member 2) is a glucose binding transmembrane protein (Mueckler and Thorens, 2013). PER1 (Period Circadian Regulator 1) is a circadian rhythm regulator and may be an oncogene (Gery et al., 2006). FOSL2 (Fos-like antigen 2) interact with the JUN family of proteins to form AP-1 transcription factor complexes associated with cell proliferation and differentiation and promotes metastasis in colon cancer (Li et al., 2018). LDLR (Low density lipoprotein receptor) binds the cholesterol carrying low-density lipoproteins and is associated with cholesterol-related diseases (Galicia-Garcia et al., 2020).

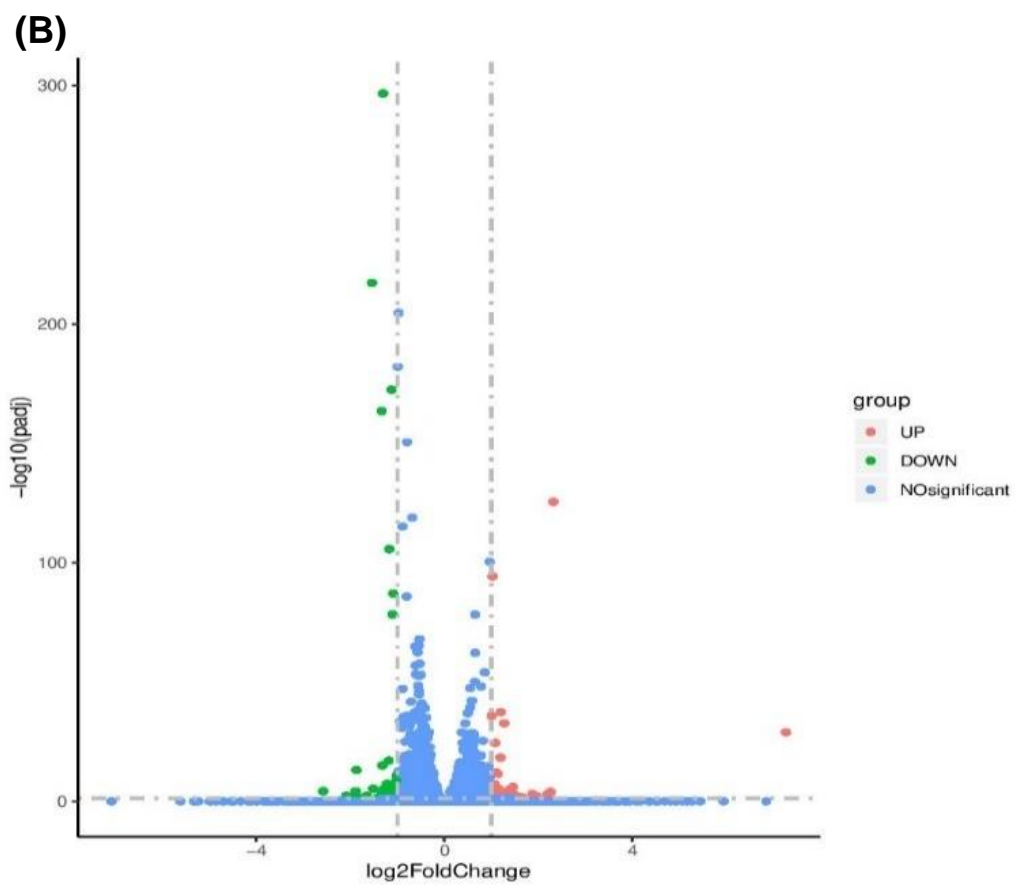
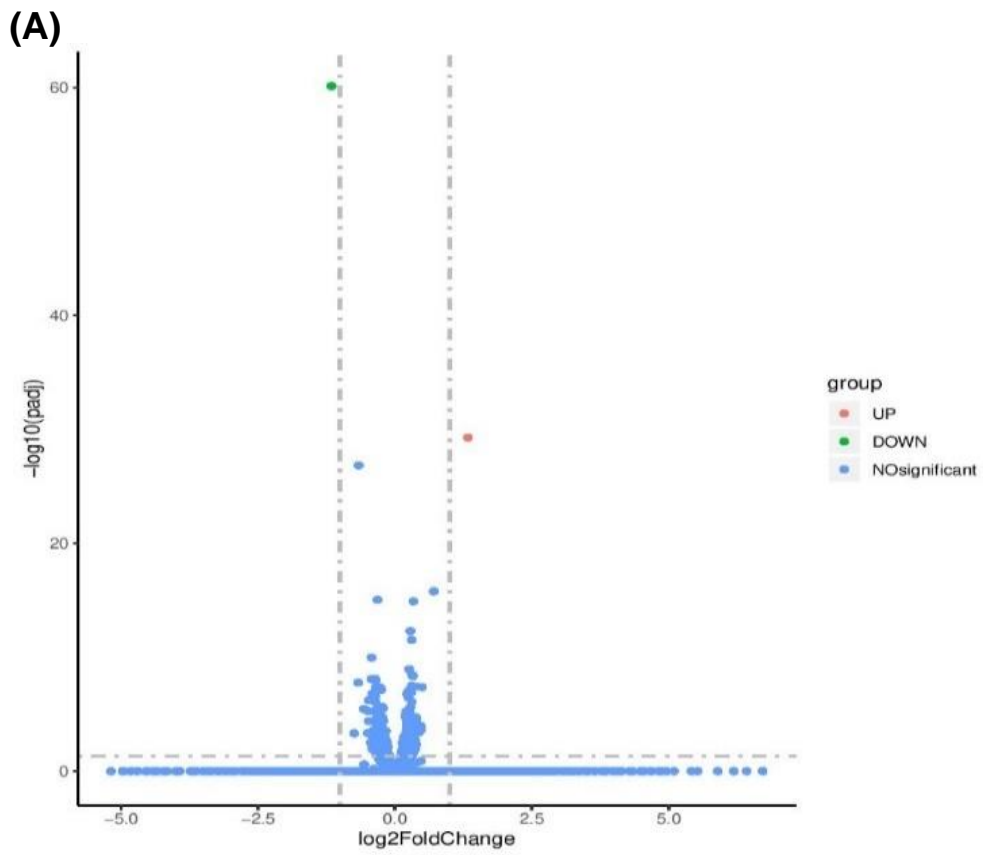


Figure 6.7: Volcano plots representing RNA-Seq results from DLD-1 FBXL5 cells

Volcano plots of RNA-Seq data of log₂ fold change in (A) normoxia and (B) hypoxia conditions. Results demonstrate that hypoxia samples had much greater significantly differentially expressed genes than normoxia samples, implying that FBXL5's oxygen-mediated stability may be more influential than previously believed.

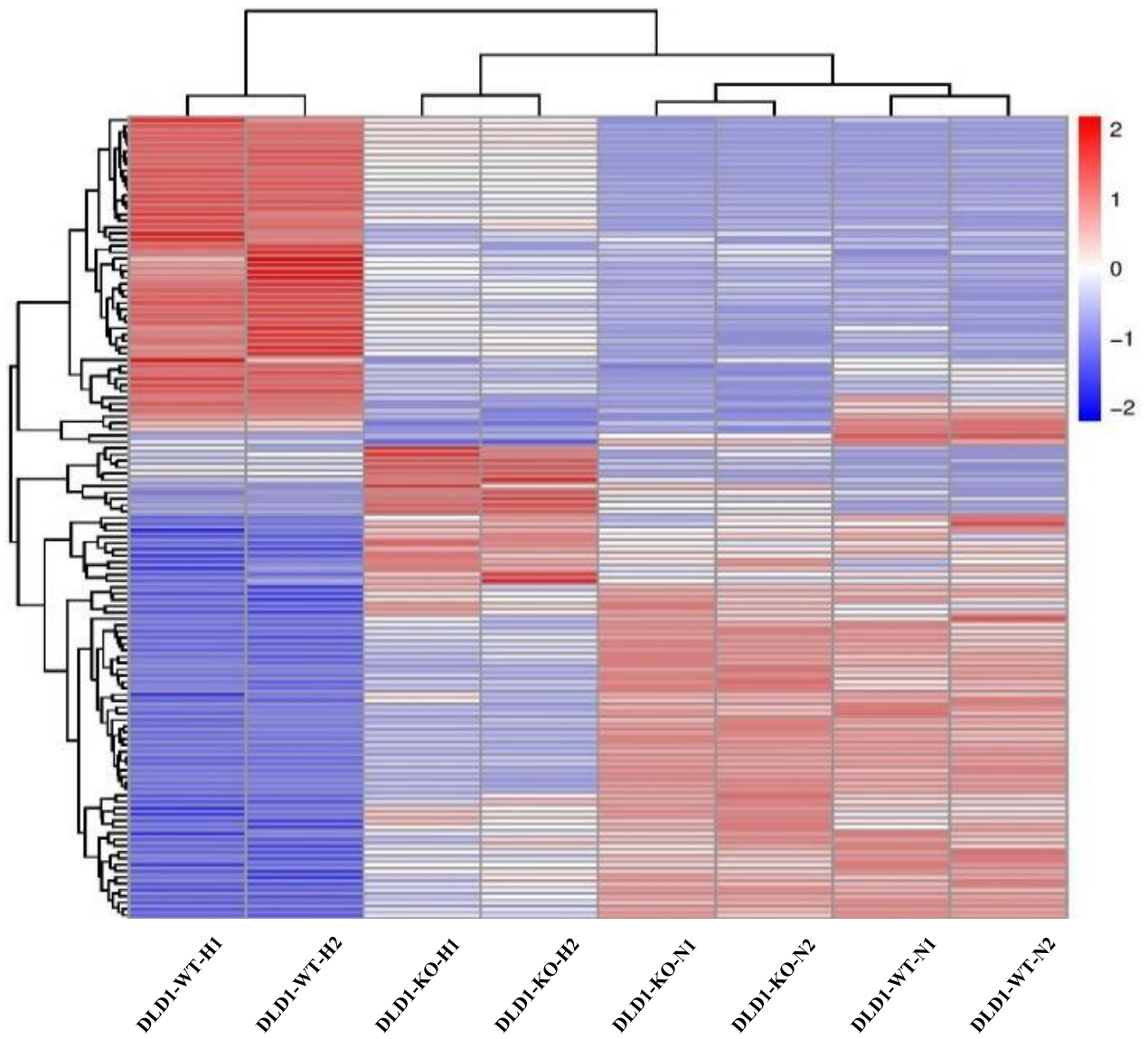


Figure 6.8: Heat map representing RNA-Seq results from DLD-1 FBXL5 cells

Heat Map identifying genes in RNA-Seq data significantly affected by either normoxia and hypoxia conditions, showing how normoxia vs hypoxia and control vs FBXL5 KO RNA-Seq expression data compare. Genes are shown $P < 0.05$ and log₂ fold change (logFC).

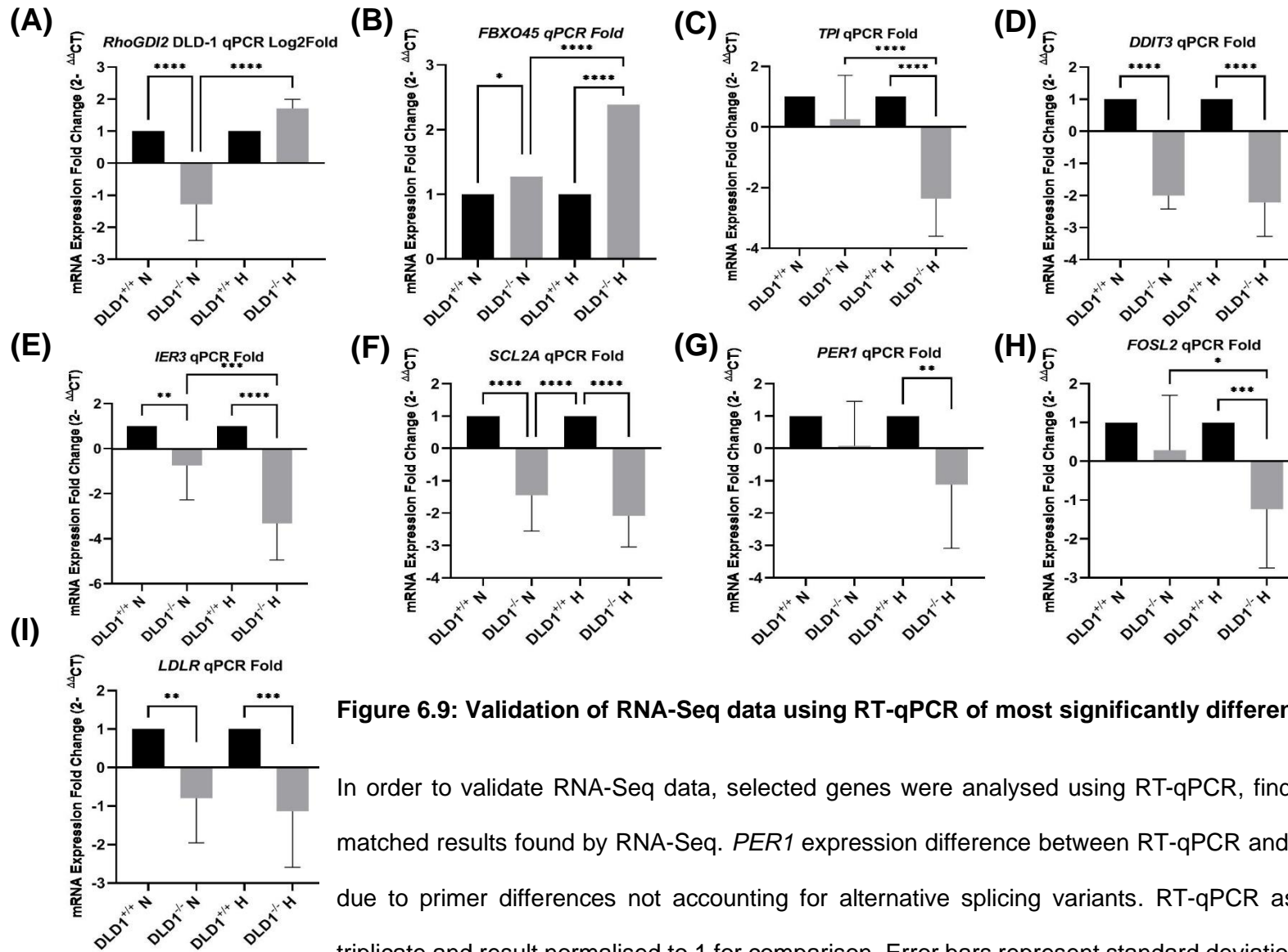


Figure 6.9: Validation of RNA-Seq data using RT-qPCR of most significantly differentiated genes.

In order to validate RNA-Seq data, selected genes were analysed using RT-qPCR, findings all but *PER1* matched results found by RNA-Seq. *PER1* expression difference between RT-qPCR and RNA-Seq may be due to primer differences not accounting for alternative splicing variants. RT-qPCR assay performed in triplicate and result normalised to 1 for comparison. Error bars represent standard deviation. $P < 0.05$ (*), $P \leq 0.01$ (**), $P \leq 0.001$ (***), $P \leq 0.0001$ (****).

RT-qPCR analysis of chosen genes largely validated results obtained by RNA-Seq analysis, however *PER1* RT-qPCR analysis (Figure 6.9 G) did not match RNA-Seq findings. Further RT-qPCR primer optimisation may be required to account for the 19 *PER1* alternative splicing variants (Howe et al., 2021). *RhoGDI2*: (DLD-1: +/+ Nor vs -/- Nor $P = <0.0001$, -/- Nor vs -/- Hyp $P = <0.0001$), *FBXO45*: (DLD-1: +/+ Nor vs -/- Nor $P = 0.0419$, +/+ Hyp vs -/- Hyp $P = <0.0001$, -/- Nor vs -/- Hyp $P = <0.0001$), *TPI*: (DLD-1: +/+ Hyp vs -/- Hyp $P = <0.0001$, -/- Nor vs -/- Hyp $P = <0.0001$), *DDIT3*: (DLD-1: +/+ Nor vs -/- Nor $P = <0.0001$, +/+ Hyp vs -/- Hyp $P = <0.0001$), *IER3*: (DLD-1: +/+ Nor vs -/- Nor $P = 0.0093$, -/- Nor vs -/- Hyp $P = 0.0001$, +/+ Hyp vs -/- Hyp $P = <0.0001$), *SCL2A*: (DLD-1: +/+ Nor vs -/- Nor $P = <0.0001$, +/+ Hyp vs -/- Hyp $P = <0.0001$, +/+ Nor vs +/+ Hyp $P = <0.0001$), *PER1*: (DLD-1: +/+ Hyp vs -/- Hyp $P = 0.003$), *FOSL2*: (DLD-1: +/+ Hyp vs -/- Hyp $P = 0.0003$, -/- Nor vs -/- Hyp $P = 0.0154$), *LDLR*: (DLD-1 +/+ Nor vs -/- Nor $P = 0.0011$, +/+ Hyp vs -/- Hyp $P = 0.0001$)

From this initial analysis of RNA-Seq data and RT-qPCR confirmation, we can conclude that *FBXL5* KO significantly dysregulates numerous genes at both normoxia and hypoxia. Interestingly, *FBXL5* KO had much greater impact on gene expression under hypoxic than normoxia condition. This further supports previous supposition that due to *FBXL5*'s unique hemerythrin-like domain and oxygen sensitivity, its activity as an E3 ubiquitinating ligase may be related to environmental and extra-cellular factors such as iron depletion and oxygen saturation.

6.1.2.2. Pathway mapping of RNA-Seq data from DLD-1 *FBXL5* KO cell lines identifies novel pathways affected by *FBXL5* knockout.

RNA-Seq analysis of DLD-1 *FBXL5* KO cell lines successfully identified numerous novel genes correlated with *FBXL5* expression. However, assessing the individual impact of each novel gene is beyond the scope of this project, although further *in vitro* analysis of this data will be invaluable to future investigations of *FBXL5* in colorectal cancer. To more effectively analyse this data, we utilised the WebGestalt online system (WEB-based Gene SeT AnaLysis Toolkit) (Liao et al., 2019) to map significantly differentially expressed genes to pathways via the KEGG Pathway Database (Kanehisa et al., 2021), thereby more clearly elucidating the function of *FBXL5* in colorectal cancer. Webgestalt is a functional enrichment analysis tool used to map large quantities of genetic data to associated pathways using the KEGG Pathway database (Kyoto Encyclopaedia of Genes and Genomes (Kanehisa et al., 2021)). The KEGG Pathway database is a collection of manually drawn pathway maps that include molecular interaction, reaction and relationship networks for metabolism, genetic information and environmental information processing, cellular processes, human disease and drug development and interaction (Kanehisa et al., 2021).

In brief: Genes with greater than 2-fold differential expression and *P* value <0.05 were uploaded to WebGestalt (Version 12-09-2019) and analysed via Over-Representation Analysis (ORA) using the KEGG Pathway database and genome reference set (normoxia 470 genes total, hypoxia 1,527 genes total). Data was sorted by False Discovery Rate (FDR) significance level using Hommel multiple test adjustment. Results of WebGestalt mapping to KEGG pathways is shown in Figures 6.10-13. Not all genes were successfully mapped to pathways. Summary tables of significantly

differentially expressed genes in normoxia and hypoxia as mapped to KEGG pathways can be found in the appendices (Appendices Tables 8.3 and 8.4).

While DLD-1 FBXL5 knockout altered transcriptome activity under normoxic conditions, these were not significantly associated with any specific pathway at Log2Fold expression (Figure 6.10 and 6.11). However, results obtained from hypoxic sample were much more significantly differentially expressed genes (Figure 6.12 and 6.13). These genes were mapped to several pathways including Epstein-Barr virus infection (0.003 FDR), Colorectal Cancer (0.003 FDR), central carbon metabolism in cancer (0.008 FDR), pancreatic cancer (0.01 FDR), viral carcinogenesis (0.015 FDR), Kaposi sarcoma-associated herpesvirus infection (0.018 FDR), IL-17 signalling (0.025 FDR), Herpes simplex infection (0.027 FDR), endocytosis (0.027 FDR), spliceosome activity (0.035 FDR), *HIF-1a* signalling (0.037 FDR), epithelial cell signalling in helicobacter pylori infection (0.042 FDR) and antifolate resistance (0.023 FDR).

While investigating every differentially expressed gene identified in this analysis is beyond the scope of this project, several are of notable interest and have not previously been associated with FBXL5. *IKBKB/IKK β* (Inhibitor of nuclear factor kappa-B) is a master regulator of NF- κ B in immune response and inflammation and is associated with cancer related processes including cell proliferation, migration and apoptosis and immune dysregulation (Dolcet et al., 2005; Slattery et al., 2018). *IRF3* (interferon regulatory factor 3) is an interferon regulatory factor, regulating innate immunity and viral infection responses and is activated by MAVS (mitochondrial antiviral signalling protein), which was also found significantly differentiated in this analysis (Peng et al., 2017b). Both *HLA-A* and *HLA-F* (human leukocyte antigen A and F), responsible for short peptide immune response and regulation were significantly differentially expressed under hypoxic conditions (Lin and Yan, 2019). *CYLD* (CYLD lysine 63

deubiquitinase) is a tumour suppressor and deubiquitinating enzyme highly conserved among multiple species and associated with Brooke-Spiegler Syndrome and familial trichoepithelioma that may regulate NF- κ B activation (Sun, 2010). Furthermore, *STAT2* (signal transducer and activator of transcription 2) may be a downstream target of interferon and have an essential role in inflammatory response and metastasis (Lee et al., 2020). Taken together, this suggests a previously unknown regulatory role for *FBXL5* in innate immunity, potentially targeting IKK β and IRF3 for ubiquitination.

Additionally: several MAP kinases including *MAPK11*, *MAP3K7* and *MAPK8* were dysregulated in knockout cells under hypoxic conditions. *FBXL5* induces phosphorylation of ERK and p38 members of the MAP kinase family (Zhong et al., 2014), however results obtained from RNA-Seq analysis suggests a larger role for *FBXL5* in MAPK regulation than previously understood. This analysis also further determined that *FBXL5* KO has dramatically greater impact on DLD-1 cells under hypoxic rather than normoxia conditions. *FBXL5*'s hemerythrin-like domain is unique among mammalian proteins for requiring iron binding during synthesis for stability and interacting with oxygen in a real-time fashion (Chollangi et al., 2012). Deletion of this domain disables *FBXL5*'s iron-dependent regulation but when oxygenised will bind IRP2 (Wang et al., 2020a). The impact of *FBXL5* KO on colorectal cancer cells hypoxic conditions has been of interest during this project, and the combination of data outlined in Section 5.1.3 and this RNA-Seq analysis has expanded understanding of *FBXL5* impact on DLD-1 cells under normoxic and hypoxic conditions. Future analysis of these significantly differentially expressed genes and pathways in additional *FBXL5* KO colorectal cancer and patient-derived models would greatly develop our understanding of *FBXL5*.

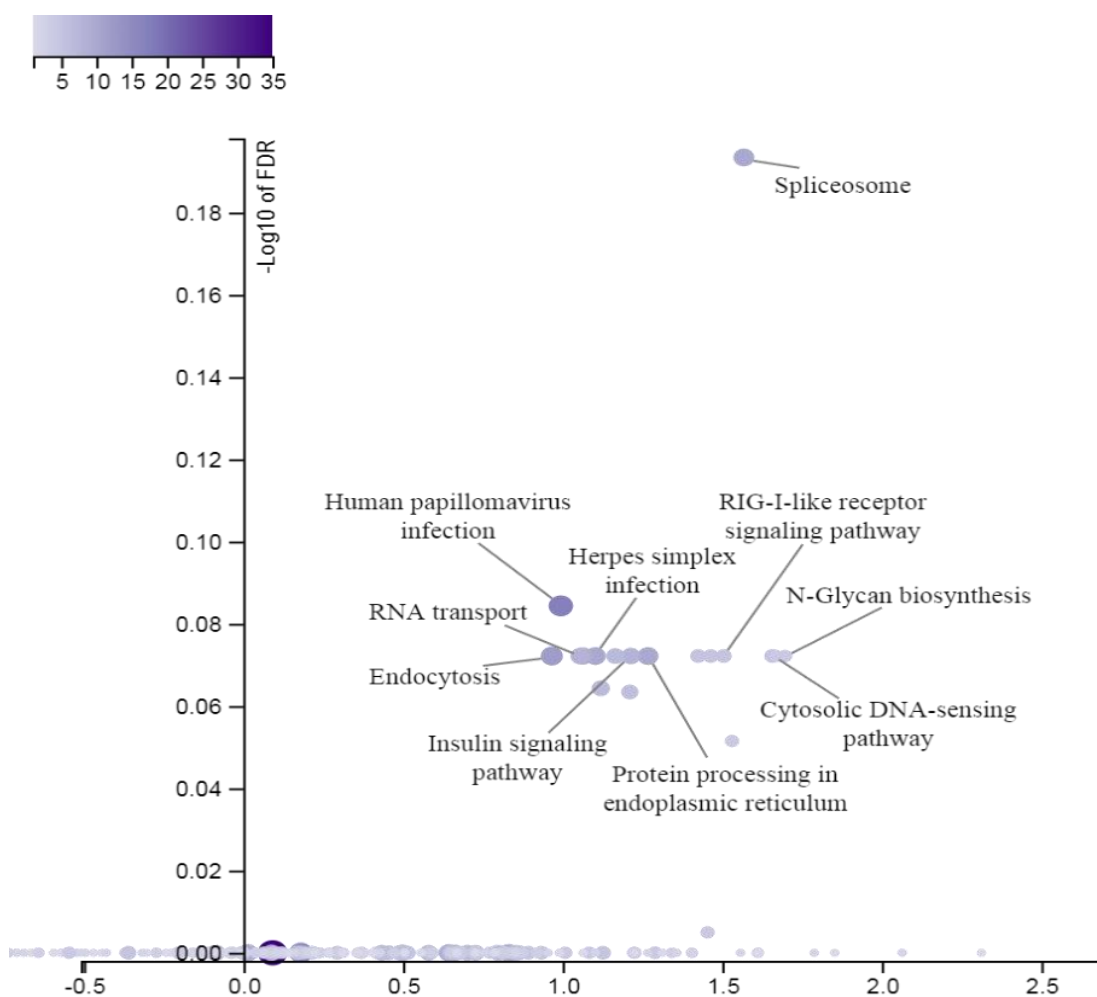
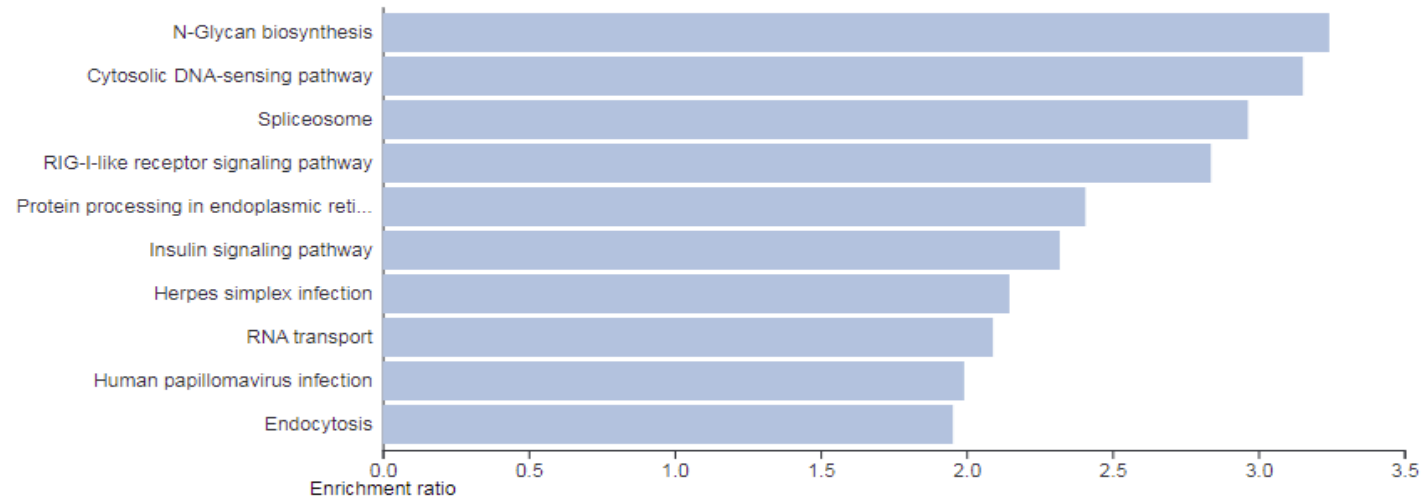


Figure 6.10: WebGestalt pathway mapping analysis of RNA-Seq normoxia data of DLD-1 and DLD-1 *FBXL5* KO cells.

Volcano plot of log2 enrichment ratio vs Log10 FDR. Significant categories coloured by gradient based on FDR (False Discovery Rate). This graph demonstrates that no pathway was significantly associated with *FBXL5* KO at normoxia in our RNA-Seq data, implying multiple smaller associations rather than major regulatory roles.

(A)

FDR ≤ 0.05 FDR > 0.05



(B)

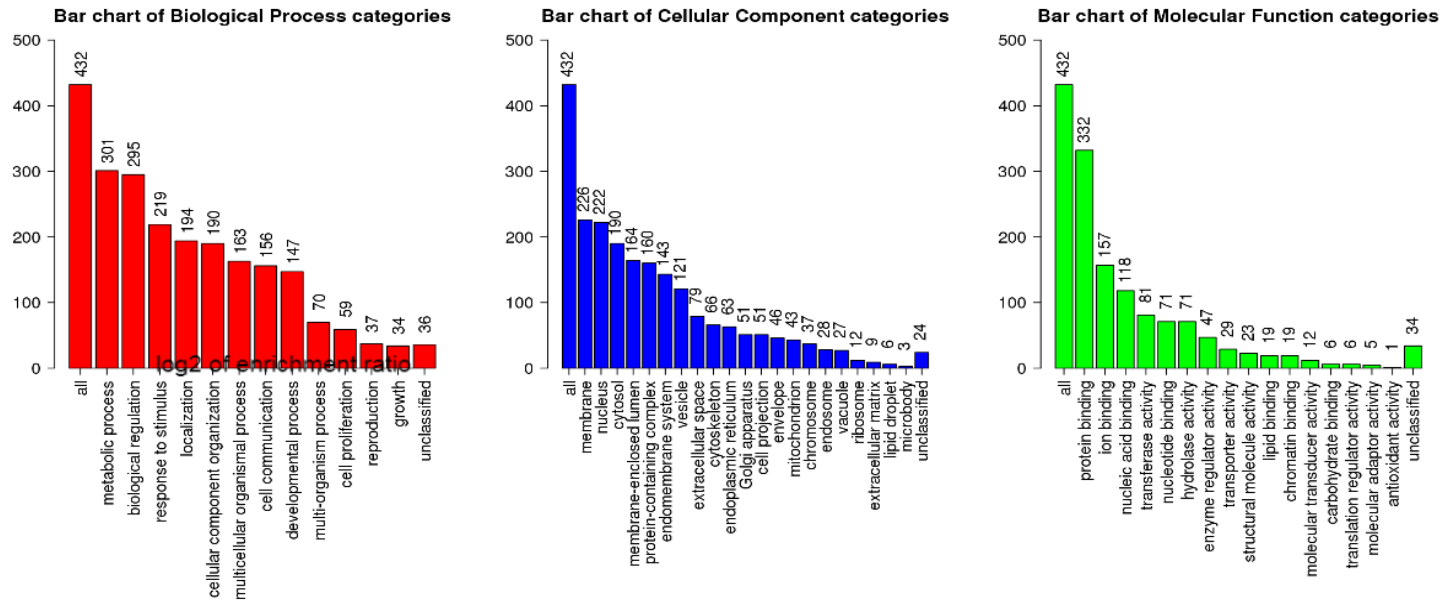


Figure 6.11: WebGestalt pathway mapping analysis of RNA-Seq normoxia data of DLD-1 and DLD-1 *FBXL5* KO cells.

(A) Summary bar graph of pathways significantly associated with *FBXL5* KO in normoxia. No pathways were found significantly associated with *FBXL5* at normoxia with Log2fold change, suggesting that *FBXL5* has small associations with numerous pathways but not significant effects on any. (B) Summary of significant genes categorised by biological process, cellular compartment and molecular function

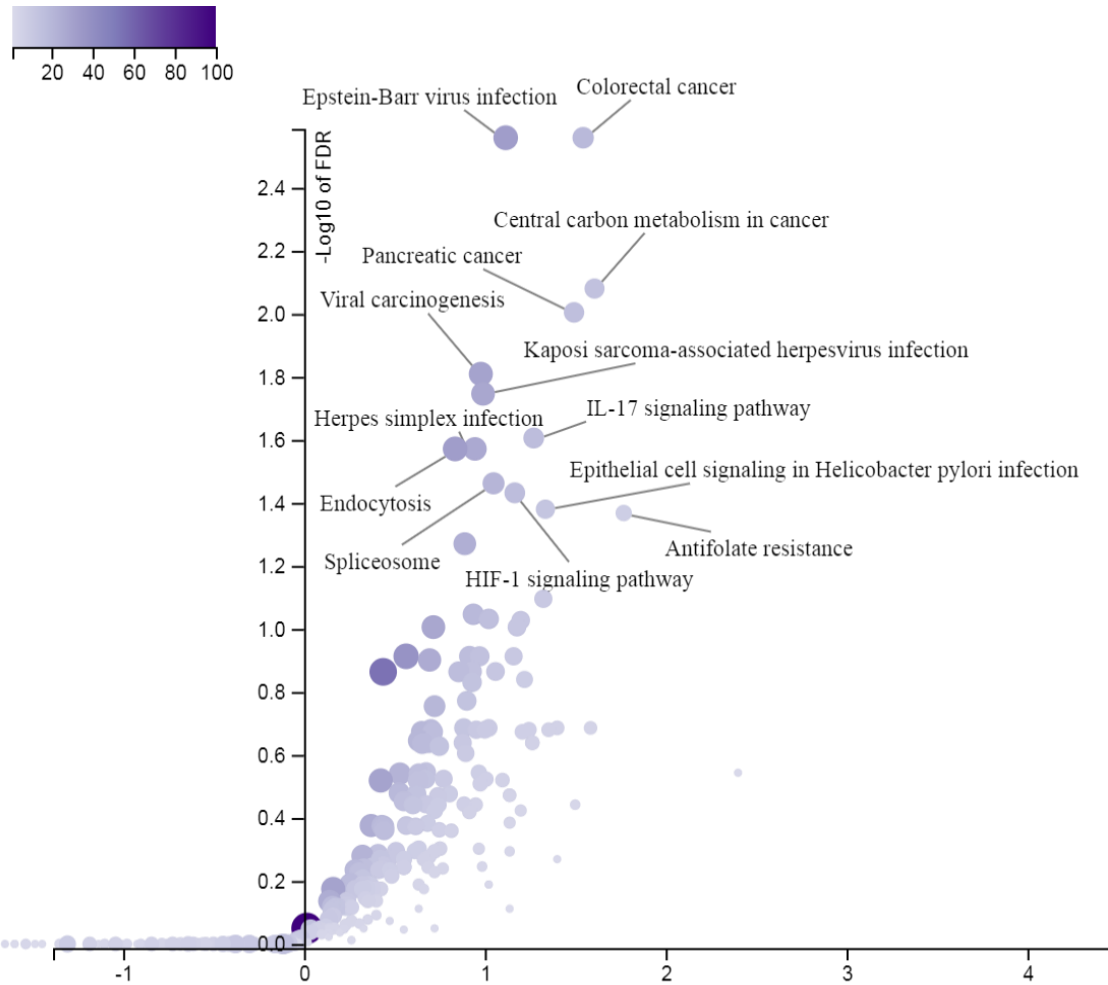


Figure 6.12: WebGestalt pathway mapping analysis of RNA-Seq hypoxia data of DLD-1 and DLD-1 *FBXL5* KO cells.

(A) Volcano plot of log₂ enrichment ratio vs Log₁₀ FDR. Significant categories coloured by gradient based on FDR. Unlike Normoxia data, *FBXL5* KO in hypoxia is significantly associated with several pathways including central carbon metabolism, colorectal and pancreatic cancers, hypoxia and immune response.

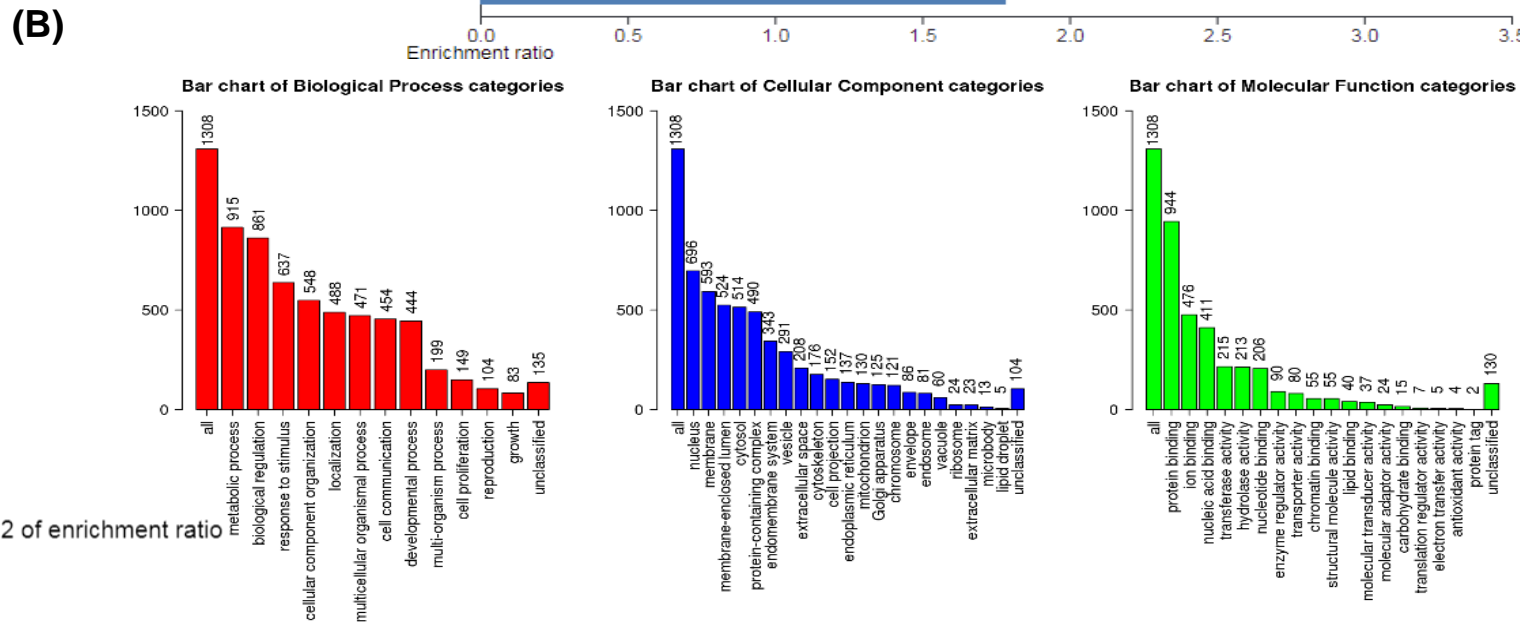
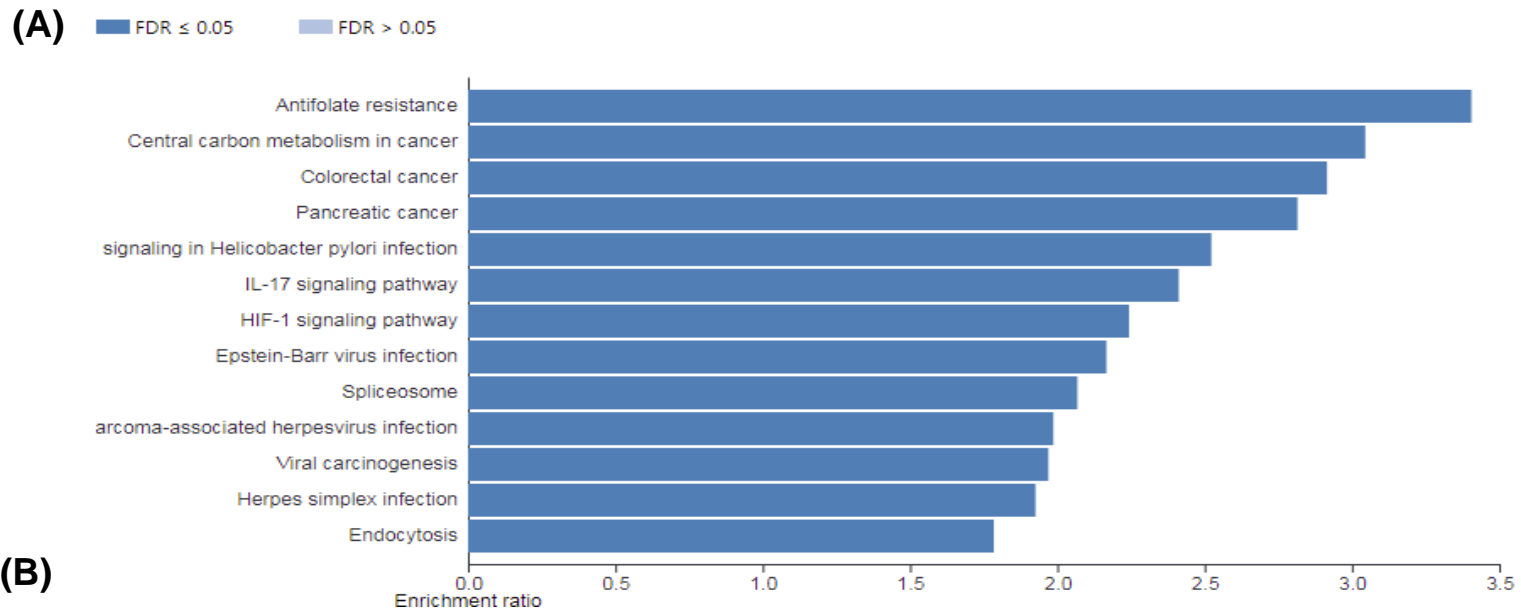


Figure 6.13: WebGestalt pathway mapping analysis of RNA-Seq hypoxia data of DLD-1 and DLD-1 *FBXL5* KO cells.

(A) Summary bar graph of pathways significantly associated with *FBXL5* KO in normoxia. Numerous pathways were found significantly associated with *FBXL5* KO at hypoxia, further supporting previous findings that *FBXL5* may have a greater role at hypoxic conditions. (B) Summary of significant genes categorised by biological process, cellular compartment and molecular function.

6.2. Discussion

The advent of accessible and effective bioinformatics tools and databases for bioscientific analysis have greatly facilitated the search for novel genetic, transcriptomic and proteogenomic associations and pathways, as broader and more accurate data can be obtained without requiring extensive technical expertise. However, data obtained from analysis of publicly accessible databases should also be validated *in vitro*. Analysis of the STRING database during this project was able to identify novel *FBXL5* proteomic associations, despite the limited available information on *FBXL5* itself (Figure 6.1, Table 6.1). Additionally, analysis using the GEPIA and UALCAN systems also identified a variety of genes correlated with *FBXL5* expression in colorectal cancer (Table 6.2, Figures 6.2 and 6.3). Several of these genes (*RAP1*, *HCFC2*, *RNF11* and *EID1*) were validated via RT-qPCR and found to be significantly downregulated by *FBXL5* KO in both DLD-1 and SW480 cells, except for *HCFC2* that was only downregulated in DLD-1 (Figure 6.4). These results not only validate the analysis of GEPIA and UALCAN databases, but also encourages use of these databases for future studies that investigate poorly understood genes and proteins of interest.

The results obtained via RNA-Seq analysis of DLD-1 FBXL5 knockout cells and subsequent pathway mapping via the Webgestalt and KEGG Pathway systems demonstrates that FBXL5 may have a substantially greater role in colorectal cancer cell and molecular dysfunction than previously suspected. The role of FBXL5 in immune functionality is of particular interest, potentially underlining its impact on both development of, and immune response to cancer (Figures 6.12 and 6.13). Further analysis of this data, for example by reducing threshold LogFold values from Log2 to Log1 may identify additional novel substrates and pathways associated with FBXL5 activity. However, more thorough analysis of this RNA-Seq data is beyond the scope of this project. Future work would also benefit from inclusion of alternative immortalised and primary cell lines to improve data validity. This initial analysis has demonstrated the significance of FBXL5 in colorectal cancer cell lines and identified numerous novel pathways and substrates for FBXL5.

Among other notable genes identified in this RNA-Seq: *mTOR* was significantly upregulated in knockout cells and *c-MYC* was downregulated, both critical oncogenes and cell cycle regulators highly associated with cancer. FBXL5 upregulates mTOR expression via PTEN degradation, and while mTOR is normally inhibited under hypoxic conditions, these results suggest that despite FBXL5 dysfunction at hypoxia, it still functions to downregulate mTOR (Brugarolas et al., 2004). FBXL5 is not associated with c-MYC, however several F-box including FBXW7 and FBXL16 are (Morel et al., 2020). *FNI/fibronectin* was dramatically upregulated in DLD-1 KO cell lines under hypoxic conditions, and is a significant contributor to physical cell structure and behaviour including adhesion, growth, migration and differentiation, as well as having both tumour suppressive functionality by preventing cellular

transformation, but also an oncogenic role by facilitating late stage metastasis via epithelial-mesenchymal dysregulation (Lin et al., 2020b).

SRSF2 (Serine and arginine rich splicing factor 2) is upregulated in knockout cells and is a primary spliceosome regulator, inhibition of which leads to decreased leukaemia in mice (Aujla et al., 2018). *BAK1* (BCL-2 homologous antagonist killer), a member of the *BCL-2* (B-cell lymphoma 2) family, is an apoptosis inducer, interacting with p53 in response to cellular stress (Westphal et al., 2014). *TSC2* (Tuberous sclerosis 2) prevents ubiquitination of *TSC1*, both acting in conjunction as cell growth, proliferation and upstream oncogene regulators (Dibble and Manning, 2010). *CDK1* (Cyclin-dependent kinase 1) is an important cell cycle regulator by forming complexes with other cyclins and phosphorylating substrates (Enserink and Kolodner, 2010). Finally, *E2F3* (E2F transcription factor 3) is a tumour suppressor regulator in bladder cancer and may interact with DNA tumour viruses, although further research is required to identify the precise mechanism involved (Feber et al., 2004).

Most interestingly, analysis of the RNA-Seq data demonstrated that *FBXL5* KO has a substantially greater effect in DLD-1 cell under hypoxic than normoxia conditions. Pathway mapping of RNA-Seq data found greater significance in hypoxia sample data than normoxia, identifying numerous novel pathways affected by *FBXL5* KO that have not been previously studied, including several cancer, viral infection and cell signalling associated pathways. *FBXL5* has a unique hemerythrin-like domain that requires iron binding during protein synthesis, but acts as a real-time oxygen sensor, however the impact of this has not been extensively studied, only noting that deletion of this domain disables *FBXL5*'s iron-dependent regulation (Chollangi et al., 2012; Wang et al., 2020a). Several other F-BOX have previously been associated with hypoxia: *FBXL14* is potentially downregulated by hypoxia in mouse cell lines (Viñas-

Castells et al., 2010) and both FBXW7 and FBX011 partially regulate HIF-1 α (Ju et al., 2015) (Cassavaugh et al., 2011). These results substantially expand our understanding of FBXL5's role in both normoxia and hypoxia and provide numerous novel targets for further research. Additionally, the pathway mapping results and RNA-Seq data findings again support previous supposition that FBXL5 KO more significantly affects pathways and mechanisms activated due to extra-cellular stimuli and environmental factors such as immune response, EMT and hypoxia.

Chapter 7: General Discussion

7. Overview

One of the fundamental limitations of current bioscience research is the lack of *in vitro* models that accurately encapsulate *in vivo* responses. Less than 8% of *in vivo* clinical trials of cancer treatments translate to human clinical trials, making animal models inefficient, expensive and ethically contentious (Mak et al., 2014). While current *in vitro* immortalised cell line models are comparatively inexpensive and accessible, their usefulness is limited by their monocellular, 2-dimensional culture and genetic drift, cross-contamination and sample misidentification issues as well as a general lack of translatability (Hughes et al., 2007).

Recently, organoids have emerged as a 3D (3-dimensional), tissue-specific, stem cell derived, multicellular *in vitro* model system that accurately encapsulates the genetic and phenotypic characteristics of the original tissue, while being compatible with many standard *in vitro* laboratory protocols (Boretto et al., 2019). Organoids are cultured by the isolation of stem cells from the tissue of interest and incubated with appropriate growth factors and stem cell niche factors, leading to an “organ in a dish” that can be passaged and expanded almost indefinitely in the same manner as immortalised cell lines (Sato et al., 2011). These organoids are more translatable than immortalised cell models and compatible with standard laboratory protocols (Aboulkheyr Es et al., 2018).

Organoids have begun to provide a viable alternative to immortalised cell lines and *in vivo* models for drug discovery and screening and organoid patient biobanking (Perrone and Zilbauer, 2021), genetic-disease and cancer modelling (Crespo et al., 2017; Di Donato et al., 2019; Geurts et al., 2020; Sun et al., 2019), immune infection reactivity (Heo et al., 2018) tumour immune microenvironment (Neal et al., 2018),

proteomics (Lindoso et al., 2019), and functional genetic studies via CRISPR/Cas-9 genomic editing (Kashfi et al., 2020). Patient derived organoids cultured from paired healthy and tumour tissue also present the unique opportunity to investigate patient-specific changes to cellular mechanisms (Kashfi et al., 2018). Organoids represent a significant step forward in the methods utilised for a wide variety of scientific studies. In particular, organoids can replace the use of animals in biosciences research by acting as a middle ground or triage/filtering method between *in vitro* immortalised cell lines and animal models, thereby improving the quality of data obtained and preventing animal wastage.

The Ubiquitin-Proteasome System (UPS) maintains protein homeostasis by targeting unnecessary proteins for degradation by proteasomes. The F-box protein family function as receptor subunits of E3 ligases and play a vital role in the specificity of the UPS activity of downstream substrates degradation. There is currently minimal information on the biological role of many F-box proteins in homeostasis, diseases, and cancer in particular (Table 1.2). Therefore, the initial aim of this project was to explore the impact of the loss of F-box genes on murine intestinal organoid development using F-box gRNAs and the Cas-9-mediated genome editing system. Five knockout murine intestinal organoid lines were identified as possessing significantly altered growth or morphology: *fbxl17*, *fbx031*, *fbxl17*, *fbxl18* and *fbxl5* (Figure 3.9). One of the candidate F-box of particular growth patterns and morphology impact on organoids, called FBXL5, was further investigated using knockout colorectal cancer cell lines.

FBXL5 KO organoids demonstrated less cohesive growth patterns than organoids, expanding laterally rather than vertically and lacking clearly defined crypt and villus regions on the outer surfaces (Figures 3.7-3.9). *FBXL5* KO organoids had significantly increased two-dimensional surface area between Days 1-5 of growth but only displayed a significantly decreased growth rate by Day 7 (Figure 3.11). Surface plot graphs of organoid images also suggest that *fbxl5* organoids may have reduced vertical growth compared to control organoids, however this requires more detailed study (Figure 3.10). Therefore, *fbxl5* may significantly affect murine intestinal stem cell growth and tissue homeostasis and requires further research to fully explore.

Previous research has also associated *FBXL5* with, among others: iron homeostasis (Jiao et al., 2019), epithelial-to-mesenchymal transition (Wu et al., 2015b) HIF-1a and hypoxia (Machado-Oliveira et al., 2015a), PI3K/AKT/mTOR pathway modulation (Yamauchi et al., 2017; Yao et al., 2018), Cisplatin resistance in colorectal cancer (Wu et al., 2016).

In Chapter 4, we initially characterise the cell behaviour of colorectal cancer cells knocked out for *FBXL5* including morphology, growth patterns, cell migration/attachment, cell division and initial follow-up on potential EMT related phenotypes. DLD-1 and SW480 *FBXL5* KO cells presented phenotypical and morphological characteristics with reduced cell-cell cohesion, spindle-like morphology and cellular elongation typical of mesenchymal cells (Figure 4.3). The flow cytometry cell-cycle analysis of *FBXL5* KO cells showed G1 and SuperG2 phase accumulation of DLD-1 cells but not SW480 cells (Figure 4.5). This accumulation in the G1 phase may be caused by environmental factors including oxidative stress and iron metabolism, which *FBXL5* may be associated with (Chollangi et al., 2012; Ruiz and Bruick, 2014).

Wound healing assay determined that by 48 hours post-scratch, FBXL5 KO reduced wound healing rate in both DLD-1 and SW480 cells (Figure 4.6). This result may potentially be explained by previously understood FBXL5 interactions with EMT via SNAIL, which may impact on migratory properties of FBXL5 KO cells (Wu et al., 2015b). Alternatively, p53 is linked to cell migration and invasion characteristics, which FBXL5 is tangentially associated with via PTEN (Yao et al., 2018) (He et al., 2019).

Western blot and RT-qPCR analysis of *FBXL5* KO cells showed significant upregulation and downregulation of EMT markers *Vimentin*, β -*Catenin*, *E-Cadherin* and *SNAIL* at both protein and mRNA stage in a cell-specific manner (Figures 4.7 and 4.8). These results imply that *FBXL5* causes a “partial” mesenchymal state rather than “Complete” EMT transition (Saitoh, 2018), when cells present characteristics of both epithelial and mesenchymal states. *FBXL5* has been previously shown to ubiquitinate SNAIL in liver cancer cells (Tanaka et al., 2016). Therefore, *FBXL5* KO may be only one of many factors regulating EMT/MET.

Growth curve analysis did not identify a significant difference between control and *FBXL5* KO cells in either cell line (Figure 4.4), despite previously published data showing that *FBXL5* KO reduced cell proliferation (Yao et al., 2018). It is unclear what technical factors may contribute to these disparate results. This project generated an incomplete *FBXL5* KO SW480 cell line using CRISPR/Cas-9, while Yao et al generated a complete KD cell line using *shRNA* methodology, which may have greater off-target effects (Jackson and Linsley, 2010). Our project utilised manual cell counting over 8 days, while Yao et al only used a CCD-8 chemiluminescence assay. It would be beneficial to future projects to utilise multiple methods for determining effects on cell proliferation and fully sequenced cell lines to determine possible

mutations. Future studies utilising patient-derived or murine tumour intestinal organoids that lack FBXL5 expression would further expand on the results presented here.

In Chapter 5, to further evaluate the effect of FBXL5 KO in the colorectal cancer cell, we determined to replicate in colorectal cancer cells published studies on FBXL5 from other cancers, including FBXL5 impact on iron homeostasis, autophagy, hypoxia and drug response.

Calcein AM staining shows that after 90 minutes incubation, Calcein AM fluorescence was dramatically increased in DLD-1 *FBXL5* KO cells compared to controls. However, no difference was found in SW480 cells (Figure 5.1), as estimates suggest that cytosolic labile iron represents <5% of total cellular iron (Kakhlon and Cabantchik, 2002), further studies using methods such as Mass Spectrometry may further advance understanding of the association between FBXL5 and labile iron.

Results of treating FBXL5 KO cells with Salinomycin show that DLD-1 and SW480 *FBXL5* KO cells demonstrated resistance to Salinomycin. SW480 control cells were less resistant than DLD-1, with SW480 cells demonstrating complete cell death after 48 hours, but DLD-1 after 72 hours. (Results Figure 5.2).

Autophagy regulates protein and cellular homeostasis by degradation of long-lived or larger proteins in addition to cellular organelles (Cui et al., 2016). Due to the cross interactions between UPS and autophagy, it was deemed a prospective FBXL5 interactor. We examined the effects of *FBXL5* KO on mRNA and protein expression of autophagy factors *ATG5*, *LC3B* and *Beclin1* (Figures 5.7 and 5.8), finding expression of all three factors were either upregulated or downregulated a cell-specific manner. *ATG5* protein expression increased in DLD-1 cells but decreased in SW480

cells and Beclin1 protein expression may be reduced in both cell lines. However, *ATG5* mRNA expression was decreased in both cell lines, and both *LC3B* and *Beclin1* mRNA expression downregulated in DLD-1 knockout cells and increased in SW480 knockout cells respectively.

In late stage tumour growth, hypoxia causes altered cell metabolism and resistance to many chemotherapeutic methods reliant on cell cycle-mediated interaction (Muz et al., 2015). Expression of CITED2 (Cbp/P300 Interacting Transactivator With Glu/Asp Rich Carboxy-Terminal Domain 2) protein, an important *HIF-1 α* regulator, is inversely correlated with FBXL5 expression under hypoxic conditions (Machado-Oliveira et al., 2015a). Despite FBXL5's unique hemerythrin-like domain and oxygen-dependent stability, its role in cellular hypoxia response is unclear (Chollangi et al., 2012). To initially assess the effect of FBXL5 on hypoxia, the clonogenic assay was utilised (Figures 5.9 and 5.10). We found that DLD-1 control and FBXL5 KO colony numbers were unaffected at normoxia but FBXL5 knockout significantly reduced colony numbers under hypoxic conditions (Figure 5.9). Similar results were found in SW480 cells, although significance was slightly greater between control and knockout cells in hypoxia than normoxia. Subsequently, five important hypoxia regulators were selected for RT-qPCR quantification: *HIF-1 α* and *HIF-2 α* , *CA9*, *VEGFR2* and *ANGPTL4* (Figure 5.11), finding that all five markers were upregulated or downregulated in a cell-specific manner in FBXL5 KO cells.

Our group recently demonstrated that *FBXL5* KO induces sensitivity to AM404 (aka Acetaminophen) in CRC cells (Ahmed et al., 2019). Therefore, to further explore the possible role of FBXL5 in drug resistance, we treated DLD-1 and SW480 *FBXL5* KO cells with the platinum-based therapeutics ("platins") Oxaliplatin, Cisplatin and 5-Fluorouracil (5-FU) and the topoisomerase inhibitor Etoposide (Riddell, 2018)

(Montecucco et al., 2015). Consistently across all three platins, *FBXL5* KO substantially increased resistance in DLD-1 while cell resistance was decreased in SW480 cells (Figure 5.12). Treatment of cells with Etoposide found that at 24-hours, *FBXL5* KO decreased resistance in both cell lines. However, this was reversed at 48 and 72-hours, whereby *FBXL5* KO cells demonstrated increased resistance to Etoposide treatment (Figure 5.13). These results further elaborate on the role of *FBXL5* in drug resistance and activity.

Recent advances have made next generation sequencing (NGS) more widely available, rapidly quantifying the entire genome and transcriptome within a sample. We utilised publicly available genomic and transcriptomics databases to identify potentially novel *FBXL5* associations in colorectal cancer patient samples, selecting the STRING protein and gene interaction database, and the GEPIA and UALCAN transcriptomic analysis systems for interrogation (Chandrashekar et al., 2017; Szklarczyk et al., 2019; Tang et al., 2017). STRING analysis was able to identify several high probability interactions with *FBXL5* almost exclusively associated with the UPS regulation, as expected for an E3 ligase such as *FBXL5* (Figure 6.1). GEPIA and UALCAN analysis identified over 5,000 differentially expressed genes correlated with *FBXL5* (Results Figure 6.2 and 6.3).

Additionally, to more comprehensively identify the effects of *FBXL5* on colorectal cancer cells, we submitted DLD-1 control and *FBXL5* KO lines for RNA-Seq analysis. Due to growing evidence of *FBXL5*'s role in hypoxic response and real-time sensitivity to cellular oxygen, samples isolated at both normoxic and hypoxic conditions were submitted. Analysis of the resulting data identified several thousand significantly differentially expressed genes between control and knockout genes at normoxia and hypoxia, with various numbers overlapping between these conditions

(Figures 6.6-6.8). Furthermore, data obtained from RNA-Seq was mapped to significantly associated pathways using Webgestalt and KEGG Pathway database, identifying novel roles for FBXL5 in viral infection, carbon metabolism, IL-17 signalling and others (Figures 6.10-6.13). Results obtained from hypoxic samples were of greater significance than at normoxia, demonstrating a much larger role for FBXL5 in cellular activity in hypoxia than previously suspected.

7.1.Future Directions and Project Limitations

While this project successfully met its initial goals, several possible future directions would expand on project successes, impacts and address limitations.

In this project we were successful in both establishing Cas-9-expressing murine intestinal organoids and utilising them to screen F-box for possible effects on intestinal stem cell activity. However, due to unknown contamination *in vitro* and unanticipated time constraints caused by both laboratory relocation and COVID, we were unable to fully screen the entire library of murine F-box gRNA, nor utilise patient-derived organoids with F-box knockouts. One possible future direction would be to complete this screening to more fully explore the possible effects of F-box proteins on intestinal stem cell activity, using either murine intestinal or patient-derived organoids.

Furthermore, while organoids are 3D models, we utilised 2D microscopy imaging to gather and evaluate phenotypical and growth data. As a result, more subtle complexities of organoid growth may have been lost, particularly in identifying F-box knockout lines that may present stemness or tumour growth alterations that may be difficult to identify in 2D imaging (Lukonin et al., 2020) (Serra et al., 2019). It is possible, for example, that some F-box knockouts may cause alterations to the 3D growth pattern of organoids or resulted in growth rate alterations that are not visible

or easily identified by 2D surface area analysis. Regrettably, our laboratory did not have access to real-time 3D *in vitro* imaging technologies for this project, which would have generated much more accurate and comprehensive data on the 3D growth and morphology of organoids by taking real-time images while in culture, rather than at specific timepoints. Future projects utilising transgenic organoids would greatly benefit from using this technology.

In addition, whole genome sequencing of *FBXL5* KO organoids would greatly benefit future studies. Generating a greater number of *FBXL5* KO immortalised cell lines and more organoid lines using alternative gRNAs would also have provided additional data from the project experiments and more effectively met the project aims. Also: the inclusion of a healthy rather than cancerous colorectal cell line and healthy patient-derived organoids could also demonstrate the impact of *FBXL5* KO on non-cancerous cells and tissue. The generation of *FBXL5* overexpression cell lines would have been highly beneficial for gain-of-function and biochemical functional analysis. Unfortunately, this project was unable to acquire healthy/non-cancerous colorectal epithelial cell lines prior to laboratory relocation in November 2019 and COVID pandemic.

The results obtained from RNA-Seq analysis of DLD-1 *FBXL5* KO cells at normoxia and hypoxia demonstrate that *FBXL5* KO has a significantly greater impact on DLD-1 cell transcriptomic activity at hypoxia. This suggests that future studies on *FBXL5* KO organoids may benefit from conducting studies under both hypoxic and normoxic conditions. Thus far, very few studies have utilised organoids in hypoxia research due to the practical difficulties of handling organoids, which are extremely sensitive to culture and environmental conditions. However, several protocols and studies have been published using both pseudo-hypoxic and “true” hypoxic conditions (Okkelman

et al., 2017) (Kip et al., 2021), which could be applied to future studies. Furthermore, to examine the potential biomarker and impact on colorectal cancer development and clinical relevance of FBXL5 and the expression of its downstream genes to CRC, future studies could utilize tissue microarrays (TMA). TMAs consist of hundreds of patient colorectal cancer tissue histology samples (available in collaboration with our pathologists' colleagues in QMC, Nottingham), which can be analysed for mRNA using in-situ hybridization (ISH), and protein expression simultaneously using immunohistochemistry (IHC) methods.

Further research could be carried out to explore the tumorigenic and chemotherapeutic properties of FBXL5 knockout cells using human colorectal cancer cell-derived xenograft (CDX) and or patient-derived organoid xenograft (PDX) models. Generating conventional and conditional *fbxl5*-knockout mouse has been reported in several groups (Moroishi et al., 2011; Muto et al., 2017; Yamauchi et al., 2017). Therefore, in the near future, we aim to apply an intestinal conditional knockout animal and investigate the role of *fbxl5* in intestinal tissue homeostasis and cancer. Intestinal conditional knockout and xenograft models would further elaborate on the effect of FBXL5 in a more translatable manner compared to immortalised cell and organoid models and allow for the more accurate assessment of FBXL5 impact on factors such as tumour microenvironment and chemotherapeutic impact *in vivo*.

7.2. Conclusions

The results obtained from this project greatly expand the current understanding of FBXL5 in human colorectal cancer cells, suggesting numerous possible pathways and mechanisms by which FBXL5 may contribute to colorectal cancer development and progression. Future studies using patient samples, patient-derived organoids or *in vivo* models may further expand on the translatability of these results. We have identified several novel FBXL5 interactions in EMT, colony formation efficiency, hypoxia, autophagy and drug resistance, all of which are critical for cancer development, metastasis and treatment. In particular, the impact of FBXL5 on response to platinum-based chemotherapeutics may facilitate more effective patient treatment in tumours displaying FBXL5 dysregulation. As such, these results provide important insight into the possible impact of FBXL5 dysregulation in human cancer and makes it a potential target biomarker for both tumour sequencing and personalised medicine. Similarly, chemotherapeutics causing ATG5-mediated autophagy may have unanticipated effects.

In addition, further investigation of RNA-Seq data obtained in this study may uncover novel insights that can be applied to the clinical relevance of FBXL5's potential associations with immune response, viral oncogenes and other pathways directly influencing patient care with colorectal cancer.

The development of a robust, high-throughput method for generating Cas-9-expressing and transgenic “knock-in” and “knockout” organoids will facilitate the use of organoids as a model system for functional genetic and disease modelling (Kashfi et al., 2020). This also includes the use of transgenic patient-derived organoids as a model system to replace or supplement immortalised cell lines. Previously, transgenic

organoid methodology was resource intensive, with electroporation of murine intestinal organoids being extremely inefficient, with <1% success rate (Schwank and Clevers, 2016). Other methods have utilised direct transduction using adeno-associated virus to generate transgenic overexpressing organoids, and while this has been more successful, it also isn't suitable for high-throughput functional studies wherein multiple genes are examined (Quinn et al., 2018). The methods developed in this project for generating Cas-9 expressing and knockout organoids with lentivirus make murine intestinal organoids a more flexible and viable model system while also being applicable to patient-derived organoids [(Kashfi et al., 2020) and unpublished data from Dr. Nateri's lab)]. Current methods of high-throughput functional gene analysis typically rely on transgenic immortalised cell lines and patient derived cell lines, which have poor translatability and are highly resource intensive respectively. By both establishing and validating this method, it will enable other researchers to utilise organoids alongside other model systems, both improving translatability of further expanding our understanding of organoids.

Animal use in drug development for both functional genomic analysis and cytotoxicity studies is substantial, with one million procedures performed per year in the UK alone (generally with one mouse per procedure) (UKHO, 2019) Approximately 33% of these procedures were conducted by the pharmaceutical industry, but failed to produce proportionately impactful results (Hepple, 2005). Less than 8% of pharmaceutical and clinical trials translate effectively between *in vitro* methods to either *in vivo* or human studies (Mak et al., 2014). Therefore, developing more representative and translatable modelling methods is critically important to both the continued development of bioscientific research and the replacement and reduction of animals in such studies. Organoids potentially offer that alternative; being more accurate and representative

than other *in vitro* assays and more practical, cost effective and ethical than *in vivo* models (Moffat et al., 2017).

This project has demonstrated that transgenic murine intestinal organoids are a suitable method for replacing and reducing the number of animals used in biosciences research while also improving translatability of results to clinical practice (Francies et al., 2019). Transgenic organoid modelling significantly reduces the overall number of animals required for future experimental projects, while being both more accessible to researchers and a fraction of the cost of *in vivo* models, facilitating the 3Rs aims of the project to replace and reduce the number of animals used in research.

Chapter 8: Appendices

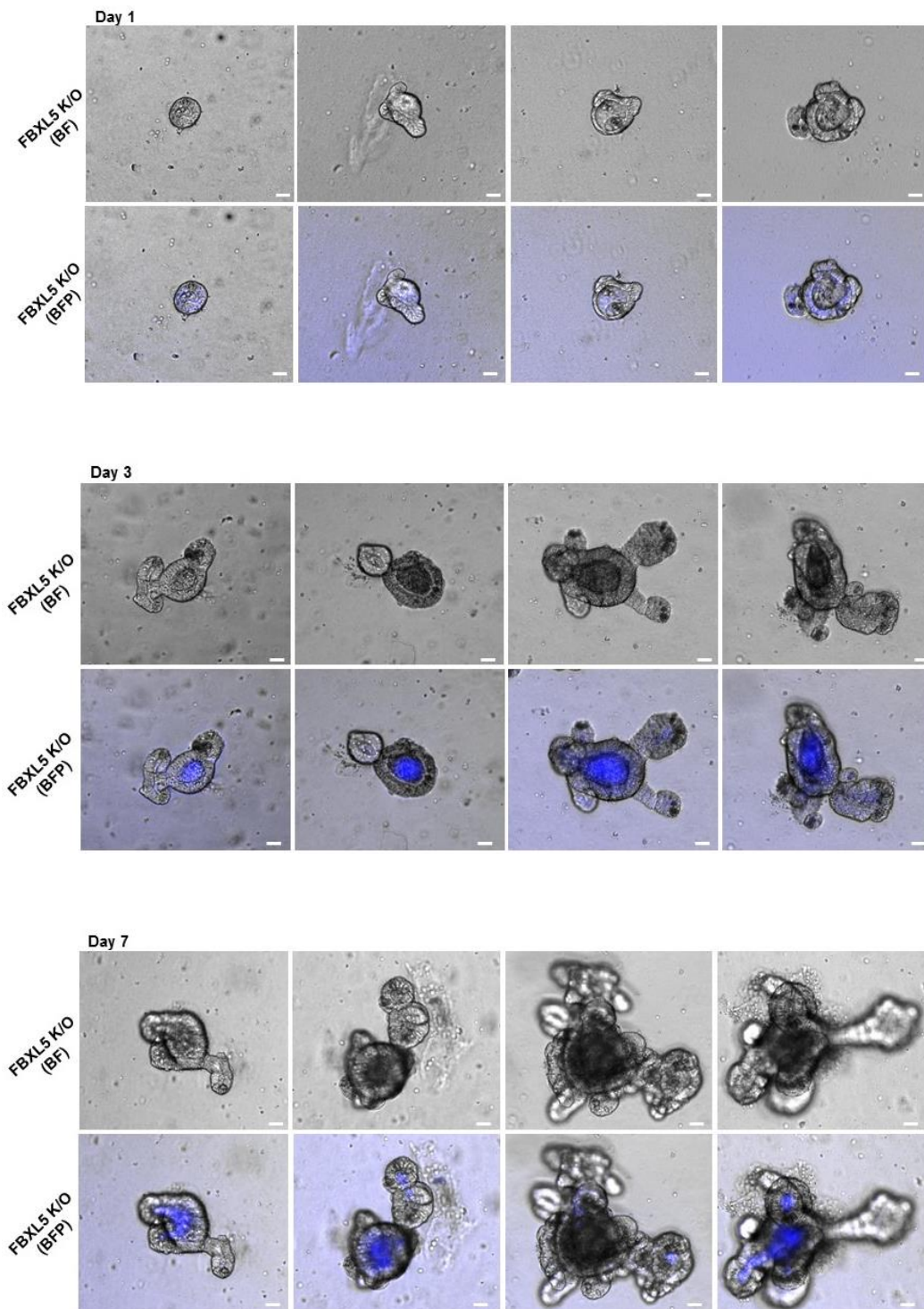


Figure 8.1: Additional representative image of *FBXL5* KO murine intestinal organoids on Days 1, 3 and 7 of growth. Scale bar 75 μ m

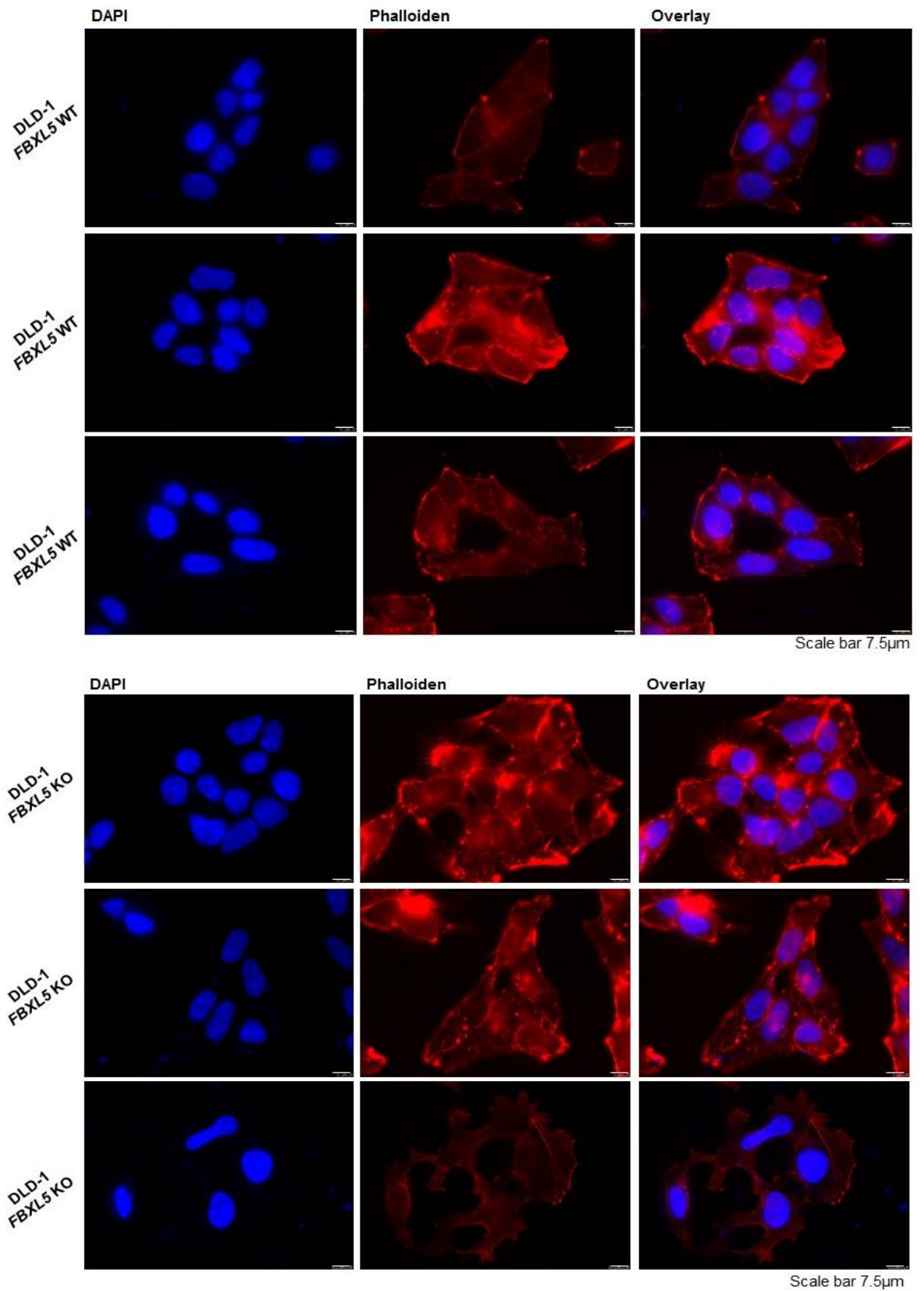


Figure 8.2: Additional representative DAPI/Phalloidin staining images of DLD-1 control and *FBXL5* KO cells

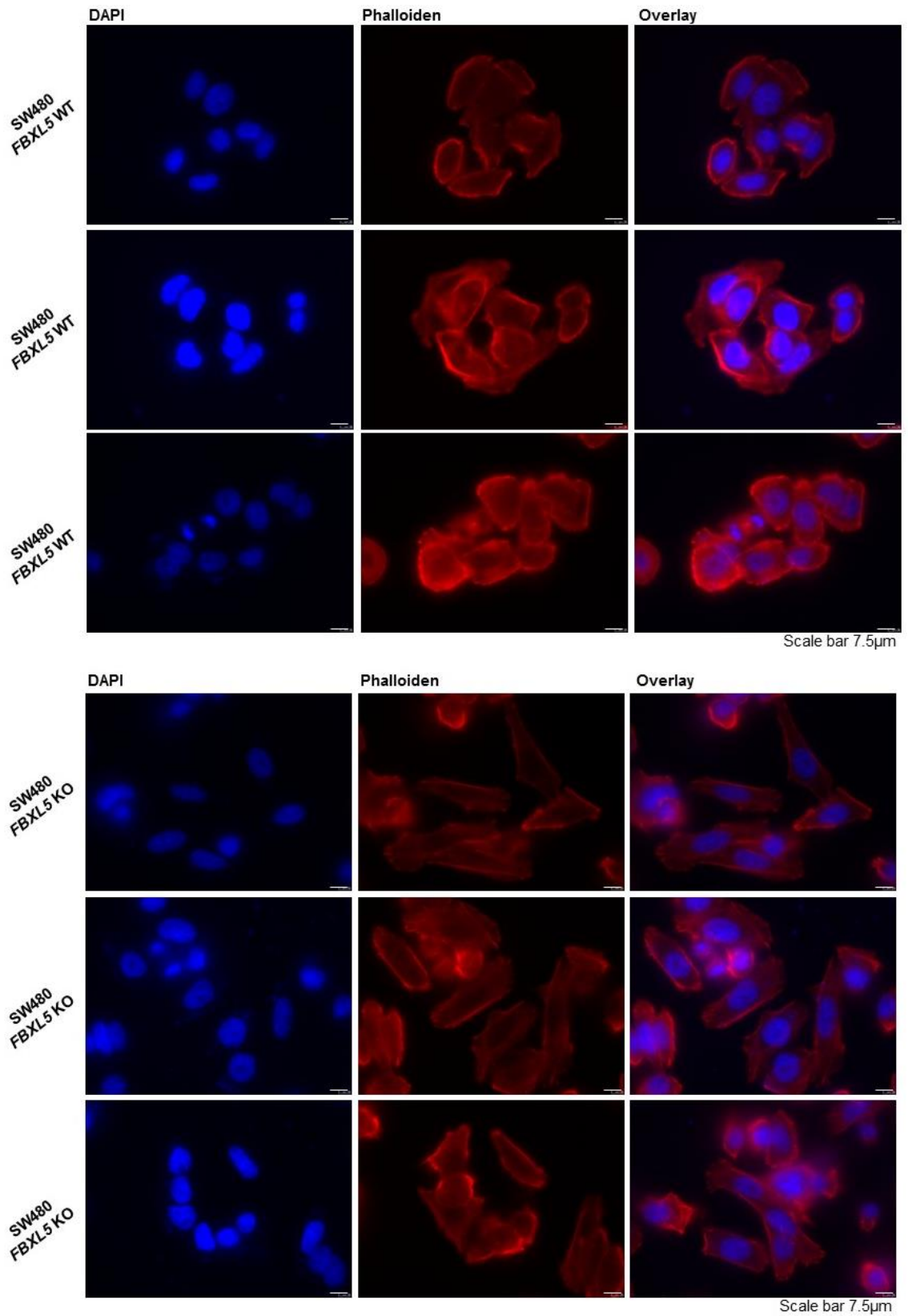


Figure 8.3: Additional representative DAPI/Phalloidin staining images of SW480 control and *FBXL5* KO cells

Figures 8.4: Original Western Blot Images

Figure 3.2: Noggin (1:1000)

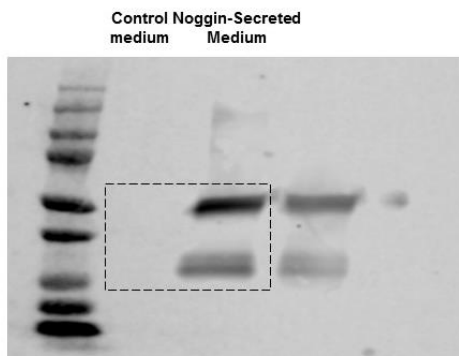


Figure 4.1: DLD-1 and SW480 cell lines expressing constitutively Cas-9 validated using Western Blot (1:1000)

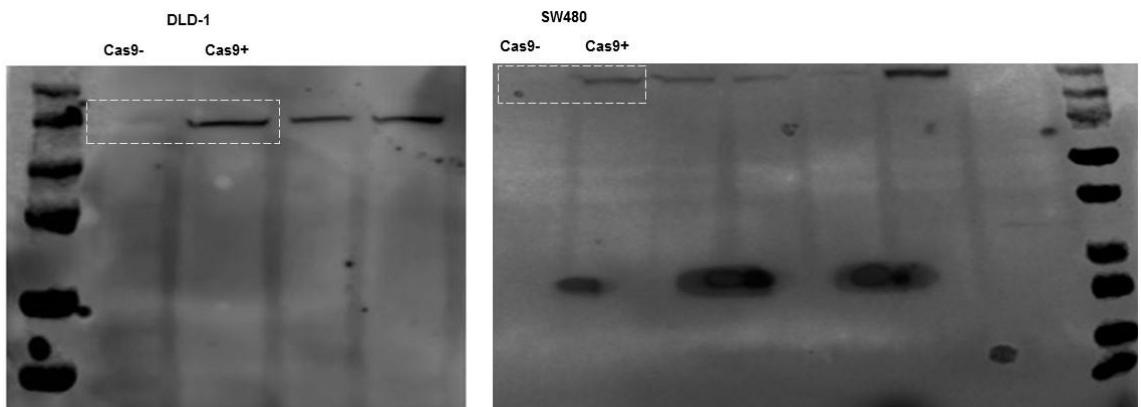


Figure 4.2: The depletion of FBXL5 expression in *FBXL5* KO cell was evaluated by Western Blot (FBXL5 1:100)

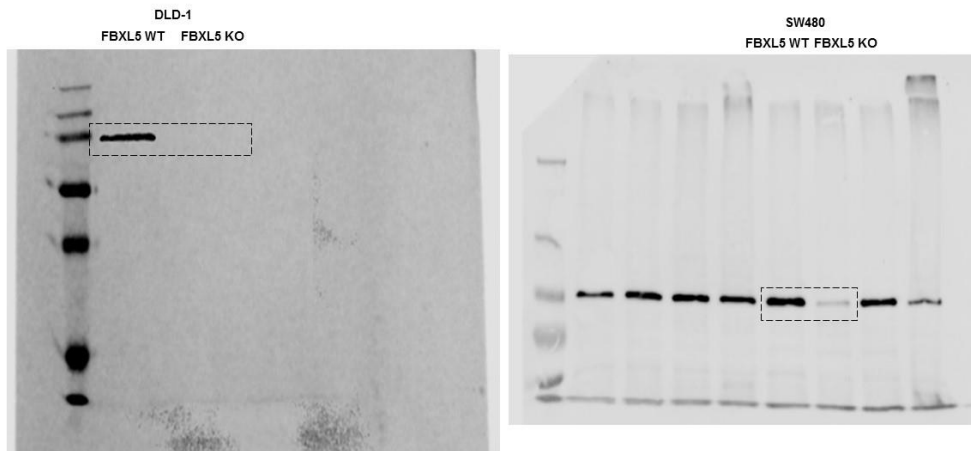
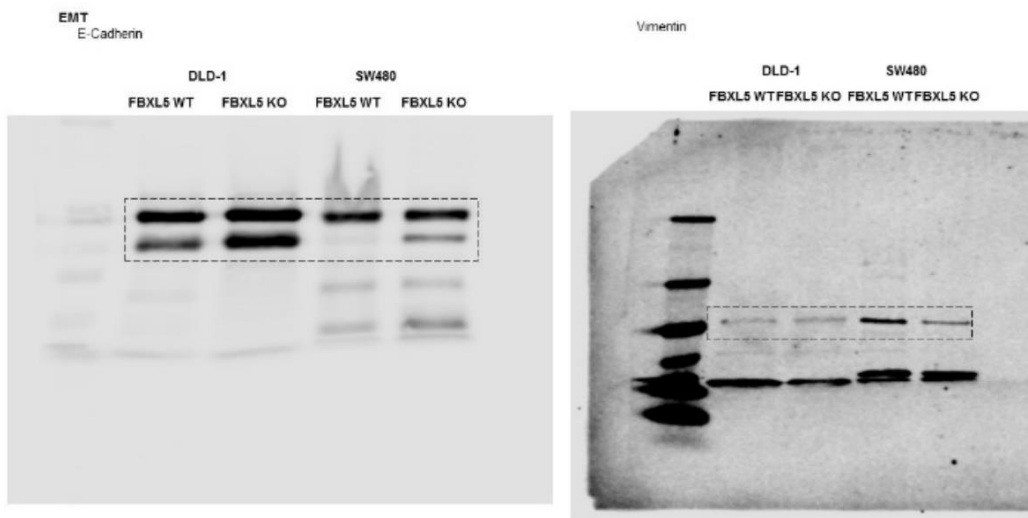


Figure 4.7: EMT markers. Vimentin (1:1000), β -catenin (1:1000), E-Cadherin (1:2500) and SNAIL (1:1000)



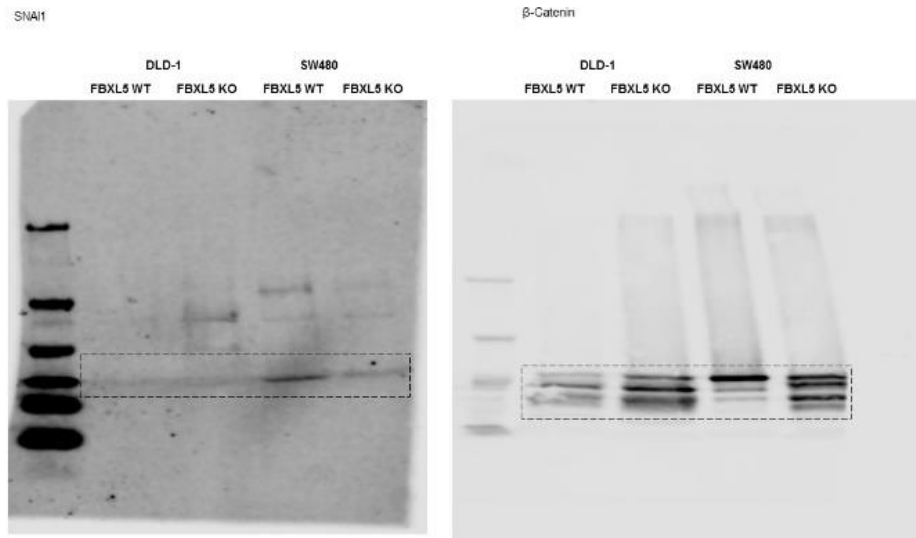
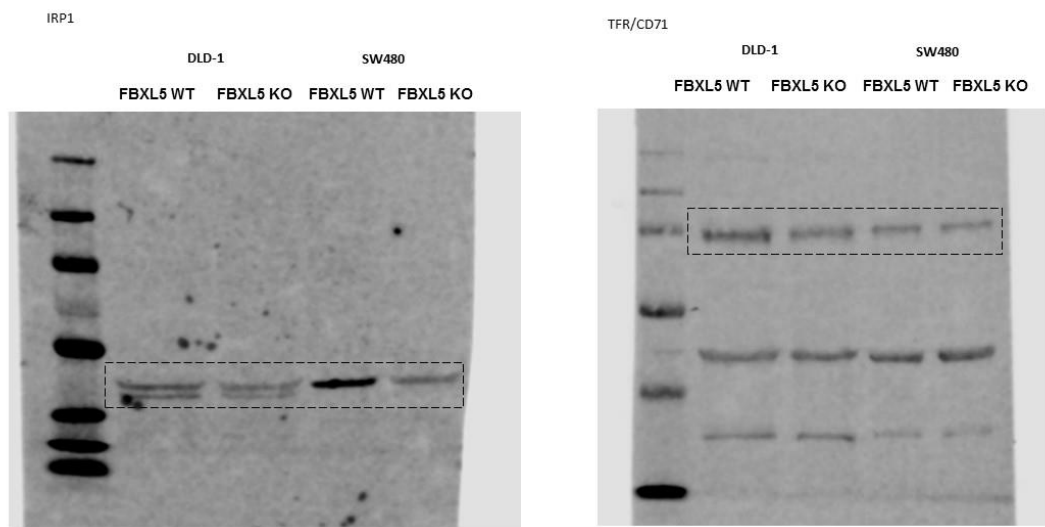


Figure 5.3: FBXL5 knockout significant affects iron homeostasis marker protein expression in DLD1 and SW480 cells. IRP1 (1:1000), TfR (1:250) and Ferritin (1:1000)



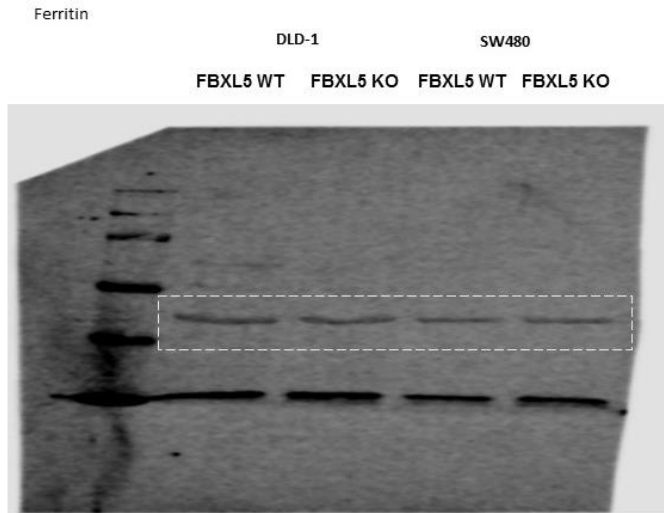


Figure 5.5: FBXL5 knockout significant dysregulates downstream iron homeostasis marker protein (RBCK 1:1000, VHL 1:1000).

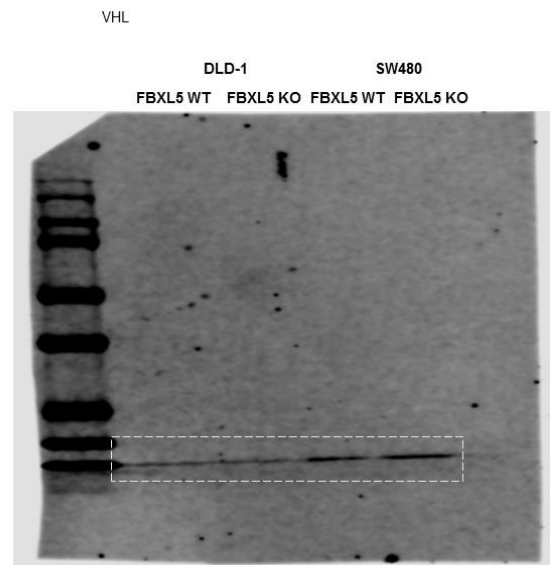
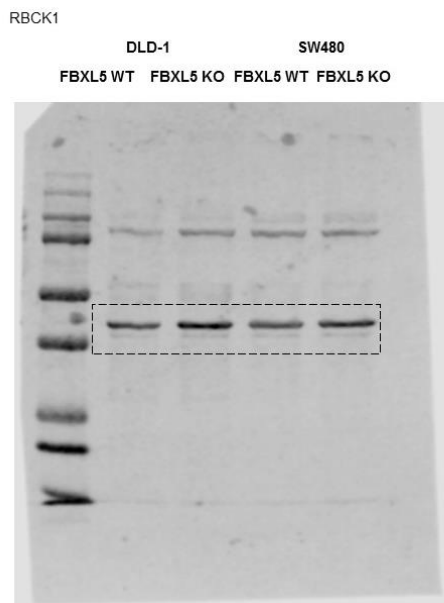


Figure 5.7: Western Blot and RT-qPCR Analysis of ATG5, LC3B and Beclin1 expression in DLD-1 and SW480 cells ATG5 (1:500), LC3B (1:500) and Beclin1 (1:500)

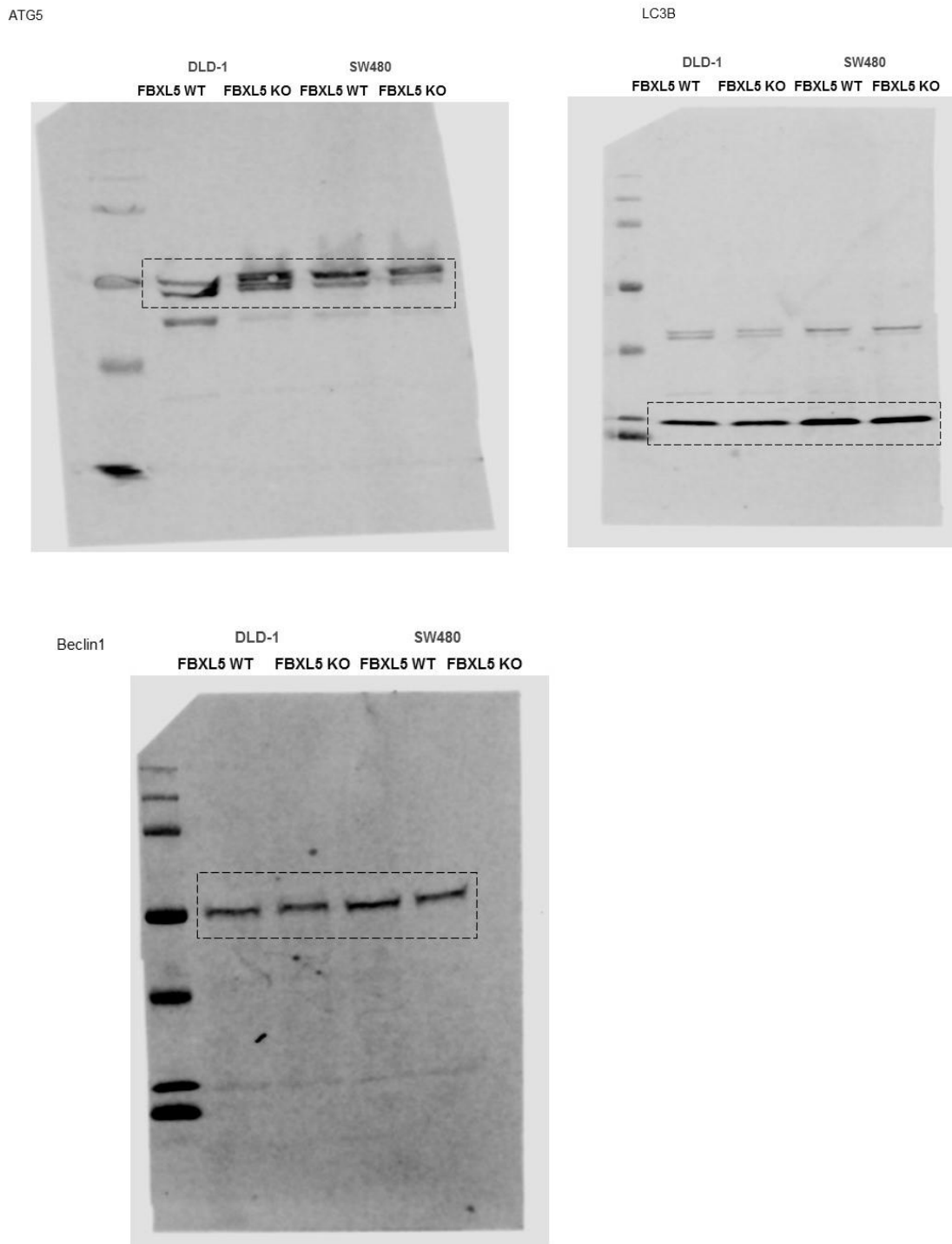


Table 8.1: F-box gRNA data sheets

Approved Symbol	Approved Name	Previous Symbols	Synonyms	Chromosome	Approved Symbol	gRNA pair	LV gRNA Sequence
<u>mFBXL2</u>	F-box and leucine rich repeat protein 2		FBL2, FBL3	3p22.3	<i>FBXL2</i>	1st gRNA	TCCAGGGCTAAGATGTTCCAGG
						2nd gRNA	GGCAGCAACTGGCAACGGGTGG
<u>mFBXL3</u>	F-box and leucine rich repeat protein 3	<i>FBXL3A</i>	FBL3, FBL3A	13q22.3	<i>FBXL3</i>	1st gRNA	CGGACTTATCTCGACTGCCCGG
						2nd gRNA	AGATCCATAAAGCTTGCCGGG
<u>mFBXL4</u>	F-box and leucine rich repeat protein 4		FBL4, FBL5	6q16.1-q16.2	<i>FBXL4</i>	1st gRNA	GTTGTGCTGCATGGTACGAAGG
						2nd gRNA	ATTGACTTCCAGTCGTATGAGG
<u>mFBXL5</u>	F-box and leucine rich repeat protein 5		FBL4, FBL5, FLR1	4p15.32	FBXL5	1st gRNA	ATATCTTTAAGCTCCTCGTAGG
						2nd gRNA	AAATGGACAGCATTACCTCAGG
<u>mFBXL6</u>	F-box and leucine rich repeat protein 6		FBL6	8q24.3	FBXL6	1st gRNA	GCTGGCAAGGGCAACCTTAAGG
						2nd gRNA	CAGCCACAGTTTACGCATTCCGGG
<u>mFBXL7</u>	F-box and leucine rich repeat protein 7		FBL7, FBL6	5p15.1	FBXL7	1st gRNA	TCTGTGCTTGAACTCACGTCGG
						2nd gRNA	CCTGAAAGTACTGACCCGCAGG
Approved Symbol	Approved Name	Previous Symbols	Synonyms	Chromosome	Approved Symbol	gRNA pair	LV gRNA Sequence
<u>mFBXL8</u>	F-box and leucine rich repeat protein 8		Fbl8	16q22.1	FBXL8	1st gRNA	GGAAGCACGAGCATCTTCGGGG
						2nd gRNA	CTTGAGCGTATAGCTGCGCAGG
<u>mFBXL13</u>	F-box and leucine rich repeat protein 13		MGC21636, Fbl13, DRC6	7q22.1	FBXL13	1st gRNA	GCTATCATTAAAAGAGGTCTGG

						2nd gRNA	ATGCTTTTATCATCAACTCTGG
<u>mFBXL14</u>	F-box and leucine rich repeat protein 14		MGC40195, Fbl14	12p13.33	<i>FBXL14</i>	1st gRNA	CTTCTGCACCTGTGCGACATGG
						2nd gRNA	GGGAACAGGCACGAGATGTGGG
<u>mFBXL15</u>	F-box and leucine rich repeat protein 15	<i>FBXO37</i>	MGC11279, Fbl15	10q24.32	FBXL15	1st gRNA	GCGCGTCAGTCGCGCCTCCGG
						2nd gRNA	AGCTGAACGAGCGCCCGGAAGG
<u>mFBXL16</u>	F-box and leucine rich repeat protein 16	C16orf22	MGC33974, Fbl16	16p13.3	FBXL16	1st gRNA	TGCCCTCGGATCACCGATATGG
						2nd gRNA	TGCCATATCGGTGATCCGAGGG
<u>mFBXL17</u>	F-box and leucine rich repeat protein 17	FBXO13	DKFZP434C1715, Fbx13, Fbl17	5q21.3	FBXL17	1st gRNA	ACCCATGAAGCCAACATACTGG
						2nd gRNA	GTTGTTCAGTTACTTCCAAAGG
Approved Symbol	Approved Name	Previous Symbols	Synonyms	Chromosome	Approved Symbol	gRNA pair	LV gRNA Sequence
<u>mFBXL18</u>	F-box and leucine rich repeat protein 18		FLJ11467, Fbl18	7p22.1	FBXL18	1st gRNA	CACTCTCACGCCGTCCTACGG
						2nd gRNA	TTGGCAAGAAGGTGCGCATTGG
<u>mFBXL19</u>	F-box and leucine rich repeat protein 19		DKFZp434K0410, Fbl19, JHDM1C, CXXC11	16p11.2	<i>FBXL19</i>	1st gRNA	GGGCTGACAATGGTGAGGAAGG
						2nd gRNA	GTGAGGAAGGCGCTAACCTAGG
<u>mFBXL20</u>	F-box and leucine rich repeat protein 20		MGC15482, Fbl2, Fbl20	17q12	<i>FBXL20</i>	1st gRNA	ACCCTGTGTCGCTGTGCTCAGG
						2nd gRNA	AGCTCTGGATGGCAGTAACTGG
<u>mFBXL22</u>	F-box and leucine rich repeat protein 22		Fbl22, FLJ39626	15q22.31	<i>FBXL22</i>	1st gRNA	TCAGCTTTCTCGGCTGCACCGG
						2nd gRNA	AGCGTGACGGACGTCAGGTTGG
<u>mKDM2A</u>	lysine demethylase 2A	<i>FBXL11</i>	KIAA1004, FBL11, LILINA, DKFZP434M1735,	11q13.2	KDM2A	1st gRNA	TCTTCATAGCGACGACGCATGG

						2nd gRNA	ATGTAGAGTATATCCAGCGGGG
Approved Symbol	Approved Name	Previous Symbols	Synonyms	Chromosome	Approved Symbol	gRNA pair	LV gRNA Sequence
<u>mKDM2B</u>	lysine demethylase 2B	FBXL10	PCCX2, CXXC2, Fbl10, JHDM1B	12q24.31	<i>KDM2B</i>	1st gRNA	GCTCCTGCTGTTGTTCCGGTTGG
						2nd gRNA	CTCTCCACACTCCGTCCGCAGG
<u>mSKP2</u>	S-phase kinase associated protein 2		FBXL1, FBL1, p45	5p13.2	<i>SKP2</i>	1st gRNA	CTGGTCCGGAATCTCCTGAAGG
						2nd gRNA	TGACGTTGCCACTCTGGTCCGG
<u>mBTRC</u>	beta-transducin repeat containing E3 ligase		bTrCP, betaTrCP, <i>FBXW1A</i> , Fwd1, bTrCP1	10q24.32	BTRC	1st gRNA	CTGAGAGTTTCCGCTGCTTGGG
						2nd gRNA	CATGATTGTGCCCAAGCAGCGG
<u>mFBXW2</u>	F-box and WD repeat domain containing 2		FBW2, Md6, Fwd2	9q33.2	<i>FBXW2</i>	1st gRNA	ATGCCCAGTGAGTGTATTCAGG
						2nd gRNA	ACTCACTGGGCATACTGAATGG
<u>mFBXW5</u>	F-box and WD repeat domain containing 5		DKFZP434B205, MGC20962, Fbw5	9q34.3	<i>FBXW5</i>	1st gRNA	GCAAACCTGGTACCCCGAGTGGG
						2nd gRNA	CCTCAGCTTCTCCCACTCGGGG
<u>mFBXW7</u>	F-box and WD repeat domain containing 7		AGO, FLJ11071, SEL-10, FBX30, CDC4, FBXW6	4q31.3	<i>FBXW7</i>	1st gRNA	ACCCACAGGCCTTCAAGAGTGG
						2nd gRNA	CATCTGTCCAACCACCCACAGG
Approved Symbol	Approved Name	Previous Symbols	Synonyms	Chromosome	Approved Symbol	gRNA pair	LV gRNA Sequence
<u>mFBXW8</u>	F-box and WD repeat domain containing 8	FBXO29	FBX29, FBW6, FBW8	12q24.22	FBXW8	1st gRNA	GTCCGTCTGCCTTACGAACTGG
<u>mFBXW9</u>	F-box and WD repeat domain containing 9		MGC10870, Fbw9	19p13.13	FBXW9	1st gRNA	AGCAGCAACACCGCATCAATGG

						2nd gRNA	CCAGCCGCCTGCATTGAGCTGG
<u>mFBXW10</u>	F-box and WD repeat domain containing 10	C17orf1, C17orf1A	SM2SH2, HREP, Fbw10	17p11.2	<i>FBXW10</i>	1st gRNA	AAAAAGTACAGCGGTACACAGG
						2nd gRNA	TCCCAATGTCCAAACATTTAGG
<u>mFBXW11</u>	F-box and WD repeat domain containing 11	<i>FBXW1B</i>	KIAA0696, Fbw1b, BTRCP2, BTRC2, Hos, Fbw11	5q35.1	<i>FBXW11</i>	1st gRNA	AGTTGGGAGGGCCATCTGTAGG
						2nd gRNA	TTAAAAACAGACCTACAGATGG
<u>mCCNF</u>	cyclin F		FBX1, FBXO1	16p13.3	CCNF	1st gRNA	TTTGTATTCTTCGTTTAGTAGG
						2nd gRNA	TCAAGATGGTTAAGTTTCTGGG
Approved Symbol	Approved Name	Previous Symbols	Synonyms	Chromosome	Approved Symbol	gRNA pair	LV gRNA Sequence
<u>mECT2L</u>	epithelial cell transforming 2 like	C6orf91	ARHGEF32, <i>FBXO49</i> , LFDH	6q24.1	ECT2L	1st gRNA	AATCCCGCCGTTGCTTGTGG
						2nd gRNA	CTGGACCAACAAGCAACGGCGG
<u>mFBXO2</u>	F-box protein 2	OCP1	FBX2, Nfb42, Fbs1, Fbg1	1p36.22	FBXO2	1st gRNA	TCCTCTGGGCTCGTCTCTCGG
				1p36.22	FBXO2	2nd gRNA	CACTTGAGCAGCCACAGTGGGG
<u>mFBXO3</u>	F-box protein 3		FBX3, FBA	11p13	<i>FBXO3</i>	1st gRNA	TACCTCCCCACGTCTGAGTAGG
						2nd gRNA	CTTTTTAATGGCGGCGTAATGG
<u>mFBXO4</u>	F-box protein 4		FBX4	5p13.1	<i>FBXO4</i>	1st gRNA	CCAGCTGGCACAGATCGTGGGG
						2nd gRNA	TTCTTGGTCTTCGGTTGATTGG
<u>mFBXO5</u>	F-box protein 5		FBX5, Fbxo31, <i>EM11</i>	6q25.2	FBXO5	1st gRNA	TGCAGTCTAAAGTCCCGCTGG
						2nd gRNA	GGCTTCACCACTTCAAGCTCGG
<u>mFBXO6</u>	F-box protein 6		FBX6, FBG2, FBS2, Fbx6b	1p36.22	FBXO6	1st gRNA	CGGATAGACTCCAACGGAGGGG

Approved Symbol	Approved Name	Previous Symbols	Synonyms	Chromosome	Approved Symbol	gRNA pair	LV gRNA Sequence
						2nd gRNA	GGCGGATAGACTCCAACGGAGG
<u>mFBX07</u>	F-box protein 7		FBX7, Fbx, PARK15	22q12.3	FBX07	1st gRNA	ATTCAGGATGCCATGAGTATGG
						2nd gRNA	AGTGATGCCTTGATAGTGCTGG
<u>mFBX08</u>	F-box protein 8		FBX8, FBS	4q34.1	<i>FBX08</i>	1st gRNA	AAAAGAAAATCCTAAAGGTGGG
						2nd gRNA	TCCTCTGGGTTGGCATTAAAGG
<u>mFBX09</u>	F-box protein 9		FBX9, NY-REN-57	6p12.1	FBX09	1st gRNA	CTGACAGAGTAGGCGATGAAGG
						2nd gRNA	GCCAGTTCCTGTCGTCCTTTGG
<u>mFBX010</u>	F-box protein 10		FBX10	9p13.2	FBX010	1st gRNA	CCAGTTCTTATCCGCCGACGGG
						2nd gRNA	GAAGAGGCACTTGCGGATAAGG
<u>mFBX011</u>	F-box protein 11		<i>FBX11</i> , UBR6	2p16.3	<i>FBX011</i>	1st gRNA	TTTTTCTGCGAAGTTGGTATGG
						2nd gRNA	TAGGACACGCTGTTCTTTTGG
<u>mFBX015</u>	F-box protein 15		MGC39671, FBX15	18q22.3	FBX015	1st gRNA	TCGCTGTGCTGGTTTCGCCAGG
						2nd gRNA	TCCATCAGTTCTATATCCCTGG
Approved Symbol	Approved Name	Previous Symbols	Synonyms	Chromosome	Approved symbol	gRNA Pair	LV gRNA Sequence
<u>mFBX016</u>	F-box protein 16		FBX16	8p21.1	FBX016	1st gRNA	TGCACAACGGCAAAGACTCCGG
						2nd gRNA	CAGGGAACAGCGCTCTAGTAGG
<u>mFBX017</u>	F-box protein 17	FBX026	FBG4, FLJ25205, MGC9379, FLJ11798, Fbx17	19q13.2	FBX017	1st gRNA	AAGTGGAGCACGGCGGAAATGG
						2nd gRNA	GTGGAAAAGAATTTGACGCTGG
<u>mFBX018</u>	F-box protein, helicase, 18		FBH1, FLJ14590, Fbx18	10p15.1	<i>FBX018</i>	1st gRNA	CTCTCAGGGTCAACACTTGGGG
						2nd gRNA	GGAGGCTGAGGCGTGCATGCGG

<u>mFBXO21</u>	F-box protein 21		FBX21, KIAA0875	12q24.22	<i>FBXO21</i>	1st gRNA	CCCCACCGACTACGTCAATTGG
						2nd gRNA	CCAATTGACGTAGTCGGTGGGG
<u>mFBXO22</u>	F-box protein 22		FBX22, FISTC1	15q24.2	<i>FBXO22</i>	1st gRNA	GATTGCTACCTGATCCCATTGG
						2nd gRNA	AGTGCTGACTACCCGATGCAGG
<u>mFBXO24</u>	F-box protein 24		FBX24	7q22.1	FBXO24	1st gRNA	AGGAGCAGTAGGGCCCGCTGGG
						2nd gRNA	TCACAGGCGCGGCTACCGGTGG
Approved Symbol	Approved Name	Previous Symbols	Synonyms	Chromosome	Approved symbol	gRNA Pair	LV gRNA Sequence
<u>mFBXO25</u>	F-box protein 25		FBX25	8p23.3	FBXO25	1st gRNA	AAATGGATCTACGTCCATAAGG
						2nd gRNA	GAGAAGTCTAGCCGGTTGAAGG
<u>mFBXO27</u>	F-box protein 27		Fbg5, Fbx27	19q13.2	FBXO27	1st gRNA	GCCAGATCCCATTGAACAGTGG
						2nd gRNA	GAACTTATCTATGACGTTCTGG
<u>mFBXO28</u>	F-box protein 28		FLJ10766, KIAA0483, Fbx28,	1q42.11	FBXO28	1st gRNA	TCAGAGAATGTTGAATCAGGGG
						2nd gRNA	TGTCAGAGAATGTTGAATCAGG
<u>mFBXO30</u>	F-box protein 30		MGC21674, Fbx30	6q24.3	<i>FBXO30</i>	1st gRNA	GGCTAATGAGGGACGTTTGTGG
						2nd gRNA	GACCAGGACCACCTTGATGAGG
<u>mFBXO31</u>	F-box protein 31		FBX14, FBXO14, Fbx31, MGC15419	16q24.2	<i>FBXO31</i>	1st gRNA	TGTGAGAACCTGCGGAAGCTGG
						2nd gRNA	TGTGATCTCCAGCTCCGCAGG
<u>mFBXO32</u>	F-box protein 32		MAFbx, ATROGIN1, Fbx32	8q24.13	<i>FBXO32</i>	1st gRNA	GGCTGCGACGTCGTAGTTCAGG
						2nd gRNA	GTTCAAAAGGAAGTACGAAGG
Approved Symbol	Approved Name	Previous Symbols	Synonyms	Chromosome	Approved symbol	gRNA Pair	LV gRNA Sequence
<u>mFBXO33</u>	F-box protein 33		Fbx33	14q21.1	<i>FBXO33</i>	1st gRNA	GCTGGACAACTTCCTTGCTGG
						2nd gRNA	GTCCAGCACGTACCTCAGCAGG

<u>mFBX036</u>	F-box protein 36		Fbx36, FLJ37592	2q36.3	<i>FBX036</i>	1st gRNA	ATGTCTTCAACCTGTGCGAAGG
						2nd gRNA	GTCAAATTTACCTTCGCACAGG
<u>mFBX038</u>	F-box protein 38		MOKA, SP329, FLJ13962, Fbx38	5q32	<i>FBX038</i>	1st gRNA	TGCCTCTCTCGGAAGCTAAAGG
						2nd gRNA	TCGCCTCTCGAGGTATCTAGGG
<u>mFBX039</u>	F-box protein 39		MGC35179, Fbx39, CT144	17p13.1	<i>FBX039</i>	1st gRNA	CTCCACAAACTTAACGTCCAGG
						2nd gRNA	TTCCTGGACGTTAAGTTTGTGG
<u>mFBX040</u>	F-box protein 40		KIAA1195, Fbx40	3q13.33	<i>FBX040</i>	1st gRNA	TCTCCTTGGGCGTACAAGCAGG
						2nd gRNA	TTGTTTGCCGGCAACCAGTAGG
<u>mFBX041</u>	F-box protein 41		KIAA1940, Fbx41	2p13.2	<i>FBX041</i>	1st gRNA	CCGAGCTGCCGTCTCCTCAGG
						2nd gRNA	AGGTGGGGGCAGTGCCTCGGGG
Approved Symbol	Approved Name	Previous Symbols	Synonyms	Chromosome	Approved symbol	gRNA Pair	LV gRNA Sequence
<u>FBX042</u>	F-box protein 42		KIAA1332, Fbx42	1p36.13	<i>FBX042</i>	1st gRNA	GATAGGGGTTCCTCCGGATAAGGG
						2nd gRNA	GCTGAGTGATAGGGGTTCCTCCGG
<u>FBX043</u>	F-box protein 43		Fbx43	8q22.2	<i>FBX043</i>	1st gRNA	TAAGGCCAAGCGACTCAGAAGG
						2nd gRNA	GTCAGAACATCCCCCAAGGGG
<u>FBX044</u>	F-box protein 44		FBX30, FBG3, MGC14140, Fbxo6a, Fbx44	1p36.22	<i>FBX044</i>	1st gRNA	AGCACAAGGGTTGTGAAGGAGG
						2nd gRNA	CTGCTGCTGCGCTGCCGACCGG
<u>FBX045</u>	F-box protein 45		Fbx45	3q29	<i>FBX045</i>	1st gRNA	GAAGTGACGACCAGAGCTGGGG
						2nd gRNA	CCATCAGTGCTCTGAGCGATGG
<u>FBX047</u>	F-box protein 47			17q12	<i>FBX047</i>	1st gRNA	GATATTGGCATGTTAAGTATGG
						2nd gRNA	ATTATATCTCAACATCATCTGG

<u>hFBXL18</u>	F-box and leucine rich repeat protein 18		FLJ11467, Fbl18	7p22.1			
					FBXL18	gRNA	CGGATGGCGGGCTCGTTGCGGGG
<u>hFBXO17</u>	F-box protein 17		FBG4, FBXO26, FLJ11798, Fbx17	19			
					FBXO17	gRNA	AAGATGAGATTGCGGCCGAAGGG

Table 8.2: Statistical analysis of organoid growth		
Day	Value measures	Statistical significance
Day 1	Surface area vs surface area raw	***
	Surface area vs surface area log	***
	Perimeter vs perimeter	***
	Perimeter vs perimeter log	***
	Surface area vs Perimeter	***
	Surface area vs Perimeter Log10	***
	Growth rate Current vs D1	NA
Day 3	Surface area vs surface area raw	***
	Surface area vs surface area log	***
	Perimeter vs perimeter	***
	Perimeter vs perimeter log	***
	Surface area vs Perimeter	***
	Surface area vs Perimeter Log10	***
	Growth rate D3 vs D1	NS
Day 5	Surface area vs surface area raw	***
	Surface area vs surface area log	***
	Perimeter vs perimeter	***
	Perimeter vs perimeter log	***
	Surface area vs Perimeter	***
	Surface area vs Perimeter Log10	***
	Growth rate D5 vs D1	NS
Day 7	Surface area vs surface area raw	**
	Surface area vs surface area log	**
	Perimeter vs perimeter	NS
	Perimeter vs perimeter log	NS
	Surface area vs Perimeter	***
	Surface area vs Perimeter Log10	***

	Growth rate D7 vs D1	***
--	----------------------	-----

Table 8.3: Significant Differentially expressed genes in DLD-1 *FBXL5* knockout cells vs controls under normoxia conditions as mapped to KEGG pathways.

Gene ID	Gene Name	Log2 expression change	Adj <i>P</i> value
N-Glycan Biosynthesis			
ALG1	ALG1, chitobiosyldiphosphodolichol beta-mannosyltransferase	-8.54689	5.40E-05
ALG8	ALG8, alpha-1,3-gucosyltransferase	-7.36061	0.008314
GANAB	glucosidase II alpha subunit	7.944773	0.007143
STT3A	STT3A, catalytic subunit of the oligosaccharyltransferase complex	5.91923	0.022017
Cytosolic DNA-sensing pathway			
IKBKB	inhibitor of nuclear factor kappa B kinase subunit beta	6.839722	0.011444
IKBKE	inhibitor of nuclear factor kappa B kinase subunit epsilon	-6.95123	0.015972
IRF3	interferon regulatory factor 3	3.756292	0.006528
MAVS	mitochondrial antiviral signalling protein	-1.59384	0.034073
POLR3C	RNA polymerase III subunit C	-6.70142	0.010186

Spliceosome			
CCDC12	coiled-coil domain containing 12	7.843184	0.003282
CRNKL1	crooked neck pre-mRNA splicing factor 1	6.147229	0.024543
DDX39B	DExD-box helicase 39B	-1.27287	0.034162
PRPF19	pre-mRNA processing factor 19	-9.42391	3.23E-05
SNRNP200	small nuclear ribonucleoprotein U5 subunit 200	1.819099	0.024409
SRSF2	serine and arginine rich splicing factor 2	1.77737	0.044515
SRSF7	serine and arginine rich splicing factor 7	-8.0569	0.023632
THOC1	THO complex 1	6.450271	0.048955
THOC2	THO complex 2	-1.10561	0.013837
U2AF1L4	U2 small nuclear RNA auxiliary factor 1 like 4	-6.6243	0.010671
RIG-I-like receptor signalling pathway			
CYLD	CYLD lysine 63 deubiquitinase	-2.05551	0.024654
IKBKB	inhibitor of nuclear factor kappa B kinase subunit beta	6.839722	0.011444
IKBKE	inhibitor of nuclear factor kappa B kinase subunit epsilon	-6.95123	0.015972
IRF3	interferon regulatory factor 3	3.756292	0.006528
MAVS	mitochondrial antiviral signalling protein	-1.59384	0.034073
Protein processing in endoplasmic reticulum			
BAK1	BCL2 antagonist/killer 1	7.156815	0.003659
CAPN1	calpain 1	-1.35438	0.000527
EIF2AK4	eukaryotic translation initiation factor 2 alpha kinase 4	-8.05148	0.010862

GANAB	glucosidase II alpha subunit	7.944773	0.007143
SEC23A	Sec23 homolog A, coat complex II component	-6.69756	0.015975
SEC23B	Sec23 homolog B, coat complex II component	-2.32381	0.025794
SEC31A	SEC31 homolog A, COPII coat complex component	-3.93153	0.000303
SSR3	signal sequence receptor subunit 3	7.722529	0.004476
SIL1	SIL1 nucleotide exchange factor	-6.06962	0.030504
STT3A	STT3A, catalytic subunit of the oligosaccharyltransferase complex	5.91923	0.022017
Insulin signalling pathway			
ACACB	acetyl-CoA carboxylase beta	6.038617	0.008743
CAL ML4	calmodulin like 4	-7.01944	0.009988
PYGL	glycogen phosphorylase L	1.09764	0.00027
IKBKB	inhibitor of nuclear factor kappa B kinase subunit beta	6.839722	0.011444
PRKAR1A	protein kinase cAMP-dependent type I regulatory subunit alpha	-7.75187	0.015935
PRKAR1B	protein kinase cAMP-dependent type I regulatory subunit beta	-8.52551	7.61E-05
SREBF1	sterol regulatory element binding transcription factor 1	-1.5399	5.33E-12
TSC2	TSC complex subunit 2	7.60003	0.000332
Herpes simplex infection			
CDK1	cyclin dependent kinase 1	6.407113	0.042218

EIF2AK4	eukaryotic translation initiation factor 2 alpha kinase 4	-8.05148	0.010862
IKBKB	inhibitor of nuclear factor kappa B kinase subunit beta	6.839722	0.011444
IKBKE	inhibitor of nuclear factor kappa B kinase subunit epsilon	-6.95123	0.015972
IRF3	interferon regulatory factor 3	3.756292	0.006528
MCRS1	microspherule protein 1	6.205375	0.046537
MAVS	mitochondrial antiviral signalling protein	-1.59384	0.034073
PER1	period circadian regulator 1	6.688929	0.001684
SRSF2	serine and arginine rich splicing factor 2	1.77737	0.044515
SRSF7	serine and arginine rich splicing factor 7	-8.0569	0.023632
RNA Transport			
DDX39B	DExD-box helicase 39B	-1.27287	0.034162
EIF1	eukaryotic translation initiation factor 1	1.056396	0.008537
NUP37	nucleoporin 37	7.378472	0.010088
NUP58	nucleoporin 58	3.230283	0.040903
PABPC4	poly(A) binding protein cytoplasmic 4	-1.63366	0.026117
PAIP1	poly(A) binding protein interacting protein 1	5.667774	0.02368
RNPS1	RNA binding protein with serine rich domain 1	7.214119	0.049065
THOC1	THO complex 1	6.450271	0.048955
THOC2	THO complex 2	-1.10561	0.013837
Human papillomavirus infection			
ATP6V1B2	ATPase H ⁺ transporting V1 subunit B2	-7.16291	0.027448

ATP6V1D	ATPase H ⁺ transporting V1 subunit D	6.710427	0.008822
BAK1	BCL2 antagonist/killer 1	7.156815	0.003659
CSNK1A1	casein kinase 1 alpha 1	-6.88714	0.044728
DLG1	discs large MAGUK scaffold protein 1	-7.52986	0.001318
FN1	fibronectin 1	7.295479	0.008311
IKBKB	inhibitor of nuclear factor kappa B kinase subunit beta	6.839722	0.011444
IKBKE	inhibitor of nuclear factor kappa B kinase subunit epsilon	-6.95123	0.015972
IRF3	interferon regulatory factor 3	3.756292	0.006528
LAMA3	laminin subunit alpha 3	9.742968	8.43E-08
LLGL1	LLGL scribble cell polarity complex component 1	-6.61469	0.01685
PKM	pyruvate kinase M1/2	-5.95389	0.028159
PPP2R2A	protein phosphatase 2 regulatory subunit Balpha	-1.29241	0.02627
RBPJ	recombination signal binding protein for immunoglobulin kappa J region	-6.07968	0.045993
TCF7L2	transcription factor 7 like 2	1.023286	0.048934
TSC2	TSC complex subunit 2	7.60003	0.000332
VEGFA	vascular endothelial growth factor A	-8.63449	0.000489
Endocytosis			
ACAP2	ArfGAP with coiled-coil, ankyrin repeat and PH domains 2	6.6719	0.013232
AGAP1	ArfGAP with GTPase domain, ankyrin repeat and PH domain 1	23.39617	0.000306

ARFGAP2	ADP ribosylation factor GTPase activating protein 2	-7.15378	0.002039
CHMP7	charged multivesicular body protein 7	-2.42236	0.012812
CYTH1	cytohesin 1	-6.85131	0.007934
EHD1	EH domain containing 1	-7.41588	0.005523
EPN2	epsin 2	-8.0809	0.010088
GIT1	GIT ArfGAP 1	-8.00306	0.001152
GIT2	GIT ArfGAP 2	3.192236	0.002923
RAB11FIP3	RAB11 family interacting protein 3	-7.24642	0.00944
SNX3	sorting nexin 3	-7.32324	0.001741
SNX5	sorting nexin 5	1.183351	0.001984

Table 8.4: Significant Differentially expressed genes in DLD-1 *FBXL5* knockout cells vs controls under hypoxic conditions as mapped to KEGG pathways

User ID	Gene name	Log2 expression change	Adj P value
Antifolate Resistance			
EGFR	epidermal growth factor receptor	1.269627	5.14E-07
FGFR2	fibroblast growth factor receptor 2	7.54772	0.00143
GLS	glutaminase	1.293412	0.011013
GLS2	glutaminase 2	5.612453	0.036661
HIF1A	hypoxia inducible factor 1 subunit alpha	1.483213	0.000351
MET	MET proto-oncogene, receptor tyrosine kinase	2.848111	0.000136
MTOR	mechanistic target of rapamycin kinase	3.535796	0.014
MYC	MYC proto-oncogene, bHLH transcription factor	-1.792742	0.034515
PDHA1	pyruvate dehydrogenase E1 alpha 1 subunit	7.280988	0.011761
PFKL	phosphofructokinase, liver type	6.981576	0.024527
PFKP	phosphofructokinase, platelet	1.334828	0.04284
PIK3CB	phosphatidylinositol-4,5-bisphosphate 3-kinase catalytic subunit beta	-1.668148	0.004965
PKM	pyruvate kinase M1/2	-8.50021	2.24E-05
SLC2A1	solute carrier family 2-member 1	1.353087	0.034577
TIGAR	<i>TP53</i> induced glycolysis regulatory phosphatase	-1.273778	3.56E-06

Central carbon metabolism in cancer			
EGFR	epidermal growth factor receptor	1.269627	5.14E-07
FGFR2	fibroblast growth factor receptor 2	7.54772	0.00143
GLS	glutaminase	1.293412	0.011013
GLS2	glutaminase 2	5.612453	0.036661
HIF1A	hypoxia inducible factor 1 subunit alpha	1.483213	0.000351
MET	MET proto-oncogene, receptor tyrosine kinase	2.848111	0.000136
MTOR	mechanistic target of rapamycin kinase	3.535796	0.014
MYC	MYC proto-oncogene, bHLH transcription factor	-1.792742	0.034515
PDHA1	pyruvate dehydrogenase E1 alpha 1 subunit	7.280988	0.011761
PFKL	phosphofructokinase, liver type	6.981576	0.024527
PFKP	phosphofructokinase, platelet	1.334828	0.04284
PIK3CB	phosphatidylinositol-4,5-bisphosphate 3-kinase catalytic subunit beta	-1.668148	0.004965
PKM	pyruvate kinase M1/2	-8.50021	2.24E-05
SLC2A1	solute carrier family 2-member 1	1.353087	0.034577
TIGAR	<i>TP53</i> induced glycolysis regulatory phosphatase	-1.273778	3.56E-06
Colorectal Cancer			
AXIN1	axin 1	1.313185	0.002336
AXIN2	axin 2	-5.23401	0.000314
BAK1	BCL2 antagonist/killer 1	7.931068	0.000576
BCL2L11	BCL2 like 11	0.001694	BCL2L11

EGFR	epidermal growth factor receptor	1.269627	5.14E-07
GADD45A	growth arrest and DNA damage inducible alpha	-4.605363	0.003069
MAPK8	mitogen-activated protein kinase 8	-5.906137	0.039295
MAPK9	mitogen-activated protein kinase 9	-1.149868	3.43E-15
MLH1	mutL homolog 1	-6.800559	0.047523
MSH2	mutS homolog 2	-5.694686	0.048605
MSH6	mutS homolog 6	-8.31627	6.90E-06
MTOR	mechanistic target of rapamycin kinase	3.535796	0.014
MYC	MYC proto-oncogene, bHLH transcription factor	-1.792742	0.034515
PIK3CB	phosphatidylinositol-4,5-bisphosphate 3-kinase catalytic subunit beta	-1.668148	0.004965
POLK	DNA polymerase kappa	1.261384	0.031771
RAC3	Rac family small GTPase 3	-5.613678	0.030199
RALGDS	ral guanine nucleotide dissociation stimulator	7.191862	0.001692
RHOA	ras homolog family member A	2.298296	0.017536
SOS1	SOS Ras/Rac guanine nucleotide exchange factor 1	-1.17328	0.000222
Pancreatic Cancer			
BAK1	BCL2 antagonist/killer 1	7.931068	0.000576
E2F3	E2F transcription factor 3	-1.127102	0.020112
EGFR	epidermal growth factor receptor	1.269627	5.14E-07
GADD45A	growth arrest and DNA damage inducible alpha	-4.605363	0.003069

IKBKB	inhibitor of nuclear factor kappa B kinase subunit beta	1.353824	0.012718
IKBKG	inhibitor of nuclear factor kappa B kinase subunit gamma	-7.690661	0.022415
MAPK8	mitogen-activated protein kinase 8	-5.906137	0.039295
MAPK9	mitogen-activated protein kinase 9	-1.149868	3.43E-15
MTOR	mechanistic target of rapamycin kinase	3.535796	0.014
NFKB1	nuclear factor kappa B subunit 1	7.054995	0.019088
PIK3CB	phosphatidylinositol-4,5-bisphosphate 3-kinase catalytic subunit beta	-1.668148	0.004965
POLK	DNA polymerase kappa	1.261384	0.031771
RAC3	Rac family small GTPase 3	-5.613678	0.030199
RALBP1	ralA binding protein 1	-1.49283	0.000131
RALGDS	ral guanine nucleotide dissociation stimulator	7.191862	0.001692
VEGFA	vascular endothelial growth factor A	1.276677	0.017583
Epithelial cell signalling in Helicobacter pylori infection			
ATP6V0B	ATPase H ⁺ transporting V0 subunit b	-7.117031	0.040701
ATP6V0E1	ATPase H ⁺ transporting V0 subunit e1	-6.763489	0.005587
ATP6V0E2	ATPase H ⁺ transporting V0 subunit e2	3.504939	0.035393
ATP6V1E1	ATPase H ⁺ transporting V1 subunit E1	6.442384	0.008465
EGFR	epidermal growth factor receptor	1.269627	5.14E-07
F11R	F11 receptor	7.689177	0.000265
IKBKB	inhibitor of nuclear factor kappa B kinase subunit beta	1.353824	0.012718

IKBKG	inhibitor of nuclear factor kappa B kinase subunit gamma	-7.690661	0.022415
MAPK11	mitogen-activated protein kinase 11	7.393051	0.006809
MAPK8	mitogen-activated protein kinase 8	-5.906137	0.039295
MAPK9	mitogen-activated protein kinase 9	-1.149868	3.43E-15
MET	MET proto-oncogene, receptor tyrosine kinase	2.848111	0.000136
NFKB1	nuclear factor kappa B subunit 1	7.054995	0.019088
IL-17 signalling pathway			
CASP8	caspase 8	-3.350445	0.030083
CSF2	colony stimulating factor 2	1.76942	1.45E-05
ELAVL1	ELAV like RNA binding protein 1	-1.095518	0.000493
FOSL1	FOS like 1, AP-1 transcription factor subunit	1.404717	4.42E-11
HSP90AA1	heat shock protein 90 alpha family class A member 1	4.055725	0.01771
HSP90B1	heat shock protein 90 beta family member 1	1.633665	0.001246
IKBKB	inhibitor of nuclear factor kappa B kinase subunit beta	1.353824	0.012718
IKBKG	inhibitor of nuclear factor kappa B kinase subunit gamma	-7.690661	0.022415
IL17RA	interleukin 17 receptor A	-1.532294	0.006849
IL17RC	interleukin 17 receptor C	6.193595	0.015723
MAP3K7	mitogen-activated protein kinase 7	-8.317256	1.53E-05
MAPK11	mitogen-activated protein kinase 11	7.393051	0.006809
MAPK8	mitogen-activated protein kinase 8	-5.906137	0.039295

MAPK9	mitogen-activated protein kinase 9	-1.149868	3.43E-15
NFKB1	nuclear factor kappa B subunit 1	7.054995	0.019088
SRSF1	serine and arginine rich splicing factor 1	-3.024418	6.21E-47
TRAF3	TNF receptor associated factor 3	-1.021403	0.048655
<i>HIF-1a</i> signalling pathway			
ALDOA	aldolase, fructose-bisphosphate A	1.28343	1.57E-07
CAMK2D	calcium/calmodulin dependent protein kinase II delta	-7.274884	0.000336
EGFR	epidermal growth factor receptor	1.269627	5.14E-07
EGLN3	egl-9 family hypoxia inducible factor 3	1.294153	9.68E-05
EIF4E2	eukaryotic translation initiation factor 4E family member 2	-1.802666	0.004824
ENO1	enolase 1	1.252703	1.01E-05
HIF1A	hypoxia inducible factor 1 subunit alpha	1.483213	0.000351
MKMK2	MAP kinase interacting serine/threonine kinase 2	-1.859024	0.014704
MTOR	mechanistic target of rapamycin kinase	3.535796	0.014
NFKB1	nuclear factor kappa B subunit 1	7.054995	0.019088
PDHA1	pyruvate dehydrogenase E1 alpha 1 subunit	7.280988	0.011761
PFKL	phosphofructokinase, liver type	6.981576	0.024527
PIK3CB	phosphatidylinositol-4,5-bisphosphate 3-kinase catalytic subunit beta	-1.668148	0.004965
SERPINE1	serpin family E member 1	1.39568	0.002123
SLC2A1	solute carrier family 2-member 1	1.353087	0.034577

<i>TfRC</i>	transferrin receptor	-1.416988	0.000159
<i>VEGFA</i>	vascular endothelial growth factor A	1.276677	0.017583
Epstein-Barr virus infection			
B2M	beta-2-microglobulin	-1.200379	1.67E-07
BAK1	BCL2 antagonist/killer 1	7.931068	0.000576
BCL2L11	BCL2 like 11	0.001694	BCL2L11
CASP8	caspase 8	-3.350445	0.030083
CCNE1	cyclin E1	-5.026565	0.049168
<i>CD44</i>	<i>CD44</i> molecule (Indian blood group)	7.224646	0.000876
CR2	complement C3d receptor 2	1.149471	0.005902
E2F3	E2F transcription factor 3	-1.127102	0.020112
GADD45A	growth arrest and DNA damage inducible alpha	-4.605363	0.003069
HLA-A	major histocompatibility complex, class I, A	6.834822	0.042176
HLA-F	major histocompatibility complex, class I, F	2.976219	0.008183
IKBKB	inhibitor of nuclear factor kappa B kinase subunit beta	1.353824	0.012718
IKBKG	inhibitor of nuclear factor kappa B kinase subunit gamma	-7.690661	0.022415
IRAK4	interleukin 1 receptor associated kinase 4	6.569757	0.002885
MAP2K7	mitogen-activated protein kinase 7	1.690924	0.000193
MAP3K7	mitogen-activated protein kinase 7	-8.317256	1.53E-05
MAPK11	mitogen-activated protein kinase 11	7.393051	0.006809
MAPK8	mitogen-activated protein kinase 8	-5.906137	0.039295
MAPK9	mitogen-activated protein kinase 9	-1.149868	3.43E-15

MDM2	MDM2 proto-oncogene	7.024809	0.002142
MYC	MYC proto-oncogene, bHLH transcription factor	-1.792742	0.034515
NCOR2	nuclear receptor corepressor 2	4.22736	0.046848
NFKB1	nuclear factor kappa B subunit 1	7.054995	0.019088
NFKBIE	NFKB inhibitor epsilon	2.193969	0.027908
PIK3CB	phosphatidylinositol-4,5-bisphosphate 3-kinase catalytic subunit beta	-1.668148	0.004965
POLK	DNA polymerase kappa	1.261384	0.031771
PSMC1	proteasome 26S subunit, ATPase 1	-7.985115	2.40E-05
RBPJ	recombination signal binding protein for immunoglobulin kappa J region	7.418208	0.007961
RIPK1	receptor interacting serine/threonine kinase 1	-1.192276	2.41E-07
SNW1	SNW domain containing 1	7.087868	0.004021
STAT2	signal transducer and activator of transcription 2	-7.111485	0.001231
TRAF3	TNF receptor associated factor 3	-1.021403	0.048655
USP7	ubiquitin specific peptidase 7	2.076468	0.014631
Spliceosome			
BCAS2	BCAS2, pre-mRNA processing factor	5.833044	0.032104
CCDC12	coiled-coil domain containing 12	7.458333	0.017436
CTNNB1	catenin beta like 1	6.646677	0.019192
DDX5	DEAD-box helicase 5	-1.034688	2.10E-52
DHX15	DEAH-box helicase 15	2.167212	2.60E-05

HNRNPC	heterogeneous nuclear ribonucleoprotein C (C1/C2)	-10.94406	6.42E-12
HNRNPM	heterogeneous nuclear ribonucleoprotein M	-1.190214	1.46E-10
HSPA8	heat shock protein family A (Hsp70) member 8	2.069245	6.46E-05
LSM4	LSM4 homolog, U6 small nuclear RNA and mRNA degradation associated	-2.463491	3.87E-05
PQBP1	polyglutamine binding protein 1	-4.276436	0.002306
PRPF19	pre-mRNA processing factor 19	-6.725819	0.002268
RBM17	RNA binding motif protein 17	-1.541196	0.015892
RBM22	RNA binding motif protein 22	-7.377144	0.002141
SF3B3	splicing factor 3b subunit 3	7.552567	0.02665
SNW1	SNW domain containing 1	7.087868	0.004021
SRSF1	serine and arginine rich splicing factor 1	-3.024418	6.21E-47
SRSF2	serine and arginine rich splicing factor 2	-1.178875	0.010057
SRSF5	serine and arginine rich splicing factor 5	-1.536168	1.65E-12
SRSF7	serine and arginine rich splicing factor 7	-1.040633	0.000551
THOC1	THO complex 1	5.965501	0.017876
THOC2	THO complex 2	7.116499	0.002266
Kaposi sarcoma-associated herpesvirus infection			
BAK1	BCL2 antagonist/killer 1	7.931068	0.000576
BECN1	Beclin 1	-6.832933	0.005935
CASP8	caspase 8	-3.350445	0.030083
CSF2	colony stimulating factor 2	1.76942	1.45E-05
E2F3	E2F transcription factor 3	-1.127102	0.020112

GABARAPL1	GABA type A receptor associated protein like 1	1.190694	0.041532
GNB5	G protein subunit beta 5	-5.905131	0.024553
HIF1A	hypoxia inducible factor 1 subunit alpha	1.483213	0.000351
HLA-A	major histocompatibility complex, class I, A	6.834822	0.042176
HLA-F	major histocompatibility complex, class I, F	2.976219	0.008183
IKBKB	inhibitor of nuclear factor kappa B kinase subunit beta	1.353824	0.012718
IKBKG	inhibitor of nuclear factor kappa B kinase subunit gamma	-7.690661	0.022415
ITPR1	inositol 1,4,5-trisphosphate receptor type 1	-7.14317	0.016638
MAP2K7	mitogen-activated protein kinase 7	1.690924	0.000193
MAPK11	mitogen-activated protein kinase 11	7.393051	0.006809
MAPK8	mitogen-activated protein kinase 8	-5.906137	0.039295
MAPK9	mitogen-activated protein kinase 9	-1.149868	3.43E-15
MTOR	mechanistic target of rapamycin kinase	3.535796	0.014
MYC	MYC proto-oncogene, bHLH transcription factor	-1.792742	0.034515
NFATC3	nuclear factor of activated T cells 3	-1.005846	0.001141
NFATC4	nuclear factor of activated T cells 4	-7.250014	0.007007
NFKB1	nuclear factor kappa B subunit 1	7.054995	0.019088
PIK3CB	phosphatidylinositol-4,5-bisphosphate 3-kinase catalytic subunit beta	-1.668148	0.004965
RCAN1	regulator of calcineurin 1	-1.370609	0.005066

STAT2	signal transducer and activator of transcription 2	-7.111485	0.001231
TRAF3	TNF receptor associated factor 3	-1.021403	0.048655
UBB	ubiquitin B	2.178554	0.001924
VEGFA	vascular endothelial growth factor A	1.276677	0.017583
Viral carcinogenesis			
BAK1	BCL2 antagonist/killer 1	7.931068	0.000576
CASP8	caspase 8	-3.350445	0.030083
CCNE1	cyclin E1	-5.026565	0.049168
DDX3X	DEAD-box helicase 3 X-linked	1.672127	0.025054
DLG1	discs large MAGUK scaffold protein 1	-2.319638	0.000334
DNAJA3	DnaJ heat shock protein family (Hsp40) member A3	-7.22464	0.000255
GTF2H1	general transcription factor IIH subunit 1	-8.24029	9.89E-05
GTF2H2	general transcription factor IIH subunit 2	-6.693275	0.001434
GTF2H3	general transcription factor IIH subunit 3	-7.20075	0.000527
HDAC7	histone deacetylase 7	8.701889	3.44E-05
HLA-A	major histocompatibility complex, class I, A	6.834822	0.042176
HLA-F	major histocompatibility complex, class I, F	2.976219	0.008183
IKBKG	inhibitor of nuclear factor kappa B kinase subunit gamma	-7.690661	0.022415
MDM2	MDM2 proto-oncogene	7.024809	0.002142
MRPS18B	mitochondrial ribosomal protein S18B	1.189542	0.029193
NFKB1	nuclear factor kappa B subunit 1	7.054995	0.019088

PIK3CB	phosphatidylinositol-4,5-bisphosphate 3-kinase catalytic subunit beta	-1.668148	0.004965
PKM	pyruvate kinase M1/2	-8.50021	2.24E-05
PSMC1	proteasome 26S subunit, ATPase 1	-7.985115	2.40E-05
RANBP1	RAN binding protein 1	-1.439007	0.031263
RBPJ	recombination signal binding protein for immunoglobulin kappa J region	7.418208	0.007961
RHOA	ras homolog family member A	2.298296	0.017536
SND1	staphylococcal nuclease and tudor domain containing 1	1.700698	0.025686
SNW1	SNW domain containing 1	7.087868	0.004021
TBP	TATA-box binding protein	7.688234	9.61E-05
TRAF3	TNF receptor associated factor 3	-1.021403	0.048655
USP7	ubiquitin specific peptidase 7	2.076468	0.014631
YWHAB	tyrosine 3-monooxygenase/tryptophan 5-monooxygenase activation protein beta	1.88929	4.07E-07
YWHAE	tyrosine 3-monooxygenase/tryptophan 5-monooxygenase activation protein epsilon	1.256017	0.016223
YWHAQ	tyrosine 3-monooxygenase/tryptophan 5-monooxygenase activation protein theta	-2.730168	0.019489
Herpes simplex infection			
ARNTL	aryl hydrocarbon receptor nuclear translocator like	-1.952218	0.006749
CASP8	caspase 8	-3.350445	0.030083
CLOCK	clock circadian regulator	-3.027147	0.021566

CSNK2A1	casein kinase 2 alpha 1	-1.768859	0.022791
EEF1D	eukaryotic translation elongation factor 1 delta	-1.500453	0.01471
EIF2S1	eukaryotic translation initiation factor 2 subunit alpha	-1.088501	0.000323
HLA-A	major histocompatibility complex, class I, A	6.834822	0.042176
HLA-F	major histocompatibility complex, class I, F	2.976219	0.008183
IKBKB	inhibitor of nuclear factor kappa B kinase subunit beta	1.353824	0.012718
IKBKG	inhibitor of nuclear factor kappa B kinase subunit gamma	-7.690661	0.022415
MAP3K7	mitogen-activated protein kinase 7	-8.317256	1.53E-05
MAPK8	mitogen-activated protein kinase 8	-5.906137	0.039295
MAPK9	mitogen-activated protein kinase 9	-1.149868	3.43E-15
MCRS1	microspherule protein 1	-7.278068	0.046806
NFKB1	nuclear factor kappa B subunit 1	7.054995	0.019088
NOP53	NOP53 ribosome biogenesis factor	1.33543	0.049653
PER1	period circadian regulator 1	1.16661	0.022601
P ML	promyelocytic leukaemia	1.177514	0.041574
SRSF1	serine and arginine rich splicing factor 1	-3.024418	6.21E-47
SRSF2	serine and arginine rich splicing factor 2	-7.088547	0.000306
SRSF5	serine and arginine rich splicing factor 5	-1.536168	1.65E-12
SRSF7	serine and arginine rich splicing factor 7	-1.040633	0.000551
STAT2	signal transducer and activator of transcription 2	-7.111485	0.001231

TAF4B	TATA-box binding protein associated factor 4b	-3.134879	0.022117
TBP	TATA-box binding protein	7.688234	9.61E-05
TRAF3	TNF receptor associated factor 3	-1.021403	0.048655
USP7	ubiquitin specific peptidase 7	2.076468	0.014631
Endocytosis			
ACAP2	ArfGAP with coiled-coil, ankyrin repeat and PH domains 2	-7.818155	0.000893
AGAP1	ArfGAP with GTPase domain, ankyrin repeat and PH domain 1	-23.47221	4.20E-05
AGAP3	ArfGAP with GTPase domain, ankyrin repeat and PH domain 3	-2.140892	0.018189
AP2M1	adaptor related protein complex 2 subunit mu 1	2.489099	0.023252
AP2S1	adaptor related protein complex 2 subunit sigma 1	1.166453	0.017593
ARAP1	ArfGAP with RhoGAP domain, ankyrin repeat and PH domain 1	7.649327	0.000209
ARF1	ADP ribosylation factor 1	6.961168	0.002208
ARPC5	actin related protein 2/3 complex subunit 5	-1.049495	7.14E-06
CHMP3	charged multivesicular body protein 3	-6.399991	0.005904
CLTC	clathrin heavy chain	1.485279	0.001995
CYTH1	cytohesin 1	8.196351	2.19E-05
DAB2	DAB2, clathrin adaptor protein	-7.033669	0.005455
EGFR	epidermal growth factor receptor	1.269627	5.14E-07
EPS15L1	epidermal growth factor receptor pathway substrate 15 like 1	6.966383	0.000692

FGFR2	fibroblast growth factor receptor 2	7.54772	0.0014-3
GIT2	GIT ArfGAP 2	-2.247987	0.027084
HLA-A	major histocompatibility complex, class I, A	6.834822	0.042176
HLA-F	major histocompatibility complex, class I, F	2.976219	0.008183
HSPA8	heat shock protein family A (Hsp70) member 8	2.069245	6.46E-05
LDLR	low density lipoprotein receptor	1.31399	0.003787
MDM2	MDM2 proto-oncogene	7.024809	0.002142
NEDD4L	neural precursor cell expressed, developmentally down-regulated 4-like, E3 ubiquitin protein ligase	-1.569832	0.003523
P ML	promyelocytic leukaemia	1.177514	0.041574
RAB11FIP3	RAB11 family interacting protein 3	6.648466	0.00254
RHOA	ras homolog family member A	2.298296	0.017536
SNX5	sorting nexin 5	-2.232802	0.001408
TfRC	transferrin receptor	-1.416988	0.000159
UBB	ubiquitin B	2.178554	0.001924
VPS28	VPS28, ESCRT-I subunit	1.117927	2.26E-05
VPS37A	VPS37A, ESCRT-I subunit	-6.937517	0.032345
VPS37D	VPS37D, ESCRT-I subunit	1.157064	2.14E-06
WASHC4	WASH complex subunit 4	9.715745	1.12E-07
ZFYVE9	zinc finger FYVE-type containing 9	-8.013985	1.92E-05

References

- (HBC), H.C.B.C. (2021). RNA-Seq Workflow diagram (<https://hbctraining.github.io/>), pp. Diagram of RNA-Seq analysis workflow.
- Abbasi, U., Abbina, S., Gill, A., Bhagat, V., and Kizhakkedathu, J.N. (2021). A facile colorimetric method for the quantification of labile iron pool and total iron in cells and tissue specimens. *Scientific Reports* *11*, 6008.
- Ablain, J., and de The, H. (2014). Retinoic acid signaling in cancer: The parable of acute promyelocytic leukemia. *International journal of cancer* *135*, 2262-2272.
- Aboulkheyr Es, H., Montazeri, L., Aref, A.R., Vosough, M., and Baharvand, H. (2018). Personalized Cancer Medicine: An Organoid Approach. *Trends in Biotechnology* *36*, 358-371.
- Abramoff, M., Magalhães, P., and Ram, S.J. (2003). Image Processing with ImageJ. *Biophotonics International* *11*, 36-42.
- Agarwal, P., Zhao, S., Bielecki, P., Rao, W., Choi, J.K., Zhao, Y., Yu, J., Zhang, W., and He, X. (2013). One-step microfluidic generation of pre-hatching embryo-like core-shell microcapsules for miniaturized 3D culture of pluripotent stem cells. *Lab on a chip* *13*, 4525-4533.
- Ahmed, D., Eide, P.W., Eilertsen, I.A., Danielsen, S.A., Eknæs, M., Hektoen, M., Lind, G.E., and Lothe, R.A. (2013a). Epigenetic and genetic features of 24 colon cancer cell lines. *Oncogenesis* *2*, e71.
- Ahmed, D., Eide, P.W., Eilertsen, I.A., Danielsen, S.A., Eknæs, M., Hektoen, M., Lind, G.E., and Lothe, R.A. (2013b). Epigenetic and genetic features of 24 colon cancer cell lines. *Oncogenesis* *2*, e71-e71.
- Ahmed, M., Jinks, N., Babaei-Jadidi, R., Kashfi, H., Castellanos-Uribe, M., May, S.T., Mukherjee, A., and Nateri, A.S. (2019). Repurposing Antibacterial AM404 as a Potential Anticancer Drug for Targeting Colorectal Cancer Stem-Like Cells. *Cancers* *12*, 106.
- Aiello, N.M., Maddipati, R., Norgard, R.J., Balli, D., Li, J., Yuan, S., Yamazoe, T., Black, T., Sahmoud, A., Furth, E.E., *et al.* (2018). EMT Subtype Influences Epithelial Plasticity and Mode of Cell Migration. *Developmental cell* *45*, 681-695.e684.
- Alberghini, A., Recalcati, S., Tacchini, L., Santambrogio, P., Campanella, A., and Cairo, G. (2005). Loss of the von Hippel Lindau tumor suppressor disrupts iron homeostasis in renal carcinoma cells. *The Journal of biological chemistry* *280*, 30120-30128.
- Alsina, M., Trudel, S., Furman, R.R., Rosen, P.J., O'Connor, O.A., Comenzo, R.L., Wong, A., Kunkel, L.A., Molineaux, C.J., and Goy, A. (2012). A phase I single-agent study of twice-weekly consecutive-day dosing of the proteasome inhibitor carfilzomib in patients with relapsed or refractory multiple myeloma or lymphoma. *Clinical cancer research : an official journal of the American Association for Cancer Research* *18*, 4830-4840.
- Amor, M., Tharaud, M., Gélabert, A., and Komeili, A. (2020). Single-cell determination of iron content in magnetotactic bacteria: implications for the iron biogeochemical cycle. *Environ Microbiol* *22*, 823-831.
- Anadón, C., van Tetering, G., Ferreira, H.J., Moutinho, C., Martínez-Cardús, A., Villanueva, A., Soler, M., Heyn, H., Moran, S., Castro de Moura, M., *et al.* (2017).

Epigenetic loss of the RNA decapping enzyme NUDT16 mediates C-MYC activation in T-cell acute lymphoblastic leukemia. *Leukemia* *31*, 1622.

Anders, S., and Huber, W. (2010). Differential expression analysis for sequence count data. *Genome Biology* *11*, R106.

Arlt, A., and Schäfer, H. (2011). Role of the immediate early response 3 (IER3) gene in cellular stress response, inflammation and tumorigenesis. *Eur J Cell Biol* *90*, 545-552.

Arsham, A.M., Plas, D.R., Thompson, C.B., and Simon, M.C. (2002). Phosphatidylinositol 3-kinase/Akt signaling is neither required for hypoxic stabilization of HIF-1 alpha nor sufficient for HIF-1-dependent target gene transcription. *The Journal of biological chemistry* *277*, 15162-15170.

Artegiani, B., van Voorthuijsen, L., Lindeboom, R.G.H., Seinstra, D., Heo, I., Tapia, P., López-Iglesias, C., Postrach, D., Dayton, T., Oka, R., *et al.* (2019). Probing the Tumor Suppressor Function of BAP1 in CRISPR-Engineered Human Liver Organoids. *Cell Stem Cell* *24*, 927-943.e926.

Augustine, T., Chaudhary, P., Gupta, K., Islam, S., Ghosh, P., Santra, M.K., and Mitra, D. (2017). Cyclin F/FBXO1 Interacts with HIV-1 Viral Infectivity Factor (Vif) and Restricts Progeny Virion Infectivity by Ubiquitination and Proteasomal Degradation of Vif Protein through SCFcyclin F E3 Ligase Machinery. *The Journal of biological chemistry* *292*, 5349-5363.

Aujla, A., Linder, K., Iragavarapu, C., Karass, M., and Liu, D. (2018). SRSF2 mutations in myelodysplasia/myeloproliferative neoplasms. *Biomarker Research* *6*, 29.

Azarova, A.M., Lyu, Y.L., Lin, C.P., Tsai, Y.C., Lau, J.Y., Wang, J.C., and Liu, L.F. (2007). Roles of DNA topoisomerase II isozymes in chemotherapy and secondary malignancies. *Proc Natl Acad Sci U S A* *104*, 11014-11019.

Babaei-Jadidi, R., Li, N., Saadeddin, A., Spencer-Dene, B., Jandke, A., Muhammad, B., Ibrahim, E.E., Muraleedharan, R., Abuzinadah, M., Davis, H., *et al.* (2011). FBXW7 influences murine intestinal homeostasis and cancer, targeting Notch, Jun, and DEK for degradation. *The Journal of Experimental Medicine* *208*, 295-312.

Baecker, A., Liu, X., La Vecchia, C., and Zhang, Z.F. (2018). Worldwide incidence of hepatocellular carcinoma cases attributable to major risk factors. *Eur J Cancer Prev* *27*, 205-212.

Bai, H., Inoue, J., Kawano, T., and Inazawa, J. (2012). A transcriptional variant of the LC3A gene is involved in autophagy and frequently inactivated in human cancers. *Oncogene* *31*, 4397-4408.

Bailey, M.L., Tieu, D., Habsid, A., Tong, A.H.Y., Chan, K., Moffat, J., and Hieter, P. (2021). Paralogous synthetic lethality underlies genetic dependencies of the cancer-mutated gene STAG2. *Life Sci Alliance* *4*.

Baker, A., Saltik, M., Lehrmann, H., Killisch, I., Mautner, V., Lamm, G., Christofori, G., and Cotten, M. (1997). Polyethylenimine (PEI) is a simple, inexpensive and effective reagent for condensing and linking plasmid DNA to adenovirus for gene delivery. *Gene Ther* *4*, 773-782.

Baker, P.R., II, Friederich, M.W., Swanson, M.A., Shaikh, T., Bhattacharya, K., Scharer, G.H., Aicher, J., Creadon-Swindell, G., Geiger, E., MacLean, K.N., *et al.* (2013). Variant non ketotic hyperglycinemia is caused by mutations in LIAS, BOLA3 and the novel gene GLRX5. *Brain* *137*, 366-379.

Banerjee, S., and Southgate, J. (2019). Bladder organoids: a step towards personalised cancer therapy? *Translational andrology and urology* *8*, S300-s302.

Bankaitis, E.D., Ha, A., Kuo, C.J., and Magness, S.T. (2018). Reserve Stem Cells in Intestinal Homeostasis and Injury. *Gastroenterology* *155*, 1348-1361.

Barbash, O., Zamfirova, P., Lin, D.I., Chen, X., Yang, K., Nakagawa, H., Lu, F., Rustgi, A.K., and Diehl, J.A. (2008). Mutations in Fbx4 inhibit dimerization of the SCF(Fbx4) ligase and contribute to cyclin D1 overexpression in human cancer. *Cancer cell* *14*, 68-78.

Bardenbacher, M., Ruder, B., Britzen-Laurent, N., Schmid, B., Waldner, M., Naschberger, E., Scharl, M., Müller, W., Günther, C., Becker, C., *et al.* (2019). Permeability analyses and three dimensional imaging of interferon gamma-induced barrier disintegration in intestinal organoids. *Stem Cell Research* *35*, 101383.

Barkauskas, C.E., Chung, M.-I., Fioret, B., Gao, X., Katsura, H., and Hogan, B.L.M. (2017). Lung organoids: current uses and future promise. *Development* *144*, 986-997.

Barker, N., van de Wetering, M., and Clevers, H. (2008). The intestinal stem cell. *Genes & development* *22*, 1856-1864.

Barrallo-Gimeno, A., and Nieto, M.A. (2005). The Snail genes as inducers of cell movement and survival: implications in development and cancer. *Development* *132*, 3151-3161.

Barratt, S.L., Blythe, T., Ourradi, K., Jarrett, C., Welsh, G.I., Bates, D.O., and Millar, A.B. (2018). Effects of hypoxia and hyperoxia on the differential expression of VEGF-A isoforms and receptors in Idiopathic Pulmonary Fibrosis (IPF). *Respiratory Research* *19*, 9.

Bartfeld, S., Bayram, T., van de Wetering, M., Huch, M., Begthel, H., Kujala, P., Vries, R., Peters, P.J., and Clevers, H. (2015). In vitro expansion of human gastric epithelial stem cells and their responses to bacterial infection. *Gastroenterology* *148*, 126-136.e126.

Bashir, T., Dorrello, N.V., Amador, V., Guardavaccaro, D., and Pagano, M. (2004). Control of the SCF(Skp2-Cks1) ubiquitin ligase by the APC/C(Cdh1) ubiquitin ligase. *Nature* *428*, 190-193.

Bassermann, F., Eichner, R., and Pagano, M. (2014). The ubiquitin proteasome system — Implications for cell cycle control and the targeted treatment of cancer. *Biochimica et Biophysica Acta (BBA) - Molecular Cell Research* *1843*, 150-162.

Basu, S., Cheriyaundath, S., and Ben-Ze'ev, A. (2018). Cell-cell adhesion: linking Wnt/ β -catenin signaling with partial EMT and stemness traits in tumorigenesis. *F1000Research* *7*, F1000 Faculty Rev-1488.

Bedford, L., Lowe, J., Dick, L.R., Mayer, R.J., and Brownell, J.E. (2011). Ubiquitin-like protein conjugation and the ubiquitin–proteasome system as drug targets. *Nature Reviews Drug Discovery* *10*, 29-46.

Bennett, E.J., Shaler, T.A., Woodman, B., Ryu, K.-Y., Zaitseva, T.S., Becker, C.H., Bates, G.P., Schulman, H., and Kopito, R.R. (2007). Global changes to the ubiquitin system in Huntington's disease. *Nature* *448*, 704.

Benson, D.A., Cavanaugh, M., Clark, K., Karsch-Mizrachi, I., Lipman, D.J., Ostell, J., and Sayers, E.W. (2013). GenBank. *Nucleic acids research* *41*, D36-D42.

Besirli, C.G., Chinsky, N.D., Zheng, Q.-D., and Zacks, D.N. (2011). Autophagy Activation in the Injured Photoreceptor Inhibits Fas-Mediated Apoptosis. *Investigative Ophthalmology & Visual Science* *52*, 4193-4199.

Bhowmick, N.A., Ghiassi, M., Bakin, A., Aakre, M., Lundquist, C.A., Engel, M.E., Arteaga, C.L., and Moses, H.L. (2001). Transforming growth factor-beta1 mediates

epithelial to mesenchymal transdifferentiation through a RhoA-dependent mechanism. *Mol Biol Cell* *12*, 27-36.

Bio-Rad Laboratories, I. (2000). Quick Start Bradford Protein Assay Instruction Manual (<http://www.bio-rad.com/webroot/web/pdf/lsr/literature/4110065A.pdf>).

Birnboim, H.C., and Doly, J. (1979). A rapid alkaline extraction procedure for screening recombinant plasmid DNA. *Nucleic Acids Res* *7*, 1513-1523.

Blancher, C., and Jones, A. (2001). SDS -PAGE and Western Blotting Techniques. *Methods Mol Med* *57*, 145-162.

Boj, S.F., Hwang, C.-I., Baker, L.A., Engle, D.D., Tuveson, D.A., and Clevers, H. (2016). Model organoids provide new research opportunities for ductal pancreatic cancer. *Molecular & Cellular Oncology* *3*, e1014757.

Booij, T.H., Price, L.S., and Danen, E.H.J. (2019). 3D Cell-Based Assays for Drug Screens: Challenges in Imaging, Image Analysis, and High-Content Analysis. *SLAS Discov* *24*, 615-627.

Boretto, M., Maenhoudt, N., Luo, X., Hennes, A., Boeckx, B., Bui, B., Heremans, R., Perneel, L., Kobayashi, H., Van Zundert, I., *et al.* (2019). Patient-derived organoids from endometrial disease capture clinical heterogeneity and are amenable to drug screening. *Nature Cell Biology* *21*, 1041-1051.

Borg, N.A., and Dixit, V.M. (2017). Ubiquitin in Cell-Cycle Regulation and Dysregulation in Cancer. *Annual Review of Cancer Biology* *1*, 59-77.

Bray, F., Ferlay, J., Soerjomataram, I., Siegel, R.L., Torre, L.A., and Jemal, A. (2018). Global cancer statistics 2018: GLOBOCAN estimates of incidence and mortality worldwide for 36 cancers in 185 countries. *CA: a cancer journal for clinicians* *68*, 394-424.

Bray, N.L., Pimentel, H., Melsted, P., and Pachter, L. (2016). Near-optimal probabilistic RNA-seq quantification. *Nature Biotechnology* *34*, 525-527.

Brown, R., and Kaganovich, D. (2016). Look Out Autophagy, Ubiquitin UPS Its Game. *Cell* *166*, 797-799.

Brown, R.A.M., Richardson, K.L., Kabir, T.D., Trinder, D., Ganss, R., and Leedman, P.J. (2020). Altered Iron Metabolism and Impact in Cancer Biology, Metastasis, and Immunology. *Front Oncol* *10*, 476-476.

Brugarolas, J., Lei, K., Hurley, R.L., Manning, B.D., Reiling, J.H., Hafen, E., Witters, L.A., Ellisen, L.W., and Kaelin, W.G., Jr. (2004). Regulation of mTOR function in response to hypoxia by REDD1 and the TSC1/TSC2 tumor suppressor complex. *Genes & development* *18*, 2893-2904.

Buchanan, C.F., Voigt, E.E., Szot, C.S., Freeman, J.W., Vlachos, P.P., and Rylander, M.N. (2014). Three-dimensional microfluidic collagen hydrogels for investigating flow-mediated tumor-endothelial signaling and vascular organization. *Tissue engineering Part C, Methods* *20*, 64-75.

Bunton-Stasyshyn, R.K., Saccon, R.A., Fratta, P., and Fisher, E.M. (2015). SOD1 Function and Its Implications for Amyotrophic Lateral Sclerosis Pathology: New and Renascent Themes. *The Neuroscientist : a review journal bringing neurobiology, neurology and psychiatry* *21*, 519-529.

Burch, W.M.S.R.a.R.L. (1959). *The Principles of Humane Experimental Technique* (London: Methuen).

Burchell, V.S., Nelson, D.E., Sanchez-Martinez, A., Delgado-Camprubi, M., Ivatt, R.M., Pogson, J.H., Randle, S.J., Wray, S., Lewis, P.A., Houlden, H., *et al.* (2013). The

Parkinson's disease-linked proteins Fbxo7 and Parkin interact to mediate mitophagy. *Nat Neurosci* *16*, 1257-1265.

Cai, L., Li, J., Zhao, J., Guo, Y., Xie, M., Zhang, X., Wang, L., Tian, H., Li, A., Li, Q., *et al.* (2019). Fbxo6 confers drug-sensitization to cisplatin via inhibiting the activation of Chk1 in non-small cell lung cancer. *FEBS Letters* *593*, 1827-1836.

Cai, T., Qi, Y., Jergens, A., Wannemuehler, M., Barrett, T.A., and Wang, Q. (2018). Effects of six common dietary nutrients on murine intestinal organoid growth. *PLoS One* *13*, e0191517.

Calcagno, D.Q., Freitas, V.M., Leal, M.F., de Souza, C.R., Demachki, S., Montenegro, R., Assumpcao, P.P., Khayat, A.S., Smith Mde, A., dos Santos, A.K., *et al.* (2013). MYC, FBXW7 and TP53 copy number variation and expression in gastric cancer. *BMC gastroenterology* *13*, 141.

Campbell, K., and Casanova, J. (2016). A common framework for EMT and collective cell migration. *Development* *143*, 4291-4300.

Cao, P., Xia, Y., He, W., Zhang, T., Hong, L., Zheng, P., Shen, X., Liang, G., Cui, R., and Zou, P. (2019). Enhancement of oxaliplatin-induced colon cancer cell apoptosis by alantolactone, a natural product inducer of ROS. *Int J Biol Sci* *15*, 1676-1684.

Cassavaugh, J.M., Hale, S.A., Wellman, T.L., Howe, A.K., Wong, C., and Lounsbury, K.M. (2011). Negative regulation of HIF-1 α by an FBW7-mediated degradation pathway during hypoxia. *J Cell Biochem* *112*, 3882-3890.

Cen, G., Ding, H.H., Liu, B., and Wu, W.D. (2014). FBXL5 targets cortactin for ubiquitination-mediated destruction to regulate gastric cancer cell migration. *Tumour biology : the journal of the International Society for Oncodevelopmental Biology and Medicine* *35*, 8633-8638.

Cenciarelli, C., Chiaur, D.S., Guardavaccaro, D., Parks, W., Vidal, M., and Pagano, M. (1999). Identification of a family of human F-box proteins. *Curr Biol* *9*, 1177-1179.

Chan, C.-H., Lee, S.-W., Wang, J., and Lin, H.-K. (2010). Regulation of Skp2 expression and activity and its role in cancer progression. *ScientificWorldJournal* *10*, 1001-1015.

Chandrashekar, D.S., Bashel, B., Balasubramanya, S.A.H., Creighton, C.J., Ponce-Rodriguez, I., Chakravarthi, B., and Varambally, S. (2017). UALCAN: A Portal for Facilitating Tumor Subgroup Gene Expression and Survival Analyses. *Neoplasia* *19*, 649-658.

Chang, C.C., Lin, H.H., Lin, J.K., Lin, C.C., Lan, Y.T., Wang, H.S., Yang, S.H., Chen, W.S., Lin, T.C., Jiang, J.K., *et al.* (2015). FBXW7 mutation analysis and its correlation with clinicopathological features and prognosis in colorectal cancer patients. *The International journal of biological markers* *30*, e88-95.

Chang, Y.S., Tu, S.J., Chiang, H.S., Yen, J.C., Lee, Y.T., Fang, H.Y., and Chang, J.G. (2020). Genome-Wide Analysis of Prognostic Alternative Splicing Signature and Splicing Factors in Lung Adenocarcinoma. *Genes (Basel)* *11*.

Chen, B.B., Glasser, J.R., Coon, T.A., and Mallampalli, R.K. (2011). FBXL2 is a ubiquitin E3 ligase subunit that triggers mitotic arrest. *Cell Cycle* *10*, 3487-3494.

Chen, B.B., Glasser, J.R., Coon, T.A., and Mallampalli, R.K. (2012). F-box protein FBXL2 exerts human lung tumor suppressor-like activity by ubiquitin-mediated degradation of cyclin D3 resulting in cell cycle arrest. *Oncogene* *31*, 2566-2579.

Chen, X., Li, X.Y., Long, M., Wang, X., Gao, Z.W., Cui, Y., Ren, J., Zhang, Z., Liu, C., Dong, K., *et al.* (2018). The FBXW7 tumor suppressor inhibits breast cancer proliferation and promotes apoptosis by targeting MTDH for degradation. *Neoplasia* *65*, 201-209.

Chen, Y., Fan, Z., Yang, Y., and Gu, C. (2019). Iron metabolism and its contribution to cancer (Review). *International journal of oncology* 54, 1143-1154.

Chen, Z.-W., Liu, B., Tang, N.-W., Xu, Y.-H., Ye, X.-Y., Li, Z.-M., Niu, X.-M., Shen, S.-P., Lu, S., and Xu, L. (2014). FBXL5-mediated degradation of single-stranded DNA-binding protein hSSB1 controls DNA damage response. *Nucleic Acids Research* 42, 11560-11569.

Chiu, H.-W., Chang, J.-S., Lin, H.-Y., Lee, H.-H., Kuei, C.-H., Lin, C.-H., Huang, H.-M., and Lin, Y.-F. (2018). FBXL7 Upregulation Predicts a Poor Prognosis and Associates with a Possible Mechanism for Paclitaxel Resistance in Ovarian Cancer. *Journal of clinical medicine* 7, 330.

Choi, J.H., Yoon, J.S., Won, Y.W., Park, B.B., and Lee, Y.Y. (2012). Chloroquine enhances the chemotherapeutic activity of 5-fluorouracil in a colon cancer cell line via cell cycle alteration. *Apmis* 120, 597-604.

Choi, M., Stottmann, R.W., Yang, Y.P., Meyers, E.N., and Klingensmith, J. (2007). The bone morphogenetic protein antagonist noggin regulates mammalian cardiac morphogenesis. *Circ Res* 100, 220-228.

Chollangi, S., Thompson, J.W., Ruiz, J.C., Gardner, K.H., and Bruick, R.K. (2012). Hemerythrin-like domain within F-box and leucine-rich repeat protein 5 (FBXL5) communicates cellular iron and oxygen availability by distinct mechanisms. *The Journal of biological chemistry* 287, 23710-23717.

Chou, J.-L., Su, H.-Y., Chen, L.-Y., Liao, Y.-P., Hartman-Frey, C., Lai, Y.-H., Yang, H.-W., Deatherage, D.E., Kuo, C.-T., Huang, Y.-W., *et al.* (2010). Promoter hypermethylation of FBXO32, a novel TGF- β /SMAD4 target gene and tumor suppressor, is associated with poor prognosis in human ovarian cancer. *Laboratory Investigation* 90, 414.

Cock, P.J.A., Fields, C.J., Goto, N., Heuer, M.L., and Rice, P.M. (2010). The Sanger FASTQ file format for sequences with quality scores, and the Solexa/Illumina FASTQ variants. *Nucleic acids research* 38, 1767-1771.

Coenye, T. (2021). Do results obtained with RNA-sequencing require independent verification? *Biofilm* 3, 100043-100043.

Consortium, G.T. (2013). The Genotype-Tissue Expression (GTEx) project. *Nature genetics* 45, 580-585.

Corrò, C., Novellasademunt, L., and Li, V.S.W. (2020). A brief history of organoids. *American Journal of Physiology-Cell Physiology* 319, C151-C165.

Costa da Silva, M., Breckwoldt, M.O., Vinchi, F., Correia, M.P., Stojanovic, A., Thielmann, C.M., Meister, M., Muley, T., Warth, A., Platten, M., *et al.* (2017). Iron Induces Anti-tumor Activity in Tumor-Associated Macrophages. *Front Immunol* 8, 1479.

Craig, D.J.B.D.M. (2018). Using wireless recording technologies to investigate cortical coherence in a mouse model of dementia (University of Exeter: National Centre for Replacement, Reduction and Refinement of Animals in Research).

Crespo, M., Vilar, E., Tsai, S.-Y., Chang, K., Amin, S., Srinivasan, T., Zhang, T., Pipalia, N.H., Chen, H.J., Witherspoon, M., *et al.* (2017). Colonic organoids derived from human induced pluripotent stem cells for modeling colorectal cancer and drug testing. *Nature Medicine* 23, 878.

Cruz, N.M., and Freedman, B.S. (2019). Differentiation of human kidney organoids from pluripotent stem cells. *Methods in cell biology* 153, 133-150.

Cui, D., Xiong, X., and Zhao, Y. (2016). Cullin-RING ligases in regulation of autophagy. *Cell division* *11*, 8-8.

Dantuma, N.P., and Bott, L.C. (2014). The ubiquitin-proteasome system in neurodegenerative diseases: precipitating factor, yet part of the solution. *Front Mol Neurosci* *7*, 70-70.

Date, S., and Sato, T. (2015). Mini-Gut Organoids: Reconstitution of the Stem Cell Niche. *Annual Review of Cell and Developmental Biology* *31*, 269-289.

Davies, D. (2021). Flow cytometric analysis of cell cycle with propidium iodide DNA staining, A. PLC, ed. (abcam.com: Abcam. PLC).

De Palma, F.D.E., D'Argenio, V., Pol, J., Kroemer, G., Maiuri, M.C., and Salvatore, F. (2019). The Molecular Hallmarks of the Serrated Pathway in Colorectal Cancer. *Cancers* *11*, 1017.

Deltcheva, E., Chylinski, K., Sharma, C.M., Gonzales, K., Chao, Y., Pirzada, Z.A., Eckert, M.R., Vogel, J., and Charpentier, E. (2011). CRISPR RNA maturation by trans-encoded small RNA and host factor RNase III. *Nature* *471*, 602-607.

Dewangan, J., Srivastava, S., and Rath, S.K. (2017). Salinomycin: A new paradigm in cancer therapy. *Tumor Biology* *39*, 1010428317695035.

DeWard, A.D., Cramer, J., and Lagasse, E. (2014). Cellular heterogeneity in the mouse esophagus implicates the presence of a nonquiescent epithelial stem cell population. *Cell Rep* *9*, 701-711.

Dey, A., Lane, D.P., and Verma, C.S. (2010). Modulating the p53 pathway. *Semin Cancer Biol* *20*, 3-9.

Di Donato, M., Cerner, G., Migliaccio, A., and Castoria, G. (2019). Nerve Growth Factor Induces Proliferation and Aggressiveness In Prostate Cancer Cells. *Cancers* *11*, 784.

Di Fiore, B., and Pines, J. (2007). Emi1 is needed to couple DNA replication with mitosis but does not regulate activation of the mitotic APC/C. *J Cell Biol* *177*, 425-437.

Dibble, C.C., and Manning, B.D. (2010). 2 - The TSC1-TSC2 Complex: A Key Signal-Integrating Node Upstream of TOR. In *The Enzymes*, F. Tamanoi, and M.N. Hall, eds. (Academic Press), pp. 21-48.

Dobin, A., Davis, C.A., Schlesinger, F., Drenkow, J., Zaleski, C., Jha, S., Batut, P., Chaisson, M., and Gingeras, T.R. (2013). STAR: ultrafast universal RNA-seq aligner. *Bioinformatics* *29*, 15-21.

Dolcet, X., Llobet, D., Pallares, J., and Matias-Guiu, X. (2005). NF-kB in development and progression of human cancer. *Virchows Archiv* *446*, 475-482.

Donaldson, J.G. (2015). Immunofluorescence Staining. *Current Protocols in Cell Biology* *69*, 4.3.1-4.3.7.

Dong, G.W., Preisler, H.D., and Priore, R. (1984). Potential limitations of in vitro clonogenic drug sensitivity assays. *Cancer Chemother Pharmacol* *13*, 206-210.

Donner, I., Kiviluoto, T., Ristimäki, A., Aaltonen, L.A., and Vahteristo, P. (2015). Exome sequencing reveals three novel candidate predisposition genes for diffuse gastric cancer. *Familial Cancer* *14*, 241-246.

Drago-García, D., Espinal-Enríquez, J., and Hernández-Lemus, E. (2017). Network analysis of EMT and MET micro-RNA regulation in breast cancer. *Scientific Reports* *7*, 13534.

Drost, J., and Clevers, H. (2018). Organoids in cancer research. *Nature Reviews Cancer* *18*, 407-418.

Drost, J., van Jaarsveld, R.H., Ponsioen, B., Zimmerlin, C., van Boxtel, R., Buijs, A., Sachs, N., Overmeer, R.M., Offerhaus, G.J., Begthel, H., *et al.* (2015). Sequential cancer mutations in cultured human intestinal stem cells. *Nature* *521*, 43.

Duan, S., Cermak, L., Pagan, J.K., Rossi, M., Martinengo, C., di Celle, P.F., Chapuy, B., Shipp, M., Chiarle, R., and Pagano, M. (2012). FBXO11 targets BCL6 for degradation and is inactivated in diffuse large B-cell lymphomas. *Nature* *481*, 90-93.

DuPage, M., Dooley, A.L., and Jacks, T. (2009). Conditional mouse lung cancer models using adenoviral or lentiviral delivery of Cre recombinase. *Nature Protocols* *4*, 1064.

Duronio, V. (2008). The life of a cell: apoptosis regulation by the PI3K/PKB pathway. *Biochem J* *415*, 333-344.

Duval, K., Grover, H., Han, L.-H., Mou, Y., Pegoraro, A.F., Fredberg, J., and Chen, Z. (2017). Modeling Physiological Events in 2D vs. 3D Cell Culture. *Physiology* *32*, 266-277.

Edfors, F., Danielsson, F., Hallström, B.M., Käll, L., Lundberg, E., Pontén, F., Forsström, B., and Uhlén, M. (2016). Gene-specific correlation of RNA and protein levels in human cells and tissues. *Molecular systems biology* *12*, 883.

El Ayadi, A., Stieren, E.S., Barral, J.M., and Boehning, D. (2012). Ubiquitin-1 regulates amyloid precursor protein maturation and degradation by stimulating K63-linked polyubiquitination of lysine 688. *Proc Natl Acad Sci U S A* *109*, 13416-13421.

Elliott, P.R., Leske, D., Wagstaff, J., Schlicher, L., Berridge, G., Maslen, S., Timmermann, F., Ma, B., Fischer, R., Freund, S.M.V., *et al.* (2021). Regulation of CYLD activity and specificity by phosphorylation and ubiquitin-binding CAP-Gly domains. *Cell Rep* *37*, 109777.

Enserink, J.M., and Kolodner, R.D. (2010). An overview of Cdk1-controlled targets and processes. *Cell division* *5*, 11-11.

Errington, T.M., Iorns, E., Gunn, W., Tan, F.E., Lomax, J., and Nosek, B.A. (2014). An open investigation of the reproducibility of cancer biology research. *eLife* *3*, e04333.

Ewing, I., Hurley, J.J., Josephides, E., and Millar, A. (2014). The molecular genetics of colorectal cancer. *Frontline Gastroenterology* *5*, 26-30.

Fan, Y., Dutta, J., Gupta, N., Fan, G., and Gélinas, C. (2008). Regulation of programmed cell death by NF-kappaB and its role in tumorigenesis and therapy. *Adv Exp Med Biol* *615*, 223-250.

Fang, X., Zhou, W., Wu, Q., Huang, Z., Shi, Y., Yang, K., Chen, C., Xie, Q., Mack, S.C., Wang, X., *et al.* (2017). Deubiquitinase USP13 maintains glioblastoma stem cells by antagonizing FBXL14-mediated Myc ubiquitination. *The Journal of experimental medicine* *214*, 245-267.

Faniello, M.C., Di Sanzo, M., Quaresima, B., Baudi, F., Di Caro, V., Cuda, G., Morrone, G., Del Sal, G., Spinelli, G., Venuta, S., *et al.* (2008). p53-mediated downregulation of H ferritin promoter transcriptional efficiency via NF-Y. *Int J Biochem Cell Biol* *40*, 2110-2119.

Feber, A., Clark, J., Goodwin, G., Dodson, A.R., Smith, P.H., Fletcher, A., Edwards, S., Flohr, P., Falconer, A., Roe, T., *et al.* (2004). Amplification and overexpression of E2F3 in human bladder cancer. *Oncogene* *23*, 1627-1630.

Feng, C., Yang, F., and Wang, J. (2017). FBXO4 inhibits lung cancer cell survival by targeting Mcl-1 for degradation. *Cancer Gene Therapy* *24*, 342-347.

Fennema, E., Rivron, N., Rouwkema, J., van Blitterswijk, C., and de Boer, J. (2013). Spheroid culture as a tool for creating 3D complex tissues. *Trends Biotechnol* 31, 108-115.

Fernandez-Barral, A., Costales-Carrera, A., Buirra, S.P., Jung, P., Ferrer-Mayorga, G., Larriba, M.J., Bustamante-Madrid, P., Dominguez, O., Real, F.X., Guerra-Pastrian, L., *et al.* (2020). Vitamin D differentially regulates colon stem cells in patient-derived normal and tumor organoids. *Febs j* 287, 53-72.

Ferrara, D., Pasetto, L., Bonetto, V., and Basso, M. (2018). Role of Extracellular Vesicles in Amyotrophic Lateral Sclerosis. *Front Neurosci* 12, 574.

Fiesel, F.C., Moussaud-Lamodière, E.L., Ando, M., and Springer, W. (2014). A specific subset of E2 ubiquitin-conjugating enzymes regulate Parkin activation and mitophagy differently. *Journal of cell science* 127, 3488-3504.

Findlay, V.J., Wang, C., Nogueira, L.M., Hurst, K., Quirk, D., Ethier, S.P., Staveley O'Carroll, K.F., Watson, D.K., and Camp, E.R. (2014). SNAI2 modulates colorectal cancer 5-fluorouracil sensitivity through miR145 repression. *Molecular cancer therapeutics* 13, 2713-2726.

Fingleton, B. (2007). Matrix metalloproteinases as valid clinical targets. *Current pharmaceutical design* 13, 333-346.

Fiorotto, R., Amenduni, M., Mariotti, V., Fabris, L., Spirli, C., and Strazzabosco, M. (2019). Liver diseases in the dish: iPSC and organoids as a new approach to modeling liver diseases. *Biochim Biophys Acta Mol Basis Dis* 1865, 920-928.

Focaccetti, C., Bruno, A., Magnani, E., Bartolini, D., Principi, E., Dallaglio, K., Bucci, E.O., Finzi, G., Sessa, F., Noonan, D.M., *et al.* (2015). Effects of 5-fluorouracil on morphology, cell cycle, proliferation, apoptosis, autophagy and ROS production in endothelial cells and cardiomyocytes. *PLoS One* 10, e0115686.

Fokas, E., Yoshimura, M., Prevo, R., Higgins, G., Hackl, W., Maira, S.M., Bernhard, E.J., McKenna, W.G., and Muschel, R.J. (2012). NVP-BEZ235 and NVP-BGT226, dual phosphatidylinositol 3-kinase/mammalian target of rapamycin inhibitors, enhance tumor and endothelial cell radiosensitivity. *Radiat Oncol* 7, 48.

Forbes, S.A., Beare, D., Boutselakis, H., Bamford, S., Bindal, N., Tate, J., Cole, C.G., Ward, S., Dawson, E., Ponting, L., *et al.* (2017). COSMIC: somatic cancer genetics at high-resolution. *Nucleic Acids Res* 45, D777-d783.

Forbes, T.A., Howden, S.E., Lawlor, K., Phipson, B., Maksimovic, J., Hale, L., Wilson, S., Quinlan, C., Ho, G., Holman, K., *et al.* (2018). Patient-iPSC-Derived Kidney Organoids Show Functional Validation of a Ciliopathic Renal Phenotype and Reveal Underlying Pathogenetic Mechanisms. *The American Journal of Human Genetics* 102, 816-831.

Fouad, S., Wells, O.S., Hill, M.A., and D'Angiolella, V. (2019). Cullin Ring Ubiquitin Ligases (CRLs) in Cancer: Responses to Ionizing Radiation (IR) Treatment. *Front Physiol* 10, 1144.

Fouad, Y.A., and Aanei, C. (2017). Revisiting the hallmarks of cancer. *American journal of cancer research* 7, 1016-1036.

Foxler, D.E., Bridge, K.S., James, V., Webb, T.M., Mee, M., Wong, S.C., Feng, Y., Constantin-Teodosiu, D., Petursdottir, T.E., Bjornsson, J., *et al.* (2012). The LIMD1 protein bridges an association between the prolyl hydroxylases and VHL to repress HIF-1 activity. *Nat Cell Biol* 14, 201-208.

Francies, H.E., Barthorpe, A., McLaren-Douglas, A., Barendt, W.J., and Garnett, M.J. (2019). Drug Sensitivity Assays of Human Cancer Organoid Cultures. *Methods in molecular biology* (Clifton, NJ) *1576*, 339-351.

Franken, N.A.P., Rodermond, H.M., Stap, J., Haveman, J., and van Bree, C. (2006). Clonogenic assay of cells in vitro. *Nature Protocols* *1*, 2315-2319.

Freeman, D.J., Li, A.G., Wei, G., Li, H.-H., Kertesz, N., Lesche, R., Whale, A.D., Martinez-Diaz, H., Rozengurt, N., Cardiff, R.D., *et al.* (2003). PTEN tumor suppressor regulates p53 protein levels and activity through phosphatase-dependent and -independent mechanisms. *Cancer cell* *3*, 117-130.

Frescas, D., Guardavaccaro, D., Bassermann, F., Koyama-Nasu, R., and Pagano, M. (2007). JHDM1B/FBXL10 is a nucleolar protein that represses transcription of ribosomal RNA genes. *Nature* *450*, 309-313.

Frescas, D., and Pagano, M. (2008). Deregulated proteolysis by the F-box proteins SKP2 and beta-TrCP: tipping the scales of cancer. *Nature reviews Cancer* *8*, 438-449.

Frese, K.K., and Tuveson, D.A. (2007). Maximizing mouse cancer models. *Nature Reviews Cancer* *7*, 654.

Fuchs, S.Y., Spiegelman, V.S., and Suresh Kumar, K.G. (2004). The many faces of β -TrCP E3 ubiquitin ligases: reflections in the magic mirror of cancer. *Oncogene* *23*, 2028-2036.

Fujii, M., Matano, M., Nanki, K., and Sato, T. (2015). Efficient genetic engineering of human intestinal organoids using electroporation. *Nature Protocols* *10*, 1474.

Funachi, Y., Tanikawa, C., Yi Lo, P.H., Mori, J., Daigo, Y., Takano, A., Miyagi, Y., Okawa, A., Nakamura, Y., and Matsuda, K. (2015). Regulation of iron homeostasis by the p53-ISCU pathway. *Sci Rep* *5*, 16497.

Galaris, D., Skiada, V., and Barbouti, A. (2008). Redox signaling and cancer: the role of "labile" iron. *Cancer Lett* *266*, 21-29.

Galicia-Garcia, U., Benito-Vicente, A., Uribe, K.B., Jebari, S., Larrea-Sebal, A., Alonso-Estrada, R., Aguilo-Arce, J., Ostolaza, H., Palacios, L., and Martin, C. (2020). Mutation type classification and pathogenicity assignment of sixteen missense variants located in the EGF-precursor homology domain of the LDLR. *Scientific Reports* *10*, 1727.

Galle, E., Thienpont, B., Cappuyens, S., Venken, T., Busschaert, P., Van Haele, M., Van Cutsem, E., Roskams, T., van Pelt, J., Verslype, C., *et al.* (2020). DNA methylation-driven EMT is a common mechanism of resistance to various therapeutic agents in cancer. *Clinical Epigenetics* *12*, 27.

Galluzzi, L., Pietrocola, F., Bravo-San Pedro, J.M., Amaravadi, R.K., Baehrecke, E.H., Cecconi, F., Codogno, P., Debnath, J., Gewirtz, D.A., Karantza, V., *et al.* (2015). Autophagy in malignant transformation and cancer progression. *The EMBO journal* *34*, 856-880.

Ganoth, D., Bornstein, G., Ko, T.K., Larsen, B., Tyers, M., Pagano, M., and Hershko, A. (2001). The cell-cycle regulatory protein Cks1 is required for SCF(Skp2)-mediated ubiquitylation of p27. *Nat Cell Biol* *3*, 321-324.

Gao, C., Xiao, G., and Hu, J. (2014). Regulation of Wnt/ β -catenin signaling by posttranslational modifications. *Cell & Bioscience* *4*, 13.

Gao, J., and Richardson, D.R. (2001). The potential of iron chelators of the pyridoxal isonicotinoyl hydrazone class as effective antiproliferative agents, IV: The mechanisms involved in inhibiting cell-cycle progression. *Blood* *98*, 842-850.

Gasiunas, G., Barrangou, R., Horvath, P., and Siksnys, V. (2012). Cas9–crRNA ribonucleoprotein complex mediates specific DNA cleavage for adaptive immunity in bacteria. *Proceedings of the National Academy of Sciences of the United States of America* *109*, E2579-E2586.

Gassen, N.C., Niemeyer, D., Muth, D., Corman, V.M., Martinelli, S., Gassen, A., Hafner, K., Papies, J., Mösbauer, K., Zellner, A., *et al.* (2019). SKP2 attenuates autophagy through Beclin1-ubiquitination and its inhibition reduces MERS-Coronavirus infection. *Nature Communications* *10*, 5770.

Gautam, V., D'Avanzo, C., Berezovska, O., Tanzi, R.E., and Kovacs, D.M. (2015). Synaptotagmins interact with APP and promote Abeta generation. *Molecular neurodegeneration* *10*, 31.

Gehart, H., and Clevers, H. (2019). Tales from the crypt: new insights into intestinal stem cells. *Nature Reviews Gastroenterology & Hepatology* *16*, 19-34.

Gelman, J.S., Sironi, J., Berezniuk, I., Dasgupta, S., Castro, L.M., Gozzo, F.C., Ferro, E.S., and Fricker, L.D. (2013). Alterations of the intracellular peptidome in response to the proteasome inhibitor bortezomib. *PloS one* *8*, e53263-e53263.

Gerez, J.A., Prymaczok, N.C., Rockenstein, E., Herrmann, U.S., Schwarz, P., Adame, A., Enchev, R.I., Courtheoux, T., Boersema, P.J., Riek, R., *et al.* (2019). A cullin-RING ubiquitin ligase targets exogenous alpha-synuclein and inhibits Lewy body-like pathology. *Science translational medicine* *11*.

Gery, S., Komatsu, N., Baldjyan, L., Yu, A., Koo, D., and Koeffler, H.P. (2006). The circadian gene *per1* plays an important role in cell growth and DNA damage control in human cancer cells. *Mol Cell* *22*, 375-382.

Geurts, M.H., de Poel, E., Amatngalim, G.D., Oka, R., Meijers, F.M., Kruisselbrink, E., van Mourik, P., Berkers, G., de Winter-de Groot, K.M., Michel, S., *et al.* (2020). CRISPR-Based Adenine Editors Correct Nonsense Mutations in a Cystic Fibrosis Organoid Biobank. *Cell Stem Cell*.

Giasson, B.I., and Lee, V.M.Y. (2003). Are Ubiquitination Pathways Central to Parkinson's Disease? *Cell* *114*, 1-8.

Gleave, A.M., Ci, X., Lin, D., and Wang, Y. (2020). A synopsis of prostate organoid methodologies, applications, and limitations. *Prostate*.

Glickman, M.H., and Ciechanover, A. (2002). The ubiquitin-proteasome proteolytic pathway: destruction for the sake of construction. *Physiological reviews* *82*, 373-428.

Gong, J., Huang, Z., and Huo, J.R. (2016). Involvement of F-box proteins in esophageal cancer (Review). *International journal of oncology* *48*, 886-894.

González-Ballester, D., de Montaigne, A., Galván, A., and Fernández, E. (2005). Restriction enzyme site-directed amplification PCR: A tool to identify regions flanking a marker DNA. *Analytical Biochemistry* *340*, 330-335.

Gouveia, K., and Hurst, J.L. (2017). Optimising reliability of mouse performance in behavioural testing: the major role of non-aversive handling. *Scientific Reports* *7*, 44999.

Grigore, A.D., Jolly, M.K., Jia, D., Farach-Carson, M.C., and Levine, H. (2016). Tumor Budding: The Name is EMT. *Partial EMT*. *Journal of clinical medicine* *5*, 51.

Gry, M., Rimini, R., Strömberg, S., Asplund, A., Pontén, F., Uhlén, M., and Nilsson, P. (2009). Correlations between RNA and protein expression profiles in 23 human cell lines. *BMC Genomics* *10*, 365.

Guerreiro Stucklin, A.S., Ramaswamy, V., Daniels, C., and Taylor, M.D. (2018). Review of molecular classification and treatment implications of pediatric brain tumors. *Current opinion in pediatrics* 30, 3-9.

Guinney, J., Dienstmann, R., Wang, X., de Reyniès, A., Schlicker, A., Sonesson, C., Marisa, L., Roepman, P., Nyamundanda, G., Angelino, P., *et al.* (2015). The consensus molecular subtypes of colorectal cancer. *Nature Medicine* 21, 1350.

Guo, X., Zhu, Y., Hong, X., Zhang, M., Qiu, X., Wang, Z., Qi, Z., and Hong, X. (2017). miR-181d and c-myc-mediated inhibition of CRY2 and FBXL3 reprograms metabolism in colorectal cancer. *Cell Death & Disease* 8, e2958.

Guo, Y., Xiao, P., Lei, S., Deng, F., Xiao, G.G., Liu, Y., Chen, X., Li, L., Wu, S., Chen, Y., *et al.* (2008). How is mRNA expression predictive for protein expression? A correlation study on human circulating monocytes. *Acta Biochim Biophys Sin (Shanghai)* 40, 426-436.

Hahn, S., Nam, M.-O., Noh, J.H., Lee, D.H., Han, H.W., Kim, D.H., Hahm, K.B., Hong, S.P., Yoo, J.-H., and Yoo, J. (2017). Organoid-based epithelial to mesenchymal transition (OEMT) model: from an intestinal fibrosis perspective. *Scientific Reports* 7, 2435.

Haifeng, W.T.L.X.T.Y.Z. (2017). Expression and clinical significance of FBXL5 in colon cancer. *Journal Of Modern Oncology* 18, 2934-2938.

Han, X., Chen, H., Zhou, J., Steed, H., Postovit, L.-M., and Fu, Y. (2018). Pharmacological Inhibition of p38 MAPK by SB203580 Increases Resistance to Carboplatin in A2780cp Cells and Promotes Growth in Primary Ovarian Cancer Cells. *Int J Mol Sci* 19, 2184.

Hapke, R.Y., and Haake, S.M. (2020). Hypoxia-induced epithelial to mesenchymal transition in cancer. *Cancer Letters* 487, 10-20.

Hardisty-Hughes, R.E., Tateossian, H., Morse, S.A., Romero, M.R., Middleton, A., Tymowska-Lalanne, Z., Hunter, A.J., Cheeseman, M., and Brown, S.D. (2006). A mutation in the F-box gene, *Fbxo11*, causes otitis media in the Jeff mouse. *Human molecular genetics* 15, 3273-3279.

Harner-Foreman, N., Vadakekolathu, J., Laversin, S.A., Mathieu, M.G., Reeder, S., Pockley, A.G., Rees, R.C., and Boockock, D.J. (2017). A novel spontaneous model of epithelial-mesenchymal transition (EMT) using a primary prostate cancer derived cell line demonstrating distinct stem-like characteristics. *Scientific reports* 7, 40633-40633.

Harrigan, J.A., Jacq, X., Martin, N.M., and Jackson, S.P. (2017). Deubiquitylating enzymes and drug discovery: emerging opportunities. *Nature Reviews Drug Discovery* 17, 57.

Hazewinkel, Y., de Wijkerslooth, T.R., Stoop, E.M., Bossuyt, P.M., Biermann, K., van de Vijver, M.J., Fockens, P., van Leerdam, M.E., Kuipers, E.J., and Dekker, E. (2014). Prevalence of serrated polyps and association with synchronous advanced neoplasia in screening colonoscopy. *Endoscopy* 46, 219-224.

He, S., Carman, C.V., Lee, J.H., Lan, B., Koehler, S., Atia, L., Park, C.Y., Kim, J.H., Mitchel, J.A., Park, J.-A., *et al.* (2019). The tumor suppressor p53 can promote collective cellular migration. *PLOS ONE* 14, e0202065.

He, Z.-J., Li, W., Chen, H., Wen, J., Gao, Y.-F., and Liu, Y.-J. (2018). miR-1306-3p targets FBXL5 to promote metastasis of hepatocellular carcinoma through suppressing snail degradation. *Biochemical and biophysical research communications* 504, 820-826.

Hein, R., Flesch-Janys, D., Dahmen, N., Beckmann, L., Lindström, S., Schoof, N., Czene, K., Mittelstraß, K., Illig, T., Seibold, P., *et al.* (2013). A genome-wide association study to identify genetic susceptibility loci that modify ductal and lobular postmenopausal breast cancer risk associated with menopausal hormone therapy use: a two-stage design with replication. *Breast Cancer Research and Treatment* 138, 529-542.

Heo, I., Dutta, D., Schaefer, D.A., Iakobachvili, N., Artegiani, B., Sachs, N., Boonekamp, K.E., Bowden, G., Hendrickx, A.P.A., Willems, R.J.L., *et al.* (2018). Modelling *Cryptosporidium* infection in human small intestinal and lung organoids. *Nature Microbiology* 3, 814-823.

Hepple, R. (2005). The use of animals for research in the pharmaceutical industry: Chapter 8, N. Bioethics, ed. (London: Nuffield Council on Bioethics).

Hirt, C., Papadimitropoulos, A., Muraro, M.G., Mele, V., Panopoulos, E., Cremonesi, E., Ivanek, R., Schultz-Thater, E., Drosler, R.A., Mengus, C., *et al.* (2015). Bioreactor-engineered cancer tissue-like structures mimic phenotypes, gene expression profiles and drug resistance patterns observed “in vivo”. *Biomaterials* 62, 138-146.

Ho, M.S., Ou, C., Chan, Y.R., Chien, C.T., and Pi, H. (2008). The utility F-box for protein destruction. *Cellular and molecular life sciences : CMLS* 65, 1977-2000.

Hochstrasser, M. (2009). Origin and function of ubiquitin-like proteins. *Nature* 458, 422-429.

Hogan, A.L., Don, E.K., Rayner, S.L., Lee, A., Laird, A.S., Watchon, M., Winnick, C., Tarr, I.S., Morsch, M., Fifita, J.A., *et al.* (2017). Expression of ALS/FTD-linked mutant CCNF in zebrafish leads to increased cell death in the spinal cord and an aberrant motor phenotype. *Human molecular genetics* 26, 2616-2626.

Holloway, E.M., Capeling, M.M., and Spence, J.R. (2019). Biologically inspired approaches to enhance human organoid complexity. *Development* 146, dev166173.

Hong, L., Huang, H.C., and Jiang, Z.F. (2014). Relationship between amyloid-beta and the ubiquitin-proteasome system in Alzheimer's disease. *Neurological research* 36, 276-282.

Horn, M., Geisen, C., Cermak, L., Becker, B., Nakamura, S., Klein, C., Pagano, M., and Antebi, A. (2014). DRE-1/FBXO11-dependent degradation of BLMP-1/BLIMP-1 governs *C. elegans* developmental timing and maturation. *Developmental cell* 28, 697-710.

Howe, K.L., Achuthan, P., Allen, J., Allen, J., Alvarez-Jarreta, J., Amode, M.R., Armean, I.M., Azov, A.G., Bennett, R., Bhai, J., *et al.* (2021). Ensembl 2021. *Nucleic Acids Research* 49, D884-D891.

Huch, M., and Koo, B.-K. (2015). Modeling mouse and human development using organoid cultures. *Development* 142, 3113-3125.

Hughes, P., Marshall, D., Reid, Y., Parkes, H., and Gelber, C. (2007). The costs of using unauthenticated, over-passaged cell lines: how much more data do we need? *BioTechniques* 43, 575-586.

Huh, D., Hamilton, G.A., and Ingber, D.E. (2011). From 3D cell culture to organs-on-chips. *Trends in cell biology* 21, 745-754.

Huse, J.T., and Holland, E.C. (2009). Genetically engineered mouse models of brain cancer and the promise of preclinical testing. *Brain pathology (Zurich, Switzerland)* 19, 132-143.

Hutagalung, A.H., and Novick, P.J. (2011). Role of Rab GTPases in membrane traffic and cell physiology. *Physiological reviews* 91, 119-149.

Itkonen, H.M., Engedal, N., Babaie, E., Luhr, M., Guldvik, I.J., Minner, S., Hohloch, J., Tsourlakis, M.C., Schlomm, T., and Mills, I.G. (2015). UAP1 is overexpressed in prostate cancer and is protective against inhibitors of N-linked glycosylation. *Oncogene* *34*, 3744-3750.

Jackson, A.L., and Linsley, P.S. (2010). Recognizing and avoiding siRNA off-target effects for target identification and therapeutic application. *Nat Rev Drug Discov* *9*, 57-67.

Jaksits, S., Kriehuber, E., Charbonnier, A.S., Rappersberger, K., Stingl, G., and Maurer, D. (1999). CD34+ cell-derived CD14+ precursor cells develop into Langerhans cells in a TGF-beta 1-dependent manner. *Journal of immunology (Baltimore, Md : 1950)* *163*, 4869-4877.

Jänne, P.A., Shaw, A.T., Pereira, J.R., Jeannin, G., Vansteenkiste, J., Barrios, C., Franke, F.A., Grinsted, L., Zazulina, V., Smith, P., *et al.* (2013). Selumetinib plus docetaxel for KRAS-mutant advanced non-small-cell lung cancer: a randomised, multicentre, placebo-controlled, phase 2 study. *The Lancet Oncology* *14*, 38-47.

Jeong, S.Y., Crooks, D.R., Wilson-Ollivierre, H., Ghosh, M.C., Sougrat, R., Lee, J., Cooperman, S., Mitchell, J.B., Beaumont, C., and Rouault, T.A. (2011). Iron insufficiency compromises motor neurons and their mitochondrial function in Irf2-null mice. *PloS one* *6*, e25404-e25404.

Jeong, Y.T., Simoneschi, D., Keegan, S., Melville, D., Adler, N.S., Saraf, A., Florens, L., Washburn, M.P., Cavasotto, C.N., Fenyö, D., *et al.* (2018). The ULK1-FBXW5-SEC23B nexus controls autophagy. *Elife* *7*.

Ji, C.H., and Kwon, Y.T. (2017). Crosstalk and Interplay between the Ubiquitin-Proteasome System and Autophagy. *Mol Cells* *40*, 441-449.

Jia, R., and Bonifacino, J.S. (2020). Regulation of LC3B levels by ubiquitination and proteasomal degradation. *Autophagy* *16*, 382-384.

Jiang, C., Liu, Y., Wen, S., Xu, C., and Gu, L. (2021). In silico development and clinical validation of novel 8 gene signature based on lipid metabolism related genes in colon adenocarcinoma. *Pharmacol Res* *169*, 105644.

Jiang, W., Hua, R., Wei, M., Li, C., Qiu, Z., Yang, X., and Zhang, C. (2015). An optimized method for high-titer lentivirus preparations without ultracentrifugation. *Scientific Reports* *5*, 13875.

Jiang, X.P., and Elliott, R.L. (2017). Decreased Iron in Cancer Cells and Their Microenvironment Improves Cytolysis of Breast Cancer Cells by Natural Killer Cells. *Anticancer Res* *37*, 2297-2305.

Jiao, L., Li, D.D., Yang, C.L., Peng, R.Q., Guo, Y.Q., Zhang, X.S., and Zhu, X.F. (2016). Reactive oxygen species mediate oxaliplatin-induced epithelial-mesenchymal transition and invasive potential in colon cancer. *Tumour biology : the journal of the International Society for Oncodevelopmental Biology and Medicine* *37*, 8413-8423.

Jiao, Q., Du, X., Wei, J., Li, Y., and Jiang, H. (2019). Oxidative Stress Regulated Iron Regulatory Protein IRP2 Through FBXL5-Mediated Ubiquitination-Proteasome Way in SH-SY5Y Cells. *Frontiers in Neuroscience* *13*.

Jinek, M., Chylinski, K., Fonfara, I., Hauer, M., Doudna, J.A., and Charpentier, E. (2012). A Programmable Dual-RNA-Guided DNA Endonuclease in Adaptive Bacterial Immunity. *Science* *337*, 816-821.

Jinek, M., Jiang, F., Taylor, D.W., Sternberg, S.H., Kaya, E., Ma, E., Anders, C., Hauer, M., Zhou, K., Lin, S., *et al.* (2014). Structures of Cas9 endonucleases reveal RNA-mediated conformational activation. *Science* *343*, 1247997.

Johnson, N.B., Deck, K.M., Nizzi, C.P., and Eisenstein, R.S. (2017). A synergistic role of IRP1 and FBXL5 proteins in coordinating iron metabolism during cell proliferation. *The Journal of biological chemistry* *292*, 15976-15989.

Jones, G.G., Del Río, I.B., Sari, S., Sekerim, A., Young, L.C., Hartig, N., Areso Zubiaur, I., El-Bahrawy, M.A., Hynds, R.E., Lei, W., *et al.* (2019). SHOC2 phosphatase-dependent RAF dimerization mediates resistance to MEK inhibition in RAS-mutant cancers. *Nat Commun* *10*, 2532.

Ju, U.I., Park, J.W., Park, H.S., Kim, S.J., and Chun, Y.S. (2015). FBXO11 represses cellular response to hypoxia by destabilizing hypoxia-inducible factor-1 α mRNA. *Biochem Biophys Res Commun* *464*, 1008-1015.

Kaelin, W.G. (2005). Proline hydroxylation and gene expression. *Annu Rev Biochem* *74*, 115-128.

Kafkafi, N., Agassi, J., Chesler, E.J., Crabbe, J.C., Crusio, W.E., Eilam, D., Gerlai, R., Golani, I., Gomez-Marin, A., Heller, R., *et al.* (2018). Reproducibility and replicability of rodent phenotyping in preclinical studies. *Neuroscience & Biobehavioral Reviews* *87*, 218-232.

Kakhlon, O., and Cabantchik, Z.I. (2002). The labile iron pool: characterization, measurement, and participation in cellular processes¹ ¹This article is part of a series of reviews on "Iron and Cellular Redox Status." The full list of papers may be found on the homepage of the journal. *Free Radical Biology and Medicine* *33*, 1037-1046.

Kalluri, R., and Weinberg, R.A. (2009). The basics of epithelial-mesenchymal transition. *The Journal of Clinical Investigation* *119*, 1420-1428.

Kaluz, S., Kaluzová, M., Liao, S.-Y., Lerman, M., and Stanbridge, E.J. (2009). Transcriptional control of the tumor- and hypoxia-marker carbonic anhydrase 9: A one transcription factor (HIF-1) show? *Biochimica et biophysica acta* *1795*, 162-172.

Kanehisa, M., Furumichi, M., Sato, Y., Ishiguro-Watanabe, M., and Tanabe, M. (2021). KEGG: integrating viruses and cellular organisms. *Nucleic Acids Res* *49*, D545-d551.

Kanie, T., Onoyama, I., Matsumoto, A., Yamada, M., Nakatsumi, H., Tateishi, Y., Yamamura, S., Tsunematsu, R., Matsumoto, M., and Nakayama, K.I. (2012). Genetic reevaluation of the role of F-box proteins in cyclin D1 degradation. *Mol Cell Biol* *32*, 590-605.

Kanner, S.A., Morgenstern, T., and Colecraft, H.M. (2017). Sculpting ion channel functional expression with engineered ubiquitin ligases. *Elife* *6*.

Karthaus, W.R., Iaquinta, P.J., Drost, J., Gracanin, A., van Boxtel, R., Wongvipat, J., Dowling, C.M., Gao, D., Begthel, H., Sachs, N., *et al.* (2014). Identification of multipotent luminal progenitor cells in human prostate organoid cultures. *Cell* *159*, 163-175.

Kashfi, H., Jinks, N., and Nateri, A.S. (2020). Generating and Utilizing Murine Cas9-Expressing Intestinal Organoids for Large-Scale Knockout Genetic Screening. *Methods in molecular biology (Clifton, NJ)* *2171*, 257-269.

Kashfi, S.M.H. (2020). Studying Colon Cancer Using Intestinal Organoid Models for Anticancer Drug and Gene Functional Analysis. In *Faculty of Medicine and Health Sciences (University of Nottingham)*, pp. 319.

Kashfi, S.M.H., Almozyan, S., Jinks, N., Koo, B.-K., and Nateri, A.S. (2018). Morphological alterations of cultured human colorectal matched tumour and healthy organoids. *Oncotarget* *9*, 10572-10584.

Kessler, M., Hoffmann, K., Brinkmann, V., Thieck, O., Jackisch, S., Toelle, B., Berger, H., Mollenkopf, H.J., Mangler, M., Sehoul, J., *et al.* (2015). The Notch and Wnt pathways regulate stemness and differentiation in human fallopian tube organoids. *Nat Commun* *6*, 8989.

Kim, H.C., and Huijbrechtse, J.M. (2009). Polyubiquitination by HECT E3s and the determinants of chain type specificity. *Mol Cell Biol* *29*, 3307-3318.

Kip, A.M., Soons, Z., Mohren, R., Duivenvoorden, A.A.M., Röth, A.A.J., Cillero-Pastor, B., Neumann, U.P., Dejong, C.H.C., Heeren, R.M.A., Olde Damink, S.W.M., *et al.* (2021). Proteomics analysis of human intestinal organoids during hypoxia and reoxygenation as a model to study ischemia-reperfusion injury. *Cell Death & Disease* *12*, 95.

Klose, J., Trefz, S., Wagner, T., Steffen, L., Preißendörfer Charrier, A., Radhakrishnan, P., Volz, C., Schmidt, T., Ulrich, A., Dieter, S.M., *et al.* (2019). Salinomycin: Anti-tumor activity in a pre-clinical colorectal cancer model. *PLOS ONE* *14*, e0211916.

Koch, A., Waha, A., Hartmann, W., Hrychyk, A., Schuller, U., Waha, A., Wharton, K.A., Jr., Fuchs, S.Y., von Schweinitz, D., and Pietsch, T. (2005). Elevated expression of Wnt antagonists is a common event in hepatoblastomas. *Clinical cancer research : an official journal of the American Association for Cancer Research* *11*, 4295-4304.

Kondo, J., and Inoue, M. (2019). Application of Cancer Organoid Model for Drug Screening and Personalized Therapy. *Cells* *8*, 470.

Kong, D., Banerjee, S., Ahmad, A., Li, Y., Wang, Z., Sethi, S., and Sarkar, F.H. (2010). Epithelial to mesenchymal transition is mechanistically linked with stem cell signatures in prostate cancer cells. *PLoS One* *5*, e12445.

Kottakis, F., Foltopoulou, P., Sanidas, I., Keller, P., Wronski, A., Dake, B.T., Ezell, S.A., Shen, Z., Naber, S.P., Hinds, P.W., *et al.* (2014). NDY1/KDM2B Functions as a Master Regulator of Polycomb Complexes and Controls Self-Renewal of Breast Cancer Stem Cells. *Cancer Research* *74*, 3935-3946.

Kraft, C., Peter, M., and Hofmann, K. (2010). Selective autophagy: ubiquitin-mediated recognition and beyond. *Nat Cell Biol* *12*, 836-841.

Kraicz, J., Nayak, K.M., Howell, K.J., Ross, A., Forbester, J., Salvestrini, C., Mustata, R., Perkins, S., Andersson-Rolf, A., Leenen, E., *et al.* (2019). DNA methylation defines regional identity of human intestinal epithelial organoids and undergoes dynamic changes during development. *Gut* *68*, 49-61.

Kraicz, J., and Zilbauer, M. (2019). Intestinal Epithelial Organoids as Tools to Study Epigenetics in Gut Health and Disease. *Stem cells international* *2019*, 7242415-7242415.

Kubaichuk, K., and Kietzmann, T. (2019). Involvement of E3 Ligases and Deubiquitinases in the Control of HIF- α Subunit Abundance. *Cells* *8*, 598.

Kubo, H., Kitajima, Y., Kai, K., Nakamura, J., Miyake, S., Yanagihara, K., Morito, K., Tanaka, T., Shida, M., and Noshiro, H. (2016). Regulation and clinical significance of the hypoxia-induced expression of ANGPTL4 in gastric cancer. *Oncology letters* *11*, 1026-1034.

Kuhn, L.C. (2009). How iron controls iron. *Cell Metab* *10*, 439-441.

Kukurba, K.R., and Montgomery, S.B. (2015). RNA Sequencing and Analysis. *Cold Spring Harb Protoc* 2015, 951-969.

Kumar, V., Palermo, R., Talora, C., Campese, A.F., Checquolo, S., Bellavia, D., Tottone, L., Testa, G., Miele, E., Indraccolo, S., *et al.* (2014). Notch and NF- κ B signaling pathways regulate miR-223/FBXW7 axis in T-cell acute lymphoblastic leukemia. *Leukemia* 28, 2324-2335.

Lai, C., Lin, X., Chandran, J., Shim, H., Yang, W.J., and Cai, H. (2007). The G59S mutation in p150(glued) causes dysfunction of dynactin in mice. *J Neurosci* 27, 13982-13990.

Laird, F.M., Farah, M.H., Ackerley, S., Hoke, A., Maragakis, N., Rothstein, J.D., Griffin, J., Price, D.L., Martin, L.J., and Wong, P.C. (2008). Motor neuron disease occurring in a mutant dynactin mouse model is characterized by defects in vesicular trafficking. *J Neurosci* 28, 1997-2005.

Land, W.G. (2018). Sessile Innate Immune Cells. *Damage-Associated Molecular Patterns in Human Diseases*, 159-186.

Landis, S.C., Amara, S.G., Asadullah, K., Austin, C.P., Blumenstein, R., Bradley, E.W., Crystal, R.G., Darnell, R.B., Ferrante, R.J., Fillit, H., *et al.* (2012). A call for transparent reporting to optimize the predictive value of preclinical research. *Nature* 490, 187-191.

Larue, L., and Bellacosa, A. (2005). Epithelial–mesenchymal transition in development and cancer: role of phosphatidylinositol 3' kinase/AKT pathways. *Oncogene* 24, 7443-7454.

Lee, C.-J., An, H.-J., Cho, E.S., Kang, H.C., Lee, J.Y., Lee, H.S., and Cho, Y.-Y. (2020). Stat2 stability regulation: an intersection between immunity and carcinogenesis. *Experimental & Molecular Medicine* 52, 1526-1536.

Lee, J.M., Lee, J.S., Kim, H., Kim, K., Park, H., Kim, J.Y., Lee, S.H., Kim, I.S., Kim, J., Lee, M., *et al.* (2012a). EZH2 generates a methyl degron that is recognized by the DCAF1/DDB1/CUL4 E3 ubiquitin ligase complex. *Mol Cell* 48, 572-586.

Lee, P.Y., Costumbrado, J., Hsu, C.-Y., and Kim, Y.H. (2012b). Agarose gel electrophoresis for the separation of DNA fragments. *J Vis Exp*, 3923.

Lee, S.-H., Hong, J.H., Park, H.K., Park, J.S., Kim, B.-K., Lee, J.-Y., Jeong, J.Y., Yoon, G.S., Inoue, M., Choi, G.-S., *et al.* (2015). Colorectal cancer-derived tumor spheroids retain the characteristics of original tumors. *Cancer Letters* 367, 34-42.

Levin, G., Zuber, S.M., Squillaro, A.I., Sogayar, M.C., Grikscheit, T.C., and Carreira, A.C.O. (2020). R-Spondin 1 (RSPO1) Increases Mouse Intestinal Organoid Unit Size and Survival in vitro and Improves Tissue-Engineered Small Intestine Formation in vivo. *Front Bioeng Biotechnol* 8, 476.

Li, F., Zhan, Z., Qian, J., Cao, C., Yao, W., and Wang, N. (2021). Naringin attenuates rat myocardial ischemia/reperfusion injury via PI3K/Akt pathway-mediated inhibition of apoptosis, oxidative stress and autophagy. *Exp Ther Med* 22, 811.

Li, H., Yang, Y., Hong, W., Huang, M., Wu, M., and Zhao, X. (2020). Applications of genome editing technology in the targeted therapy of human diseases: mechanisms, advances and prospects. *Signal Transduction and Targeted Therapy* 5, 1.

Li, J., Li, S.X., Gao, X.H., Zhao, L.F., Du, J., Wang, T.Y., Wang, L., Zhang, J., Wang, H.Y., Dong, R., *et al.* (2019a). HIF1A and VEGF regulate each other by competing endogenous RNA mechanism and involve in the pathogenesis of peritoneal fibrosis. *Pathol Res Pract* 215, 644-652.

Li, N., Babaei-Jadidi, R., Lorenzi, F., Spencer-Dene, B., Clarke, P., Domingo, E., Tulchinsky, E., Vries, R.G.J., Kerr, D., Pan, Y., *et al.* (2019b). An FBXW7-ZEB2 axis links EMT and tumour microenvironment to promote colorectal cancer stem cells and chemoresistance. *Oncogenesis* 8, 13-13.

Li, S., Fang, X.-d., Wang, X.-y., and Fei, B.-y. (2018). Fos-like antigen 2 (FOSL2) promotes metastasis in colon cancer. *Experimental Cell Research* 373, 57-61.

Li, Y., Bouchlaka, M.N., Wolff, J., Grindle, K.M., Lu, L., Qian, S., Zhong, X., Pflum, N., Jobin, P., Kahl, B.S., *et al.* (2016). FBXO10 deficiency and BTK activation upregulate BCL2 expression in mantle cell lymphoma. *Oncogene* 35, 6223-6234.

Li, Y., and Hao, B. (2010). Structural basis of dimerization-dependent ubiquitination by the SCF(Fbx4) ubiquitin ligase. *The Journal of biological chemistry* 285, 13896-13906.

Liang, J.T., Huang, K.C., Cheng, Y.M., Hsu, H.C., Cheng, A.L., Hsu, C.H., Yeh, K.H., Wang, S.M., and Chang, K.J. (2002). P53 overexpression predicts poor chemosensitivity to high-dose 5-fluorouracil plus leucovorin chemotherapy for stage IV colorectal cancers after palliative bowel resection. *International journal of cancer* 97, 451-457.

Liao, Y., Smyth, G.K., and Shi, W. (2014). featureCounts: an efficient general purpose program for assigning sequence reads to genomic features. *Bioinformatics* 30, 923-930.

Liao, Y., Wang, J., Jaehnig, E.J., Shi, Z., and Zhang, B. (2019). WebGestalt 2019: gene set analysis toolkit with revamped UIs and APIs. *Nucleic Acids Research* 47, W199-W205.

Lin, A., and Yan, W.-H. (2019). The Emerging Roles of Human Leukocyte Antigen-F in Immune Modulation and Viral Infection. *Frontiers in immunology* 10, 964-964.

Lin, D.I., Barbash, O., Kumar, K.G.S., Weber, J.D., Harper, J.W., Klein-Szanto, A.J.P., Rustgi, A., Fuchs, S.Y., and Diehl, J.A. (2006). Phosphorylation-dependent ubiquitination of cyclin D1 by the SCF(FBX4- α B crystallin) complex. *Molecular cell* 24, 355-366.

Lin, L., Yang, S., Xiao, Z., Hong, P., Sun, S., Zhou, C., and Qian, Z.J. (2021). The Inhibition Effect of the Seaweed Polyphenol, 7-Phloro-Eckol from *Ecklonia Cava* on Alcohol-Induced Oxidative Stress in HepG2/CYP2E1 Cells. *Mar Drugs* 19.

Lin, M., Wang, Z.-w., and Zhu, X. (2020a). FBXO45 is a potential therapeutic target for cancer therapy. *Cell Death Discovery* 6, 55.

Lin, P., Fu, J., Zhao, B., Lin, F., Zou, H., Liu, L., Zhu, C., Wang, H., and Yu, X. (2011). Fbxw8 is involved in the proliferation of human choriocarcinoma JEG-3 cells. *Mol Biol Rep* 38, 1741-1747.

Lin, T.-C., Yang, C.-H., Cheng, L.-H., Chang, W.-T., Lin, Y.-R., and Cheng, H.-C. (2020b). Fibronectin in Cancer: Friend or Foe. *Cells* 9, 27.

Lin, Y.-C., Boone, M., Meuris, L., Lemmens, I., Van Roy, N., Soete, A., Reumers, J., Moisse, M., Plaisance, S., Drmanac, R., *et al.* (2014). Genome dynamics of the human embryonic kidney 293 lineage in response to cell biology manipulations. *Nature Communications* 5, 4767.

Lin, Y.-T., and Wu, K.-J. (2020). Epigenetic regulation of epithelial-mesenchymal transition: focusing on hypoxia and TGF- β signaling. *Journal of Biomedical Science* 27, 39.

Lindoso, R.S., Kasai-Brunswick, T.H., Monnerat Cahli, G., Collino, F., Bastos Carvalho, A., Campos de Carvalho, A.C., and Vieyra, A. (2019). Proteomics in the World of Induced Pluripotent Stem Cells. *Cells* 8, 703.

Liu, F., Huang, X., Luo, Z., He, J., Haider, F., Song, C., Peng, L., Chen, T., and Wu, B. (2019a). Hypoxia-Activated PI3K/Akt Inhibits Oxidative Stress via the Regulation of Reactive Oxygen Species in Human Dental Pulp Cells. *Oxid Med Cell Longev* 2019, 6595189-6595189.

Liu, F.H., Cui, Y.P., He, Y.K., and Shu, R.H. (2019b). FBXO17 promotes malignant progression of hepatocellular carcinoma by activating wnt/ β -catenin pathway. *Eur Rev Med Pharmacol Sci* 23, 8265-8273.

Liu, H., Yang, J., Zhang, Y., Han, J., Yang, Y., Zhao, Z., Dai, X., Wang, H., Ding, X., Liu, Y., *et al.* (2021). Psychological stress drives progression of malignant tumors via DRD2/HIF-1 α signaling. *Cancer Res*.

Liu, J., Lv, L., Gong, J., Tan, Y., Zhu, Y., Dai, Y., Pan, X., Huen, M.S.Y., Li, B., Tsao, S.W., *et al.* (2018). Overexpression of F-box only protein 31 predicts poor prognosis and deregulates p38 α - and JNK-mediated apoptosis in esophageal squamous cell carcinoma. *International journal of cancer* 142, 145-155.

Liu, J., Song, T., Zhou, W., Xing, L., Wang, S., Ho, M., Peng, Z., Tai, Y.-T., Hideshima, T., Anderson, K.C., *et al.* (2019c). A genome-scale CRISPR-Cas9 screening in myeloma cells identifies regulators of immunomodulatory drug sensitivity. *Leukemia* 33, 171-180.

Liu, M.L., Zang, F., and Zhang, S.J. (2019d). RBCK1 contributes to chemoresistance and stemness in colorectal cancer (CRC). *Biomed Pharmacother* 118, 109250.

Liu, X., Ni, Q., Sheng, C., Ma, J., and Wang, Q. (2014). [Expression and clinicopathological significance of Emi1 in breast carcinoma]. *Zhonghua yi xue za zhi* 94, 2008-2012.

Liu, Z., Qi, L., Li, Y., Zhao, X., and Sun, B. (2017). VEGFR2 regulates endothelial differentiation of colon cancer cells. *BMC Cancer* 17, 593.

Livak, K.J., and Schmittgen, T.D. (2001). Analysis of relative gene expression data using real-time quantitative PCR and the 2^{(-Delta Delta C(T))} Method. *Methods* 25, 402-408.

Loboda, A., Jozkowicz, A., and Dulak, J. (2010). HIF-1 and HIF-2 transcription factors--similar but not identical. *Mol Cells* 29, 435-442.

Longley, D.B., Harkin, D.P., and Johnston, P.G. (2003). 5-Fluorouracil: mechanisms of action and clinical strategies. *Nature Reviews Cancer* 3, 330-338.

Longo, P.A., Kavran, J.M., Kim, M.-S., and Leahy, D.J. (2013). Transient Mammalian Cell Transfection with Polyethylenimine (PEI). *Methods in enzymology* 529, 227-240.

Lorenzi, F., Babaei-Jadidi, R., Sheard, J., Spencer-Dene, B., and Nateri, A.S. (2016a). Fbxw7-associated drug resistance is reversed by induction of terminal differentiation in murine intestinal organoid culture. *Mol Ther Methods Clin Dev* 3, 16024-16024.

Lorenzi, F., Babaei-Jadidi, R., Sheard, J., Spencer-Dene, B., and Nateri, A.S. (2016b). Fbxw7-associated drug resistance is reversed by induction of terminal differentiation in murine intestinal organoid culture. *Molecular therapy Methods & clinical development* 3, 16024.

Lu, S., Yan, D., Wu, Z., Jiang, T., Chen, J., Yuan, L., Lin, J., Peng, Z., and Tang, H. (2014). Ubiquitin-like with PHD and ring finger domains 2 is a predictor of survival and a potential therapeutic target in colon cancer. *Oncology reports* 31, 1802-1810.

Lucey, B.P., Nelson-Rees, W.A., and Hutchins, G.M. (2009). Henrietta Lacks, HeLa Cells, and Cell Culture Contamination. *Archives of Pathology & Laboratory Medicine* 133, 1463-1467.

Lukonin, I., Serra, D., Challet Meylan, L., Volkmann, K., Baaten, J., Zhao, R., Meeusen, S., Colman, K., Maurer, F., Stadler, M.B., *et al.* (2020). Phenotypic landscape of intestinal organoid regeneration. *Nature* 586, 275-280.

Lynch, H.T., Snyder, C.L., Shaw, T.G., Heinen, C.D., and Hitchins, M.P. (2015). Milestones of Lynch syndrome: 1895–2015. *Nature Reviews Cancer* 15, 181-194.

Machado-Oliveira, G., Guerreiro, E., Matias, A.C., Facucho-Oliveira, J., Pacheco-Leyva, I., and Braganca, J. (2015a). FBXL5 modulates HIF-1 α transcriptional activity by degradation of CITED2. *Archives of biochemistry and biophysics* 576, 61-72.

Machado-Oliveira, G., Guerreiro, E., Matias, A.C., Facucho-Oliveira, J., Pacheco-Leyva, I., and Bragança, J. (2015b). FBXL5 modulates HIF-1 α transcriptional activity by degradation of CITED2. *Archives of biochemistry and biophysics* 576, 61-72.

Magori, S., and Citovsky, V. (2011). Hijacking of the Host SCF Ubiquitin Ligase Machinery by Plant Pathogens. *Frontiers in plant science* 2, 87.

Maimets, M., Rocchi, C., Bron, R., Pringle, S., Kuipers, J., Giepmans, Ben N.G., Vries, Robert G.J., Clevers, H., de Haan, G., van Os, R., *et al.* (2016). Long-Term In Vitro Expansion of Salivary Gland Stem Cells Driven by Wnt Signals. *Stem Cell Reports* 6, 150-162.

Majuelos-Melguizo, J., Rodríguez, M.I., López-Jiménez, L., Rodríguez-Vargas, J.M., Martí Martín-Consuegra, J.M., Serrano-Sáenz, S., Gavard, J., de Almodóvar, J.M.R., and Oliver, F.J. (2015). PARP targeting counteracts gliomagenesis through induction of mitotic catastrophe and aggravation of deficiency in homologous recombination in PTEN-mutant glioma. *Oncotarget* 6, 4790-4803.

Mak, I.W., Evaniew, N., and Ghert, M. (2014). Lost in translation: animal models and clinical trials in cancer treatment. *Am J Transl Res* 6, 114-118.

Malonia, S.K., Dutta, P., Santra, M.K., and Green, M.R. (2015). F-box protein FBXO31 directs degradation of MDM2 to facilitate p53-mediated growth arrest following genotoxic stress. *Proceedings of the National Academy of Sciences of the United States of America* 112, 8632-8637.

Manasanch, E.E., and Orlowski, R.Z. (2017). Proteasome inhibitors in cancer therapy. *Nat Rev Clin Oncol* 14, 417-433.

Marchitti, S.A., Orlicky, D.J., and Vasiliou, V. (2007). Expression and initial characterization of human ALDH3B1. *Biochemical and biophysical research communications* 356, 792-798.

Margineantu, D.H., Gregory Cox, W., Sundell, L., Sherwood, S.W., Beechem, J.M., and Capaldi, R.A. (2002). Cell cycle dependent morphology changes and associated mitochondrial DNA redistribution in mitochondria of human cell lines. *Mitochondrion* 1, 425-435.

Margottin-Goguet, F., Hsu, J.Y., Loktev, A., Hsieh, H.-M., Reimann, J.D.R., and Jackson, P.K. (2003). Prophase Destruction of Emi1 by the SCF β TrCP/Slimb Ubiquitin Ligase Activates the Anaphase Promoting Complex to Allow Progression beyond Prometaphase. *Developmental cell* 4, 813-826.

Marin, I., and Ferrus, A. (2002). Comparative genomics of the RBR family, including the Parkinson's disease-related gene parkin and the genes of the ariadne subfamily. *Mol Biol Evol* 19, 2039-2050.

Martin, M. (2011). CUTADAPT removes adapter sequences from high-throughput sequencing reads. *EMBnetjournal* 17.

Marx, V. (2020). Reality check for organoids in neuroscience. *Nature Methods* 17, 961-964.

Marzio, A., Puccini, J., Kwon, Y., Maverakis, N.K., Arbin, A., Sung, P., Bar-Sagi, D., and Pagano, M. (2019). The F-Box Domain-Dependent Activity of EMI1 Regulates PARPi Sensitivity in Triple-Negative Breast Cancers. *Molecular Cell* 73, 224-237.e226.

Mason, B., Flach, S., Teixeira, F.R., Manzano Garcia, R., Rueda, O.M., Abraham, J.E., Caldas, C., Edwards, P.A.W., and Laman, H. (2020). Fbxl17 is rearranged in breast cancer and loss of its activity leads to increased global O-GlcNAcylation. *Cellular and molecular life sciences : CMLS* 77, 2605-2620.

Matano, M., Date, S., Shimokawa, M., Takano, A., Fujii, M., Ohta, Y., Watanabe, T., Kanai, T., and Sato, T. (2015). Modeling colorectal cancer using CRISPR-Cas9-mediated engineering of human intestinal organoids. *Nature Medicine* 21, 256.

Matsumoto, A., Arcaroli, J., Chen, Y., Gasparetto, M., Neumeister, V., Thompson, D.C., Singh, S., Smith, C., Messersmith, W., and Vasiliou, V. (2017). Aldehyde dehydrogenase 1B1: a novel immunohistological marker for colorectal cancer. *British Journal of Cancer* 117, 1537-1543.

Mattioni, A., Castagnoli, L., and Santonico, E. (2020). RNF11 at the Crossroads of Protein Ubiquitination. *Biomolecules* 10.

McGehee, A.M., Strijbis, K., Guillen, E., Eng, T., Kirak, O., and Ploegh, H.L. (2011). Ubiquitin-dependent control of class II MHC localization is dispensable for antigen presentation and antibody production. *PLoS One* 6, e18817.

Metzger, M.B., Pruneda, J.N., Klevit, R.E., and Weissman, A.M. (2014). RING-type E3 ligases: Master manipulators of E2 ubiquitin-conjugating enzymes and ubiquitination. *Biochimica et Biophysica Acta (BBA) - Molecular Cell Research* 1843, 47-60.

Milne, A.N., Leguit, R., Corver, W.E., Morsink, F.H., Polak, M., de Leng, W.W., Carvalho, R., and Offerhaus, G.J. (2010). Loss of CDC4/FBXW7 in gastric carcinoma. *Cellular oncology : the official journal of the International Society for Cellular Oncology* 32, 347-359.

Min, K.W., Park, M.H., Hong, S.R., Lee, H., Kwon, S.Y., Hong, S.H., Joo, H.J., Park, I.A., An, H.J., Suh, K.S., *et al.* (2013). Clear cell carcinomas of the ovary: a multi-institutional study of 129 cases in Korea with prognostic significance of Emi1 and Galectin-3. *International journal of gynecological pathology : official journal of the International Society of Gynecological Pathologists* 32, 3-14.

Miniaci, M.C., Irace, C., Capuozzo, A., Piccolo, M., Di Pascale, A., Russo, A., Lippiello, P., Lepre, F., Russo, G., and Santamaria, R. (2016). Cysteine Prevents the Reduction in Keratin Synthesis Induced by Iron Deficiency in Human Keratinocytes. *J Cell Biochem* 117, 402-412.

Moffat, J.G., Vincent, F., Lee, J.A., Eder, J., and Prunotto, M. (2017). Opportunities and challenges in phenotypic drug discovery: an industry perspective. *Nat Rev Drug Discov* 16, 531-543.

Mogil, J.S. (2009). Animal models of pain: progress and challenges. *Nature Reviews Neuroscience* 10, 283.

Mohamed, N.-V., Larroquette, F., Beitel, L.K., Fon, E.A., and Durcan, T.M. (2019). One Step Into the Future: New iPSC Tools to Advance Research in Parkinson's Disease and Neurological Disorders. *J Parkinsons Dis* 9, 265-281.

Mojica, F.J.M., and Rodriguez-Valera, F. (2016). The discovery of CRISPR in archaea and bacteria. *The FEBS Journal* 283, 3162-3169.

Montecucco, A., Zanetta, F., and Biamonti, G. (2015). Molecular mechanisms of etoposide. *EXCLI J* 14, 95-108.

Moon, H.-G., Jeong, S.-H., Ju, Y.-T., Jeong, C.-Y., Lee, J.S., Lee, Y.-J., Hong, S.-C., Choi, S.-K., Ha, W.-S., Park, S.-T., *et al.* (2010). Up-regulation of RhoGDI2 in human breast cancer and its prognostic implications. *Cancer Res Treat* 42, 151-156.

Morel, M., Shah, K.N., and Long, W. (2020). The F-box protein FBXL16 up-regulates the stability of C-MYC oncoprotein by antagonizing the activity of the F-box protein FBW7. *The Journal of biological chemistry* 295, 7970-7980.

Moroishi, T., Nishiyama, M., Takeda, Y., Iwai, K., and Nakayama, Keiichi I. (2011). The FBXL5-IRP2 Axis Is Integral to Control of Iron Metabolism In Vivo. *Cell Metabolism* 14, 339-351.

Moroishi, T., Yamauchi, T., Nishiyama, M., and Nakayama, K.I. (2014). HERC2 targets the iron regulator FBXL5 for degradation and modulates iron metabolism. *The Journal of biological chemistry* 289, 16430-16441.

Morris, M.R., Hughes, D.J., Tian, Y.M., Ricketts, C.J., Lau, K.W., Gentle, D., Shuib, S., Serrano-Fernandez, P., Lubinski, J., Wiesener, M.S., *et al.* (2009). Mutation analysis of hypoxia-inducible factors HIF1A and HIF2A in renal cell carcinoma. *Anticancer Res* 29, 4337-4343.

Mueckler, M., and Thorens, B. (2013). The SLC2 (GLUT) family of membrane transporters. *Mol Aspects Med* 34, 121-138.

Mukhopadhyay, D., and Riezman, H. (2007). Proteasome-independent functions of ubiquitin in endocytosis and signaling. *Science* 315, 201-205.

Müller, I., Moroni, A.S., Shlyueva, D., Sahadevan, S., Schoof, E.M., Radzishewska, A., Højfeldt, J.W., Tatar, T., Koche, R.P., Huang, C., *et al.* (2021). MPP8 is essential for sustaining self-renewal of ground-state pluripotent stem cells. *Nat Commun* 12, 3034.

Muller, P.A.J., Vousden, K.H., and Norman, J.C. (2011). p53 and its mutants in tumor cell migration and invasion. *The Journal of cell biology* 192, 209-218.

Muto, Y., Moroishi, T., Ichihara, K., Nishiyama, M., Shimizu, H., Eguchi, H., Moriya, K., Koike, K., Mimori, K., Mori, M., *et al.* (2019). Disruption of FBXL5-mediated cellular iron homeostasis promotes liver carcinogenesis. *The Journal of Experimental Medicine*, jem.20180900.

Muto, Y., Nishiyama, M., Nita, A., Moroishi, T., and Nakayama, K.I. (2017). Essential role of FBXL5-mediated cellular iron homeostasis in maintenance of hematopoietic stem cells. *Nature Communications* 8, 16114.

Muz, B., de la Puente, P., Azab, F., and Azab, A.K. (2015). The role of hypoxia in cancer progression, angiogenesis, metastasis, and resistance to therapy. *Hypoxia (Auckl)* 3, 83-92.

Nakayama, K.I., and Nakayama, K. (2006). Ubiquitin ligases: cell-cycle control and cancer. *Nat Rev Cancer* 6, 369-381.

Nam, M.O., Hahn, S., Jee, J.H., Hwang, T.S., Yoon, H., Lee, D.H., Kwon, M.S., and Yoo, J. (2018). Effects of a small molecule R-spondin-1 substitute RS-246204 on a mouse intestinal organoid culture. *Oncotarget* 9, 6356-6368.

Nanba, S., Ikeda, F., Baba, N., Takaguchi, K., Senoh, T., Nagano, T., Seki, H., Takeuchi, Y., Moritou, Y., Yasunaka, T., *et al.* (2016). Association of hepatic oxidative stress and

iron dysregulation with HCC development after interferon therapy in chronic hepatitis C. *Journal of clinical pathology* 69, 226-233.

Nandi, D., Tahiliani, P., Kumar, A., and Chandu, D. (2006). The ubiquitin-proteasome system. *Journal of biosciences* 31, 137-155.

Napoli, E., Song, G., Panoutsopoulos, A., Riyadh, M.A., Kaushik, G., Halmi, J., Levenson, R., Zarbalis, K.S., and Giulivi, C. (2018). Beyond autophagy: a novel role for autism-linked Wdfy3 in brain mitophagy. *Scientific Reports* 8, 11348.

Narayan, G., Bourdon, V., Chaganti, S., Arias-Pulido, H., Nandula, S.V., Rao, P.H., Gissmann, L., Durst, M., Schneider, A., Pothuri, B., *et al.* (2007). Gene dosage alterations revealed by cDNA microarray analysis in cervical cancer: identification of candidate amplified and overexpressed genes. *Genes Chromosomes Cancer* 46, 373-384.

Nateri, A.S., Riera-Sans, L., Da Costa, C., and Behrens, A. (2004). The ubiquitin ligase SCFFbw7 antagonizes apoptotic JNK signaling. *Science* 303, 1374-1378.

Nathan, J.A., Tae Kim, H., Ting, L., Gygi, S.P., and Goldberg, A.L. (2013). Why do cellular proteins linked to K63-polyubiquitin chains not associate with proteasomes? *The EMBO Journal* 32, 552-565.

Nazemalhosseini Mojarad, E., Kuppen, P.J., Aghdaei, H.A., and Zali, M.R. (2013). The CpG island methylator phenotype (CIMP) in colorectal cancer. *Gastroenterol Hepatol Bed Bench* 6, 120-128.

NCBI (2018). Database resources of the National Center for Biotechnology Information. *Nucleic Acids Res* 46, D8-d13.

Neal, J.T., Li, X., Zhu, J., Giangarra, V., Grzeskowiak, C.L., Ju, J., Liu, I.H., Chiou, S.-H., Salahudeen, A.A., Smith, A.R., *et al.* (2018). Organoid Modeling of the Tumor Immune Microenvironment. *Cell* 175, 1972-1988.e1916.

Ng, A., and Xavier, R.J. (2011). Leucine-rich repeat (LRR) proteins: Integrators of pattern recognition and signaling in immunity. *Autophagy* 7, 1082-1084.

Nguyen, H.T., and Duong, H.Q. (2018). The molecular characteristics of colorectal cancer: Implications for diagnosis and therapy. *Oncology letters* 16, 9-18.

Nguyen, L.H., Goel, A., and Chung, D.C. (2020). Pathways of Colorectal Carcinogenesis. *Gastroenterology* 158, 291-302.

Nishida, Y., Arakawa, S., Fujitani, K., Yamaguchi, H., Mizuta, T., Kanaseki, T., Komatsu, M., Otsu, K., Tsujimoto, Y., and Shimizu, S. (2009). Discovery of Atg5/Atg7-independent alternative macroautophagy. *Nature* 461, 654-658.

Nolan, T., Hands, R.E., and Bustin, S.A. (2006). Quantification of mRNA using real-time RT-PCR. *Nature Protocols* 1, 1559-1582.

Nordquist, K.A., Dimitrova, Y.N., Brzovic, P.S., Ridenour, W.B., Munro, K.A., Soss, S.E., Caprioli, R.M., Klevit, R.E., and Chazin, W.J. (2010). Structural and functional characterization of the monomeric U-box domain from E4B. *Biochemistry* 49, 347-355.

Nussinov, R., Jang, H., Zhang, M., Tsai, C.J., and Sablina, A.A. (2020). The Mystery of Rap1 Suppression of Oncogenic Ras. *Trends Cancer* 6, 369-379.

O'Brien, R.J., and Wong, P.C. (2011). Amyloid precursor protein processing and Alzheimer's disease. *Annu Rev Neurosci* 34, 185-204.

Oh, B.Y., Hong, H.K., Lee, W.Y., and Cho, Y.B. (2017). Animal models of colorectal cancer with liver metastasis. *Cancer Letters* 387, 114-120.

Okkelman, I.A., Foley, T., Papkovsky, D.B., and Dmitriev, R.I. (2017). Multi-Parametric Imaging of Hypoxia and Cell Cycle in Intestinal Organoid Culture. *Adv Exp Med Biol* 1035, 85-103.

Olive, P.L., Aquino-Parsons, C., MacPhail, S.H., Liao, S.Y., Raleigh, J.A., Lerman, M.I., and Stanbridge, E.J. (2001). Carbonic anhydrase 9 as an endogenous marker for hypoxic cells in cervical cancer. *Cancer Res* 61, 8924-8929.

Oliveira, B., Cerag Yahya, A., and Novarino, G. (2019). Modeling cell-cell interactions in the brain using cerebral organoids. *Brain Res* 1724, 146458.

Oliveira, R.C., Abrantes, A.M., Tralhão, J.G., and Botelho, M.F. (2020). The role of mouse models in colorectal cancer research-The need and the importance of the orthotopic models. *Animal Model Exp Med* 3, 1-8.

Orellana, E.A., and Kasinski, A.L. (2016). Sulforhodamine B (SRB) Assay in Cell Culture to Investigate Cell Proliferation. *Bio-protocol* 6, e1984.

Orhon, I., and Reggiori, F. (2017). Assays to Monitor Autophagy Progression in Cell Cultures. *Cells* 6, 20.

Orozco, J.I.J., Knijnenburg, T.A., Manughian-Peter, A.O., Salomon, M.P., Barkhoudarian, G., Jalas, J.R., Wilmott, J.S., Hothi, P., Wang, X., Takasumi, Y., *et al.* (2018). Epigenetic profiling for the molecular classification of metastatic brain tumors. *Nature Communications* 9, 4627.

Ortega, Z., and Lucas, J.J. (2014). Ubiquitin-proteasome system involvement in Huntington's disease. *Front Mol Neurosci* 7, 77-77.

Otto, T., and Sicinski, P. (2017). Cell cycle proteins as promising targets in cancer therapy. *Nature reviews Cancer* 17, 93-115.

Ougolkov, A., Zhang, B., Yamashita, K., Bilim, V., Mai, M., Fuchs, S.Y., and Minamoto, T. (2004). Associations among beta-TrCP, an E3 ubiquitin ligase receptor, beta-catenin, and NF-kappaB in colorectal cancer. *Journal of the National Cancer Institute* 96, 1161-1170.

Ozsolak, F., and Milos, P.M. (2011). RNA sequencing: advances, challenges and opportunities. *Nature Reviews Genetics* 12, 87-98.

Paisan-Ruiz, C., Guevara, R., Federoff, M., Hanagasi, H., Sina, F., Elahi, E., Schneider, S.A., Schwingenschuh, P., Bajaj, N., Emre, M., *et al.* (2010). Early-onset L-dopa-responsive parkinsonism with pyramidal signs due to ATP13A2, PLA2G6, FBXO7 and spatacsin mutations. *Movement disorders : official journal of the Movement Disorder Society* 25, 1791-1800.

Papadatos-Pastos, D., Rabbie, R., Ross, P., and Sarker, D. (2015). The role of the PI3K pathway in colorectal cancer. *Critical Reviews in Oncology/Hematology* 94, 18-30.

Park, C.K., Heo, J., Ham, W.S., Choi, Y.D., Shin, S.J., and Cho, N.H. (2021). Ferroportin and FBXL5 as Prognostic Markers in Advanced Stage Clear Cell Renal Cell Carcinoma. *Cancer Res Treat.*

Parzych, K.R., and Klionsky, D.J. (2014). An overview of autophagy: morphology, mechanism, and regulation. *Antioxid Redox Signal* 20, 460-473.

Pastorekova, S., and Gillies, R.J. (2019). The role of carbonic anhydrase IX in cancer development: links to hypoxia, acidosis, and beyond. *Cancer and Metastasis Reviews* 38, 65-77.

Pastoreková, S., Zavadová, Z., Kostál, M., Babusíková, O., and Závada, J. (1992). A novel quasi-viral agent, MaTu, is a two-component system. *Virology* 187, 620-626.

Pastuła, A., Middelhoff, M., Brandtner, A., Tobiasch, M., Höhl, B., Nuber, A.H., Demir, I.E., Neupert, S., Kollmann, P., Mazzuoli-Weber, G., *et al.* (2016). Three-Dimensional Gastrointestinal Organoid Culture in Combination with Nerves or Fibroblasts: A Method to Characterize the Gastrointestinal Stem Cell Niche. *Stem Cells Int* 2016, 3710836.

Paul, S. (2008). Dysfunction of the ubiquitin-proteasome system in multiple disease conditions: therapeutic approaches. *Bioessays* 30, 1172-1184.

Peng, D., Wang, Z., Huang, A., Zhao, Y., and Qin, F.X.-F. (2017a). A Novel Function of F-Box Protein FBXO17 in Negative Regulation of Type I IFN Signaling by Recruiting PP2A for IFN Regulatory Factor 3 Deactivation. *The Journal of Immunology Author Choice* 198, 808-819.

Peng, D., Wang, Z., Huang, A., Zhao, Y., and Qin, F.X.-F. (2017b). A Novel Function of F-Box Protein FBXO17 in Negative Regulation of Type I IFN Signaling by Recruiting PP2A for IFN Regulatory Factor 3 Deactivation. *Journal of immunology (Baltimore, Md : 1950)* 198, 808-819.

Perkhofer, L., Frappart, P.O., Muller, M., and Kleger, A. (2018). Importance of organoids for personalized medicine. *Personalized medicine* 15, 461-465.

Perrone, F., and Zilbauer, M. (2021). Biobanking of human gut organoids for translational research. *Experimental & Molecular Medicine* 53, 1451-1458.

Ponthan, F., Brown, M., Playle, E., and Booth, C. (2019). Abstract 1061: Animal models of prostate cancer. *Cancer Research* 79, 1061-1061.

Puklowski, A., Homsy, Y., Keller, D., May, M., Chauhan, S., Kossatz, U., Grünwald, V., Kubicka, S., Pich, A., Manns, M.P., *et al.* (2011). The SCF–FBXW5 E3-ubiquitin ligase is regulated by PLK4 and targets HsSAS-6 to control centrosome duplication. *Nature Cell Biology* 13, 1004.

Quadrato, G., Nguyen, T., Macosko, E.Z., Sherwood, J.L., Min Yang, S., Berger, D.R., Maria, N., Scholvin, J., Goldman, M., Kinney, J.P., *et al.* (2017). Cell diversity and network dynamics in photosensitive human brain organoids. *Nature* 545, 48.

Quinn, P.M., Buck, T.M., Ohonin, C., Mikkers, H.M.M., and Wijnholds, J. (2018). Production of iPS-Derived Human Retinal Organoids for Use in Transgene Expression Assays. *Methods in molecular biology (Clifton, NJ)* 1715, 261-273.

Qureshi, R., Arora, H., and Rizvi, M.A. (2015). EMT in cervical cancer: Its role in tumour progression and response to therapy. *Cancer Letters* 356, 321-331.

Rafehi, H., Orłowski, C., Georgiadis, G.T., Ververis, K., El-Osta, A., and Karagiannis, T.C. (2011). Clonogenic assay: adherent cells. *J Vis Exp*, 2573.

Randle, S.J., and Laman, H. (2016). F-box protein interactions with the hallmark pathways in cancer. *Seminars in Cancer Biology* 36, 3-17.

Rao JN, W.J. (2010). *Intestinal Stem Cells: Regulation of Gastrointestinal Mucosal Growth.* (San Rafael (CA)).

Rao, W. (2010). *Intestinal Stem Cells: Regulation of Gastrointestinal Mucosal Growth.* (San Rafael (CA)).

Rape, M., Reddy, S.K., and Kirschner, M.W. (2006). The processivity of multiubiquitination by the APC determines the order of substrate degradation. *Cell* 124, 89-103.

Ravindranath, A.K., Kaur, S., Wernyj, R.P., Kumaran, M.N., Milette-Gonzalez, K.E., Chan, R., Lim, E., Madura, K., and Rodriguez-Rodriguez, L. (2015). CD44 promotes

multi-drug resistance by protecting P-glycoprotein from FBXO21-mediated ubiquitination. *Oncotarget* 6, 26308-26321.

Reits, E., Griekspoor, A., Neijssen, J., Groothuis, T., Jalink, K., van Veelen, P., Janssen, H., Calafat, J., Drijfhout, J.W., and Neefjes, J. (2003). Peptide diffusion, protection, and degradation in nuclear and cytoplasmic compartments before antigen presentation by MHC class I. *Immunity* 18, 97-108.

Ren, W., Lewandowski, B.C., Watson, J., Aihara, E., Iwatsuki, K., Bachmanov, A.A., Margolskee, R.F., and Jiang, P. (2014). Single Lgr5- or Lgr6-expressing taste stem/progenitor cells generate taste bud cells ex vivo. *Proc Natl Acad Sci U S A* 111, 16401-16406.

Ren, Y., and Walczyk, T. (2014). Quantification of ferritin bound iron in human serum using species-specific isotope dilution mass spectrometry. *Metallomics* 6, 1709-1717.

Riccardi, C., and Nicoletti, I. (2006). Analysis of apoptosis by propidium iodide staining and flow cytometry. *Nat Protoc* 1, 1458-1461.

Richard, D.J., Bolderson, E., Cubeddu, L., Wadsworth, R.I., Savage, K., Sharma, G.G., Nicolette, M.L., Tsvetanov, S., McIlwraith, M.J., Pandita, R.K., *et al.* (2008). Single-stranded DNA-binding protein hSSB1 is critical for genomic stability. *Nature* 453, 677-681.

Richter, K.T., Kschonsak, Y.T., Vodicska, B., and Hoffmann, I. (2020). FBXO45-MYCBP2 regulates mitotic cell fate by targeting FBXW7 for degradation. *Cell Death & Differentiation* 27, 758-772.

Riddell, I.A. (2018). Cisplatin and Oxaliplatin: Our Current Understanding of Their Actions. *Met Ions Life Sci* 18.

Rio, D.C., Ares, M., Hannon, G.J., and Nilsen, T.W. (2010). Purification of RNA Using TRIzol (TRI Reagent). *Cold Spring Harb Protoc* 2010, pdb.prot5439.

Robinson, D.R., Wu, Y.-M., Lonigro, R.J., Vats, P., Cobain, E., Everett, J., Cao, X., Rabban, E., Kumar-Sinha, C., Raymond, V., *et al.* (2017). Integrative clinical genomics of metastatic cancer. *Nature* 548, 297-303.

Rochette, P.J., Bastien, N., Lavoie, J., Guérin, S.L., and Drouin, R. (2005). SW480, a p53 double-mutant cell line retains proficiency for some p53 functions. *J Mol Biol* 352, 44-57.

Rockfield, S., Guergues, J., Rehman, N., Smith, A., Bauckman, K.A., Stevens, S.M., Jr., and Nanjundan, M. (2018). Proteomic Profiling of Iron-Treated Ovarian Cells Identifies AKT Activation that Modulates the CLEAR Network. *Proteomics* 18, e1800244.

Rodríguez-Almazán, C., Arreola, R., Rodríguez-Larrea, D., Aguirre-López, B., de Gómez-Puyou, M.T., Pérez-Montfort, R., Costas, M., Gómez-Puyou, A., and Torres-Larios, A. (2008). Structural basis of human triosephosphate isomerase deficiency: mutation E104D is related to alterations of a conserved water network at the dimer interface. *The Journal of biological chemistry* 283, 23254-23263.

Rodriguez, L.G., Wu, X., and Guan, J.L. (2005). Wound-healing assay. *Methods in molecular biology (Clifton, NJ)* 294, 23-29.

Rozpedek, W., Pytel, D., Mucha, B., Leszczynska, H., Diehl, J.A., and Majsterek, I. (2016). The Role of the PERK/eIF2 α /ATF4/CHOP Signaling Pathway in Tumor Progression During Endoplasmic Reticulum Stress. *Curr Mol Med* 16, 533-544.

Ruiz, J.C., and Bruick, R.K. (2014). F-box and leucine-rich repeat protein 5 (FBXL5): sensing intracellular iron and oxygen. *Journal of inorganic biochemistry* 133, 73-77.

Runwal, G., Stamatakou, E., Siddiqi, F.H., Puri, C., Zhu, Y., and Rubinsztein, D.C. (2019). LC3-positive structures are prominent in autophagy-deficient cells. *Scientific Reports* *9*, 10147.

Sachs, N., de Ligt, J., Kopper, O., Gogola, E., Bounova, G., Weeber, F., Balgobind, A.V., Wind, K., Gracanin, A., Begthel, H., *et al.* (2018). A Living Biobank of Breast Cancer Organoids Captures Disease Heterogeneity. *Cell* *172*, 373-386.e310.

Said, N. (2019). Establishing and characterization of human and murine bladder cancer organoids. *Translational andrology and urology* *8*, S310-s313.

Sailo, B.L., Banik, K., Girisa, S., Bordoloi, D., Fan, L., Halim, C.E., Wang, H., Kumar, A.P., Zheng, D., Mao, X., *et al.* (2019). FBXW7 in Cancer: What Has Been Unraveled Thus Far? *Cancers* *11*, 246.

Saitoh, M. (2018). Involvement of partial EMT in cancer progression. *The Journal of Biochemistry* *164*, 257-264.

Sakib, S., Goldsmith, T., Voigt, A., and Dobrinski, I. (2019). Testicular organoids to study cell-cell interactions in the mammalian testis. *Andrology*.

Samson, J., Derlipanska, M., Zaheed, O., and Dean, K. (2021). Molecular and cellular characterization of two patient-derived ductal carcinoma in situ (DCIS) cell lines, ETCC-006 and ETCC-010. *BMC Cancer* *21*, 790.

Santana-Codina, N., and Mancias, J.D. (2018). The Role of NCOA4-Mediated Ferritinophagy in Health and Disease. *Pharmaceuticals (Basel)* *11*, 114.

Sato, T., Stange, D.E., Ferrante, M., Vries, R.G., Van Es, J.H., Van den Brink, S., Van Houdt, W.J., Pronk, A., Van Gorp, J., Siersema, P.D., *et al.* (2011). Long-term expansion of epithelial organoids from human colon, adenoma, adenocarcinoma, and Barrett's epithelium. *Gastroenterology* *141*, 1762-1772.

Sato, T., Vries, R.G., Snippert, H.J., van de Wetering, M., Barker, N., Stange, D.E., van Es, J.H., Abo, A., Kujala, P., Peters, P.J., *et al.* (2009a). Single Lgr5 stem cells build crypt-villus structures in vitro without a mesenchymal niche. *Nature* *459*, 262.

Sato, T., Vries, R.G., Snippert, H.J., van de Wetering, M., Barker, N., Stange, D.E., van Es, J.H., Abo, A., Kujala, P., Peters, P.J., *et al.* (2009b). Single Lgr5 stem cells build crypt-villus structures in vitro without a mesenchymal niche. *Nature* *459*, 262.

Schellinck, H.M., Cyr, D.P., and Brown, R.E. (2010). Chapter 7 - How Many Ways Can Mouse Behavioral Experiments Go Wrong? Confounding Variables in Mouse Models of Neurodegenerative Diseases and How to Control Them. In *Advances in the Study of Behavior*, H.J. Brockmann, T.J. Roper, M. Naguib, K.E. Wynne-Edwards, J.C. Mitani, and L.W. Simmons, eds. (Academic Press), pp. 255-366.

Schneider, C., Kon, N., Amadori, L., Shen, Q., Schwartz, F.H., Tischler, B., Bossennec, M., Dominguez-Sola, D., Bhagat, G., Gu, W., *et al.* (2016). FBXO11 inactivation leads to abnormal germinal-center formation and lymphoproliferative disease. *Blood* *128*, 660-666.

Schnell, J.D., and Hicke, L. (2003). Non-traditional functions of ubiquitin and ubiquitin-binding proteins. *The Journal of biological chemistry* *278*, 35857-35860.

Scholata, T, B.P., Malek. NP (2016). Role of FBXW5 in the induction of centrosome abnormalities and liver tumor formation. *Gastroenterol* *54*, 1343-1404.

Schreiber, A., Stengel, F., Zhang, Z., Enchev, R.I., Kong, E.H., Morris, E.P., Robinson, C.V., da Fonseca, P.C.A., and Barford, D. (2011). Structural basis for the subunit assembly of the anaphase-promoting complex. *Nature* *470*, 227.

Schuh, J.C. (2004). Trials, tribulations, and trends in tumor modeling in mice. *Toxicologic pathology* 32 *Suppl 1*, 53-66.

Schulman, B.A., and Wade Harper, J. (2009). Ubiquitin-like protein activation by E1 enzymes: the apex for downstream signalling pathways. *Nature Reviews Molecular Cell Biology* 10, 319-331.

Schwank, G., and Clevers, H. (2016). CRISPR/Cas9-Mediated Genome Editing of Mouse Small Intestinal Organoids. *Methods in molecular biology (Clifton, NJ)* 1422, 3-11.

Seok, J., Warren, H.S., Cuenca, A.G., Mindrinos, M.N., Baker, H.V., Xu, W., Richards, D.R., McDonald-Smith, G.P., Gao, H., Hennessy, L., *et al.* (2013). Genomic responses in mouse models poorly mimic human inflammatory diseases. *Proc Natl Acad Sci U S A* 110, 3507-3512.

Serra, D., Mayr, U., Boni, A., Lukonin, I., Rempfler, M., Challet Meylan, L., Stadler, M.B., Strnad, P., Papasaikas, P., Vischi, D., *et al.* (2019). Self-organization and symmetry breaking in intestinal organoid development. *Nature* 569, 66-72.

Seyed Mohammad Hossein Kashfi, S.A., Nicholas Jinks, Bon-Kyoung Koo and Abdolrahman S. Nateri (2018). Morphological alterations of cultured human colorectal matched tumour and healthy organoids. *Oncotarget* 9, 10572-10584.

Shaheen, S., Ahmed, M., Lorenzi, F., and Nateri, A.S. (2016). Spheroid-Formation (Colonsphere) Assay for in Vitro Assessment and Expansion of Stem Cells in Colon Cancer. *Stem cell reviews* 12, 492-499.

Shen, B., Yuan, Y., Zhang, Y., Yu, S., Peng, W., Huang, X.e., and Feng, J. (2017). Long non-coding RNA FBXL19-AS1 plays oncogenic role in colorectal cancer by sponging miR-203. *Biochemical and Biophysical Research Communications* 488, 67-73.

Shen, S., Park, J.W., Lu, Z.-x., Lin, L., Henry, M.D., Wu, Y.N., Zhou, Q., and Xing, Y. (2014). rMATS: Robust and flexible detection of differential alternative splicing from replicate RNA-Seq data. *Proceedings of the National Academy of Sciences* 111, E5593.

Shi, D., and Grossman, S.R. (2010). Ubiquitin becomes ubiquitous in cancer: emerging roles of ubiquitin ligases and deubiquitinases in tumorigenesis and as therapeutic targets. *Cancer Biol Ther* 10, 737-747.

Shi, X., Walter, N.A.R., Harkness, J.H., Neve, K.A., Williams, R.W., Lu, L., Belknap, J.K., Eshleman, A.J., Phillips, T.J., and Janowsky, A. (2016). Genetic Polymorphisms Affect Mouse and Human Trace Amine-Associated Receptor 1 Function. *PLOS ONE* 11, e0152581.

Shia, J., Schultz, N., Kuk, D., Vakiani, E., Middha, S., Segal, N.H., Hechtman, J.F., Berger, M.F., Stadler, Z.K., Weiser, M.R., *et al.* (2017). Morphological characterization of colorectal cancers in The Cancer Genome Atlas reveals distinct morphology-molecular associations: clinical and biological implications. *Mod Pathol* 30, 599-609.

Shimizu, N., Nakajima, N.I., Tsunematsu, T., Ogawa, I., Kawai, H., Hirayama, R., Fujimori, A., Yamada, A., Okayasu, R., Ishimaru, N., *et al.* (2013). Selective enhancing effect of early mitotic inhibitor 1 (Emi1) depletion on the sensitivity of doxorubicin or X-ray treatment in human cancer cells. *The Journal of biological chemistry* 288, 17238-17252.

Shin, J.S., Ebersold, M., Pypaert, M., Delamarre, L., Hartley, A., and Mellman, I. (2006). Surface expression of MHC class II in dendritic cells is controlled by regulated ubiquitination. *Nature* 444, 115-118.

Shoket, H., Parvez, S., Sharma, M., Pandita, M., Sharma, V., Kumar, P., and Bairwa, N.K. (2020). Deletion of Autophagy gene *ATG1* and F-box motif encoding gene *YDR131C* together leads to Synthetic Growth Defects and Flocculation behaviour in *Saccharomyces cerevisiae*. *bioRxiv*, 2020.2003.2003.974519.

Shu, C., Sung, M.W., Stewart, M.D., Igumenova, T.I., Tan, X., and Li, P. (2012). The structural basis of iron sensing by the human F-box protein FBXL5. *Chembiochem* *13*, 788-791.

Siegel, R.L., Miller, K.D., Goding Sauer, A., Fedewa, S.A., Butterly, L.F., Anderson, J.C., Cercek, A., Smith, R.A., and Jemal, A. (2020). Colorectal cancer statistics, 2020. *CA: a cancer journal for clinicians* *70*, 145-164.

Signoretti, S., Di Marcotullio, L., Richardson, A., Ramaswamy, S., Isaac, B., Rue, M., Monti, F., Loda, M., and Pagano, M. (2002). Oncogenic role of the ubiquitin ligase subunit Skp2 in human breast cancer. *J Clin Invest* *110*, 633-641.

Simons, M., Gordon, E., and Claesson-Welsh, L. (2016). Mechanisms and regulation of endothelial VEGF receptor signalling. *Nature Reviews Molecular Cell Biology* *17*, 611-625.

Singh, S., Warren, H.R., Hiltunen, T.P., McDonough, C.W., El Rouby, N., Salvi, E., Wang, Z., Garofalidou, T., Fyhrquist, F., Kontula, K.K., *et al.* (2019). Genome-Wide Meta-Analysis of Blood Pressure Response to beta1-Blockers: Results From ICAPS (International Consortium of Antihypertensive Pharmacogenomics Studies). *Journal of the American Heart Association* *8*, e013115.

Sinnberg, T., Sauer, B., Holm, P., Spangler, B., Kuphal, S., Bosserhoff, A., and Schitteck, B. (2012). MAPK and PI3K/AKT mediated YB-1 activation promotes melanoma cell proliferation which is counteracted by an autoregulatory loop. *Exp Dermatol* *21*, 265-270.

Skaar, J.R., Pagan, J.K., and Pagano, M. (2013). Mechanisms and function of substrate recruitment by F-box proteins. *Nat Rev Mol Cell Biol* *14*, 369-381.

Skardal, A., Shupe, T., and Atala, A. (2016). Organoid-on-a-chip and body-on-a-chip systems for drug screening and disease modeling. *Drug Discovery Today* *21*, 1399-1411.

Slattery, M.L., Mullany, L.E., Sakoda, L., Samowitz, W.S., Wolff, R.K., Stevens, J.R., and Herrick, J.S. (2018). The NF- κ B signalling pathway in colorectal cancer: associations between dysregulated gene and miRNA expression. *Journal of cancer research and clinical oncology* *144*, 269-283.

Slorach, E.M., Chou, J., and Werb, Z. (2011). Zeppo1 is a novel metastasis promoter that represses E-cadherin expression and regulates p120-catenin isoform expression and localization. *Genes & development* *25*, 471-484.

Smith, T.F. (2008). Diversity of WD-repeat proteins. *Sub-cellular biochemistry* *48*, 20-30.

Smith, T.F., Gaitatzes, C., Saxena, K., and Neer, E.J. (1999). The WD repeat: a common architecture for diverse functions. *Trends in Biochemical Sciences* *24*, 181-185.

Smits, B.M.G., Traun, B.D., Devries, T.L., Tran, A., Samuelson, D., Haag, J.D., and Gould, M. (2012). An insulator loop resides between the synthetically interacting elements of the human/rat conserved breast cancer susceptibility locus MCS5A/Mcs5a. *Nucleic acids research* *40*, 132-147.

Sobin, L.H., In Gospodarowicz, M. K., In Wittekind, C., & International Union against Cancer (2016). The TNM Classification of Malignant Tumours 8th edition (Chichester, West Sussex, UK: Wiley-Blackwell).

Soucy, T.A., Smith, P.G., Milhollen, M.A., Berger, A.J., Gavin, J.M., Adhikari, S., Brownell, J.E., Burke, K.E., Cardin, D.P., Critchley, S., *et al.* (2009). An inhibitor of NEDD8-activating enzyme as a new approach to treat cancer. *Nature* 458, 732-736.

Spratt, D.E., Walden, H., and Shaw, G.S. (2014). RBR E3 ubiquitin ligases: new structures, new insights, new questions. *Biochem J* 458, 421-437.

Stanescu, R.S., Bordeianu, G., Stoica, B., Ungureanu, D., Rusu, M., and Petrescu-Danila, E. (2014). Rad51 overexpression and resistance to genotoxic agents. A study in the fission yeast *Schizosaccharomyces pombe*. *Rev Med Chir Soc Med Nat Iasi* 118, 133-140.

Stankiewicz, E., Mao, X., Mangham, D.C., Xu, L., Yeste-Velasco, M., Fisher, G., North, B., Chaplin, T., Young, B., Wang, Y., *et al.* (2017). Identification of FBXL4 as a Metastasis Associated Gene in Prostate Cancer. *Scientific Reports* 7, 5124.

Stark, R., Grzelak, M., and Hadfield, J. (2019). RNA sequencing: the teenage years. *Nature Reviews Genetics* 20, 631-656.

Stewart, A.K., Rajkumar, S.V., Dimopoulos, M.A., Masszi, T., Spicka, I., Oriol, A., Hajek, R., Rosinol, L., Siegel, D.S., Mihaylov, G.G., *et al.* (2015). Carfilzomib, lenalidomide, and dexamethasone for relapsed multiple myeloma. *The New England journal of medicine* 372, 142-152.

Stewart, M.D., Ritterhoff, T., Klevit, R.E., and Brzovic, P.S. (2016). E2 enzymes: more than just middle men. *Cell research* 26, 423-440.

Su, J.-L., Cheng, X., Yamaguchi, H., Chang, Y.-W., Hou, C.-F., Lee, D.-F., Ko, H.-W., Hua, K.-T., Wang, Y.-N., Hsiao, M., *et al.* (2011). FOXO3a-Dependent Mechanism of E1A-Induced Chemosensitization. *Cancer Research* 71, 6878-6887.

Suber, T.L., Nikolli, I., O'Brien, M.E., Londino, J., Zhao, J., Chen, K., Mallampalli, R.K., and Zhao, Y. (2018). FBXO17 promotes cell proliferation through activation of Akt in lung adenocarcinoma cells. *Respiratory Research* 19, 206.

Summers, R.M. (2010). Polyp size measurement at CT colonography: what do we know and what do we need to know? *Radiology* 255, 707-720.

Sun, L., Wang, Y., Cen, J., Ma, X., Cui, L., Qiu, Z., Zhang, Z., Li, H., Yang, R.Z., Wang, C., *et al.* (2019). Modelling liver cancer initiation with organoids derived from directly reprogrammed human hepatocytes. *Nat Cell Biol.*

Sun, S.C. (2010). CYLD: a tumor suppressor deubiquitinase regulating NF- κ B activation and diverse biological processes. *Cell Death & Differentiation* 17, 25-34.

Sun, X., Wang, T., Guan, Z.-R., Zhang, C., Chen, Y., Jin, J., and Hua, D. (2018a). FBXO2, a novel marker for metastasis in human gastric cancer. *Biochemical and Biophysical Research Communications* 495, 2158-2164.

Sun, Y., Jiang, W., Lu, W., Song, M., Liu, K., Chen, P., Chang, A., Ling, J., Chiao, P.J., Hu, Y., *et al.* (2018b). Identification of cisplatin sensitizers through high-throughput combinatorial screening. *International journal of oncology* 53, 1237-1246.

Szabova, L., Bupp, S., Kamal, M., Householder, D.B., Hernandez, L., Schlomer, J.J., Baran, M.L., Yi, M., Stephens, R.M., Annunziata, C.M., *et al.* (2014). Pathway-Specific Engineered Mouse Allograft Models Functionally Recapitulate Human Serous Epithelial Ovarian Cancer. *PLOS ONE* 9, e95649.

Szklarczyk, D., Gable, A.L., Lyon, D., Junge, A., Wyder, S., Huerta-Cepas, J., Simonovic, M., Doncheva, N.T., Morris, J.H., Bork, P., *et al.* (2019). STRING v11: protein-protein association networks with increased coverage, supporting functional discovery in genome-wide experimental datasets. *Nucleic Acids Res* 47, D607-d613.

Takahashi, T. (2019). Organoids for Drug Discovery and Personalized Medicine. *Annual review of pharmacology and toxicology* 59, 447-462.

Takeda, H., Kataoka, S., Nakayama, M., Ali, M.A.E., Oshima, H., Yamamoto, D., Park, J.-W., Takegami, Y., An, T., Jenkins, N.A., *et al.* (2019). CRISPR-Cas9-mediated gene knockout in intestinal tumor organoids provides functional validation for colorectal cancer driver genes. *Proceedings of the National Academy of Sciences*, 201904714.

Tan, Y., Sangfelt, O., and Spruck, C. (2008). The Fbxw7/hCdc4 tumor suppressor in human cancer. *Cancer Letters* 271, 1-12.

Tanaka, S., Kobayashi, W., Haraguchi, M., Ishihata, K., Nakamura, N., and Ozawa, M. (2016). Snail1 expression in human colon cancer DLD-1 cells confers invasive properties without N-cadherin expression. *Biochemistry and Biophysics Reports* 8, 120-126.

Tang, N.-W., Shen, S.-P., Ye, X.-Y., Niu, X.-M., Xu, Y.-H., Chen, Z.-W., Li, Z.-M., Lu, S., Liu, B., and Xu, L. (2014). FBXL5-mediated degradation of single-stranded DNA-binding protein hSSB1 controls DNA damage response. *Nucleic Acids Research* 42, 11560-11569.

Tang, X. (2013). Tumor-associated macrophages as potential diagnostic and prognostic biomarkers in breast cancer. *Cancer Lett* 332, 3-10.

Tang, Z., Li, C., Kang, B., Gao, G., Li, C., and Zhang, Z. (2017). GEPIA: a web server for cancer and normal gene expression profiling and interactive analyses. *Nucleic Acids Research* 45, W98-W102.

Tanksley, J.P., Chen, X., and Coffey, R.J. (2013). NEDD4L is downregulated in colorectal cancer and inhibits canonical WNT signaling. *PLoS One* 8, e81514.

Taylor, K. (2019). *Animal Experimentation: Working Towards a Paradigm Change*.

Taylor, W.R., and Stark, G.R. (2001). Regulation of the G2/M transition by p53. *Oncogene* 20, 1803-1815.

Tchaikovsky, A., Schoeberl, A., Schueffl, H., Raab, A., Emin, S., Slany, A., Heffeter, P., Koellensperger, G., and Swart, C. (2020). Quantification of ferritin-bound iron in murine samples for Alzheimer's disease studies using species-specific isotope dilution mass spectrometry. *Metrologia* 57, 042101.

Tenopoulou, M., Kurz, T., Doulias, P.-T., Galaris, D., and Brunk, U.T. (2007). Does the calcein-AM method assay the total cellular 'labile iron pool' or only a fraction of it? *The Biochemical journal* 403, 261-266.

Terzi, E.M., Sviderskiy, V.O., Alvarez, S.W., Whiten, G.C., and Possemato, R. (2021). Iron-sulfur cluster deficiency can be sensed by IRP2 and regulates iron homeostasis and sensitivity to ferroptosis independent of IRP1 and FBXL5. *Science Advances* 7, eabg4302.

Thurtle-Schmidt, D.M., and Lo, T.W. (2018). Molecular biology at the cutting edge: A review on CRISPR/CAS9 gene editing for undergraduates. *Biochem Mol Biol Educ* 46, 195-205.

Timmerbeul, I., Garrett-Engele, C.M., Kossatz, U., Chen, X., Firpo, E., Grunwald, V., Kamino, K., Wilkens, L., Lehmann, U., Buer, J., *et al.* (2006). Testing the importance of

p27 degradation by the SCFskp2 pathway in murine models of lung and colon cancer. *Proc Natl Acad Sci U S A* *103*, 14009-14014.

Todhunter, M.E., Jee, N.Y., Hughes, A.J., Coyle, M.C., Cerchiari, A., Farlow, J., Garbe, J.C., LaBarge, M.A., Desai, T.A., and Gartner, Z.J. (2015). Programmed synthesis of three-dimensional tissues. *Nature Methods* *12*, 975-981.

Tzatsos, A., Paskaleva, P., Ferrari, F., Deshpande, V., Stoykova, S., Contino, G., Wong, K.K., Lan, F., Trojer, P., Park, P.J., *et al.* (2013). KDM2B promotes pancreatic cancer via Polycomb-dependent and -independent transcriptional programs. *J Clin Invest* *123*, 727-739.

Uddin, S., Bhat, A.A., Krishnankutty, R., Mir, F., Kulinski, M., and Mohammad, R.M. (2016). Involvement of F-BOX proteins in progression and development of human malignancies. *Seminars in Cancer Biology* *36*, 18-32.

Uhlen, M., Fagerberg, L., Hallstrom, B.M., Lindskog, C., Oksvold, P., Mardinoglu, A., Sivertsson, A., Kampf, C., Sjostedt, E., Asplund, A., *et al.* (2015). Proteomics. Tissue-based map of the human proteome. *Science* *347*, 1260419.

UKHO, U.K.H.O. (2019). Annual Statistics of Scientific Procedures on Living Animals Great Britain 2018 (United Kingdom).

Valkov, N.I., and Sullivan, D.M. (2003). Tumor p53 status and response to topoisomerase II inhibitors. *Drug Resist Updat* *6*, 27-39.

Verdoodt, B., Vogt, M., Schmitz, I., Liffers, S.-T., Tannapfel, A., and Mirmohammadsadegh, A. (2012). Salinomycin induces autophagy in colon and breast cancer cells with concomitant generation of reactive oxygen species. *PloS one* *7*, e44132-e44132.

Viñas-Castells, R., Beltran, M., Valls, G., Gómez, I., García, J.M., Montserrat-Sentís, B., Baulida, J., Bonilla, F., de Herreros, A.G., and Díaz, V.M. (2010). The hypoxia-controlled FBXL14 ubiquitin ligase targets SNAIL1 for proteasome degradation. *The Journal of biological chemistry* *285*, 3794-3805.

Viñas-Castells, R., Frías, Á., Robles-Lanuza, E., Zhang, K., Longmore, G.D., García de Herreros, A., and Díaz, V.M. (2014). Nuclear ubiquitination by FBXL5 modulates Snail1 DNA binding and stability. *Nucleic Acids Research* *42*, 1079-1094.

Vlachogiannis, G., Hedayat, S., Vatsiou, A., Jamin, Y., Fernandez-Mateos, J., Khan, K., Lampis, A., Eason, K., Huntingford, I., Burke, R., *et al.* (2018). Patient-derived organoids model treatment response of metastatic gastrointestinal cancers. *Science* *359*, 920-926.

Von Rosen, D. (1991). The growth curve model: a review. *Communications in Statistics - Theory and Methods* *20*, 2791-2822.

Wade, B.E., Zhao, J., Ma, J., Hart, C.M., and Sutliff, R.L. (2017). Hypoxia-Induced Changes in the Ubiquitin Proteasome System in a Mouse Model of Pulmonary Hypertension. *The FASEB Journal* *31*, 1016.1017-1016.1017.

Walseng, E., Furuta, K., Bosch, B., Weih, K.A., Matsuki, Y., Bakke, O., Ishido, S., and Roche, P.A. (2010). Ubiquitination regulates MHC class II-peptide complex retention and degradation in dendritic cells. *Proc Natl Acad Sci U S A* *107*, 20465-20470.

Wang, C., Li, X., Zhang, J., Ge, Z., Chen, H., and Hu, J. (2018a). EZH2 contributes to 5-FU resistance in gastric cancer by epigenetically suppressing FBXO32 expression. *Onco Targets Ther* *11*, 7853-7864.

Wang, H., Bauzon, F., Ji, P., Xu, X., Sun, D., Locker, J., Sellers, R.S., Nakayama, K., Nakayama, K.I., Cobrinik, D., *et al.* (2009). Skp2 is required for survival of aberrantly

proliferating Rb1-deficient cells and for tumorigenesis in Rb1+/- mice. *Nature genetics* 42, 83.

Wang, H., Shi, H., Rajan, M., Canarie, E.R., Hong, S., Simoneschi, D., Pagano, M., Bush, M.F., Stoll, S., Leibold, E.A., *et al.* (2020a). FBXL5 Regulates IRP2 Stability in Iron Homeostasis via an Oxygen-Responsive [2Fe2S] Cluster. *Mol Cell* 78, 31-41.e35.

Wang, K., Qu, X., Liu, S., Yang, X., Bie, F., Wang, Y., Huang, C., and Du, J. (2018b). Identification of aberrantly expressed F-box proteins in squamous-cell lung carcinoma. *Journal of Cancer Research and Clinical Oncology* 144, 1509-1521.

Wang, L., Liao, J., Yang, X., Feng, W., Chen, S., and Zheng, G. (2014a). Abstract 4433: Fbxw11 promotes leukemia development by activating the NF- κ B signaling pathway. *Cancer Research* 74, 4433-4433.

Wang, N., Ma, Q., Peng, P., Yu, Y., Xu, S., Wang, G., Ying, Z., and Wang, H. (2020b). Autophagy and Ubiquitin-Proteasome System Coordinate to Regulate the Protein Quality Control of Neurodegenerative Disease-Associated DCTN1. *Neurotox Res* 37, 48-57.

Wang, N., Wang, X., Tan, H.Y., Li, S., Tsang, C.M., Tsao, S.W., and Feng, Y. (2016). Berberine Suppresses Cyclin D1 Expression through Proteasomal Degradation in Human Hepatoma Cells. *Int J Mol Sci* 17.

Wang, Y., Ren, F., Wang, Y., Feng, Y., Wang, D., Jia, B., Qiu, Y., Wang, S., Yu, J., Sung, J.J., *et al.* (2014b). CHIP/Stub1 functions as a tumor suppressor and represses NF- κ B-mediated signaling in colorectal cancer. *Carcinogenesis* 35, 983-991.

Wang, Z., Liu, P., Inuzuka, H., and Wei, W. (2014c). Roles of F-box proteins in cancer. *Nat Rev Cancer* 14, 233-247.

Wang, Z., Zhou, L., Xiong, Y., Yu, S., Li, H., Fan, J., Li, F., Su, Z., Song, J., Sun, Q., *et al.* (2019). Salinomycin exerts anti-colorectal cancer activity by targeting the β -catenin/T-cell factor complex. *Br J Pharmacol* 176, 3390-3406.

Weinstein, J.N., Collisson, E.A., Mills, G.B., Shaw, K.R., Ozenberger, B.A., Ellrott, K., Shmulevich, I., Sander, C., and Stuart, J.M. (2013). The Cancer Genome Atlas Pan-Cancer analysis project. *Nat Genet* 45, 1113-1120.

Weizer-Stern, O., Adamsky, K., Margalit, O., Ashur-Fabian, O., Givol, D., Amariglio, N., and Rechavi, G. (2007). Hcpidin, a key regulator of iron metabolism, is transcriptionally activated by p53. *Br J Haematol* 138, 253-262.

Wendler, A., and Wehling, M. (2010). The translatability of animal models for clinical development: biomarkers and disease models. *Curr Opin Pharmacol* 10, 601-606.

Wenzel, D.M., Lissounov, A., Brzovic, P.S., and Klevit, R.E. (2011). UBC7 reactivity profile reveals parkin and HHARI to be RING/HECT hybrids. *Nature* 474, 105-108.

Westphal, D., Kluck, R.M., and Dewson, G. (2014). Building blocks of the apoptotic pore: how Bax and Bak are activated and oligomerize during apoptosis. *Cell Death Differ* 21, 196-205.

Whiteaker, J.R., Halusa, G.N., Hoofnagle, A.N., Sharma, V., MacLean, B., Yan, P., Wrobel, J.A., Kennedy, J., Mani, D.R., Zimmerman, L.J., *et al.* (2014). CPTAC Assay Portal: a repository of targeted proteomic assays. *Nature Methods* 11, 703-704.

Wilkinson, K.D. (2005). The discovery of ubiquitin-dependent proteolysis. *Proceedings of the National Academy of Sciences* 102, 15280-15282.

Williams, G.H., and Stoeber, K. (2012). The cell cycle and cancer. *The Journal of Pathology* 226, 352-364.

Wilson, M.J., Dekker, J.W., Bruns, E., Borstlap, W., Jeekel, J., Zwaginga, J.J., and Schipperus, M. (2018). Short-term effect of preoperative intravenous iron therapy in colorectal cancer patients with anemia: results of a cohort study. *Transfusion* 58, 795-803.

Winklhofer, K.F., Tatzelt, J., and Haass, C. (2008). The two faces of protein misfolding: gain- and loss-of-function in neurodegenerative diseases. *Embo j* 27, 336-349.

Wirawan, E., Vanden Berghe, T., Lippens, S., Agostinis, P., and Vandenabeele, P. (2012). Autophagy: for better or for worse. *Cell Res* 22, 43-61.

Wolf, J.B.W. (2013). Principles of transcriptome analysis and gene expression quantification: an RNA-seq tutorial. *Molecular Ecology Resources* 13, 559-572.

Wong M, C.P. (2012). mTOR and Epileptogenesis in Developmental Brain Malformations. In Jasper's Basic Mechanisms of the Epilepsies [Internet] 4th edition R.M. Avoli M, et al., ed. (Bethesda (MD): National Center for Biotechnology Information (US); 2012).

Wouters, B.G., and Koritzinsky, M. (2008). Hypoxia signalling through mTOR and the unfolded protein response in cancer. *Nature Reviews Cancer* 8, 851-864.

Wu, B., Liu, Z.-Y., Cui, J., Yang, X.-M., Jing, L., Zhou, Y., Chen, Z.-N., and Jiang, J.-L. (2017). F-Box Protein FBXO22 Mediates Polyubiquitination and Degradation of CD147 to Reverse Cisplatin Resistance of Tumor Cells. *Int J Mol Sci* 18, 212.

Wu, M., Xia, X., Hu, J., Fowlkes, N.W., and Li, S. (2021). WSX1 act as a tumor suppressor in hepatocellular carcinoma by downregulating neoplastic PD-L1 expression. *Nat Commun* 12, 3500.

Wu, P., Wang, F., Wang, Y., Men, H., Zhu, X., He, G., Ma, W., Xin, S., Wu, J., Liao, W., et al. (2015a). Significance of FBX8 in progression of gastric cancer. *Experimental and Molecular Pathology* 98, 360-366.

Wu, W., Ding, H., Cao, J., and Zhang, W. (2015b). FBXL5 Inhibits Metastasis of Gastric Cancer Through Suppressing Snail1. *Cellular Physiology and Biochemistry* 35, 1764-1772.

Wu, W.D., Wang, M., Ding, H.H., and Qiu, Z.J. (2016). FBXL5 attenuates RhoGDI2-induced cisplatin resistance in gastric cancer cells. *Eur Rev Med Pharmacol Sci* 20, 2551-2557.

Xiao, G.G., Zhou, B.S., Somlo, G., Portnow, J., Juhasz, A., Un, F., Chew, H., Gandara, D., and Yen, Y. (2008). Identification of F-box/LLR-repeated protein 17 as potential useful biomarker for breast cancer therapy. *Cancer Genomics Proteomics* 5, 151-160.

Xiao, Y., Yin, C., Wang, Y., Lv, H., Wang, W., Huang, Y., Perez-Losada, J., Snijders, A.M., Mao, J.H., and Zhang, P. (2018). FBXW7 deletion contributes to lung tumor development and confers resistance to gefitinib therapy. *Molecular oncology* 12, 883-895.

Xie, C.-M., Wei, W., and Sun, Y. (2013). Role of SKP1-CUL1-F-box-protein (SCF) E3 ubiquitin ligases in skin cancer. *J Genet Genomics* 40, 97-106.

Xiong, Y., Sun, F., Dong, P., Watari, H., Yue, J., Yu, M.-f., Lan, C.-y., Wang, Y., and Ma, Z.-b. (2017). iASPP induces EMT and cisplatin resistance in human cervical cancer through miR-20a-FBXL5/BTG3 signaling. *Journal of Experimental & Clinical Cancer Research* 36, 48.

Xu, J., Zhou, W., Yang, F., Chen, G., Li, H., Zhao, Y., Liu, P., Li, H., Tan, M., Xiong, X., et al. (2017). The β -TrCP-FBXW2-SKP2 axis regulates lung cancer cell growth with FBXW2 acting as a tumour suppressor. *Nature Communications* 8, 14002.

Yamanaka, K., Ishikawa, H., Megumi, Y., Tokunaga, F., Kanie, M., Rouault, T.A., Morishima, I., Minato, N., Ishimori, K., and Iwai, K. (2003). Identification of the ubiquitin-protein ligase that recognizes oxidized IRP2. *Nat Cell Biol* 5, 336-340.

Yamauchi, T., Nishiyama, M., Moroishi, T., Kawamura, A., and Nakayama, K.I. (2017). FBXL5 Inactivation in Mouse Brain Induces Aberrant Proliferation of Neural Stem Progenitor Cells. *Molecular and Cellular Biology* 37.

Yan, L., Lin, M., Pan, S., Assaraf, Y.G., Wang, Z.-w., and Zhu, X. (2020). Emerging roles of F-box proteins in cancer drug resistance. *Drug Resistance Updates* 49, 100673.

Yang, C., Zhou, Q., Li, M., Tong, X., Sun, J., Qing, Y., Sun, L., Yang, X., Hu, X., Jiang, J., *et al.* (2016). Upregulation of CYP2S1 by oxaliplatin is associated with p53 status in colorectal cancer cell lines. *Scientific Reports* 6, 33078.

Yang, H., Lu, X., Liu, Z., Chen, L., Xu, Y., Wang, Y., Wei, G., and Chen, Y. (2015). FBXW7 suppresses epithelial-mesenchymal transition, stemness and metastatic potential of cholangiocarcinoma cells. *Oncotarget* 6, 6310-6325.

Yang, H., Wu, J., Zhang, J., Yang, Z., Jin, W., Li, Y., Jin, L., Yin, L., Liu, H., and Wang, Z. (2019). Integrated bioinformatics analysis of key genes involved in progress of colon cancer. *Mol Genet Genomic Med* 7, e00588.

Yang, J., Antin, P., Berx, G., Blanpain, C., Brabletz, T., Bronner, M., Campbell, K., Cano, A., Casanova, J., Christofori, G., *et al.* (2020). Guidelines and definitions for research on epithelial–mesenchymal transition. *Nature Reviews Molecular Cell Biology* 21, 341-352.

Yao, H., Su, S., Xia, D., Wang, M., Li, Z., Chen, W., Ren, L., and Xu, L. (2018). F-box and leucine-rich repeat protein 5 promotes colon cancer progression by modulating PTEN/PI3K/AKT signaling pathway. *Biomedicine & Pharmacotherapy* 107, 1712-1719.

Ye, Y., and Rape, M. (2009). Building ubiquitin chains: E2 enzymes at work. *Nature Reviews Molecular Cell Biology* 10, 755.

Yeh, C.-H., Bellon, M., and Nicot, C. (2018). FBXW7: a critical tumor suppressor of human cancers. *Mol Cancer* 17, 115-115.

Yin, Y., Bijvelds, M., Dang, W., Xu, L., van der Eijk, A.A., Knipping, K., Tuysuz, N., Dekkers, J.F., Wang, Y., de Jonge, J., *et al.* (2015). Modeling rotavirus infection and antiviral therapy using primary intestinal organoids. *Antiviral Research* 123, 120-131.

Yin, Z., Haynie, J., Yang, X., Han, B., Kiatchosakun, S., Restivo, J., Yuan, S., Prabhakar, N.R., Herrup, K., Conlon, R.A., *et al.* (2002). The essential role of Cited2, a negative regulator for HIF-1 α , in heart development and neurulation. *Proceedings of the National Academy of Sciences* 99, 10488-10493.

Yokobori, T., Yokoyama, Y., Mogi, A., Endoh, H., Altan, B., Kosaka, T., Yamaki, E., Yajima, T., Tomizawa, K., Azuma, Y., *et al.* (2014). FBXW7 mediates chemotherapeutic sensitivity and prognosis in NSCLCs. *Molecular cancer research : MCR* 12, 32-37.

Young, M.-J., Hsu, K.-C., Lin, T.E., Chang, W.-C., and Hung, J.-J. (2019). The role of ubiquitin-specific peptidases in cancer progression. *Journal of Biomedical Science* 26, 42.

Yousefi, S., Perozzo, R., Schmid, I., Ziemiecki, A., Schaffner, T., Scapozza, L., Brunner, T., and Simon, H.U. (2006). Calpain-mediated cleavage of Atg5 switches autophagy to apoptosis. *Nat Cell Biol* 8, 1124-1132.

Yurgelun, M.B., Masciari, S., Joshi, V.A., Mercado, R.C., Lindor, N.M., Gallinger, S., Hopper, J.L., Jenkins, M.A., Buchanan, D.D., Newcomb, P.A., *et al.* (2015). Germline

TP53 Mutations in Patients With Early-Onset Colorectal Cancer in the Colon Cancer Family Registry. *JAMA Oncol* 1, 214-221.

Zaky, W., Manton, C., Miller, C.P., Khatua, S., Gopalakrishnan, V., and Chandra, J. (2017). The ubiquitin-proteasome pathway in adult and pediatric brain tumors: biological insights and therapeutic opportunities. *Cancer metastasis reviews* 36, 617-633.

Zarogoulidis, P., Lampaki, S., Turner, J.F., Huang, H., Kakolyris, S., Syrigos, K., and Zarogoulidis, K. (2014). mTOR pathway: A current, up-to-date mini-review (Review). *Oncology letters* 8, 2367-2370.

Zerr, M. (2021). Ubiquitin-Proteasome System, pp. Diagram of Ubiquitin Proteasome System.

Zhang, C., Li, X., Adelmant, G., Dobbins, J., Geisen, C., Oser, M.G., Wucherpfenning, K.W., Marto, J.A., and Kaelin, W.G. (2015). Peptidic degron in EID1 is recognized by an SCF E3 ligase complex containing the orphan F-box protein FBXO21. *Proceedings of the National Academy of Sciences* 112, 15372-15377.

Zhang, F., Wang, W., Tsuji, Y., Torti, S.V., and Torti, F.M. (2008). Post-transcriptional modulation of iron homeostasis during p53-dependent growth arrest. *The Journal of biological chemistry* 283, 33911-33918.

Zhang, H., Chen, F., He, Y., Yi, L., Ge, C., Shi, X., Tang, C., Wang, D., Wu, Y., and Nian, W. (2017). Sensitivity of non-small cell lung cancer to erlotinib is regulated by the Notch/miR-223/FBXW7 pathway. *Bioscience reports* 37.

Zhang, H., Wong, C.-M., Wei, H., Gilkes, D., Korangath, P., Chaturvedi, P., Schito, L., Chen, J., Krishnamachary, B., Winnard, P., *et al.* (2011). HIF-1-dependent Expression of Angiopoietin-like 4 and L1CAM Mediates Vascular Metastasis of Hypoxic Breast Cancer Cells to the Lungs. *Oncogene* 31, 1757-1770.

Zhang, N., Liu, J., Ding, X., Aikhionbare, F., Jin, C., and Yao, X. (2007). FBXL5 interacts with p150Glued and regulates its ubiquitination. *Biochemical and Biophysical Research Communications* 359, 34-39.

Zhang, X., Zhang, W., Ma, S.F., Miasniakova, G., Sergueeva, A., Ammosova, T., Xu, M., Nekhai, S., Nourai, M., Wade, M.S., *et al.* (2014). Iron deficiency modifies gene expression variation induced by augmented hypoxia sensing. *Blood Cells Mol Dis* 52, 35-45.

Zhang, Y., and Zhang, B. (2006). D4-GDI, a Rho GTPase Regulator, Promotes Breast Cancer Cell Invasiveness. *Cancer Research* 66, 5592-5598.

Zhang, Z., Yao, L., Yang, J., Wang, Z., and Du, G. (2018). PI3K/Akt and HIF-1 signaling pathway in hypoxia-ischemia (Review). *Mol Med Rep* 18, 3547-3554.

Zhao, N., Powell, R.T., Yuan, X., Bae, G., Roarty, K.P., Stossi, F., Strempl, M., Toneff, M.J., Johnson, H.L., Mani, S.A., *et al.* (2021a). Morphological screening of mesenchymal mammary tumor organoids to identify drugs that reverse epithelial-mesenchymal transition. *Nature Communications* 12, 4262.

Zhao, Q., Xu, N., Guo, H., and Li, J. (2020). Identification of the diagnostic signature of sepsis based on bioinformatic analysis of gene expression and machine learning. *Comb Chem High Throughput Screen*.

Zhao, Y., Li, M.-C., Konaté, M.M., Chen, L., Das, B., Karlovich, C., Williams, P.M., Evrard, Y.A., Doroshov, J.H., and McShane, L.M. (2021b). TPM, FPKM, or Normalized Counts? A Comparative Study of Quantification Measures for the Analysis of RNA-seq

Data from the NCI Patient-Derived Models Repository. *Journal of Translational Medicine* 19, 269.

Zheng, C., Schneider, J.W., and Hsieh, J. (2020). Role of RB1 in human embryonic stem cell-derived retinal organoids. *Dev Biol*.

Zheng, N., Wang, Z., and Wei, W. (2016a). Ubiquitination-mediated degradation of cell cycle-related proteins by F-box proteins. *The International Journal of Biochemistry & Cell Biology* 73, 99-110.

Zheng, Q., Huang, T., Zhang, L., Zhou, Y., Luo, H., Xu, H., and Wang, X. (2016b). Dysregulation of Ubiquitin-Proteasome System in Neurodegenerative Diseases. *Front Aging Neurosci* 8, 303-303.

Zheng, Z., He, X.-Y., Li, J.-F., Yu, B.-Q., Chen, X.-H., Ji, J., Zhang, J.-N., Gu, Q.-L., Zhu, Z.-G., and Liu, B.-Y. (2013). RhoGDI2 confers resistance to 5-fluorouracil in human gastric cancer cells. *Oncology letters* 5, 255-260.

Zhong, W., Zhu, H., Sheng, F., Tian, Y., Zhou, J., Chen, Y., Li, S., and Lin, J. (2014). Activation of the MAPK11/12/13/14 (p38 MAPK) pathway regulates the transcription of autophagy genes in response to oxidative stress induced by a novel copper complex in HeLa cells. *Autophagy* 10, 1285-1300.

Zhou, H., Liu, Y., Zhu, R., Ding, F., Wan, Y., Li, Y., and Liu, Z. (2017). FBXO32 suppresses breast cancer tumorigenesis through targeting KLF4 to proteasomal degradation. *Oncogene* 36, 3312-3321.

Zhou, L., Zhang, W., Sun, Y., and Jia, L. (2018). Protein neddylation and its alterations in human cancers for targeted therapy. *Cell Signal* 44, 92-102.

Zhou, Z., Zwelling, L.A., Ganapathi, R., and Kleinerman, E.S. (2001). Enhanced etoposide sensitivity following adenovirus-mediated human topoisomerase IIalpha gene transfer is independent of topoisomerase IIbeta. *Br J Cancer* 85, 747-751.

Zhou, Z.D., Sathiyamoorthy, S., Angeles, D.C., and Tan, E.K. (2016). Linking F-box protein 7 and parkin to neuronal degeneration in Parkinson's disease (PD). *Molecular Brain* 9, 41.

Zhu, E., Wu, H., Chen, W., Qin, Y., Liu, J., Fan, S., Ma, S., Wu, K., Mao, Q., Luo, C., *et al.* (2021a). Classical swine fever virus employs the PERK- and IRE1-dependent autophagy for viral replication in cultured cells. *Virulence* 12, 130-149.

Zhu, J., Deng, S., Duan, J., Xie, X., Xu, S., Ran, M., Dai, X., Pu, Y., and Zhang, X. (2014a). FBXL20 acts as an invasion inducer and mediates E-cadherin in colorectal adenocarcinoma. *Oncology letters* 7, 2185-2191.

Zhu, J., Deng, S., Duan, J., Xie, X., Xu, S., Ran, M., Dai, X., Pu, Y., and Zhang, X. (2014b). FBXL20 acts as an invasion inducer and mediates E-cadherin in colorectal adenocarcinoma. *Oncology letters* 7, 2185-2191.

Zhu, Y., Huang, S., Chen, S., Chen, J., Wang, Z., Wang, Y., and Zheng, H. (2021b). SOX2 promotes chemoresistance, cancer stem cells properties, and epithelial-mesenchymal transition by β -catenin and Beclin1/autophagy signaling in colorectal cancer. *Cell Death Dis* 12, 449.